Jan Petr

Processing and application of arterial spin labeling magnetic resonance imaging

Czech Technical University in Prague

Faculty of Electrical Engineering

Department of Cybernetics

Habilitation Thesis

Processing and application of arterial spin labeling magnetic resonance imaging

Prague, August 2022 **Jan Petr**

Copyright

Abstract

This thesis focuses on the image processing methods for brain perfusion measurement using a magnetic resonance imaging (MRI) sequence called arterial spin labeling (ASL). We show the importance of dealing with brain volume changes as a measurement confounder, we propose a framework for integrating all processing steps in a robust processing pipeline, and lastly, we show an application of the ASL acquisition and processing to adverse effect measurements in healthy brain tissue of patients undergoing brain radio-chemotherapy demonstrating the usefulness of the method in uncovering structural and physiological changes in the brain.

Anotace

Tato habilitační práce se soustředí na použití metod zpracování obrazu k meření prokrvení mozku magnetickou rezonancí (MRI) pomocí sekvence zvané arterial spin labeling (ASL). Ukazujeme zde význam korekce změn objemu mozku jakožto faktoru ovlivnující měření. Dále navrhujeme obecný rámec pro integrování hlavních kroků zpracování obrazu do robustního softwarového balíku. Nakonec předvádíme aplikaci meření a zpracování ASL dat pro měření vedlejších účinků radiochemoterapie na zdravou mozkovou tkán. Na závěr ukazujeme výsledky použití této metody na odhalení anatomických a fyziologických změn na mozku v důsledku této terapie.

Keywords

arterial spin labeling, ASL, brain perfusion, cerebral blood flow, CBF, image processing, radiochemotherapy, magnetic resonance imaging, MRI

Klíčová slova

arterial spin labeling, ASL, mozkové prokrvení, zpracování obrazu, radiochemoterapie, magnetická rezonance, MRI

Acknowledgment

The work presented in this thesis and publications that are listed on my CV are a product of joint collaborative effort that would not have been possible without the help, inspiring discussions, and sharing of data from a lot of people.

I thank the entire team from the Helmholtz-Zentrum Dresden-Rossendorf. Thank you all - Jens Maus, Jens Langner, Frank Hofheinz, Pavel Nikulin, Georg Schramm, and Alexander Lougovski - for the great years at the Endstation Rossendorf.

I thank all the clinical colleagues from the University Hospital Dresden - Bettina Beuthien-Baumann, Annekatrin Seidlitz, Ivan Platzek, Jörg Kotzerke, Mechtild Krause, and Jennifer Linn - for all the consultations and datasets.

I thank the team VISAGES/EMPENN from INRIA Rennes, for showing me the world of medical imaging and for being great friends as well. I thank Elise Bannier, Aymeric Topodoko Stamm, Camille Maumet, Olivier Commowick, Daniel Münch, Daniel García-Lorenzo, Fernanda Palhano, Nicolas Wiest-Daesslé, Benoit Combès, Pierre Maurel, Hélène Raoult, Jean-Christophe Ferré, Alexander Krupa, and Christian Barillot for the three great years.

I thank my supervisors from the Institute of Radiopharmaceutical Cancer Research at HZDR - Jörg Steinbach, Klaus Kopka, Michael Bachmann - for their continuous moral support, and for the more practical always-in-time contract prolongations.

I would like to thank Frederik Barkhof for adopting me to the VUmc team and all the great colleagues I met there - Joost Kuijer, Alle Meije Wink, Philip de Witt Hamer, Niels Verburg, Koen Baas, Vera Keil, Ivar Wamelink. Special thanks go to the kids that make me very proud - Mathijs Dijsselhof and Beatriz Padrela.

I would like to thank all the colleagues that collaborated with me in the last years despite that our common work is not included in this thesis explicitly. I thank the team from the Technical University of Munich - Christine Preibisch, Stephan Kaczmarcz, and Jens Göttler. My big gratitude goes to the team from the University of Ghent - Rik Achten, Patricia Clement, and Pieter Vandemaele. I also thank Saima Hilal from the University of Singapore for all the interesting collaboration; the team from the Motol University Hospital - Jakub Otáhal and Yeva Prysiazhniuk; the team from Erasmus medical center in Rotterdam - Catherine de Planque, Marjolein Dremmen, and Irene Mathijssen. I thank the wonderful people from Norway - Wibeke Nordhøy, Beathe Sitter, Wilhelm Iversen, and Øystein Bech Gadmar - no workshop or defense is complete without you singing a scientific cover of a known pop song. Lastly, I would like to thank everybody from the GliMR and the ASL crowds for both scientific collaborations and all the non-scientific fun as well.

On a semi-personal, semi-scientific note, I thank my partner in crime Henk-Jan Mutsaerts and Rik Achten for all the great conference biking and T2-allstar entertainment, Enrico de Vita for

juggling lessons and surfing, and Iris Asllani for the intellectually stimulating part of the conference meetings.

I thank my family - my parents and my sister Zuzka for their support, and my wife and daughters, Markéta, Sára, Klára, and Sofie, for making me happy and giving me enough time to finish writing this document. And now for something completely different. I thank my group leader prof. Jörg van den Hoff for great leadership in the last years, for always keeping the scientific focus on scientific integrity, and for standing behind me and supporting my work. You are truly like a bat's piss.

Content

1. General motivation regarding perfusion imaging

While perfusion is defined in general as the passage of any fluid through an organ or a tissue, we will focus here solely on blood perfusion. Blood is essential for the transport of oxygen and nutrients and clearing of the waste products of metabolism, and perfusion defines the rate at which the blood is delivered to the tissue typically measured in units ml of blood per minute per 100 g of tissue [ml/min/100g]. Keeping a normal rate of perfusion is absolutely essential for the normal function of the body as chronic or acute disruption of blood delivery can have severe consequences on the function of the affected tissue or even cell death.

The main focus of this thesis is the perfusion of the brain tissue - the cerebral blood flow (CBF). Blood is delivered to the brain by a pair of internal carotid arteries and vertebral arteries. Passing through the Circle-of-Willis and branching into distributing arteries, the blood is finally delivered to capillaries where oxygen and nutrients are delivered across the blood-brain barrier to the recipient tissue. This process can be disrupted at any level - starting at the reduced cardiac output, or plaques, clots, or constriction at either macrovessel or microcapillary level - causing problems with the blood flow delivery. Acute or chronic changes in CBF are at the root of several diseases ranging from an abrupt and nearly complete disruption in blood flow in cerebral ischemic stroke, chronic hypoperfusion typical for certain types of dementia, to hyperperfusion due to an abrupt growth of new vessels accompanying certain types of brain tumors. Changes in perfusion patterns are, however, present in neurodevelopmental disorders, epilepsies, or mental illnesses. CBF is thus an important prognostic and diagnostic tool in a wide range of diseases and also neuroscientific studies of normal brain function.

While non-invasive measurement of blood flow in even bigger arteries was not possible decades ago, with the advent of new imaging methods, it is possible to obtain images of a spectrum of different brain structures and processes ranging from anatomical imaging to metabolic and physiological imaging. Perfusion, as one of the most important physiological processes in the brain, has been in the focus for a long time and due to the recent advances in magnetic resonance imaging (MRI), it is possible now to obtain detailed quantitative maps of perfusion. Further research and development are, however, needed to validate the methods and enable their application outside of the field of clinical research in everyday clinical routine.

2. Introduction

Cerebral blood flow (CBF), the amount of blood that perfuses unit volume of tissue per unit time is an important physiological parameter, which has a very wide range of applications from neurodegenerative diseases and neoplasm to brain development and psychological studies in healthy volunteers.

The most common clinical modalities that provide information about blood delivery status are computer tomography (CT) and ultrasound. CT can measure the ability of blood to reach

different parts of tissue by dynamically measuring the distribution of a special intravenously injected contrast agent [1]. The ultrasound, on the other hand, measures the velocity of blood flow in vessels [2]. While both diagnostic procedures are relatively cheap and easy to perform, they have serious shortcomings. Invasiveness, a non-negligible dose of ionizing radiation, and the inability to provide quantitative images of perfusion is the drawback of the CT-based method. The ultrasound can only measure velocity in bigger vessels and is not well suited for the brain.

The real opportunities to obtain 3D maps of perfusion came with magnetic resonance imaging (MRI). MRI is a complex imaging modality that uses the spin properties of hydrogen atoms placed in a strong external magnetic field and is perfect for imaging soft-tissue contrast [3]. While MRI started uniquely as a method for measuring tissue structure, novel methods are now emerging that are able to, with software-only modifications of the measurement protocol, obtain qualitative and even quantitative maps of physiological and metabolic processes in the living tissue. If we exclude positron emission tomography and a ^{15}O-H_2O tracer that has a half-life too short for any meaningful clinical use [4], MRI is the only modality that is able to reliably obtain 3D maps of perfusion.

Two basic strategies exist to measure perfusion with MRI - with and without injection of gadolinium-based-contrast agent (GBCA). GBCA is a liquid substance containing bound gadolinium that, upon injection into vessels, locally modifies the magnetic properties of blood and thus allows imaging distribution of the blood mixed with this contrast agent using MRI. Two types of GBCA sequences exist - dynamic susceptibility contrast (DSC) and dynamic contrast-enhanced (DCE). DSC sequence relies upon signal loss in the presence of GBCA caused by shortening of the T2-relaxation time. DCE sequence, on the contrary, relies on the signal increase due to T1-relaxation time shortening. Both methods are relatively reliable and can produce maps of CBF and cerebral blood volume (CBV) in the case of DSC [5], and K_{trans} maps of transfer rate across the blood-brain-barrier in the case of DCE [6]. The drawback of both methods is the difficulty of obtaining reliable absolute quantitative values [7]. Moreover, GBCA can be dangerous for patients with impaired renal function, and there are growing concerns and GBCA instability causing a release of free gadolinium from the GBCA and its subsequent accumulation in the brain [8]. An alternative for perfusion measurement to techniques using GBCA is called arterial spin labeling (ASL) [9]. ASL uses magnetically labeled water as an endogenous tracer, and it is thus completely non-invasive. As it avoids the use of GBCA, ASL is immediately repeatable, it does not have pharmacological side effects, and it is also easier to acquire, cheaper, and more comfortable than DCE or DSC sequences. Finally, it also allows quantitative estimation of CBF at comparable accuracy to the gold standard of ^{15}O-H_2O-PET [4]. The main disadvantage of ASL is its lower availability at clinical sites, more complex processing and interpretation, and insufficient level of validation for widespread clinical use.

3. State of the art

3.1 Magnetic resonance imaging

Magnetic Resonance Imaging (MRI) is a medical imaging modality that utilizes an extremely strong static magnetic field to align and measure the summed magnetization of specific protons, mostly hydrogen. This magnetization cannot be measured directly. Instead, it is probed by exciting the tissue through radio frequency (RF) pulses – at a resonance frequency proportional to the magnetic field strength – to a higher energy state and then measuring the retransmitted signal as the system returns to equilibrium. The amount and time profile of the released energy provides us with information about the magnetic properties of the tissue that are directly dependent on the density and molecular binding of the hydrogen atoms.

Unfortunately, the resonance frequency is too small to allow spatial encoding of the signal source to produce images. However, because of its dependence on the strength of the magnetic field, it is possible to encode the signal location for each voxel to its frequency. For this purpose, three relatively weak orthogonally positioned gradient magnets are added inside the scanner bore to introduce small and spatially dependent magnetic field strength changes on top of the main magnetic field. By modifying the resonance frequency locally and using a narrow band excitation RF pulses, we are able to perform spatial selective tissue excitation. By further modifying the magnetic gradients during the signal readout, we can encode the signal's spatial position into its frequency and phase and thus obtain images of the magnetic properties of the tissue.

Specialized acquisition sequences composed of excitation RF pulses and a specific scheme of magnetic gradient switching are then used for various types of image encoding. Image contrast then depends on different magnetic properties of the tissue and can be weighted by tissue parameters like hydrogen density or T1 and T2 relaxation time. The images are sensitive to, e.g., water, fat, or macromolecular content in the tissue. The first MRI applications were used to obtain structural images only. However, due to the high versatility of MRI, new sequences have emerged that acquire images of tissue molecular composition and also metabolic or physiological processes.

3.2 Arterial spin labeling

Arterial spin labeling (ASL) is a non-invasive MRI technique that uses blood water as an endogenous tracer to measure perfusion [10]. ASL uses a dedicated 180-degree RF pulse to invert the magnetization of blood in the feeding arteries - in the neck in the case of brain perfusion measurement. After a brief period of 1.5-2 seconds to allow the blood to reach imaged organ, a standard image of the region of interest is acquired called the label image. A second image, called a control image, is subsequently acquired without prior labeling. There is a slight difference in the signal between those two images (typically around 1-2%) caused by the inflow of blood with inverted magnetization. When the control and label images are

subtracted, the difference is proportional to the amount of labeled blood that arrived in the tissue and can be used to calculate quantitative images of perfusion [11].

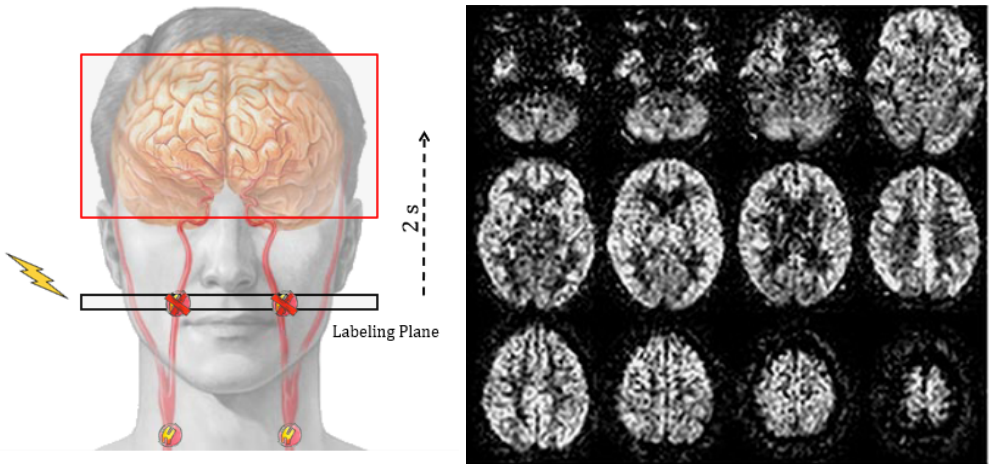

Figure 1. Left - a visual scheme of the pseudo-continuous ASL labeling plane labeling blood at the internal carotid arteries, and the field-of-view brain image volume acquired after a specific waiting time called post-labeling delay (usually around 1.5 to 2 seconds). On the right, there are several axial slices displaying the perfusion-weighted difference image obtained with ASL.

First ASL experiments were done in 1992, demonstrating the feasibility of measuring brain perfusion [10]. Since then, many practical improvements on the acquisition side had to be made, such as the optimization of the time between the labeling and the acquisition [12], reducing the signal in the static tissue to improve the SNR of the subtraction [13,14], and improving the labeling from a single large slab to a train of thin pulses applied for about one or two seconds [15]. These additional features improved the quality of ASL images to a level where first pilot studies could have been done in small clinical datasets of, e.g., patients with cerebrovascular and neurodegenerative diseases [16,17].

Following these pilot studies, more work was done on ASL to validate it and prepare it for use in clinical research. Several studies were performed to evaluate the reproducibility of ASL in single-subjects [18,19], in multi-center studies [20,21], and in comparison with ^{15}O-H_2O PET [4,22].

3.3 ASL data processing

With ASL being technically and methodologically sound, several large multicenter observational studies and clinical trials used it for acquiring perfusion data [23–25]. However, on the side of image processing, there is still a rather large disparity between the software used for ASL image processing [26–32]. This can lead to different results being achieved at different labs depending on the pipeline and the exact approach used to process and evaluate the data. This heterogeneity decreases the reproducibility of the ASL research and complicates meta-analysis and comparison of results across studies. Therefore, a consensus on the basics and best practices to robustly process ASL data is needed to reduce the possible bias across studies stemming from the use of different methodologies.

3.4 Partial volume processing

Despite the general improvements in ASL image quality, the spatial resolution of ASL has remained relatively low to ensure sufficient SNR, typically being on the order of around 3-4 mm isotropic. As a result, most ASL voxels contain a mixture of perfusion signals from various types of brain tissue - gray matter (GM), white matter (WM), and cerebrospinal fluid (CSF). Usually, perfusion is highest in the cerebral cortex and lower in the tissue composed chiefly of neuronal axons. Thus, perfusion is typically reported to be 2–4.5 times higher in GM than in WM [33,34], with CSF not being perfused at all. This makes the measured ASL signal in each voxel highly dependent on its fractional composition of GM and WM - an effect called partial volume. Unfortunately, most of the clinically relevant evaluations of perfusion are performed using tissue-specific values. Theforeofe, these partial volume effects can bias analysis, especially if major differences between GM and WM volumes between individuals or groups are expected as a result of disease or aging [35]. While partial volume correction (PVC) methods were introduced for correcting these effects, there is still no consensus on their real added value.

3.5 Application to neurooncology

Following the methodological development and first pilot results in clinical data, ASL is now becoming increasingly used in clinical applications [36,37]. Brain tumors are one of the diagnoses where ASL can provide relevant information, for example, by helping to distinguish the tumor grade or to evaluate the treatment response [38–41]. A further possibility for ASL application in neurooncology is the assessment of adverse effects of cancer therapy on healthy brain tissue. Radiochemotherapy of both brain and body solid tumors is associated with a range of adverse events from cognitive decline and decreased quality of life to structural damage to the tissue [42,43]. While certain mechanisms of damage are being investigated and genetic predisposition for treatment damage is present in some patients, the complete mechanism of the damage and its individual sensitivity is not understood. Non-invasive biomarkers of treatment-induced damage in normal tissue are thus needed to be able to study the etiology of damage and also to obtain early markers of tissue damage to allow timely adjustment of treatment. ASL-measured CBF is a marker of damage to vascular endothelial cells and associated damage to the microvasculature is one form of damage frequently encountered in patients undergoing radiochemotherapy.

4. General aims of the thesis

The presented cumulative thesis comprises seven peer-reviewed journal papers [A1-A7] with the following aims:

(i) To design and validate new methods for partial volume correction of ASL data;

(ii) To propose a concept of a robust pipeline for processing ASL data;

(iii) To apply ASL to image adverse effects of radiochemotherapy treatment in patients with brain tumors.

5. General methods

5.1 Partial volume correction

In this part of the work, we have analyzed the added value of partial volume correction (PVC) methods that remove the unwanted effect of partial volume from ASL data by using images of the GM and WM partial volumes obtained by segmenting high-resolution structural MRI images. We have first analyzed, through simulations, if PVC gives more accurate results than the typical thresholding of the ASL data [A2], we have then studied if there are better ways for obtaining segmented GM and WM images for PVC than using structural MRI data [A1]. Finally, we have checked the added value of PVC on the individual to mean CBF comparisons for discovering regions of CBF irregularities [A3].

For [A1], data from 5 volunteers (mean age 30±3.7 years, 4 men) were acquired on a 3T Philips scanner. The protocol contained 3D T1-weighted images with 1mm isotropic resolution, repetition time (TR)/echo time (TE) 1880/3.7ms, and flip angle of 8 degrees. ASL was acquired with PULSAR labeling [44], Q2TIPS saturation [45], and Look-Locker EPI readout [46]. Further ASL parameters were: TR/TE 4000/17 ms, flip angles 35 and 11.7 degrees, voxel size 3.5x3.5x7mm^3, label thickness 150 mm, Q2TIPS saturation from 940-2140 ms, and 24 averages for the higher and 2 for the lower flip angle.

For [A2], 22 healthy young volunteers (age 22.6 ± 2.1 years, 13 women) were scanned twice at a 3T GE MR750 and 3T Philips Intera. Every time a 3D T1-weighted 1mm isotropic scan and a pseudo-continuous ASL scan were acquired. On the Philips scanner, pCASL parameters were: 2D EPI, voxel size 3×3×7 mm^3, TE/TR 17 ms/4000 ms, labeling duration 1650 ms, post-labeling delay 1525 ms, and 33 averages. On the GE scanner, the parameters were: a 3D Spiral with 3.8×3.8×4 mm^3 resolution, TE/TR 10.5 ms/4600 ms, labeling duration 1450 ms, post-labeling delay 1525 ms, and 3 averages [19].

For [A3], 25 healthy subjects (31.6±8.3 years, 14 women) were included for the evaluation of basal perfusion. The second group of 12 subjects (28.6±2.7 years, 7 women) was included for motor activation-related perfusion evaluation. MR imaging was performed on a 3T Magnetom Verio Siemens scanner. 3D T1-weighted 1 mm isotropic images and pulsed ASL images were acquired. PASL parameters were the following: 30 averages, a Q2TIPS saturation pulse at 700 ms, the inversion time of 1700 ms, an EPI readout with 3x3x7mm^3 resolution, TR/TE 3000/25 ms. Functional ASL contained 7 alternating 30 s-phases (10 control and labeled images) of rest and a right-hand motor task.

In [A1], the T1-weighted images were segmented into GM and WM maps. B_1-inhomogeneities were corrected by using the low and high-flip angle data [47]. CBF images were quantified from the multi-delay data [48]. Additionally, partial volume maps were obtained by segmenting the T1-time maps obtained from the inversion recovery of the Look-Locker EPI

data using the FRASIER method [49]. Partial volume correction was performed using the linear regression methods [33], employing both the standard and the new methods extracting GM and WM images from either T1-weighted structural images or the Look-Locker images obtained together with the ASL data, respectively. Residual errors from the partial volume correction were compared between the two different segmented maps to determine the better-suited segmentation method [A1].

In [A2], the T1-weighted and ASL images were segmented and processed in the standard way. Rigid-body and non-linear registrations were used to co-register the two sequences. Moreover, resolution differences between ASL and T1-weighted images were estimated using the CBF and GM images, which have similar contrast. The obtained registrations and resolutions were used as a realistic sample of deformation and resolution issues in the ASL data. Based on these, GM and WM segmented images in high resolution were used to generate simulated maps of CBF for each subject, assuming GM CBF of 60 ml/min/100g and WM CBF of 20 ml/min/100g. Deformation and resolution issues were then simulated in this data using the previously obtained realistic data. This enabled us to have a set of ground-truth simulated data with realistic deformations and resolution issues. On these datasets, we have investigated the behavior of different partial volume correction methods when using a perfect set of GM and WM segmented maps or those that contained the aforementioned errors. Two methods of partial volume correction (standard thresholding of GM maps and PVC through linear regression) were then investigated to establish their performance in real-world conditions.

In [A3], all T1-weighted images were segmented and aligned to the MNI space using the DARTEL segmentation. ASL was quantified and aligned to MNI space through co-registration with T1-weighted images. A group CBF average was created for the healthy subject group in the MNI space. For the functional group, regions of activation were obtained through analysis using a generalized linear model. Subsequently, all mean CBF images in the OFF and ON phases were created for each subject. There were compared against the healthy template, and regions of hypo and hyper-perfusion with respect to the healthy dataset were obtained by thresholding the Z-scores. The regions obtained by a standard functional analysis and by comparison with the template were compared for templates created with and without using partial volume correction.

5.2 ASL processing pipeline

In [A4], we have provided a recommended approach to process and evaluate ASL data in a form of a review paper. In this review, we have provided details, justification, and caveats for the following ASL post-processing steps divided into four principal procedure parts: data import and conversion, structural analysis, ASL analysis, and population analysis. See visualization in Figure 2. This approach follows our implementation of the ExploreASL pipeline but can be in theory used for other ASL pipelines as well.

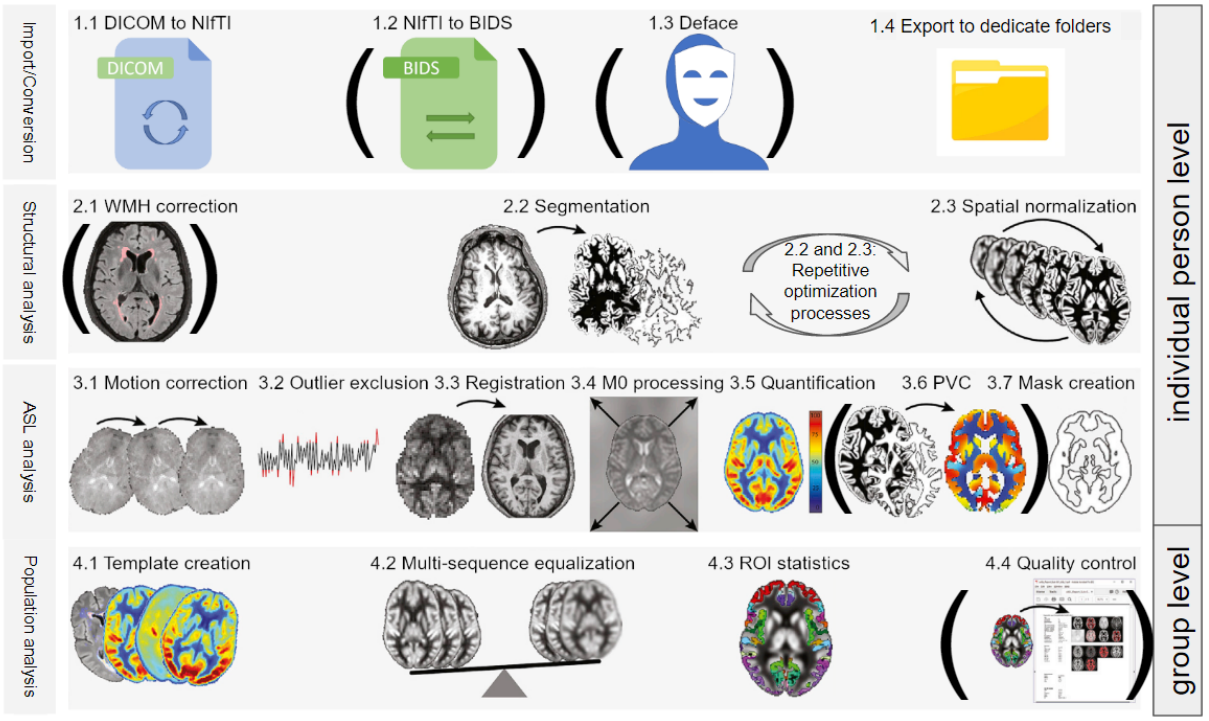

Figure 2 Overview of all ASL post-processing steps on the individual- and group-level (adapted from [50]). Strictly optional steps are marked in parentheses.

The data import and conversion steps transform the MRI data generated by the scanner into a processable format, organized in the folder structure required for analysis. This processing part includes the steps of DICOM to NIfTI conversion, NIfTI to BIDS conversion, defacing, and exportation to the dedicated folders.

The second step, the structural analysis, aims to prepare structural data from T1-weighted and FLAIR sequences to be more easily comparable between individuals. The T1-weighted images are optionally corrected for white matter lesions detected on FLAIR scans. Then the data are spatially normalized and segmented, which later allows using various anatomical atlases for regional data evaluation. It further allows the use of segmented tissue volumes for tissue-specific analysis and partial volume correction.

The third step deals with ASL quantification itself. ASL data must be first pre-processed, which is normally done through motion correction, outlier exclusion, co-registration with the structural images, and finally processing and calibration of M0 scans and CBF quantification with possible partial volume correction with the previously obtained GM and WM partial volume maps.

The last processing step involves population analysis and gathering and aggregating all the results for further statistical analysis. This includes mask creation using tissue masks and anatomical atlases, calculating regional statistics, and finally, quality control (QC) of both acquired and derived data.

To show the reproducibility of the processing, we have included three clinical populations: perinatally infected HIV children from the NOVICE study [25], healthy adults from a sleep study [51], and elderly with mild cognitive complaints from the European Prevention of Alzheimer's Dementia (EPAD) study [52]. Multi-center ASL studies can be processed on computers using different operating systems and software versions, and these can also update during a longitudinal study. We have tested if the performance of image processing stays comparable independent of these factors.

5.3 Adverse effects of radiochemotherapy

In the last part of the work, we studied the adverse effects of radiochemotherapy on normal brain tissue in patients with glioblastoma. In [A5-7], data were drawn from the PETra study where 72 patients diagnosed with primary glioblastoma were included (mean age 54.3±14.2 years, 43 male), 51 undergoing photon- and 21 proton radiotherapy [53]. MR imaging was performed before radiochemotherapy and after surgery. The first MR session was performed after surgery and before the start of the radiochemotherapy. Follow-up was done 3 months after the end of the radiotherapy and then in 3 months intervals. Imaging was performed on a 3T Philips Ingenuity MRI. On each session, a 3D Turbo Field Echo T1-weighted (T1w) with 1 mm isotropic resolution was acquired. A PCASL scan was acquired with 2.75x2.75x6mm^3 resolution, TR/TE 3765/11 ms, 30 averages, labeling time of 1650 ms, and a post-labeling delay of 1525 ms.

The T1w data were segmented to GM and WM, and ASL images were processed using the ExploreASL pipeline. The follow-up sessions were registered to the baseline scans. Treatment planning CT was co-registered with the baseline T1w, and radiotherapy planning maps - aligned with the planning CT - were then aligned with the baseline T1w to allow voxel-wise assessment of the delivered radiation dose. Mean relative CBF and GM and WM volume decreases were investigated in the healthy hemisphere at 3 and 6 months follow-ups compared to the post-surgical baseline. The mean radiation dose delivered to the healthy hemisphere was also calculated, and regional decreases were calculated per isodoses of 10 [A5-6]. Additionally, since there were previous issues with the segmentation of tissue containing the tumor and edema, we have investigated the differences between segmenting the entire brain with pathological tissue or just segmenting the healthy hemisphere alone [A7].

6. Discussion of main findings and potential impact of the thesis

6.1 Partial volume correction

There is a consensus in the ASL community on the origin and existence of the partial volume effect, and there is a growing concern that this can affect studies where brain atrophy is a major confounder [54]. However, a single clear strategy to address this has not been defined, and several approaches for PV correction have been proposed. All of these approaches rely on the use of partial volume GM and WM maps obtained from segmenting the

high-resolution T1-weighted images that allow estimating the GM and WM volume ratios in the larger ASL voxels. Originally, an approach commonly used in PET was to use a fixed ratio between GM and WM perfusion [55]. Later, a linear regression method was used to separate the GM and WM CBF using the know GM and WM volumes within a localized spatially defined kernel [33]. The most trivial approach that is now commonly used for ASL is to obtain GM CBF by calculating mean CBF across the mask of voxels obtained by thresholding the GM image by a relatively high threshold (60-80%), ensuring that a majority of voxels are from this tissue type.

Minimal attention was attributed to the quality of the GM and WM maps. Our results showed that GM and WM partial volume maps are only seemingly fitting the ASL data. There are important differences in geometric distortions and effective resolution between the ASL and T1w scans. These differences manifest as errors in the GM and WM segmented, and when they are used for partial volume correction, they can seriously influence the CBF computation [A2]. One solution to address this problem with GM and WM segmented maps is to use a dedicated sequence with the same readout as ASL and obtain the segmented maps from the inversion recovery of the signal sampled at several time points. While this approach delivers better results, such additional acquisition is not widely available and, therefore, seriously limits its practical use [A1]. On the practical level, we have demonstrated through simulations that part of the issues with the quality of the partial volume maps and their influence on partial volume correction can be alleviated. This can be done by proper correction for deformation using non-linear registration, and by correct estimation of post-spread function differences between ASL and T1-weighted data and their application during resampling of the segmented maps between these two spaces [A2]. What is even more important is that we have addressed the issue of the use of partial volume correction in general. It is often advocated that partial volume correction can decrease the quality of the results by propagating errors from the partial volume maps into the final results. We have, however, shown that using the standard method of partial-volume map thresholding, used in next to all ASL studies, leads to an equal propagation of partial volume map errors to the final results as is encountered with a partial volume correction through linear regression. This then allows dismissing completely the arguments advocating for avoiding the use of partial volume correction on the grounds of propagating the segmentation errors. Lastly, we have also managed to show practically, that accounting for partial volume effects increases the detection power of CBF irregularities when comparing normal and pathological data [A3].

6.2 ASL processing pipeline

A basic version of CBF quantification according to the consensus recommendation [11] is readily available on the MRI scanner consoles of the major MRI vendors. While this is perfectly sufficient for visual analysis, offline image processing is recommended to optimize the image quality and to perform large-scale population analysis. Several ASL pipelines are publicly available, notably ASLtbx [26], ASAP [30], MRICloud [31], BASIL [56]BASIL (Chappell et al., 2009), CBFBIRN [27], and VANDPIRE [57]. However, there is no consensus on the processing standard for ASL, not a basic list of steps with a sufficient explanation. We have

tried to close this gap with the ExploreASL pipeline and a review summarizing and explaining all these steps.

The software package ExploreASL was initiated through the EU-funded ASL workgroup COST-action BM1103 "ASL In Dementia" (www.aslindementia.org/) with the aim of developing a comprehensive pipeline for reproducible multi-center ASL image processing. ExploreASL was used in more than 50 studies consisting of more than 15000 ASL scans from various sequences. ExploreASL focused on optimizing the processing of clinical studies with diverse populations and sequences. Besides a module for ASL processing and quantification, it has an integrated module for structural image processing, population statistics, and quality check. It is freely available on GitHub with the possibility to report errors and request new features. There are several missing features that are scheduled for future releases, including full BIDS support [58]; support for further vendors like Hitachi and Canon datasets; a GUI for easier configuration and execution; and integration of the BASIL toolbox to allow quantification of more complex multi-timepoint sequences [29].

6.3 Adverse effects of radiochemotherapy

Radiotherapy (RT) and other systemic cancer therapy like chemotherapy and immunotherapy have been reported to cause irreversible pathological changes to the brain, as well as cognitive dysfunction and a decrease in the quality of life [59,60]. A decrease in the volume of brain parenchyma, which exceeds the tissue loss common in normal aging, was well documented during brain radiochemotherapy [61]. It is also speculated that radiotherapy damages capillary and large vessels and impairs their autoregulation mechanism [62]. CBF changes have already been demonstrated in healthy tissue after brain radiosurgery [63,64]. But while RT-induced CBF decrease could explain post-therapy cognitive changes, CBF changes following brain radiochemotherapy have not been yet systematically studied. Previous studies had not used a common methodology for evaluating the results or considering the confounding factors. Moreover, the previous studies had too heterogeneous groups.

In our study, we have focused solely on glioblastoma, and we have studied the perfusion changes in a range of regions depending on the spatial position and radiotherapy dose. Moreover, to be able to separate the radiotherapy-related and unrelated effects we have recruited both patients with normal photon therapy and with proton therapy that has minimal radiation deposition to the healthy hemisphere. To rule out the effect of bevacizumab [65], no angiogenesis inhibitors were used for treatment in our study.

A clear decrease in CBF of around 10% was reported in our data at both 3 and 6 months after the end of radiotherapy. However, we have not seen any changes between the two follow-up intervals and the decrease was not correlated with the total dose in the healthy hemisphere. Moreover, no difference was found between the patient treated with photon and with proton therapy, and regional differences in perfusion decrease were also not correlated with the regional dose of radiation. This mostly points to either a systemic effect of the radiotherapy

or the temozolomide chemotherapy [A5,A6]. More work would, however, be needed to prove the crucial role of chemotherapy.

On the contrary, the loss of brain-tissue volume was strongly correlated with the mean radiation dose received in the healthy hemisphere and there were also important differences between the two modes of therapy, showing a clear influence of the radiation dose on the amount of damage [A6]. While mixed results were shown in previous studies [66], we have adapted our methodology to avoid the influence of the tumor and peri-tumoral changes, e.g. edema, on the segmentation results in the healthy tissue [A7]. Therefore, we have observed a clear decrease in both GM and WM. Unlike CBF changes, we saw a progressive worsening of the tissue lost in time. However, it remains to be further studied if this is only delayed damage of the radiotherapy or secondary damage related to perfusion loss.

7. Conclusion

The main contribution of the research presented in this habilitation thesis can be summarized into six points corresponding to the three general aims:

7.1 General contributions of the thesis

1. We have shown the limits of performing partial volume correction of ASL data using the segmented maps obtained from T1-weighted structural images. The main issues are the small differences in geometrical deformations between the T1-weighted and ASL acquisitions. Using segmented partial volume maps obtained from the inversion recovery of images obtained with a Look-Locker version of the same readout as used for the ASL data showed to improve the partial volume correction and this pointed out the real importance of having perfectly segmented tissue maps for this processing step.
2. We have shown through simulations that using the traditional GM and WM maps, obtained from T1-weighted high-resolution scans, introduces important errors into partial volume correction through issues with resolution and deformation differences between the ASL and T1-weighted sequences. Correction of these differences through non-linear co-registration and proper resampling between these two image spaces can alleviate a large part of this problem. Moreover, we could show that these errors similarly affect both the standard method of tissue thresholding and partial volume correction through linear regression. This presents a strong argument for a practical application of partial volume correction in clinical trials, which was until recently scarcely used for fear of introducing errors into the analysis.
3. We have shown that accounting for partial volume effects increases the detection power of CBF irregularities when comparing pathological data and functional data containing regions of hypo and hyper-perfusion with a normative database of healthy subjects.
4. We have introduced a versatile ASL pipeline called ExploreASL, which can process a wide range of ASL data in different pathologies and is adapted for multi-center image

processing. We anticipate that ExploreASL will enable more flexible collaboration amongst clinicians and scientists.

5. We have shown that the segmentation of GM volumes in patients with brain tumors might be biased in the healthy tissue following pathological changes in different brain regions. This bias can be minimized by carefully excluding those problematic parts. By using this approach, we have then shown that radiochemotherapy is related to loss of GM and WM tissue. Local radiation dose was correlated to the amount of tissue loss. Therefore, using a proton therapy, which has a minimal dose delivered to healthy tissue, significantly minimizes early-delayed brain parenchymal volume loss.
6. Lastly, we have shown a significant 10% CBF decrease in healthy tissue in patients diagnosed with glioblastomas undergoing radiochemotherapy. The amount of CBF decrease was, however, not correlated with the radiation dose received locally or in the entire healthy hemisphere. Also, the proton therapy patients receiving minimal doses in the healthy tissue had a comparable CBF decrease. This points out the effect of systemic chemotherapy.

7.2 Future work

There are several important goals related to the future research and application of ASL that remain to be solved in future research:

1. While better performance in partial volume correction was shown with maps acquired using Look-Locker readout, a few things need to be improved before putting the method into practice. A more optimal acquisition protocol needs to be developed to allow full brain coverage. A better method for estimating GM and WM relaxation times is needed for a more accurate delineation of the GM/WM border.
2. With the newly acquired knowledge about partial volume correction, we might need to revisit some of the existing studies on CBF changes during brain aging as they might have been confounded by the reported issues in partial volume correction.
3. While DICOM and NIFTI file formats are established for neuroimaging data and allow easy data sharing, they do not allow storing all necessary ASL metadata. This complicates data sharing of ASL data across different centers without access to the original raw data and imaging protocols. This in turn makes ASL research less reliable and less reproducible. We work on introducing a new standard for ASL data sharing using the BIDS format, and we aim to adapt ExploreASL pipeline to this format.
4. Further research has to be done to study the dependence of brain tissue loss on radiation dose also in the long term. Besides the radiation dose, there could be more effects on the localized data that could be studied with respect to tumor location and disruptions of white matter fibers. Studying structural networks can provide more insight into this.
5. CBF decrease has been previously identified as a possible reason for later GM decrease. We have seen that patients undergoing proton therapy had minimal initial GM decrease, which accelerated at later stages. A working hypothesis is that the CBF decrease present in all patients could be the driver behind the secondary

parenchymal tissue loss. Moreover, CBF changes have to be studied in the long term as, unlike volume changes, CBF changes can be reversible. Therefore, the prognostic value of early and later CBF changes on the long-term cognitive outcome has to be studied.

8. References

1. Dani KA, Thomas RGR, Chappell FM, Shuler K, MacLeod MJ, Muir KW, et al. Computed tomography and magnetic resonance perfusion imaging in ischemic stroke: definitions and thresholds. Ann Neurol. 2011;70: 384–401.

2. Lal BK, Hobson RW 2nd, Tofighi B, Kapadia I, Cuadra S, Jamil Z. Duplex ultrasound velocity criteria for the stented carotid artery. J Vasc Surg. 2008;47: 63–73.

3. Lauterbur PC. Image Formation by Induced Local Interactions: Examples Employing Nuclear Magnetic Resonance. Nature. 1973. pp. 190–191. doi:10.1038/242190a0

4. Heijtel DFR, Mutsaerts HJMM, Bakker E, Schober P, Stevens MF, Petersen ET, et al. Accuracy and precision of pseudo-continuous arterial spin labeling perfusion during baseline and hypercapnia: A head-to-head comparison with 15O H2O positron emission tomography. Neuroimage. 2014;92: 182–192.

5. Boxerman JL, Schmainda KM, Weisskoff RM. Relative cerebral blood volume maps corrected for contrast agent extravasation significantly correlate with glioma tumor grade, whereas uncorrected maps do not. AJNR Am J Neuroradiol. 2006;27: 859–867.

6. Barnes SL, Whisenant JG, Loveless ME, Yankeelov TE. Practical dynamic contrast enhanced MRI in small animal models of cancer: data acquisition, data analysis, and interpretation. Pharmaceutics. 2012;4: 442–478.

7. Emblem, Bjornerud. An automatic procedure for normalization of cerebral blood volume maps in dynamic susceptibility contrast−based glioma imaging. Am J Physiol Renal Physiol. Available: http://www.ajnr.org/content/30/10/1929.short

8. Kanda T, Nakai Y, Aoki S, Oba H, Toyoda K, Kitajima K, et al. Contribution of metals to brain MR signal intensity: review articles. Jpn J Radiol. 2016;34: 258–266.

9. Williams DS, Detre JA, Leigh JS, Koretsky AP. Magnetic resonance imaging of perfusion using spin inversion of arterial water. Proc Natl Acad Sci U S A. 1992;89: 212–216.

10. Detre JA, Leigh JS, Williams DS, Koretsky AP. Perfusion imaging. Magn Reson Med. 1992;23: 37–45.

11. Alsop DC, Detre JA, Golay X, Günther M, Hendrikse J, Hernandez-Garcia L, et al. Recommended implementation of arterial spin-labeled perfusion MRI for clinical applications: A consensus of the ISMRM perfusion study group and the European consortium for ASL in dementia. Magn Reson Med. 2015;73: 102–116.

12. Alsop DC, Detre JA. Reduced transit-time sensitivity in noninvasive magnetic resonance imaging of human cerebral blood flow. J Cereb Blood Flow Metab. 1996;16: 1236–1249.

13. Alsop DC, Detre JA. Background suppressed 3D RARE ASL perfusion imaging. International Society for Magnetic Resonance in Medicine. Philadelphia; 1999. p. 601.

14. Ye FQ, Frank J a., Weinberger DR, McLaughlin a. C. Noise reduction in 3D perfusion imaging by attenuating the static signal in arterial spin tagging (ASSIST). MRM. 2000;44: 92–100.

15. Dai W, Garcia D, De BC, Alsop DC. Continuous flow-driven inversion for arterial spin labeling using pulsed radio frequency and gradient fields. Magn Reson Med. 2008;60: 1488–1497.

16. Detre JA, Alsop DC, Vives LR, Maccotta L, Teener JW, Raps EC. Noninvasive MRI evaluation of cerebral blood flow in cerebrovascular disease. Neurology. 1998;50: 633–641.

17. Alsop DC, Detre JA, Grossman M. Assessment of cerebral blood flow in Alzheimer's disease by spin-labeled magnetic resonance imaging. Ann Neurol. 2000;47: 93–100.

18. Chen Y, Wang DJJ, Detre JA. Test-retest reliability of arterial spin labeling with common labeling strategies. J Magn Reson Imaging. 2011;33: 940–949.

19. Mutsaerts HJMM, Steketee RME, Heijtel DFR, Kuijer JPA, Van Osch MJPMJP, Majoie CBLM, et al. Inter-vendor reproducibility of pseudo-continuous arterial spin labeling at 3 Tesla. PLoS One. 2014;9. doi:10.1371/journal.pone.0104108

20. Petersen ET, Mouridsen K, Golay X, Thade E, Mouridsen K, Golay X. The QUASAR reproducibility study, Part II: Results from a multi-center Arterial Spin Labeling test-retest study. Neuroimage. 2010;49: 104–113.

21. Mutsaerts HJMM, van Osch MJP, Zelaya FO, Wang DJJ, Nordhøy W, Wang Y, et al. Multi-vendor reliability of arterial spin labeling perfusion MRI using a near-identical sequence: Implications for multi-center studies. Neuroimage. 2015;113: 143–152.

22. Fan AP, An H, Moradi F, Rosenberg J, Ishii Y, Nariai T, et al. Quantification of brain oxygen extraction and metabolism with [15O]-gas PET: A technical review in the era of PET/MRI. Neuroimage. 2020;220: 117136.

23. Jack CR, Bernstein MA, Borowski B, Gunter JL, Fox NC, Thompson P, et al. Update on the magnetic resonance imaging core of the Alzheimer's disease neuroimaging initiative. Alzheimers Dement. 2010;6: 212–220.

24. Almeida JRC, Greenberg T, Lu H, Chase HW, Fournier JC, Cooper CM, et al. Test-retest reliability of cerebral blood flow in healthy individuals using arterial spin labeling: Findings from the EMBARC study. Magn Reson Imaging. 2018;45: 26–33.

25. Blokhuis C, Mutsaerts HJMM, Cohen S, Scherpbier HJ, Caan MWA, Majoie CBLM, et al. Higher subcortical and white matter cerebral blood flow in perinatally HIV-infected children. Medicine . 2017;96: e5891.

26. Wang Z, Aguirre GK, Rao H, Wang J, Fernández-Seara MA, Childress AR, et al. Empirical optimization of ASL data analysis using an ASL data processing toolbox: ASLtbx. Magn

Reson Imaging. 2008;26: 261–269.

27. Shin DD, Ozyurt IB, Brown GG, Fennema-Notestine C, Liu TT. The Cerebral Blood Flow Biomedical Informatics Research Network (CBFBIRN) data repository. Neuroimage. 2016;124: 1202–1207.

28. Melbourne A, Toussaint N, Owen D, Simpson I, Anthopoulos T, De Vita E, et al. NiftyFit: a Software Package for Multi-parametric Model-Fitting of 4D Magnetic Resonance Imaging Data. Neuroinformatics. 2016;14: 319–337.

29. Chappell MA, MacIntosh BJ, Donahue MJ, Günther M, Jezzard P, Woolrich MW. Separation of macrovascular signal in multi-inversion time arterial spin labelling MRI. Magn Reson Med. 2010;63: 1357–1365.

30. Mato Abad V, García-Polo P, O'Daly O, Hernández-Tamames JA, Zelaya F. ASAP (Automatic Software for ASL Processing): A toolbox for processing Arterial Spin Labeling images. Magn Reson Imaging. 2016;34: 334–344.

31. Li Y, Liu P, Li Y, Fan H, Su P, Peng S-L, et al. ASL-MRICloud: An online tool for the processing of ASL MRI data. NMR Biomed. 2018; e4051.

32. Bron EE, Steketee RME, Houston GC, Oliver RA, Achterberg HC, Loog M, et al. Diagnostic classification of arterial spin labeling and structural MRI in presenile early stage dementia. Hum Brain Mapp. 2014;35: 4916–4931.

33. Asllani I, Borogovac A, Brown TR. Regression algorithm correcting for partial volume effects in arterial spin labeling MRI. Magn Reson Med. 2008;60: 1362–1371.

34. Zhang K, Herzog H, Mauler J, Filss C, Okell TW, Kops ER, et al. Comparison of cerebral blood flow acquired by simultaneous [15O]water positron emission tomography and arterial spin labeling magnetic resonance imaging. J Cereb Blood Flow Metab. 2014;34: 1373–1380.

35. Asllani I, Habeck C, Borogovac A, Brown TR, Brickman AM, Stern Y. Separating function from structure in perfusion imaging of the aging brain. HBM. 2009;30: 2927–2935.

36. Telischak N a., Detre J a., Zaharchuk G. Arterial spin labeling MRI: Clinical applications in the brain. J Magn Reson Imaging. 2015;41: 1165–1180.

37. Keil VC, Hartkamp NS, Connolly DJA, Morana G, Dremmen MHG, Mutsaerts HJMM, et al. Added value of arterial spin labeling magnetic resonance imaging in pediatric neuroradiology: pitfalls and applications. Pediatr Radiol. 2019;49: 245–253.

38. Alsaedi A, Doniselli F, Jäger HR, Panovska-Griffiths J, Rojas-Garcia A, Golay X, et al. The value of arterial spin labelling in adults glioma grading: systematic review and meta-analysis. Oncotarget. 2019;10: 1589–1601.

39. Delgado AF, De Luca F, Hanagandi P, van Westen D, Delgado AF. Arterial Spin-Labeling in Children with Brain Tumor: A Meta-Analysis. AJNR Am J Neuroradiol. 2018;39: 1536–1542.

40. Clement P, Booth T, Borovečki F, Emblem KE, Figueiredo P, Hirschler L, et al. GliMR: Cross-Border Collaborations to Promote Advanced MRI Biomarkers for Glioma. J Med Biol Eng. 2020; 1–11.

41. Henriksen OM, Del Mar Álvarez-Torres M, Figueiredo P, Hangel G, Keil VC, Nechifor RE, et al. High-grade glioma treatment response monitoring biomarkers: A position statement on the evidence supporting the use of advanced MRI techniques in the clinic, and the latest bench-to-bedside developments. Part 1: Perfusion and diffusion techniques. Front Oncol. 2022;12: 810263.

42. Makale MT, McDonald CR, Hattangadi-Gluth JA, Kesari S. Mechanisms of radiotherapy-associated cognitive disability in patients with brain tumours. Nat Rev Neurol. 2017;13: 52–64.

43. Ahles TA, Root JC, Ryan EL. Cancer- and Cancer Treatment–Associated Cognitive Change: An Update on the State of the Science. Journal of Clinical Oncology. 2012. pp. 3675–3686. doi:10.1200/jco.2012.43.0116

44. Golay X, Petersen ET, Hui F. Pulsed star labeling of arterial regions (PULSAR): a robust regional perfusion technique for high field imaging. Magn Reson Med. 2005;53: 15–21.

45. Luh W-M, Wong EC, Bandettini PA, Hyde JS. QUIPSS II with thin-slice TI1 periodic saturation: A method for improving accuracy of quantitative perfusion imaging using pulsed arterial spin labeling. Magnetic Resonance in Medicine. 1999. pp. 1246–1254. doi:10.1002/(sici)1522-2594(199906)41:6<1246::aid-mrm22>3.0.co;2-n

46. Look DC, Locker DR. Time Saving in Measurement of NMR and EPR Relaxation Times. Review of Scientific Instruments. 1970. pp. 250–251. doi:10.1063/1.1684482

47. Stollberger R, Wach P. Imaging of the active B1 field in vivo. Magn Reson Med. 1996;35: 246–251.

48. Günther M, Bock M, Schad LR. Arterial spin labeling in combination with a look-locker sampling strategy: Inflow turbo-sampling EPI-FAIR (ITS-FAIR). Magnetic Resonance in Medicine. 2001. pp. 974–984. doi:10.1002/mrm.1284

49. Shin W, Geng X, Gu H, Zhan W, Zou Q, Yang Y. Automated brain tissue segmentation based on fractional signal mapping from inversion recovery Look–Locker acquisition. Neuroimage. 2010;52: 1347–1354.

50. Mutsaerts HJMM, Petr J, Groot P, Vandemaele P, Ingala S, Robertson AD, et al. ExploreASL: an image processing pipeline for multi-center ASL perfusion MRI studies. Neuroimage. 2020; 117031.

51. Elvsåshagen T, Mutsaerts HJ, Zak N, Norbom LB, Quraishi SH, Pedersen PØ, et al. Cerebral blood flow changes after a day of wake, sleep, and sleep deprivation. Neuroimage. 2019;186: 497–509.

52. Ritchie CW, Molinuevo JL, Truyen L, Satlin A, Van der Geyten S, Lovestone S. Development of interventions for the secondary prevention of Alzheimer's dementia: the European Prevention of Alzheimer's Dementia (EPAD) project. The Lancet Psychiatry.

2016;3: 179–186.

53. Seidlitz, Beuthien-Baumann, Löck, Jentsch. Final Results of the Prospective Biomarker Trial PETra:[11C]-MET-Accumulation in Postoperative PET/MRI Predicts Outcome after Radiochemotherapy in …. Clin Cancer Drugs. Available: https://aacrjournals.org/clincancerres/article-abstract/27/5/1351/83858

54. Steketee RME, Bron EE, Meijboom R, Houston GC, Klein S, Mutsaerts HJMM, et al. Early-stage differentiation between presenile Alzheimer's disease and frontotemporal dementia using arterial spin labeling MRI. Eur Radiol. 2016;26: 244–253.

55. Aston JAD, Cunningham VJ, Asselin M-C, Hammers A, Evans AC, Gunn RN. Positron emission tomography partial volume correction: estimation and algorithms. J Cereb Blood Flow Metab. 2002;22: 1019–1034.

56. Chappell MA, Groves AR, Whitcher B, Woolrich MW. Variational Bayesian Inference for a Nonlinear Forward Model. IEEE Trans Signal Process. 2009;57: 223–236.

57. Arteaga DF, Strother MK, Davis LT, Fusco MR, Faraco CC, Roach BA, et al. Planning-free cerebral blood flow territory mapping in patients with intracranial arterial stenosis. J Cereb Blood Flow Metab. 2017;37: 1944–1958.

58. Gorgolewski KJ, Auer T, Calhoun VD, Craddock RC, Das S, Duff EP, et al. The brain imaging data structure, a format for organizing and describing outputs of neuroimaging experiments. Scientific Data. 2016;3: 160044.

59. Taphoorn MJB, Klein M. Cognitive deficits in adult patients with brain tumours. Lancet Neurol. 2004;3: 159–168.

60. Roman DD, Sperduto PW. Neuropsychological effects of cranial radiation: current knowledge and future directions. Int J Radiat Oncol Biol Phys. 1995;31: 983–998.

61. Nagtegaal SHJ, David S, van der Boog ATJ, Leemans A, Verhoeff JJC. Changes in cortical thickness and volume after cranial radiation treatment: A systematic review. Radiother Oncol. 2019;135: 33–42.

62. O'Connor MM, Mayberg MR. Effects of radiation on cerebral vasculature: a review. Neurosurgery. 2000;46: 138–49; discussion 150–1.

63. Taki S, Higashi K, Oguchi M, Tamamura H, Tsuji S, Ohta K, et al. Changes in regional cerebral blood flow in irradiated regions and normal brain after stereotactic radiosurgery. Ann Nucl Med. 2002;16: 273–277.

64. Jakubovic R, Sahgal A, Ruschin M, Pejović-Milić A, Milwid R, Aviv RI. Non Tumor Perfusion Changes Following Stereotactic Radiosurgery to Brain Metastases. Technol Cancer Res Treat. 2015;14: 497–503.

65. Andre JB, Nagpal S, Hippe DS, Ravanpay AC, Schmiedeskamp H, Bammer R, et al. Cerebral Blood Flow Changes in Glioblastoma Patients Undergoing Bevacizumab Treatment Are Seen in Both Tumor and Normal Brain. Neuroradiol J. 2015;28: 112–119.

66. Chamberlain MC, Dietrich J, Prust M. Standard chemoradiation for glioblastoma results in progressive brain volume lossAuthor Response. Neurology. 2016. pp. 979–979. doi:10.1212/01.wnl.0000481823.96137.39

9. List of author's publications

[A1] **Petr, J.**, Schramm, G., Hofheinz, F., Langner, J., & van den Hoff, J. (2013). Partial volume correction in arterial spin labeling using a Look-Locker sequence. Magnetic resonance in medicine, 70(6), 1535-1543.

[A2] **Petr, J.**, Mutsaerts, H. J., De Vita, E., Steketee, R. M., Smits, M., Nederveen, A. J., ... & Asllani, I. (2018). Effects of systematic partial volume errors on the estimation of gray matter cerebral blood flow with arterial spin labeling MRI. Magnetic Resonance Materials in Physics, Biology and Medicine, 31(6), 725-734.

[A3] **Petr, J.**, Ferré, J. C., Raoult, H., Bannier, E., Gauvrit, J. Y., & Barillot, C. (2014). Template-based approach for detecting motor task activation-related hyperperfusion in pulsed ASL data. Human brain mapping, 35(4), 1179-1189.

[A4] Mutsaerts, H. J., **Petr, J.***, Groot, P., Vandemaele, P., Ingala, S., Robertson, A. D., ... & Barkhof, F. (2020). ExploreASL: an image processing pipeline for multi-center ASL perfusion MRI studies. Neuroimage, 219, 117031.

[A5] **Petr, J.**, Platzek, I., Seidlitz, A., Mutsaerts, H. J., Hofheinz, F., Schramm, G., ... & Van Den Hoff, J. (2016). Early and late effects of radiochemotherapy on cerebral blood flow in glioblastoma patients measured with non-invasive perfusion MRI. Radiotherapy and Oncology, 118(1), 24-28.

[A6] **Petr, J.**, Platzek, I., Hofheinz, F., Mutsaerts, H. J., Asllani, I., van Osch, M. J., ... & van den Hoff, J. (2018). Photon vs. proton radiochemotherapy: Effects on brain tissue volume and perfusion. Radiotherapy and Oncology, 128(1), 121-127.

[A7] Gommlich, A., Raschke, F., **Petr, J.***, Seidlitz, A., Jentsch, C., Platzek, I., ... & Troost, E. G. C. (2022). Overestimation of grey matter atrophy in glioblastoma patients following radio (chemo) therapy. Magnetic resonance materials in physics, biology and medicine, 35(1), 145-152.

* shared first authorship

Appendices

Appendix A1

Partial volume correction in arterial spin labeling using a Look-Locker sequence

Petr, J., Schramm, G., Hofheinz, F., Langner, J., & van den Hoff, J. (2013). Partial volume correction in arterial spin labeling using a Look-Locker sequence. Magnetic resonance in medicine, 70(6), 1535-1543.

Journal name (category): Magnetic resonance in medicine (Radiology, nuclear medicine & medical imaging)

Quartile in category: **Q2**

Impact factor: **3.737**

Number of WoS citations: **19**

Partial Volume Correction in Arterial Spin Labeling Using a Look-Locker Sequence

Jan Petr,* Georg Schramm, Frank Hofheinz, Jens Langner, and Jörg van den Hoff

Purpose: Partial volume (PV) effects are caused by limited spatial resolution and significantly affect cerebral blood flow investigations with arterial spin labeling. Therefore, accurate PV correction (PVC) procedures are required. PVC is commonly based on PV maps obtained from segmented high-resolution T_1-weighted images. Segmentation of these images is error-prone, and it can be difficult to coregister these images accurately with the single-shot ASL images such as those created by echo-planar imaging (EPI). In this paper, an alternative method for PV map generation is proposed.
Methods: The Look-Locker EPI (LL-EPI) acquisition is used for analyzing the T_1-recovery curve and for subsequent PV map generation. The new method was evaluated in five healthy volunteers (mean age 30 ± 3.7 years).
Results: By applying a linear regression method for PVC, a 12% decrease in regression error was reached with the new method.
Conclusion: PV maps extraction from LL-EPI is a viable, possibly superior alternative to the standard approach based on segmentation of high-resolution T_1-weighted images. **Magn Reson Med 70:1535–1543, 2013. © 2012 Wiley Periodicals, Inc.**

Key words: partial volume effect; look-locker; ASL; arterial spin labeling; cerebral blood flow

Arterial spin labeling (ASL) is an MRI method for noninvasive assessment of regional tissue perfusion. It is mainly used in the brain [1,2]. However, successful applications in other organs such as retina, kidneys, liver, muscles, and prostate have been reported [3,4]. A crucial limitation of ASL is the relatively low spatial resolution which leads to the so-called partial volume effect: image voxels near the boundary between different tissue types contain a spatially variant mixture of the respective tissues. The problem is manifest especially in ASL brain studies, where the signal in most cortex voxels represents mixtures of gray matter (GM) and white matter (WM). Since CBF is around three times higher for GM than for WM in adults (almost four times higher in children) [5,6], the PV effect has a large influence on the observed CBF in each voxel. Consequently, partial volume correction (PVC) is required for correct CBF quantification. PVC requires reliable methods to determine the contributing tissue fractions on a per-voxel basis.

PET Center, Institute of Radiopharmacy, Helmholtz-Zentrum Dresden-Rossendorf, Dresden, Germany.
*Correspondence to: Jan Petr, Ph.D., HZDR, POB 51 01 19, 01314 Dresden, Germany. E-mail: j.petr@hzdr.de
Received 1 October 2012; revised 7 November 2012; accepted 21 November 2012.
DOI 10.1002/mrm.24601
Published online 27 December 2012 in Wiley Online Library (wileyonlinelibrary.com).

PVC in ASL is often based on additionally acquired high-resolution T_1-weighted images. Segmentation of these images provides maps of GM, WM, and cerebrospinal fluid (CSF), respectively, from which the fractional tissue volumes in each voxel are derived. The simplest PVC approach in ASL is to restrict the analysis to voxels exceeding a certain GM partial volume threshold (see, e.g., [7,8]). An alternative is CBF normalization according to the observed GM volume fraction [9–11]. In 2008, Asllani et al. [12] introduced a method for correcting PV effect using linear regression. In this method, the GM, WM, and CSF ASL signals are separated using the maps of GM, WM, and CSF partial volume. The separated GM, WM, and CSF signals are then quantified separately using a model adapted to the respective tissue type. This PVC method was successfully applied in several studies. Asllani et al. [13] have shown that GM atrophy can be misinterpreted as decreased CBF and that PVC leads to a smaller decrease of GM CBF in elderly subjects than in [5,6]. A more detailed analysis of CBF reduction and the PV effect was presented by Chen et al. [8]. Borogovac et al. [14] showed the PV corrected CBF to be more sensitive to functional changes than the uncorrected CBF. Lately, Chappell et al. extended PVC to multiple-TI (inversion time) ASL [15] and Liang et al. [16] used trimmed least-squares to limit the spatial blurring caused by the square kernel in the original method.

All above-mentioned approaches use segmented high-resolution T_1-weighted images to obtain the PV fractions which has serious shortcomings. First, segmentation of T_1-weighted images can be imperfect/erroneous in certain brain regions. Furthermore, the T_1-weighted data must be coregistered with the ASL images. Affine transformations are usually used which cannot completely compensate for the geometrical distortions of the single-shot sequences as echo-planar imaging (EPI) that are frequently used to acquire the ASL images. Ultimately, the resulting PV maps are suboptimal for PVC of ASL data.

In this article, we propose an alternative method for extraction of the PV fractions that uses the Look-Locker EPI (LL-EPI) acquisition [17] performed with two different flip angles to allow for flip angle correction due to B_1-field inhomogeneities. The FRASIER method [18] for deriving the PV fractions from the T_1-recovery curve in each pixel is used. An alternative method of T_1-time determination is applied as the approach used in the FRASIER method is not suitable for low-resolution data. Measurements in five healthy volunteers were performed. PV maps obtained with the conventional approach (from segmented T_1-weighted images) were compared with those derived when using the proposed LL-EPI based approach. It was shown that the LL-EPI data are more suitable for PVC of the ASL data.

METHODS

Acquisition

Five healthy volunteers gave written informed consent to be enrolled in the study (four men and one woman, mean age 30 ± 3.7 years). MR imaging was performed on a 3T Ingenuity TF PET/MR (Philips, Cleveland, US) with an eight-channel head coil. The used protocol consisted of a T_1-weighted acquisition, multiphase ASL (MP-ASL) using multiple TIs, and two Look-Locker EPI sequences with different flip angles. The total acquisition time was under 10 min (T_1-*w*: 4 min 12 s, MP-ASL: 3 min 20 s, each LL-EPI: 24 s).

High-resolution 3D TFE T_1-weighted images were obtained with these parameters: field-of-view (FOV) 192 × 224 mm^2, acquisition matrix 192 × 224, 192 sagittal slabs, voxel size 1 × 1 × 1 mm^3, repetition time (TR)/echo time (TE) 1880/3.7 ms, flip angle 8°.

MP-ASL images were acquired employing the PULSAR labeling [19], Q2TIPS bolus saturation [20], vascular signal crushing [21], and standard multislice/single-shot EPI readout with LL acquisition [22]. Only seven slices were obtained due to time constraints (slice thickness: 6 mm, interslice gap: 1 mm) in the AC-PC plane with the center of the first slice passing 7 mm above the AC-PC plane. Further acquisition parameters were: FOV 224 × 224 mm^2, in-plane pixel-size 3.5 × 3.5 mm^2, TR/TE 4000/17 ms, flip angle 35°, SENSE factor 2, label thickness/gap 150/20 mm, Q2TIPS saturation start/stop times 940/2140 ms, bipolar crusher gradients with cutoff speed 5 cm/s in all directions (b = 1.6 s/mm^2), and 24 averages. A 90° saturation of the imaging plane was followed by 13 EPI acquisitions starting at 40 ms after labeling and repeated every 300 ms. The Q2TIPS pulses were interleaved with slice acquisition. For continuous bolus saturation, 2 cm thick pulses with 25 ms spacing are usually used [20]. In MP-ASL, acquisition of a single slice took 38.3 ms including the saturation. The thickness of the saturation pulses was increased to 3 cm to accommodate for this increased interpulse delay.

For the PV estimation, two LL-EPI acquisitions were obtained with flip angles 35° and 11.7° with two averages. The imaging parameters were similar to MP-ASL except that SPIR saturation was used to suppress the fat signal and Q2TIPS was not used to avoid magnetization transfer (MT) effects [23]. Thirteen EPI acquisitions with similar timing as in MP-ASL were acquired.

The MP-ASL and LL-EPI sequences were acquired in a multislice mode and thus the actual TI values of all slices differed. The lowest slices were acquired at the TIs indicated and each following slice was acquired with an additional delay of 38.3 ms (MP-ASL) and 42.7 ms (LL-EPI) after the previous slice.

Data Processing

Data were processed using the SPM8 toolbox and in-house routines written in Matlab (MathWorks, Natick, MA, USA) and the R language and environment for statistical computing (R Development Core Team [24]). First, all EPI images were registered to the last TI of the first control image of the MP-ASL sequence (3D affine transformation with a sum-of-squares-differences cost function). The inhomogeneity bias in the T_1-weighted images was corrected and segmentation into GM, WM, and CSF classes was performed using the SPM8 toolbox [25]. The tissue probability template (MNI152) [26] was used as prior information for tissue classification. The T_1-weighted image was coregistered with the mean MP-ASL control image (3D affine transformation with a normalized mutual-information cost function). This transformation was applied to the GM and WM segmented images similarly as in [15]. The images were first transformed using a third-degree B-spline interpolation to a high-resolution space with the same resolution as the T_1-weighted images. PV fractions maps matching the MP-ASL voxel grid were derived by integrating the transformed images over a volume corresponding to each low-resolution voxel (denoted PV_{T1} in the following).

Flip Angle Correction

To compensate for the B_1-field inhomogeneities, the LL-EPI sequence was acquired for two different flip angles θ_1 and θ_2 such that $\theta_1 = 3\theta_2$ [27,28]. Two corresponding effective (observed) relaxation times T_{1e1} and T_{1e2} were obtained from the T_1-recovery curve for each voxel. The true T_1-relaxation time of the tissue T_1 was estimated from T_{1ei} [29]:

$$\frac{1}{T_1} = \frac{1}{T_{1ei}} + \frac{\ln(\cos(\theta_{ai}))}{\Delta TI}, \quad [1]$$

where ΔTI is the delay between the acquisitions and θ_{ai} is the actual flip angle. The actual flip angle θ_{ai} deviates locally from the assumed flip angle θ_i because of B_1-field inhomogeneities, however, the relation $\theta_{a1} = 3\theta_{a2}$ was assumed to hold in every voxel. The actual flip angle in every voxel was obtained by setting the left hand sides of Eq. [1] equal for T_{1e1} and T_{1e2}:

$$\theta_{a2} = \arccos\sqrt{\frac{\exp\left(\Delta TI\left(\frac{1}{T_{1e2}} - \frac{1}{T_{1e1}}\right)\right) + 3}{4}}. \quad [2]$$

Partial Volume Determination

The FRASIER segmentation was used to obtain tissue PV fractions [18] from the LL-EPI data with a flip angle 35°. The measured signal after the 90° saturation is:

$$S(t) = \sum_i s_i M_{ss,i}\left(1 - \exp\left(-\frac{t}{T_{1e,i}}\right)\right), \quad [3]$$

where s_i is the fractional signal of tissue type i with effective relaxation time $T_{1e,i}$ (Eq. [1]). The term $M_{ss,i}$ describes the tissue specific equilibrium magnetization for the LL-EPI acquisition:

$$M_{ss,i} = \frac{1 - \exp\left(-\frac{\Delta TI}{T_{1,i}}\right)}{1 - \cos\theta_a \exp\left(-\frac{\Delta TI}{T_{1,i}}\right)}, \quad [4]$$

where $T_{1,i}$ is the true relaxation time and θ_a is the actual flip angle in each voxel Eq. [2]. Determination of the

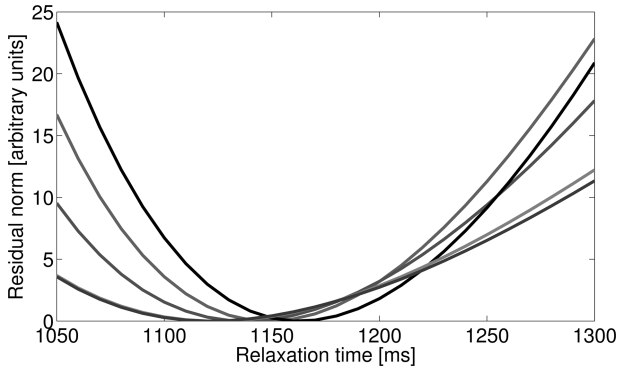

FIG. 1. Residual norm of the solution of Eq. [3] for different GM T_1-times. Normalized results for all five subjects are shown for comparison. Clear global minimum and absence of local minima are visible.

T_1-relaxation times for each tissue type is described in the following section. Equation [3] is linear in the unknowns s_i which, therefore, can be derived from a linear least squares fit. The PV fractions p_i were obtained by correcting for the variable water density in the different tissues according to:

$$p_i = \frac{\frac{S_i}{\varrho_i}}{\sum_j \frac{s_j}{\varrho_j}}, \qquad [5]$$

where the relative water densities ϱ_i in WM, GM, and CSF were 73%, 89%, and 100%, respectively [30]. The PV fractions derived using this LL-EPI based approach are denoted PV_{LL} in the following.

T_1-Time Determination

The T_1-relaxation times and actual flip angles were calculated for each pixel from Eqs. [1] and [2]. The histogram-fitting method for GM/WM/CSF T_1-time determination used by Shin et al. [18] is not suitable for low-resolution data. Therefore, a novel method for T_1-time determination is presented. The voxels with T_1-time between 642 ms and 814 ms were selected as containing high PV fraction of WM (mean + 2 standard deviations margin of expected WM T_1-times [31]). To remove voxels containing also GM and CSF, the boundary voxels were removed from this mask. Given the voxel size of 3.5 × 3.5 × 6 mm^3, removal of this boundary layer is assumed to be sufficient. The WM T_1-time was determined as the mean T_1-time of the remaining voxels.

This method cannot be used for GM T_1-time estimation as, contrary to WM, there are almost no voxels containing pure GM. Instead, GM T_1-time was determined iteratively along with the PV-fractions estimation:

1. The GM T_1-time was set to 1200 ms.
2. PV fractional signals were estimated from Eq. [3].
3. The mean square residual norm of the estimation was calculated for all voxels (Eq. [3]).
4. The GM T_1-time was optimized using gradient descent by iterating steps 2 and 3 until the minimum norm was reached.
5. PV fractions were calculated from Eqs. [3] and [4] using the optimal value of GM T_1-time.

The residual norm is plotted against the GM T_1-times in Figure 1 to illustrate that the global minimum can be easily reached.

The determination of CSF relaxation time was not feasible due to low number of CSF-only pixels. Therefore, the value was fixed to 4300 ms [31].

Partial Volume Correction

In each voxel of the ASL data, the (control - label) difference signal ΔM is a PV-weighted sum of perfusion dependent signals from GM, WM (zero ASL difference signal is assumed in CSF) [12]:

$$\Delta M = \Delta M_{GM} p_{GM} + \Delta M_{WM} p_{WM}, \qquad [6]$$

where ΔM_{GM} and ΔM_{WM} are the tissue-specific perfusion dependent signals from GM and WM, respectively. The signal separation was done independently for each voxel using the approach of Asllani et al. [12]: the unknown ΔM_{GM} and ΔM_{WM} are assumed to be constant in an $n \times n \times 1$ neighborhood of each voxel i. Using this assumption, Eq. [6] can be replaced by a linear system of equations that is then solved in the least-squares sense for the ΔM_{GM} and ΔM_{WM}.

The partial volume corrected signal ΔM_{GM} and ΔM_{WM} was calculated using both PV maps from PV_{T1} and PV_{LL}. Five different neighborhood sizes (3 × 3 × 1 up to 11 × 11 × 1 voxels) were used.

CBF Quantification

The CBF value f and the bolus arrival time t_a were calculated from the MP-ASL data by least-squares fitting of the model proposed by Günther et al. [29]:

$$\Delta M(t) = \begin{cases} 0 & 0 < t < t_a \\ \frac{-2M_{0,b}f}{\delta R} e^{-\frac{t}{T_{1,b}}}\left(1 - e^{\delta R(t-t_a)}\right) & t_a < t < t_a + t_d \\ \frac{-2M_{0,b}f}{\delta R} e^{-\frac{t_a+t_d}{T_{1,b}}}\left(1 - e^{\delta R t_d}\right) e^{R_{1app}(t-t_a-t_d)} & t_a + t_d < t \end{cases}, \qquad [7]$$

where t_d is the bolus width defined by the Q2TIPS saturation (t_d = 940 ms), $R_{1app} = 1/T_{1,t} + f/\lambda_t - (\ln \cos \theta_a)/\Delta TI$, $\delta R = 1/T_{1,b} - R_{1app}$, the delay between LL-EPI acquisitions was ΔTI = 300 ms, and $T_{1,b}$ is the T_1-relaxation time of blood ($T_{1,b}$ = 1664 ms). The actual flip angle θ_a estimated for each voxel was used (Eq. [2]). The previously estimated tissue relaxation times $T_{1,t}$ were used. Blood–brain partition coefficient values λ_{WM} = 0.86 for WM and λ_{GM} = 0.98 for GM were used [32]. The equilibrium magnetization of blood $M_{0,b}$ was derived from the mean equilibrium magnetization of WM ($M_{0,WM}$) from voxels with p_{WM} exceeding 90% as proposed in [33].

Three types of quantification were used: CBF_{NOPV}, CBF_{GMPV}, and CBF_{2TPV} using Eq. [7] for all of them. CBF_{GMPV} and CBF_{2TPV} were calculated using both PV_{T1} and PV_{LL} maps. The quantification without PV correction (CBF_{NOPV}) was obtained from the total difference signal ΔM considering all pixels to contain only GM. That means that relaxation times $T_{1,t}$ of GM and blood–brain partition coefficient λ of GM were used for all pixels. CBF_{NOPV} served as ground truth for the

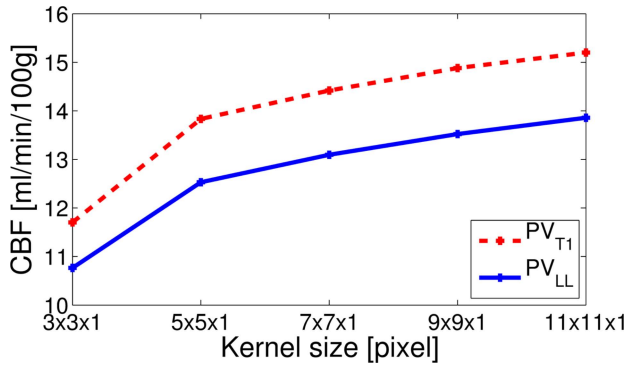

FIG. 2. Regression error of the PVC algorithm in mL/min/100 mL. The RMS values of the differences $CBF_{NOPV} - CBF_{GMPV}$ are shown for different kernel sizes. In all cases, RMS is higher for the PV_{T1} method than for the PV_{LL} method. Furthermore, the RMS is increasing with increasing kernel size. [Color figure can be viewed in the online issue, which is available at wileyonlinelibrary.com.]

PV-determination validation as no PV correction was applied to this volume.

For the CBF_{GMPV} quantification, ΔM_{GM} and ΔM_{WM} were quantified separately using Eq. [7] giving quantified values $CBF_{GMPV,GM}$ and $CBF_{GMPV,WM}$. The GM parameters $T_{1,GM}$ and λ_{GM} were used for quantifying both GM and WM. The total CBF was:

$$CBF_{GMPV} = CBF_{GMPV,WM} \cdot p_{WM} + CBF_{GMPV,GM} \cdot p_{GM}. \quad [8]$$

It was possible to directly compare CBF_{GMPV} with the ground-truth CBF_{NOPV}, as GM parameters only were used for quantification in all voxels in both cases. This comparison served for quantitative validation of PV_{T1} and PV_{LL} maps.

Finally, CBF_{2TPV} was computed in a way similar to [15]. The quantification of ΔM_{GM} and ΔM_{WM} was done separately, and proper tissue-specific parameters $T_{1,t}$ and λ_t of GM and WM were used yielding $CBF_{2TPV,GM}$ and $CBF_{2TPV,WM}$, respectively, which were then summed:

$$CBF_{2TPV} = CBF_{2TPV,WM} \cdot p_{WM} + CBF_{2TPV,GM} \cdot p_{GM}. \quad [9]$$

This quantification was considered the most realistic and it was used for assessing the global effect of the PV correction on CBF.

Validation

The quality of the PV fractions obtained with PV_{T1} and PV_{LL} were compared as follows. The regression error of the estimation in Eq. [6] was computed as the root mean squares (RMS) difference between the uncorrected CBF_{NOPV} the corrected CBF_{GMPV}. The regression error is influenced by the errors in the PV maps and by smoothing the tissue-specific signal. It was assumed that the errors from the smoothing were similar for both PV_{T1} and PV_{LL}. The difference in the regression error for PV_{T1} and PV_{LL}, thus, reflected mainly the errors in the PV maps. The error was computed using absolute CBF values instead of ΔM_{GM} values as was done in [12]. This way, the error was given in terms of absolute CBF deviations. The error was calculated for all kernel sizes of the PV correction.

The RMS error was computed also between the uncorrected CBF_{NOPV} and the PV corrected CBF_{2TPV}. The appropriate T_1 and λ were used for CBF_{2TPV} calculation. However, T_1 and λ of GM were used for calculation of all voxels in CBF_{NOPV}. Thus, the comparison of CBF_{NOPV} with CBF_{2TPV} cannot be used to evaluate the quality of PV-fractions estimation. However, it was used to investigate the effect of PV correction with different maps on the resulting CBF values.

The RMS error and the CBF values were measured both on the whole brain and on WM and GM masks where the PV fraction exceeded 80%.

RESULTS

The T_1-relaxation times derived automatically from the LL-EPI data were 702 ± 4 ms for WM and 1138 ± 18 ms for GM, respectively.

Figure 2 shows the regression errors. On average, the error for PV_{T1} between CBF_{NOPV} and CBF_{GMPV} was 12% higher than the error for PV_{LL} for all kernel sizes. The difference between the PV_{T1} and PV_{LL} errors was significant for all kernel sizes ($P < 0.05$). The absolute difference between PV_{T1} error and PV_{LL} error was monotonically increasing with increasing kernel size. The difference between the PV_{T1} and PV_{LL} errors for the kernel size 11 × 11 × 1 was 14% higher than the difference for the kernel size 3 × 3 × 1. An example of the PV maps and corresponding perfusion images is shown in Figure 3. The CBF after PVC CBF_{GMPV} is shown for both

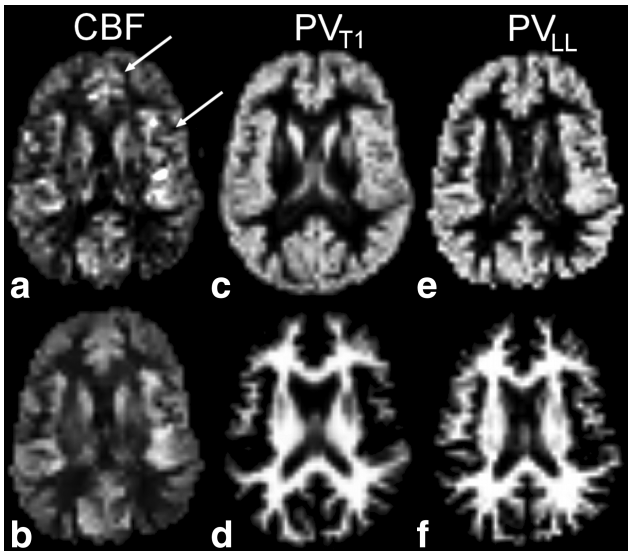

FIG. 3. Comparison of partial volume maps for one selected slice. **a**: The PV uncorrected quantification CBF_{NOPV}; **b**: the PV corrected quantification CBF_{2TPV} using PV_{LL} maps (kernel size 3 × 3 × 1). The corresponding GM (**c,e**) and WM (**d,f**) PV maps are shown for the PV_{T1} method (c,d) and the PV_{LL} method (e,f). Note that the GM in (e) differs from (c) and the same difference is visible also in the WM images in (d) and (f). Two areas are marked with arrows. The WM is very thin there and thus remains undetected on the PV_{T1} maps whereas the detailed WM structure is visible on the PV_{LL} maps. Decreased signal in the CBF image CBF_{NOPV} in (a) corresponds better to the WM regions in the PV_{LL} map than in the PV_{T1} maps.

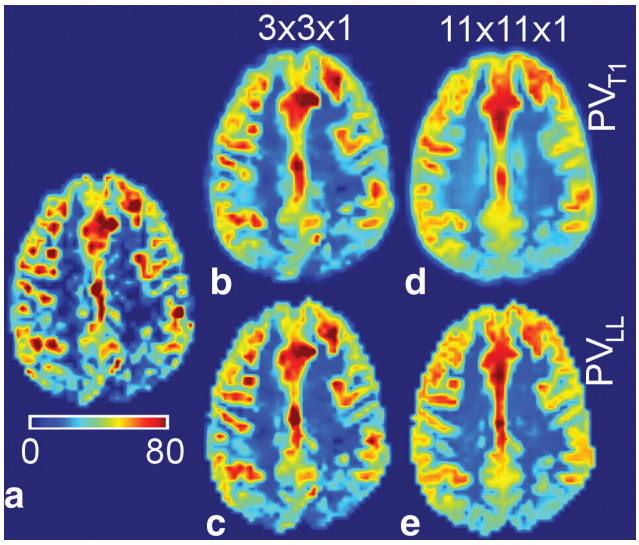

FIG. 4. Comparison of CBF images before and after PVC. The uncorrected CBF image CBF_{NOPV} is shown in (**a**). CBF is specified in units of mL/min/100 mL. The PV corrected images CBF_{GMPV} with a kernel size of 3 × 3 × 1 (**b,c**) and 11 × 11 × 1 (**d,e**) used for the PV correction, respectively, and with both investigated methods, PV_{T1} (b,d) and PV_{LL} (c,e) are shown. As in Figure 3, there are distinct differences between original and corrected data that become especially obvious for higher kernel sizes (d,e). Blurring of most GM structures and appearance of structures not visible in the noncorrected image (a) is obvious in (b) and especially in (d). The same structures are well preserved when using PV_{LL} maps (c) even for bigger kernel sizes (e).

methods and for kernel sizes 3 × 3 × 1 and 11 × 11 × 1 in Figures 4 and 5 in more details. It is clearly visible, that the corrected CBF differed increasingly from the original one with increasing kernel size for PV_{T1} as a result of shortcomings of the PV maps. This effect was much less pronounced in the PV_{LL} results.

All calculated CBF values are shown in Table 1. The GM/WM CBF ratio was 3.4 for the uncorrected CBF_{NOPV}, however, it decreased to 3 for CBF_{GMPV} and to 1.9 for CBF_{2TPV}. Slight increase of 8% (PV_{T1}) and 3% (PV_{LL}) in the mean GM CBF between CBF_{NOPV} and CBF_{GMPV} was observed for kernel size 3 × 3 × 1, see Table 1 and also Figure 6. The increase in GM CBF was 10% (PV_{T1}) and 6% (PV_{LL}) between CBF_{NOPV} and CBF_{2TPV}. And an important difference was found for WM CBF between CBF_{NOPV} and CBF_{2TPV}. The CBF increased by 92% (PV_{T1}) and 93% (PV_{LL}), respectively.

The influence of the PV maps on the corrected CBF value CBF_{2TPV} is shown in Figure 6. The subject-mean CBF_{2TPV} values differ for PV_{T1} and PV_{LL}. The mean difference for all subjects and kernel sizes was significant for total CBF (difference 0.5 mL/min/100 mL, 1.2% difference, $P = 0.03$) and for GM CBF (3.5 mL/min/100 mL, 5.9%, $P = 0.007$). Pixelwise CBF values comparison showed even more significant differences than for the subject-mean CBF. The whole-brain CBF difference was 6.9 mL/min/100 mL (17%, $P = 6e{-}5$) and the difference in GM CBF was 7.6 mL/min/100 mL (13%, $P = 3e{-}5$).

DISCUSSION

Our investigation has shown that LL-EPI-based PVC in ASL is feasible. It was compared with the frequently used method of extracting the PV maps from segmented T_1-weighted images. The PV_{LL} method turned out to yield superior PV maps according to regression error.

Shin et al. [18] used the FRASIER segmentation on images with voxel size 1.7 × 1.7 × 4 mm^3. This method can be used also on lower-resolution data as mixing of different tissues in most voxels is expected. However, GM and WM T_1-time determination becomes difficult when low-resolution data are used. Shin et al. propose to obtain the relaxation times by fitting four Gaussians to the frequency distribution of T_1-times [18,34]. Reasonable results are obtained for high-resolution images where there are many voxels containing pure GM or WM tissue. This, however, does not apply for low-resolution images such as ASL images. Moreover, it is not guaranteed that the PV fraction distribution around the pure tissue is symmetric. This could cause a systematic error in the T_1

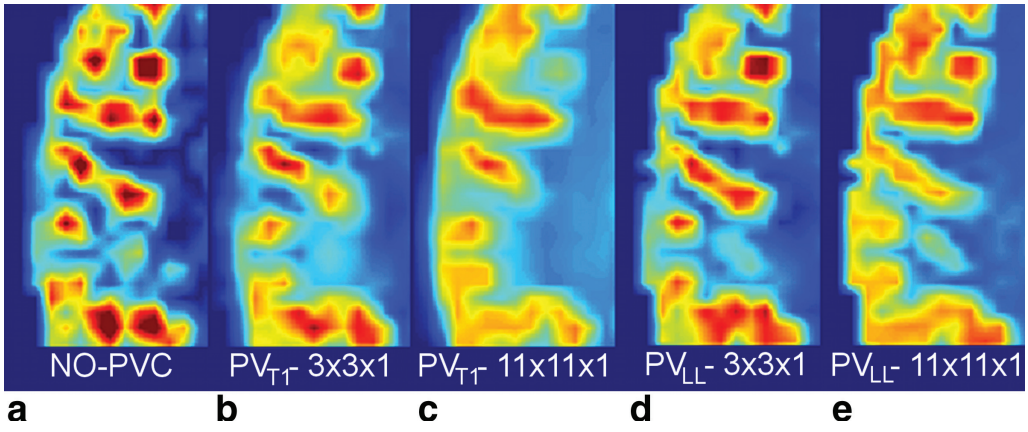

FIG. 5. Detail from Figure 4. Although some smoothing is visible, the GM structure can be clearly recognized when using the 3 × 3 × 1 kernel (**b,d**). However, for the 11 × 11 × 1 kernel the influence of errors in PV_{T1} is clearly visible (**c**): some GM structures are blurred or are completely missing and spurious structures arise not present in the original image (**a**). The quality of the PV_{LL}-based result (d) remains, however, satisfactory even for this large kernel and although some blurring is apparent the GM structure is generally much better preserved.

Table 1
Mean and Standard Deviation of CBF Values Over the Five Subjects

	CBF_{NOPV}	CBF_{GMPV}+PV_{T1}	CBF_{GMPV}+PV_{LL}	CBF_{2TPV}+PV_{T1}	CBF_{2TPV}+PV_{LL}
Total	34.1 ± 1.9	35.5 ± 1.9	35.0 ± 1.9	41.9 ± 1.9	41.6 ± 1.6
GM	56.5 ± 1.6	61.3 ± 2.3	58.0 ± 1.9	62.3 ± 1.6	60.1 ± 1.0
WM	16.8 ± 1.6	20.0 ± 1.8	20.3 ± 1.6	32.3 ± 2.3	32.4 ± 1.9

The values are shown in mL/min/100 mL for the whole brain and for GM and WM regions. The WM and GM regions were defined by demanding a PV fraction > 80% in the PV_{T1} maps. The uncorrected (CBF_{NOPV}) as well as the PV corrected (CBF_{GMPV}, CBF_{GMPV}) values are shown. The corrected values are shown for both PV_{LL} and PV_{T1} maps used for kernel size 3 × 3 × 1.

estimation, especially for GM. The method proposed in this paper is not negatively influenced by the low resolution as enough pure WM voxels were found. The GM T_1-time determination is independent of the GM PV-fraction distribution and no pure GM voxels are needed. The obtained T_1-time values were not significantly different from literature values [31] of the occipital GM ($P = 0.77$), frontal GM ($P = 0.18$), and frontal WM ($P = 0.87$). The T_1 of WM differed scarcely significantly from the occipital WM ($P = 0.03$). This suggests that the values can be used for PV fractions determination. Further investigation needs to be carried out to determine the T_1-times regionally as substantial regional differences are presented in [31]. The T_1-time values determined in this paper are on average equivalent to 1560 ± 86 ms for GM, 846 ± 19 ms for WM if no pixel-wise flip angle correction were applied. These values were calculated over region with GM/WM PV fractions exceeding 80%. Although the values roughly correspond to the ASL literature, any proper comparison is difficult as the flip angle correction is used only rarely in ASL.

The measured values of CBF were also compared with literature. Comparison of absolute CBF values is in general difficult as there is a large number of acquisition sequences and quantification methods yielding substantially different results. The mean uncorrected CBF_{NOPV} in GM (PV > 80%) is around 16% higher than the results of the multicenter QUASAR PASL study (47.4 ±

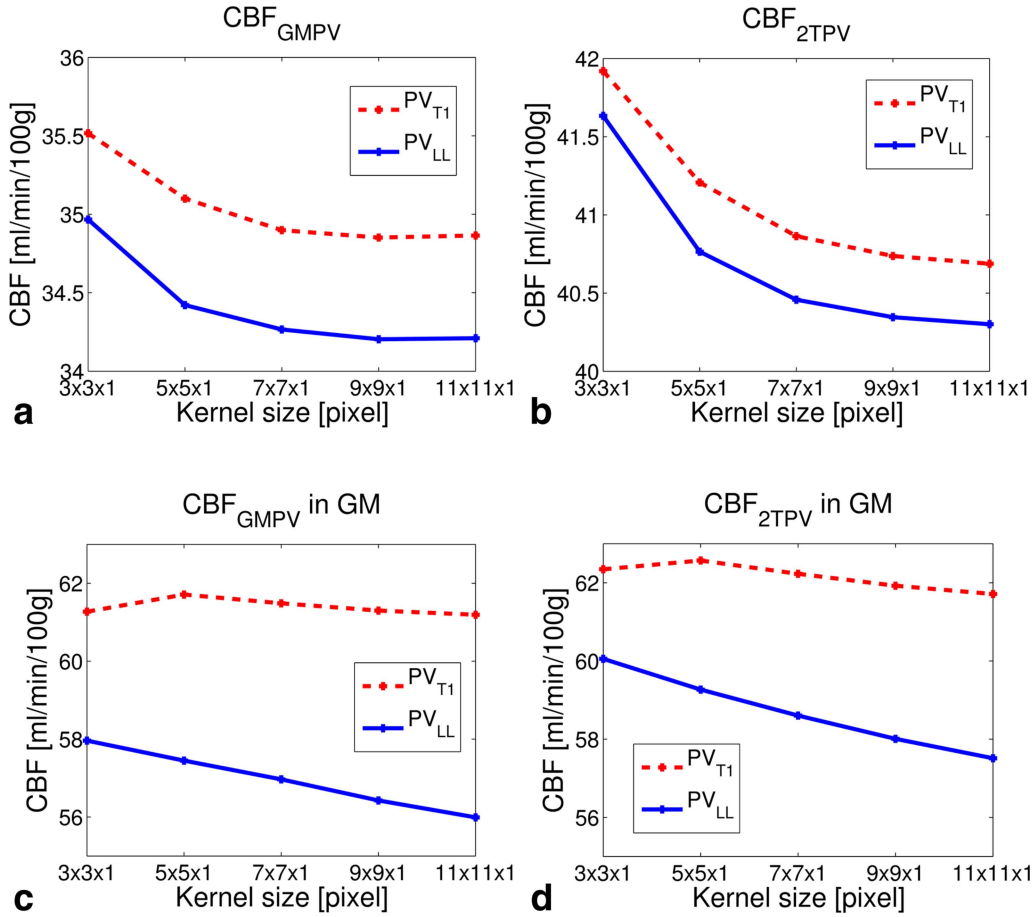

FIG. 6. Mean CBF of the PV corrected images CBF_{GMPV} (**a,c**) and CBF_{2TPV} (**b,d**) is shown as a function of the used kernel size for both PV_{LL} and PV_{T1}. The mean results for the whole brain (a,b) and in GM (PV fraction > 80%) are shown. The mean CBF difference between both methods is 1.8% for CBF_{GMPV} and 1.2% for CBF_{2TPV} in the whole brain, and 7.8% and 5.9% in GM, respectively. [Color figure can be viewed in the online issue, which is available at wileyonlinelibrary.com.]

7.5 mL/min/100 mL; $P = 0.008$) where the model-free approach was used [35]. However, up to 25% difference between the model-free and three-parameter fit quantification of the multi-TI data (used in this article) was presented by the same group [36]. The whole-brain average CBF was compared with the results presented in [37] where a similar multi-TI sequences was used. The results are not significantly different ($P = 0.18$) but this should be interpreted with care given that sample sizes were small in both studies. The difference between our measurement (34.1 ± 1.9 mL/min/100 mL) and the literature value (40.5 ± 9.5 mL/mL/100 mL) is 16%. This difference might be explained by the fact that a different planning was used (only five slices for multi-TI acquisition in [37]) and that a different method for $M_{0,b}$ estimation was used in both studies. Also, flip angle correction and subject-specific measured values of T_1-relaxation times were used in this study but not in [35–37]. The GM/WM perfusion ratio of 3.5 for the dominantly male group with mean age 30 years is concordant with the literature values by Biagi et al. (3.6, age 16 years; 2.9, age 40 years) [5] and Asllani et al. (3.5, age 70 years; 3.9, age 26 years) [13], although much larger than the value of 2.5 reported by Parkes et al. [6]. The ratio decreased to 1.9 for CBF_{2TPV}. This is a direct consequence of the increased CBF in WM caused by using appropriate parameters for WM CBF quantification (as discussed also below).

The evaluated regression error is influenced by two factors. The first one is due to errors in the PV maps. Second, the linear regression with a square kernel does smooth the tissue-specific signal (including the noise) to a certain extent. Therefore, there would be a finite $CBF_{NOPV} - CBF_{GMPV}$ difference even if the PV maps were perfect. We assume that actual errors of the PV maps are dominating the observed regression error for PV_{T1} as well as for PV_{LL} PVC.

A single tissue type was assumed in the quantification to allow comparison with the noncorrected data. The error is lower for PV_{LL} PVC for all kernel sizes. The difference between PV_{LL} and PV_{T1} increased with increasing kernel size. The influence of the PV maps on the PV corrected CBF is increasing with increasing kernel size. The increasing error difference between the methods thus indicates more error in the PV_{T1} estimated PV maps than in those estimated with PV_{LL}. The regression error is around 15%–20% of mean CBF for kernel size $3 \times 3 \times 1$ to $11 \times 11 \times 1$. The regression error in literature is given only for continuous ASL in [12] and it is around 9%–13%. However, this error was computed for the PV-corrected control images where the signal is expected to be smoother. Furthermore, these images are considerably less noisy which also considerably decreases the regression error. The reason for decreased regression error for PV_{LL} is probably the fact that the LL-EPI sequence used for obtaining the PV_{LL} maps is similar to the EPI sequence used for the ASL acquisition and, therefore, the resulting PV_{LL} maps contain the same geometrical distortions as the ASL data. Misplacement of GM structures in the PV_{T1} maps caused by the EPI distortions causes blurring of the GM structures in the PV corrected CBF_{GMPV}, see Figures 4 and 5. The second reason is illustrated in Figure 3. The PV_{T1} maps are less accurate in regions where the WM (or GM) is thin. The intensity contrast between the region and the background is then very subtle in T_1-weighted images which can lead to incorrect segmentation and disappearance of these regions from the PV_{T1} maps. In PV_{LL}, the PV fractions are obtained from the sum signal of the voxel. The tissue spatial distribution inside the voxel, thus, does not influence the PV fraction determination. Studying the effect of PVC on CBF showed a mean CBF increase of around 8% in GM and almost 92% in WM between CBF_{NOPV} and CBF_{2TPV} regardless the PV maps used. The increase in GM can be explained by inherent smoothing of the PVC method. The mean CBF is computed over regions with GM PV > 80%. A high GM CBF value next to this region can increase the mean value inside the region. This improved by using a bigger kernel, where the difference decreased to 2% for $11 \times 11 \times 1$ for PV_{LL} while it stayed at 10% for PV_{T1}. The difference in WM CBF between CBF_{NOPV} and CBF_{2TPV} is caused by the fact that appropriate parameters were used for WM quantification instead of quantifying it using GM parameters. This subsequently leads to increase in CBF as WM relaxation time is shorter than for GM relaxation time. Note also the shape of the plots in Figure 6. The mean CBF is decreasing for increasing kernel size in most cases because of the smoothing effect of PVC and uneven distribution of CBF in the brain. However, the mean GM CBF of PV_{LL} (Fig. 6c,d) increases for small kernel sizes. This might be caused by the fact, that the PV_{LL} maps contain errors which makes the PVC less stable for smaller kernel sizes. These errors are not apparent on the whole-brain mean CBF but show on the GM CBF only, as only few areas have GM exceeding 80%.

Currently, there is no well-established methodology for validating CBF measurements using ASL. Comparisons with PET or other modalities have not yet reached sufficient accuracy to decide which of the tested PV corrected maps gives more accurate results. Validation of the PV fraction determination thus can only be done using the comparison of CBF_{NOPV} and CBF_{GMPV}. The difference between the quantified values of CBF_{2TPV} for PV_{T1} and PV_{LL} only serves as an indicator of the magnitude of the overall effect the different method for PV determination has on the quantification. Although the difference in the mean CBF was significant, the increase of 1.2% in the whole-brain CBF and 5.9% in the GM CBF is not so pronounced. However computed pixel-wise, there is an important difference in the CBF quantification (17% for total CBF and 13% for GM CBF). This indicates that although the PVC with PV_{T1} maps gives reasonable values on average, its regional difference from the PV_{LL} is important.

The FRASIER segmentation [18] was already applied to the domain of ASL by Ahlgren et al. [34] to improve the $M_{0,b}$ estimation. Contrary to this approach which uses the QUASAR sequence [35], we acquired the LL-EPI images separately. This takes slightly more time (less than 30 s) but has clear advantages. The SPIR saturation was used to suppress fat-shift artifacts. These artifacts normally cancel out in the difference image and do not influence CBF quantification. However, they can spoil the analysis of the T_1-recovery curve. Additionally, no Q2TIPS saturation was used. It is known that Q2TIPS

produces MT effect which shortens the T_1-relaxation time in the control images during the period when the saturation is switched on [23]. Therefore, it negatively influences also the T_1-time measurement and the PV determination.

The proposed method (PV_{LL}) can directly replace the PV_{T1} method in all applications that use PV maps for ROI definition [7,8], CBF normalization in GM [9–11] or PVC [12,14,15] on subjects for which brain tissue segmentation is not problematic (for example Alzheimer, Parkinson and stroke patients; healthy volunteers). In patients that have serious deformations in brain structure, the spatial normalization to MNI becomes difficult. The segmentation, thus, does not work optimally and the PV_{T1} method can fail. On the other hand, the PV_{LL} method does not use any prior information and, thus, it can in principle work also on deformed images. Prospectively, the PV_{LL} method might also be usable in other organs or in tumors by adding corresponding T_1-times to the segmentation. This conjecture, however, needs to be investigated further to prove that the method is sensitive enough.

The LL acquisition with 300 ms time frames allows the acquisition of only seven slices at the given resolution. To increase the coverage a second acquisition could be performed since the sequence acquisition time is short. Alternatively, the delay between frames could be optimized to allow acquisition of more slices. The effect of changes in this delay (and of flip angle and the number of repetitions) on the quality of PV estimation should then be investigated. The fitting procedure currently fits the model only to the high-flip angle data with corrected flip angle value. The simultaneous estimation from both low and high flip angle measurements might further increase accuracy.

In conclusion, a new method for PV maps estimation (PV_{LL}) has been presented and compared with the standard method (PV_{T1}). The hypothesis that the PV_{LL} maps are more suitable for PVC of ASL data is supported by the fact that the regression error is lower for the PV_{LL} maps. Moreover, more artifacts in the PV corrected CBF maps were observed with PV_{T1} than with PV_{LL}. Therefore, we believe that extracting PV maps from the LL-EPI sequence is an attractive and superior alternative to the current approach of using high-resolution T_1-weighted images. The method has also potential to be applied to different organs and to pathological brain images where the standard procedure would fail.

REFERENCES

1. Williams DS, Detre JA, Leigh JS, Koretsky AP. Magnetic resonance imaging of perfusion using spin inversion of arterial water. Proc Natl Acad Sci USA 1992;89:212–216.
2. Golay X, Hendrikse J, Lim TCC. Perfusion imaging using arterial spin labeling. Top Magn Reson Imaging 2004;15:10–27.
3. Cutajar M, Thomas DL, Banks T, Clark CA, Golay X, Gordon I. Repeatability of renal arterial spin labelling MRI in healthy subjects. Magma 2012;25:145–153.
4. Maleki N, Dai W, Alsop DC. Optimization of background suppression for arterial spin labeling perfusion imaging. Magma 2012;25: 127–133.
5. Biagi L, Abbruzzese A, Bianchi MC, Alsop DC, Del Guerra A, Tosetti M. Age dependence of cerebral perfusion assessed by magnetic resonance continuous arterial spin labeling. J Magn Reson Imaging 2007; 25:696–702.
6. Parkes LM, Rashid W, Chard DT, Tofts PS. Normal cerebral perfusion measurements using arterial spin labeling: reproducibility, stability, and age and gender effects. Mag Reson Med 2004;51:736–743.
7. Wu W-C, Jiang S-F, Yang S-C, Lien S-H. Pseudocontinuous arterial spin labeling perfusion magnetic resonance imaging—a normative study of reproducibility in the human brain. NeuroImage 2011;56: 1244–1250.
8. Chen Y, Wang DJJ, Detre JA. Test-retest reliability of arterial spin labeling with common labeling strategies. J Magn Reson Imaging 2011;33:940–949.
9. Taki Y, Hashizume H, Sassa Y, Takeuchi H, Wu K, Asano M, Asano K, Fukuda H, Kawashima R. Gender differences in partial-volume corrected brain perfusion using brain MRI in healthy children. NeuroImage 2011;58:709–715.
10. Mak HKF, Chan Q, Zhang Z, Petersen ET, Qiu D, Zhang L, Yau KKW, Chu L-W, Golay X. Quantitative assessment of cerebral hemodynamic parameters by QUASAR arterial spin labeling in alzheimer's disease and cognitively normal elderly adults at 3-Tesla. J Alzheimers Dis 2012;31:33–44.
11. Wang Y, Saykin AJ, Pfeuffer J, Lin C, Mosier KM, Shen L, Kim S, Hutchins GD. Regional reproducibility of pulsed arterial spin labeling perfusion imaging at 3T. NeuroImage 2011;54:1188–1195.
12. Asllani I, Borogovac A, Brown TR. Regression algorithm correcting for partial volume effects in arterial spin labeling MRI. Magn Reson Med 2008;60:1362–1371.
13. Asllani I, Habeck C, Borogovac A, Brown TR, Brickman AM, Stern Y. Separating function from structure in perfusion imaging of the aging brain. Hum Brain Mapp 2009;30:2927–2935.
14. Borogovac A, Habeck C, Small SA, Asllani I. Mapping brain function using a 30-day interval between baseline and activation: a novel arterial spin labeling fMRI approach. J Cereb Blood Flow Metab 2010;30: 1721–1733.
15. Chappell MA, Groves AR, MacIntosh BJ, Donahue MJ, Jezzard P, Woolrich MW. Partial volume correction of multiple inversion time arterial spin labeling MRI data. Magn Reson Med 2011;65: 1173–1183.
16. Liang X, Connelly A, Calamante F. Improved partial volume correction for single inversion time arterial spin labeling data. Magn Reson Med 2013;69:531–537.
17. Petr J, Schramm G, Hofheinz F, Langner J, Steinbach J, van den Hoff J. Look-locker acquisition for estimation of partial volume fractions in ASL Data. In Proceedings of the 20th Annual Meeting of ISMRM, Melbourne, Australia, 2012. p. 2001.
18. Shin W, Geng X, Gu H, Zhan W, Zou Q, Yang Y. Automated brain tissue segmentation based on fractional signal mapping from inversion recovery Look-Locker acquisition. NeuroImage 2010;52: 1347–1354.
19. Golay X, Petersen ET, Hui F. Pulsed star labeling of arterial regions (PULSAR): a robust regional perfusion technique for high field imaging. Magn Reson Med 2005;53:15–21.
20. Luh WM, Wong EC, Bandettini PA, Hyde JS. QUIPSS II with thin-slice TI1 periodic saturation: a method for improving accuracy of quantitative perfusion imaging using pulsed arterial spin labeling. Magn Reson Med 1999;41:1246–1254.
21. Ye FQ, Mattay VS, Jezzard P, Frank JA, Weinberger DR, McLaughlin AC. Correction for vascular artifacts in cerebral blood flow values measured by using arterial spin tagging techniques. Magn Reson Med. 1997;37:226–235.
22. Look DC, Locker DR. Time saving in measurement of NMR and EPR relaxation times. Rev Sci Instrum 1970;41:250–251.
23. De Vita E, Günther M, Golay X, Thomas DL. Magnetisation transfer effects of Q2TIPS pulses in ASL. Magma 2012;25:113–126.
24. R Development Core Team. R: A Language and Environment for Statistical Computing. Vienna, Austria: 2010.
25. Ashburner J, Friston KJ. Unified segmentation. NeuroImage 2005;26: 839–851.
26. Mazziotta JC, Toga AW, Evans A, Fox P, Lancaster J. A probabilistic atlas of the human brain: theory and rationale for its development. NeuroImage 1995;2:89–101.
27. Stollberger R, Wach P. Imaging of the active B1 field in vivo. Magn Reson Med 1996;35:246–251.
28. Petersen ET, Zimine I, Ho YCL, Golay X. An improved QUASAR sequence for user-independent quantitative and reproducible perfusion measurements. In Proceedings of the 15th Annual Meeting of ISMRM, Berlin, Germany, 2007. p. 376.

29. Günther M, Bock M, Schad LR. Arterial spin labeling in combination with a look-locker sampling strategy: inflow turbo-sampling EPI-FAIR (ITS-FAIR). Magn Reson Med 2001;46:974–984.
30. Donahue MJ, Lu H, Jones CK, Edden RAE, Pekar JJ, van Zijl PCM. Theoretical and experimental investigation of the VASO contrast mechanism. Magn Reson Med 2006;56:1261–1273.
31. Lu H, Nagae-Poetscher LM, Golay X, Lin D, Pomper M, van Zijl PC. Routine clinical brain MRI sequences for use at 3.0 Tesla. J Magn Reson Imaging 2005;22:13–22.
32. Herscovitch P, Raichle ME. What is the correct value for the brain–blood partition coefficient for water? J Cereb Blood Flow Metab 1985;5:65–69.
33. Cavuşoğlu M, Pfeuffer J, Uğurbil K, Uludağ K. Comparison of pulsed arterial spin labeling encoding schemes and absolute perfusion quantification. Magn Reson Med 2009;27:1039–1045.
34. Ahlgren A, Wirestam R, Ståhlberg F, Knutsson L. Using fractional segmentation for estimation of the equilibrium magnetization of arterial blood in model-free arterial spin labeling. In Proceedings of the 28th Annual Meeting of ESMRMB, Leipzig, Germany, 2011. p. 554.
35. Petersen ET, Mouridsen K, Golay X. The QUASAR reproducibility study, Part II: results from a multi-center arterial spin labeling test-retest study. NeuroImage 2010;49:104–113.
36. Ho Y-CL, Petersen ET, Golay X. Measuring arterial and tissue responses to functional challenges using arterial spin labeling. NeuroImage 2010;49:478–487.
37. Gevers S, van Osch MJ, Bokkers RP, Kies DA, Teeuwisse WM, Majoie CB, Hendrikse J, Nederveen AJ. Intra- and multicenter reproducibility of pulsed, continuous and pseudo-continuous arterial spin labeling methods for measuring cerebral perfusion. J Cereb Blood Flow Metab 2011;31:1706–1715.

Appendix A2

Effects of systematic partial volume errors on the estimation of gray matter cerebral blood flow with arterial spin labeling MRI

Petr, J., Mutsaerts, H. J., De Vita, E., Steketee, R. M., Smits, M., Nederveen, A. J., ... & Asllani, I. (2018). Effects of systematic partial volume errors on the estimation of gray matter cerebral blood flow with arterial spin labeling MRI. Magnetic Resonance Materials in Physics, Biology and Medicine, 31(6), 725-734.

Journal name (category): **Magnetic resonance materials in physics, biology and medicine** (Radiology, nuclear medicine & medical imaging)

Quartile in category: **Q3**

Impact factor: **2.533**

Number of WoS citations: **11**

Magnetic Resonance Materials in Physics, Biology and Medicine (2018) 31:725–734
https://doi.org/10.1007/s10334-018-0691-y

RESEARCH ARTICLE

Effects of systematic partial volume errors on the estimation of gray matter cerebral blood flow with arterial spin labeling MRI

Jan Petr[1,2] · Henri J. M. M. Mutsaerts[2,3,4,5] · Enrico De Vita[6,7] · Rebecca M. E. Steketee[8] · Marion Smits[8] · Aart J. Nederveen[4] · Frank Hofheinz[1] · Jörg van den Hoff[1,9] · Iris Asllani[2]

Received: 9 March 2018 / Revised: 22 May 2018 / Accepted: 23 May 2018 / Published online: 18 June 2018

Abstract

Objective Partial volume (PV) correction is an important step in arterial spin labeling (ASL) MRI that is used to separate perfusion from structural effects when computing the mean gray matter (GM) perfusion. There are three main methods for performing this correction: (1) GM-threshold, which includes only voxels with GM volume above a preset threshold; (2) GM-weighted, which uses voxel-wise GM contribution combined with thresholding; and (3) PVC, which applies a spatial linear regression algorithm to estimate the flow contribution of each tissue at a given voxel. In all cases, GM volume is obtained using PV maps extracted from the segmentation of the T1-weighted (T1w) image. As such, PV maps contain errors due to the difference in readout type and spatial resolution between ASL and T1w images. Here, we estimated these errors and evaluated their effect on the performance of each PV correction method in computing GM cerebral blood flow (CBF).

Materials and methods Twenty-two volunteers underwent scanning using 2D echo planar imaging (EPI) and 3D spiral ASL. For each PV correction method, GM CBF was computed using PV maps simulated to contain estimated errors due to spatial resolution mismatch and geometric distortions which are caused by the mismatch in readout between ASL and T1w images. Results were analyzed to assess the effect of each error on the estimation of GM CBF from ASL data.

Results Geometric distortion had the largest effect on the 2D EPI data, whereas the 3D spiral was most affected by the resolution mismatch. The PVC method outperformed the GM-threshold even in the presence of combined errors from resolution mismatch and geometric distortions. The quantitative advantage of PVC was 16% without and 10% with the combined errors for both 2D and 3D ASL. Consistent with theoretical expectations, for error-free PV maps, the PVC method extracted the true GM CBF. In contrast, GM-weighted overestimated GM CBF by 5%, while GM-threshold underestimated it by 16%. The presence of PV map errors decreased the calculated GM CBF for all methods.

Conclusion The quality of PV maps presents no argument for the preferential use of the GM-threshold method over PVC in the clinical application of ASL.

Keywords Arterial spin labeling · Perfusion magnetic resonance imaging · Cerebral blood flow · Partial volume

✉ Jan Petr
j.petr@hzdr.de

[1] Helmholtz-Zentrum Dresden-Rossendorf, Institute of Radiopharmaceutical Cancer Research, Dresden, Germany

[2] Department of Biomedical Engineering, Rochester Institute of Technology, Rochester, NY, USA

[3] Sunnybrook Research Institute, Toronto, Canada

[4] Department of Radiology, Academic Medical Center Amsterdam, Amsterdam, The Netherlands

[5] Department of Radiology, University Medical Center Utrecht, Utrecht, The Netherlands

[6] Lysholm Department of Neuroradiology, National Hospital for Neurology and Neurosurgery, London, UK

[7] Department of Biomedical Engineering, School of Biomedical Engineering and Imaging Sciences, Kings College London, Kings Health Partners, St Thomas Hospital, London, UK

[8] Department of Radiology and Nuclear Medicine, Erasmus MC-University Medical Center Rotterdam, Rotterdam, The Netherlands

[9] Department of Nuclear Medicine, University Hospital Carl Gustav Carus, Technical University Dresden, Dresden, Germany

Introduction

The quality of arterial spin labeling ASL perfusion MRI has improved significantly with the increased availability of multi-channel coils [1], 3T scanners [2], more advanced 3D readouts [3, 4], background-suppression schemes [5, 6], and improvements in labeling efficiency [7]. As a result, the application of ASL in clinical research has been on the rise [8, 9].

Despite these developments, the spatial resolution of ASL has remained relatively low. Therefore, the majority of voxels in ASL images contain a mixture of perfusion signals from gray matter (GM), white matter (WM), and CSF, a phenomenon referred to as partial volume (PV) effects. Since GM perfusion is reported to be 2–4.5 times higher than WM perfusion [10, 11], and CSF is not perfused, the measured ASL signal in a given voxel is dependent on the fractional contributions of GM and WM, i.e. its tissue composition. Consequently, differences in measured perfusion across regions within a subject or for the same region across subjects could, to a varying degree, be attributable to differences in tissue composition rather than actual changes in perfusion. This hypothesis was borne out in an ASL study of healthy aging which showed that around 50% of the difference in cerebral blood flow (CBF) between healthy elderly and young participants could be accounted for by atrophy alone [12]. It is therefore of principal relevance to separate changes in CBF from structural variability in studies when the latter cannot be ruled out [13, 14].

In this context, several approaches for PV correction have been proposed. Originally, a fixed ratio between GM and WM perfusion was assumed [15]. Later, a linear regression was used to model the relation of the observed CBF and GM and WM PV maps, to solve for the unknown PV-corrected GM and WM CBF within a spatially defined kernel [10]. The main focus of the subsequent work on PV correction in ASL has been to reduce the smoothing effects inherent in the original algorithm [16, 17]. Less attention, however, has been given to the quality of the GM and WM PV maps from which the algorithms receive the structural information, and which can influence the results of the PV correction [18]. Typically, the PV maps (obtained from the segmentation of high-resolution T1-weighted [T1w] images) are co-registered and resampled to match the low-resolution ASL image space. Therefore, differences in geometric distortion and effective resolution between the ASL and T1w readouts are propagated to the PV maps and subsequently in the PV correction process and CBF computation [19–22]. Differences in ASL readout schemes [23] can also influence the efficacy of the PV correction and thus may lead to bias and additional variance in estimating mean GM CBF in data from multi-center studies. However, the magnitude of the errors stemming from differences in processing strategies and readout schemes has not yet been systematically quantified in either PV-corrected or PV-uncorrected data.

In this study, we have addressed these issues by estimating the errors in PV maps due to geometric distortion and resolution mismatch between ASL and T1w images. To test for the effect of ASL readout on the magnitude of these errors, two of the commonly used ASL readout schemes—2D EPI and 3D spiral—were analyzed. The goal was to explore the effect of these errors on the computation of mean GM CBF using different methods for PV correction. Simulated CBF images, constructed based on real ASL data acquired on 22 subjects with the two different readout schemes, were analyzed using the PVC method and two different GM thresholding methods. The results of this study provide further insight into the utility of PV correction and sources of error in the computation of mean GM CBF.

Materials and methods

Imaging

Twenty-two healthy young volunteers (mean age 22.6 ± 2.1 years, 9 men) underwent scanning twice, at two imaging centers operating two different 3T MRI systems—Discovery MR750 (GE Healthcare, Chicago, IL, USA) and Intera (Philips Healthcare, Best, Netherlands)—both equipped with the same 8-channel head coil (Invivo, Gainesville, FL, USA). The study was approved by the local medical research ethics committees of both sites—the Erasmus MC-University Medical Center, Rotterdam, and the Academic Medical Center, Amsterdam—and was conducted in accordance with the Declaration of Helsinki. All participants provided written informed consent and received financial compensation for participation.

Each imaging session included a pseudo-continuous ASL (pCASL) scan and a 1 mm isotropic 3D T1w structural scan. On the Philips scanner, pCASL was acquired using a 2D gradient-echo single-shot echo planar imaging (EPI) readout with voxel size $3 \times 3 \times 7$ mm^3, TE/TR 17 ms/4000 ms, labeling duration 1650 ms, post-labeling delay 1525 ms, and number of averages 33, resulting in total acquisition time of 4:33 min. On the GE scanner, a 3D fast spin-echo interleaved stack-of-spirals (3D spiral) readout with 512 points on 8 spirals was used with acquisition resolution $3.8 \times 3.8 \times 4$ mm^3, reconstructed by default to $1.9 \times 1.9 \times 4$ mm^3 voxel size, TE/TR 10.5 ms/4600 ms, labeling duration 1450 ms, post-labeling delay 1525 ms, number of averages 3, and total acquisition time 4:29 min. A detailed description of the recruitment criteria and imaging protocols can be found in [24].

Image processing

Images were processed using in-house MATLAB (MathWorks, Natick, MA, USA) routines using SPM12 (Wellcome Trust Centre for Neuroimaging, London, UK). Image processing was geared towards estimation of CBF quantification errors associated with: (1) differences in geometric deformation between the ASL and T1w images due to the difference in contrast between the two modalities, and (2) differences between the acquisition and effective resolution of the ASL images. In both cases, the quantification errors were estimated independently for the 2D EPI and 3D spiral ASL readout sequences.

Below, we detail the main processing steps, also outlined in Fig. 1, and provide the rationale behind each step. Briefly, following the processing of the ASL and T1w data (step A), the geometric distortions (step B) and effective resolution (step C) were estimated and subsequently applied to estimate their effect on GM CBF calculation (step D).

Preprocessing (step A)

Each subject's T1w image was segmented into GM and WM PV maps (denoted as pGM and pWM, respectively) using CAT12 (C. Gaser, Structural Brain Mapping Group, Jena University Hospital, Jena, Germany).

For the 2D EPI data, all control and label pairs were corrected for motion, and pairwise subtraction was then performed. For the 3D spiral data, the perfusion-weighted images were provided, by default, directly from the scanner. CBF images, referred to as CBF_{real}, were quantified using the single-compartment model for both types of ASL readouts [25].

In addition to the CBF_{real} image, a pseudo-CBF (CBF_{pseudo}) image was also computed based on the pGM and pWM maps, assuming a GM–WM CBF ratio of 3.4 [10] (Fig. 1a). In contrast to the CBF_{real} image, the CBF_{pseudo} image perfectly matches the T1w image in terms of geometric deformations and spatial resolution. The CBF_{real} image was up-sampled using B-spline interpolation to match the voxel size of the T1w space so that a direct comparison with CBF_{pseudo} could be made to estimate the deformations and resolution as detailed in the sections "Estimation of geometric distortions between the T1w and ASL images" and "Estimation of the difference between the effective spatial resolution of the ASL and T1w images".

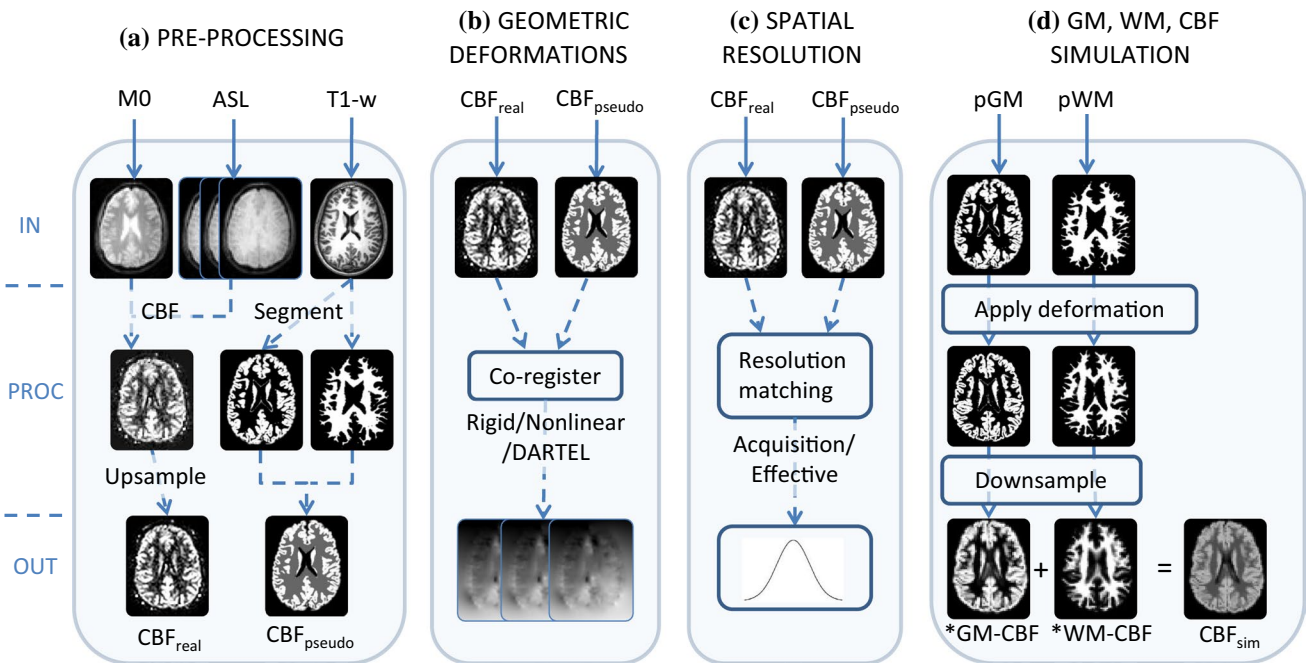

Fig. 1 Diagram of image processing pipeline. For each column, the input images (top row), the processing steps (middle row), and the output images (bottom row) are displayed. (a) Preprocessing: a CBF_{real} was computed and up-sampled to the image matrix of the T1w image; a CBF_{pseudo} was also created using GM and WM tissue partial volume maps (pGM and pWM, respectively) obtained from segmentation of the T1w image. (b) Estimation of geometric distortions between CBF_{real} and CBF_{pseudo} was performed using Rigid, Nonlinear, or DARTEL. (c) The effective resolution of ASL images was estimated via iterative resolution matching of CBF_{real} and CBF_{pseudo} images. (d) Simulation of CBF images containing deformations introduced in steps (B) and (C) was conducted by applying the deformations to the original pGM and pWM maps (A) and recomputing the CBF image based on these maps

Estimation of geometric distortions between the T1w and ASL images (step B)

Three commonly used co-registration algorithms were applied to co-register the ASL and T1w images represented by the CBF_{real} and CBF_{pseudo} images, respectively: Rigid (6-parameter rigid-body transformation), Nonlinear (affine transformation followed by low-dimensional nonlinear transformation using discrete cosine basis functions [26]), or DARTEL (high-dimensional warping with a diffeomorphic registration algorithm [27]). For Rigid, mutual information criterion was used. For Nonlinear and DARTEL, sum-of-squares criterion was used while first adjusting the GM and WM CBF in CBF_{pseudo} to minimize the voxel-wise difference. For each subject, six deformation fields were computed, one from each co-registration algorithm—rigid, nonlinear, DARTEL—repeated for each ASL readout scheme—2D EPI and 3D spiral (Fig. 1b). We assume that the DARTEL algorithm has sufficient degrees of freedom to fully reflect the geometric distortions between the ASL and T1w images [28], and was thus used as a comparative reference.

Estimation of the difference between the effective spatial resolution of the ASL and T1w images (step C)

The difference in spatial resolution between the ASL and T1w images must be taken into account to avoid errors in GM CBF analysis. For this purpose, the true resolution of the ASL images needs to be used instead of the ASL acquisition resolution or the reconstructed voxel size. The reconstructed voxel size does not need to match the resolution, and in the case of 3D acquisition, the acquisition resolution and the true resolution often differ because of substantial smoothing effects of the acquisition, which may lead to GM CBF underestimation.

Here, we estimated the effective spatial resolution of each ASL readout by assuming a Gaussian point spread function (PSF) and by quantifying the resolution difference between T1w and ASL images, represented by CBF_{pseudo} and CBF_{real} images, respectively, that were co-registered using the Nonlinear method, which reduces the influence of mis-registration (step B). Resolution of the T1w images was assumed to be 1 mm^3 isotropic with Gaussian PSF. First, the spatially varying GM and WM CBF values were estimated using PV correction via linear regression to account for perfusion nonuniformity. The estimated values were then used to generate a CBF_{pseudo} image. Lastly, the effective resolution of the ASL images was estimated by iterative smoothing of the CBF_{pseudo} image with a varying anisotropic Gaussian kernel. The downhill simplex method was used to determine the minimum root mean square deviation between the CBF_{real} and CBF_{pseudo}. Three iterations of PV correction and iterative smoothing were used.

Simulation of CBF images and PV maps (step D)

The goal of this step was to simulate a reference CBF image and PV maps that contained different amounts of geometric deformations (step B, Fig. 1), and with and without estimating the effective resolution (step C, Fig. 1), in order to evaluate the errors associated with each. To this end, we applied the three estimated deformation fields obtained from Rigid/Nonlinear/DARTEL transformation (Fig. 1b) to the original pGM and pWM maps (Fig. 1a). The resulting pGM and pWM maps were then down-sampled to the original low-resolution ASL space. The image matrix of the ASL image was preserved. The down-sampled pGM and pWM values were obtained by integrating over the PV values in the high-resolution space and assuming a Gaussian PSF with either the acquisition resolution of the ASL images (referred to as "acq") or the estimated effective resolution obtained in step C (referred to as "eff").

Six sets of pGM and pWM images were thus produced for each subject and each ASL readout: Rigid-acq, Rigid-eff, Nonlinear-acq, Nonlinear-eff, DARTEL-acq, and DARTEL-eff. The CBF image was simulated for each subject using the PV maps from DARTEL-eff ($CBF_{DARTEL\text{-}eff}$). Each type of investigated error was produced by the respective difference between these six PV maps when used for calculating GM CBF from the reference CBF image ($CBF_{DARTEL\text{-}eff}$). Specifically, the DARTEL-eff set was used as the reference, assuming that DARTEL-eff and DARTEL-acq PV maps reflect purely the difference between the acquired and effective resolution; the Rigid-eff and Nonlinear-eff contained residual geometric distortions due to suboptimal co-registration of T1w to ASL, not fully encompassing the differences between the two sequences; the Rigid-acq and Nonlinear-acq contained both geometric distortions and resolution mismatches.

For the quantitative analyses of error propagation, Gaussian noise with a standard deviation of 4 mL/100g/min was added to the $CBF_{DARTEL\text{-}eff}$ images [29]. For all simulations, a uniform GM CBF of 80 mL/100g/min and GM CBF/WM CBF ratio of 3.4 was assumed [10].

Quantitative evaluation of errors

The mean GM CBF of the $CBF_{DARTEL\text{-}eff}$ images was obtained by thresholding the low-resolution pGM maps at threshold levels of 10, 20, 30, ..., 90, and 95%. Three methods for calculating the GM CBF were compared:

– *GM-threshold*, obtained as mean CBF within the GM region of interest (GM ROI);

– *GM-weighted*, the mean CBF within the GM ROI divided by the mean pGM within the same GM ROI, i.e. weighted mean;
– *Partial volume correction (PVC)*, the mean of PV-corrected GM CBF (within the GM ROI) computed according to the Asllani method using a $5 \times 5 \times 1$ kernel [10].

To ensure that the results were not dependent on the absolute quantification of CBF, the obtained GM CBF value was divided by 80 mL/100 g/min, the preset GM CBF value of the simulated data. A mean relative error in GM CBF was calculated as the average error across all participants.

Results

The mismatch between the effective and acquisition resolution for both the 2D EPI and 3D spiral ASL images is qualitatively shown in Fig. 2. For the 2D EPI readout, the mismatch was mainly in the left–right and anterior–posterior directions, with effective resolution full width at half maximum (FWHM), mean (SD) 3.0 (0.15) × 3.2 (0.16) × 7.4 (0.35) mm^3, on average around 10% larger than the acquisition resolution of $3 \times 3 \times 7$ mm^3. The difference was more pronounced for the 3D spiral readout, for which the effective resolution across the whole population was 4.6 (0.20) × 4.3 (0.37) × 11.8 (0.39) mm^3, versus the acquisition resolution of $3.8 \times 3.8 \times 4$ mm^3, representing on average a 200% mismatch in the slice-encoding direction.

The mean relative errors in GM CBF calculated using the three different methods—GM-threshold, GM-weighted, and PVC—are shown in Fig. 3 for all pGM thresholds. Results for the commonly used pGM threshold of 70% are also summarized in Table 1. We chose a relatively high pGM threshold to ensure a better validation with the PVC method even in elderly populations.

For the calculation based on PV maps without errors (DARTEL-eff), as expected, the PVC method fully extracted the GM CBF signal, whereas the standard methods, GM-threshold and GM-weighted, scaled with the partial volume effects (Fig. 3) for both the 2D EPI and 3D spiral readouts. For the GM ROI with 70% threshold (GM $ROI_{70\%}$), the GM-threshold method underestimated GM CBF by 16.5%, while the GM-weighted method overestimated it by more than 5.3%.

For the 2D EPI readout, the largest sources of error were geometric deformations typical of the 2D EPI sequence. The error in PVC results increased by 3% when the Nonlinear registration was used to model the deformations, and by 8% with the Rigid registration.

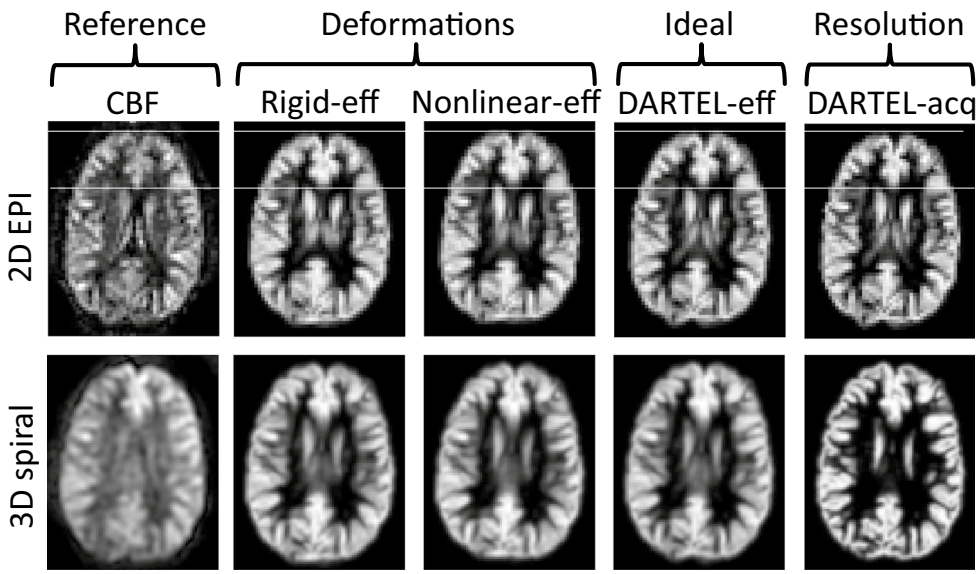

Fig. 2 A CBF_{real} image and pGM maps co-registered to the ASL image using the three different transformations (Rigid-eff/Nonlinear-eff/DARTEL-eff) and two different resolutions (DARTEL-acq/DARTEL-eff) are shown for the 2D EPI (top row) and 3D spiral (bottom row) ASL readouts. DARTEL-eff should be the closest match of the pGM maps to the CBF_{real} image in terms of both resolution and deformations. The difference between PV maps containing deformations (Rigid-eff, Nonlinear-eff) was more pronounced in the 2D EPI images. White lines help to note the prolongation artifact in the phase-encoding direction typical for EPI acquisition. The 3D spiral sequence had only minor deformations, and therefore the PV maps (Rigid-eff/Nonlinear-eff/DARTEL-eff) were similar for all co-registrations. Visible difference in resolution can be seen between the 3D spiral images DARTEL-eff and DARTEL-acq and also between the DARTEL and the CBF_{real} image

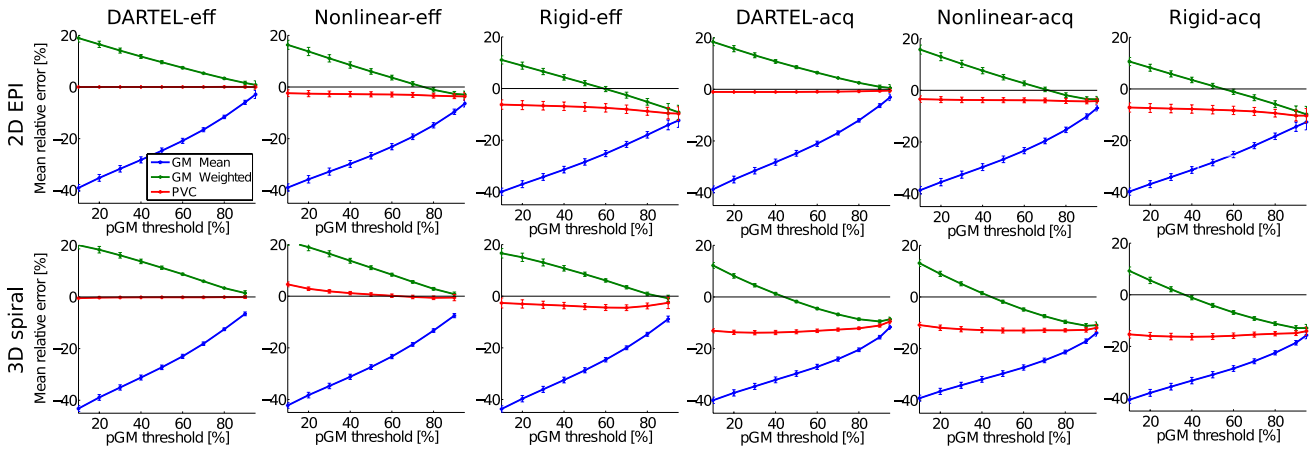

Fig. 3 Mean relative error in GM CBF calculation for the 2D EPI (top row) and 3D spiral (bottom row) ASL sequences. The columns represent cases when the PV maps used for calculation contained (left to right) no errors (DARTEL-eff PV maps), deformation errors with nonlinear co-registration (Nonlinear-eff), deformation errors (Rigid-eff), resolution errors (DARTEL-acq), resolution and deformation errors with nonlinear co-registration (Nonlinear-acq), and both deformation and resolution errors (Rigid-acq). Note that without errors in the PV maps, the GM-threshold method underestimates the CBF and the GM-weighted overestimates the CBF. Resolution and deformation errors both cause underestimation of the GM CBF

Table 1 Mean relative error in GM CBF calculation for the 2D EPI and 3D spiral readouts*

Type	PV type	DARTEL-eff	Nonlinear-eff	Rigid-eff	DARTEL-acq	Nonlinear-acq	Rigid-acq
2D EPI	GM-threshold	− 16.5	− 19.3	−21.6	− 16.9	− 19.6	− 21.9
	GM-weighted	5.3	1.2	− 2.6	4.4	0.4	− 3.4
	PVC	< 0.01	− 3.0	−8.0	− 0.9	− 3.9	− 8.7
3D spiral	GM-threshold	− 18.1	− 18.7	− 20.0	− 24.1	− 24.6	− 25.7
	GM-weighted	6.1	5.5	3.5	− 6.8	− 7.4	− 9.2
	PVC	< 0.01	− 0.3	− 4.5	− 12.6	− 12.9	− 15.4

*Values are shown as a percentage (%) relative to the preset reference GM CBF value of 80 mL/min/100 g. Results are shown for GM $ROI_{70\%}$. Results for all other threshold levels are shown in Fig. 3

For the 3D spiral acquisition, the resolution mismatch was the main source of additional error: 6.0 and 12.5% in CBF images computed with the GM-threshold and PVC methods, respectively. For the CBF computed with the GM-weighted, a 6.1% overestimation turned into a 6.8% underestimation of GM CBF.

Independently, errors due to the geometric distortions and resolution mismatch were 16.5 and 18.0% lower for the PVC method than the GM-threshold method for the 2D EPI and 3D spiral readouts, respectively. For the combined geometric distortion and resolution mismatch effects, the PVC method yielded 13.2 and 10.3% lower error than GM-threshold, respectively. The reason that these effects added less error for the GM-threshold than the PVC method is the already high absolute error of GM-threshold for optimal PV maps. On the other hand, PVC yielded 5.3 and 6.0% lower error than the GM-weighted method for the 2D EPI and the 3D spiral readouts, respectively, without assuming the combined effects of distortion and resolution, and 5.3 and 6.2% higher error, respectively, with these effects.

The GM values in each of the simulated GM maps were compared with the reference DARTEL-eff GM map (see the joint histograms in Fig. 4). For the 2D EPI, a large variance around the line of identity is visible for the Rigid and Nonlinear registration. For the 3D spiral, a large deviation from the line of identity is visible for the acquisition resolution. These results indicate that the largest source of error for 3D spiral readouts is related to the resolution mismatch, whereas for the 2D EPI, the geometric deformations are the main source of error.

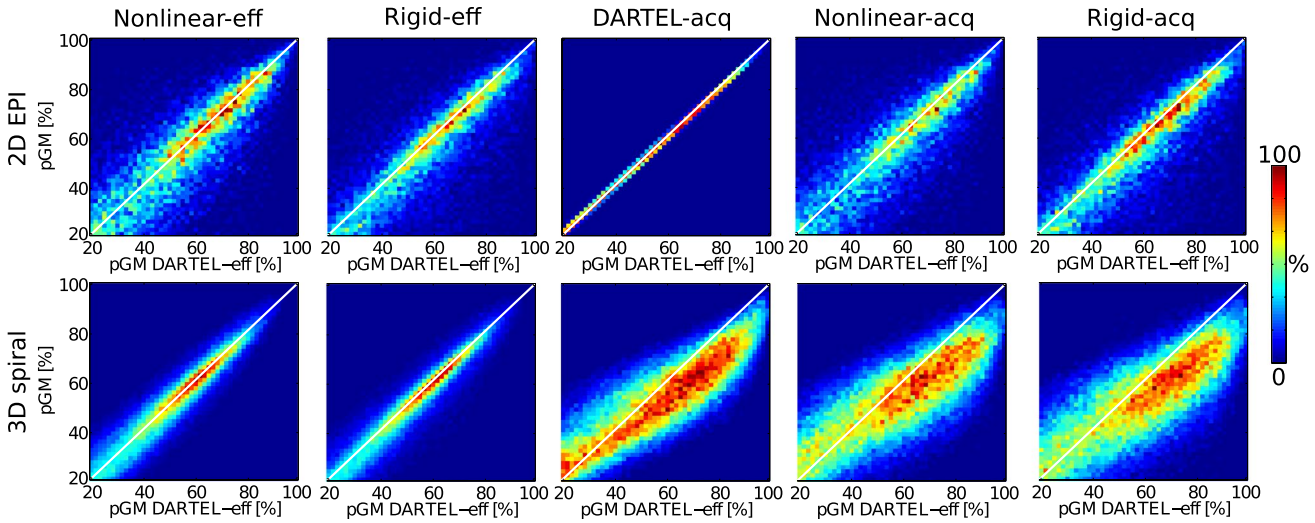

Fig. 4 Joint histograms of 2D EPI and 3D spiral readout schemes for a randomly selected subject. The line of identity, corresponding to a perfect match of the PV volumes, is indicated in white

Discussion

We measured the effects of two sources of error—geometric distortion and resolution mismatch—in computing GM CBF using ASL images. These errors are inherent in the current ASL methods, which are based on the extraction of PV maps from the segmentation of the high-resolution T1w images. Geometric distortions result mainly from the difference in readout between ASL and T1w, whereas resolution mismatch is due to the intrinsic difference in spatial resolution between the two modalities. The effects of these errors were estimated for three different PV correction methods, i.e. GM-threshold, GM-weighted, and PVC, and two different ASL readout sequences, 2D EPI and 3D spiral. While the presence of these effects is generally acknowledged [18–20, 22, 30], we have now provided empirical data on how they affect PV maps and consequently the GM CBF calculation.

The key finding of this study was that errors associated with resolution mismatch and geometric deformation had similar effects on the mean GM CBF independent of whether PV correction was used. This result, combined with the fact that PVC outperformed the other two PV correction methods, should pave the way for a broader application of PVC in clinical settings. However, PV maps can contain additional errors, such as those resulting from inadequate segmentation of the T1w image. In this case, the use of linear regression is not optimal, as it assumes that the PV maps (the independent variables) are error-free. Using a method such as total least squares, which accounts for uncertainties in the independent variables, might thus be an effective alternative. Another drawback of the PVC method is the use of a spatial kernel which inherently leads to blurring of the PV-corrected CBF images. This blurring may be especially problematic in multi-center studies, as equal levels of smoothing might be difficult to achieve for sequences with different resolution and matrix size. Performing the PV correction on a global basis and controlling for the smoothness of the resulting corrected CBF maps—for example, by modeling the results using B-spline functions—should be a subject of further research.

A novel approach for estimating the PV maps directly in the ASL native space using fractional signal modeling was recently introduced by Petr et al. and Ahlgren et al. [19, 20]. Better agreement between the PV and CBF maps was demonstrated in both studies relative to the PV maps estimated from the high-resolution T1w images. This improvement is most likely due to the use of the same readout for PV estimation as for the ASL acquisition. Such PV maps can potentially lead to improved PV correction, as they do not suffer from the detrimental effects of the resolution and deformation issues presented in this study. This statement, however, requires further validation.

We have shown that although the PVC method for computation of GM CBF was the one most affected by the geometric deformations (in 2D EPI ASL) and resolution discrepancies (in 3D spiral ASL), it nevertheless outperformed the commonly used GM-threshold method irrespective of the PV map quality. With error-free PV maps, PVC outperforms the GM-weighted method. However, the GM CBF overestimation inherent in the GM-weighted method is canceled out in the presence of PV map errors due to deformation and resolution issues. The GM-weighted method thus can have a smaller error than PVC under certain conditions. Nevertheless, the GM-weighted method is still more dependent on the tissue volume than PVC, and a general advantage

of the GM-weighted method over PVC is not warranted for regional and voxel-wise studies.

Although the resolution mismatch was relatively small for the 2D EPI acquisition, our findings show that geometric deformations due to EPI susceptibility artifacts can cause around 8% underestimation in GM CBF when the rigid-body transformation is used for co-registration across the modalities. The use of SPM's nonlinear co-registration [26] reduced this effect by 5%. In contrast, geometric distortion had negligible effects on the multi-segment 3D spiral readout, which was, however, significantly affected by the resolution mismatch between the effective and acquisition ASL resolution. The effective resolution we estimated was about 200% higher in the slice-encoding direction. This can be explained by a convolution effect of acquisition PSF, motion, and smoothing performed during the scanner's reconstruction phase. Using the expected acquisition resolution instead of the estimated effective resolution can result in significant underestimation of the mean CBF, regardless of PV correction. A similar effect was shown previously by Zhao et al. and Petr et al., but the results are not directly comparable, as a simulated smoothing with an isotropic Gaussian kernel was used [18, 22]. Here, we showed that this issue can be solved by down-sampling the PV maps to the estimated effective resolution before the mean GM CBF calculation. However, to achieve this, the effective resolution needs to be estimated either as performed in the current study, or using literature values, provided that a similar acquisition method was used. The mean GM CBF increased 8% on average when CBF images were "deblurred". Compensating for the resolution mismatch by deconvolution of CBF data rather than by correctly down-sampling the PV maps is likely to be more prone to noise and more computationally demanding. On the other hand, the results of the PVC method are not affected by the mismatch and will be similar when a regional mean CBF is evaluated. However, deconvolution might still be preferable in order to increase the visual quality of the images and improve the localization of the perfusion signal in voxel-wise analysis. Deblurring by deconvolution was used by Chappell et al. and Boscolo Galazzo et al. for 3D gradient- and spin-echo (GRASE) data sets [16, 31]. However, these data sets all contained time-series (i.e. multiple-post-labeling delay or several control/label repetitions), and therefore the PSF could be estimated from noise autocorrelation.

Another limitation of our study is that we focused on only two ASL readout schemes. The GM CBF errors might add up differently for other ASL readout types or even different acquisition parameters. We regret the lack of 3D GRASE data, which is another frequently used ASL acquisition method. However, we anticipate that the geometric distortion and effective resolution of 3D GRASE in most cases will lie between those for 2D EPI and 3D spiral [32].

Also, while only global GM CBF was evaluated, it can be hypothesized that a similar magnitude of error can be expected in voxel-wise analysis. This, however, remains to be verified.

There were several differences between the two acquisitions used in this study that may have added to the observed discrepancy in the GM CBF calculation between acquisitions. Because no M0 image was obtained for the 2D EPI sequence, B1 inhomogeneities may be present in the 2D EPI CBF images that were not present in the 3D spiral data. We assume that this difference does not influence the results, since simulated CBF maps were used. Motion correction could not be performed for 3D spiral data; however, very little motion was observed in the 2D EPI data. Hence, considering that both 2D EPI and 3D spiral data were acquired on the same participants, we assume the motion effect to be negligible.

Inter-vendor differences in T1w segmentation can also affect the PV correction; however, the assessment of these effects was outside the scope of the current study. Here, we used T1w images from a single vendor to exclude this potential source of variability.

Another drawback of this study was the choice of the DARTEL transformation as reference for ASL-T1w registration. We did not compare this with acquiring ancillary parameters such as a B0 field or repeating the acquisition with reversed phase-encoding directions [33]. While DARTEL is typically not used for ASL-T1w registration, researchers have previously shown that nonlinear registration performs well for EPI images [34], and can even outperform geometric distortion correction using the B0 field [28]. This was the basis of our assumption for using DARTEL in lieu of ground truth in this study, where participants were young, healthy volunteers. This assumption might not hold in diseased populations, due to a poorer signal-to-noise ratio (SNR) and the presence of ASL image artifacts, and precludes the use of DARTEL in clinical studies to actually obtain the deformation field.

For the resolution estimation, an anisotropic Gaussian PSF was assumed. For the 3D spiral acquisition, the estimated effective resolution is slightly lower (11.8 vs. 8 mm FWHM in the slice-encoding direction) than in a previous study by Oliver at al. [30] and in good agreement with a study by Vidorreta et al. ($4.6 \times 4.3 \times 11.8$ mm^3 vs. $4.64 \times 4.64 \times 9.04$ mm^3 FWHM) [4]. For the 2D EPI, the AFNI [Analysis of Functional NeuroImages] toolbox estimated the resolution from noise autocorrelation to be $3.3 \times 3.6 \times 6.2$ mm^3, versus our $3.0 \times 3.2 \times 7.4$ mm^3 resolution-matching method (less than 2% difference in voxel volume). Both these differences could be explained by the additive effect of several factors including motion, vessel artifacts, suboptimal co-registration, and segmentation errors. Specifically, in comparison to AFNI results,

the values estimated here for 2D EPI probably include segmentation errors. With regard to the 3D spiral values, in contrast to those obtained by Oliver et al. [30] and Vidorreta et al. [4] for an optimal acquisition, the values obtained here were likely influenced by motion [35] or smoothing during reconstruction. This discrepancy between the anticipated and actual estimated effective resolution emphasizes the need for estimation of the effective resolution independently for each study in order to ensure that PVC is performed on the correct resolution.

Conclusion

Careful minimization of geometric distortion and differences in effective resolution between ASL and T1w images significantly reduces errors in GM CBF calculation, independent of the PV correction method used, including no correction for PV effects at all. Even without the minimization of these differences, PVC remains the most accurate way to calculate GM CBF. Therefore, errors in PV maps caused by geometric deformations and resolution issues afford no argument for excluding PVC from the analysis of ASL data. Furthermore, the quantification errors induced by the ASL-T1w differences have a similar magnitude as the CBF effects in many clinical studies. Therefore, minimizing the errors resulting from the ASL-T1w differences are key to increasing the statistical power of ASL imaging and in being able to separate perfusion from structural effects in clinical studies.

Acknowledgements We thank Matthias J.P. van Osch for his insightful thoughts and comments. The authors also wish to thank the COST-AID (European Cooperation in Science and Technology-Arterial spin labeling Initiative in Dementia) Action BM1103 for facilitating meetings for researchers to discuss various application of ASL. Part of this work was supported by The Gleason Foundation (IA).

Author contributions Study conception and design: JP, HJMMM, IA, JVDH. Acquisition of data: RMES, MS, AJN. Analysis and interpretation of data: JP, HJMMM, FH, IA. Drafting of manuscript: JP, HJMMM, IA. Critical revision: JP, HJMMM, IA, EDV, RMES, MS, AJN, FH, JVDH.

Compliance with ethical standards

Conflict of interest The authors declare that they have no conflict of interest.

Ethical approval All procedures performed in studies involving human participants were in accordance with the ethical standards of the institutional and/or national research committee and with the 1964 Helsinki declaration and its later amendments or comparable ethical standards.

Informed consent Informed consent was obtained from all individual participants included in the study.

References

1. Ferré JC, Petr J, Bannier E, Barillot C, Gauvrit JY (2012) Improving quality of arterial spin labeling MR imaging at 3 Tesla with a 32-channel coil and parallel imaging. J Magn Reson Imaging 35(5):1233. https://doi.org/10.1002/jmri.23586
2. Detre JA, Leigh JS, Williams DS, Koretsky AP (1992) Perfusion imaging. Magn Reson Med 23:37
3. Günther M, Oshio K, Feinberg DA (2005) Single-shot 3D imaging techniques improve arterial spin labeling perfusion measurements. Magn Reson Med 54(2):491. https://doi.org/10.1002/mrm.20580
4. Vidorreta M, Balteau E, Wang Z, De Vita E, Pastor MA, Thomas DL, Detre JA, Fernández-Seara MA (2014) Evaluation of segmented 3D acquisition schemes for whole-brain high-resolution arterial spin labeling at 3 T. NMR Biomed 27(11):1387. https://doi.org/10.1002/nbm.3201
5. Ye FQ, Frank JA, Weinberger DR, McLaughlin AC (2000) Noise reduction in 3D perfusion imaging by attenuating the static signal in arterial spin tagging (ASSIST). Magn Reson Med 44(1):92
6. Garcia DM, Duhamel G, Alsop DC (2005) Efficiency of inversion pulses for background suppressed arterial spin labeling. Magn Reson Med 54(2):366. https://doi.org/10.1002/mrm.20556
7. Dai W, Garcia D, de Bazelaire C, Alsop DC (2008) Continuous flow-driven inversion for arterial spin labeling using pulsed radio frequency and gradient fields. Magn Reson Med 60(6):1488
8. Telischak NA, Detre JA, Zaharchuk G (2015) Arterial spin labeling MRI: clinical applications in the brain. J Magn Reson Imaging 41(5):1165. https://doi.org/10.1002/jmri.24751
9. Haller S, Zaharchuk G, Thomas DL, Lovblad KO, Barkhof F, Golay X (2016) Arterial spin labeling perfusion of the brain: emerging clinical applications. Radiology 281(2):337. https://doi.org/10.1148/radiol.2016150789
10. Asllani I, Borogovac A, Brown TR (2008) Regression algorithm correcting for partial volume effects in arterial spin labeling MRI. Magn Reson Med 60(6):1362. https://doi.org/10.1002/mrm.21670
11. Zhang K, Herzog H, Mauler J, Filss C, Okell TW, Kops ER, Tellmann L, Fischer T, Brocke B, Sturm W, Coenen HH, Shah NJ (2014) Comparison of cerebral blood flow acquired by simultaneous [15O]water positron emission tomography and arterial spin labeling magnetic resonance imaging. J Cereb Blood Flow Metab 34(8):1373. https://doi.org/10.1038/jcbfm.2014.92
12. Asllani I, Habeck C, Borogovac A, Brown TR, Brickman AM, Stern Y (2009) Separating function from structure in perfusion imaging of the aging brain. Hum Brain Mapp 30(9):2927. https://doi.org/10.1002/hbm.20719
13. Bron EE, Steketee RME, Houston GC, Oliver RA, Achterberg HC, Loog M, van Swieten JC, Hammers A, Niessen WJ, Smits M, Klein S (2014) Diagnostic classification of arterial spin labeling and structural MRI in presenile early stage dementia. Hum Brain Mapp 35(9):4916. https://doi.org/10.1002/hbm.22522
14. Steketee RME, Bron EE, Meijboom R, Houston GC, Klein S, Mutsaerts HJMM, Mendez Orellana CP, de Jong FJ, van Swieten JC, van der Lugt A, Smits M (2016) Early-stage differentiation between presenile Alzheimer's disease and frontotemporal dementia using arterial spin labeling MRI. Eur Radiol 26(1):244. https://doi.org/10.1007/s00330-015-3789-x
15. Aston JA, Cunningham VJ, Asselin MC, Hammers A, Evans AC, Gunn RN (2002) Positron emission tomography partial volume correction: estimation and algorithms. J Cereb Blood Flow Metab 22(8):1019
16. Chappell MA, Groves AR, MacIntosh BJ, Donahue MJ, Jezzard P, Woolrich MW (2011) Partial volume correction of multiple inversion time arterial spin labeling MRI data. Magn Reson Med 65(4):1173. https://doi.org/10.1002/mrm.22641

17. Liang X, Connelly A, Calamante F (2013) Improved partial volume correction for single inversion time arterial spin labeling data. Magn Reson Med 69(2):531. https://doi.org/10.1002/mrm.24279
18. Zhao MY, Mezue M, Segerdahl AR, Okell TW, Tracey I, Xiao Y, Chappell MA (2017) A systematic study of the sensitivity of partial volume correction methods for the quantification of perfusion from pseudo-continuous arterial spin labeling MRI. NeuroImage 162:384
19. Petr J, Schramm G, Hofheinz F, Langner J, van den Hoff J (2013) Partial volume correction in arterial spin labeling using a Look-Locker sequence. Magn Reson Med 70(6):1535. https://doi.org/10.1002/mrm.24601
20. Ahlgren A, Wirestam R, Petersen ET, Ståhlberg F, Knutsson L (2014) Partial volume correction of brain perfusion estimates using the inherent signal data of time-resolved arterial spin labeling. NMR Biomed 27(9):1112. https://doi.org/10.1002/nbm.3164
21. Oliver R, De Vita E, Golay X, Thomas D (2014) Partial Volume Correction of 3D GRASE ASL images using T1 maps acquired with the same readout scheme. In: Proceedings of the 22nd Joint Annual Meeting of ISMRM-ESMRMB, Milan, p 418
22. Petr J, Mutsaerts HJMM, De Vita E, Maus J, van den Hoff J, Asllani I (2016) Deformation and resolution issues in partial volume correction of 2D arterial spin labeling data. In: Proceedings of the 24th Scientific Meeting and Exhibition of the International Society for Magnetic Resonance in Medicine (ISMRM, 2016), vol 24, p 1496
23. Mutsaerts HJ, van Osch MJ, Zelaya FO, Wang DJ, Nordhøy W, Wang Y, Wastling S, Fernandez-Seara MA, Petersen E, Pizzini FB, Fallatah S, Hendrikse J, Geier O, Günther M, Golay X, Nederveen AJ, Bjørnerud A, Groote IR (2015) Multi-vendor reliability of arterial spin labeling perfusion MRI using a near-identical sequence: Implications for multi-center studies. NeuroImage 113:143. https://doi.org/10.1016/j.neuroimage.2015.03.043
24. Mutsaerts HJMM, Steketee RME, Heijtel DFR, Kuijer JPA, van Osch MJP, Majoie CBLM, Smits M, Nederveen AJ (2014) Inter-vendor reproducibility of pseudo-continuous arterial spin labeling at 3 tesla. PloS One 9(8):e104108. https://doi.org/10.1371/journal.pone.0104108
25. Alsop DC, Detre JA, Golay X, Günther M, Hendrikse J, Hernandez-Garcia L, Lu H, MacIntosh BJ, Parkes LM, Smits M, van Osch MJP, Wang DJJ, Wong EC, Zaharchuk G (2015) Recommended implementation of arterial spin-labeled perfusion MRI for clinical applications: a consensus of the ISMRM perfusion study group and the European consortium for ASL in dementia. Magn Reson Med 73(1):102
26. Ashburner J, Friston KJ et al (1999) Nonlinear spatial normalization using basis functions. Hum Brain Mapp 7(4):254
27. Ashburner J (2007) A fast diffeomorphic image registration algorithm. Neuroimage 38(1):95
28. Huang H, Ceritoglu C, Li X, Qiu A, Miller MI, van Zijl PC, Mori S (2008) Correction of b0 susceptibility induced distortion in diffusion-weighted images using large-deformation diffeomorphic metric mapping. Magn Reson Imaging 26(9):1294
29. Qiu Y, Borogovac A, Laine A, Hirsch J, Asllani I (2014) Tissue specific arterial spin labeling fMRI: a superior method for imaging cerebral blood flow in aging and disease. Conf Proc IEEE Eng Med Biol Soc 2014:6687-6690
30. Oliver R, Ly L, Wang C, Beadnall H, Boscolo Galazzo I, Chappell M, Golay X, De Vita E, Thomas D, Barnett M (2016) Complete partial volume solution for ASL brain perfusion data applied to relapse remitting multiple sclerosis patients. In: Proceedings of the 24th Annual Meeting of ISMRM, Singapore, p 1899
31. Boscolo Galazzo I, Chappell MA, Thomas DL, Golay X, Manganotti P, De Vita E (2014) Reducing blurring artifacts in 3D-GRASE ASL by integrating new acquisition and analysis strategies. In: Proceedings of the 22nd Joint Annual Meeting of ISMRM-ESMRMB, Milan, p 2704
32. Mutsaerts HJ, Petr J, Thomas DL, Vita ED, Cash DM, Osch MJV, Golay X, Groot PF, Ourselin S, Swieten JV, Laforce R, Tagliavini F, Borroni B, Galimberti D, Rowe JB, Graff C, Pizzini FB, Finger E, Sorbi S, Castelo Branco M, Rohrer JD, Masellis M, MacIntosh BJ (2018) Comparison of arterial spin labeling registration strategies in the multi-center genetic frontotemporal dementia initiative (GENFI). J Magn Reson Imaging 47(1):131–140. https://doi.org/10.1002/jmri.25751
33. Andersson JL, Skare S, Ashburner J (2003) How to correct susceptibility distortions in spin-echo echo-planar images: application to diffusion tensor imaging. Neuroimage 20(2):870
34. Kybic J, Thévenaz P, Nirkko A, Unser M (2000) Unwarping of unidirectionally distorted EPI images. IEEE Trans Med imaging 19(2):80
35. Petr J, Mutsaerts H, De Vita E, Shirzadi Z, Cohen S, Blokhuis C, Pajkrt D, Hofheinz F, van den Hoff J, Asllani I (2016) Influence of realignment-induced interpolation errors on the estimation of cerebral blood flow using arterial spin labeling fMRI. In: Proceedings of the 33rd Annual Meeting of ESMRMB, Vienna, Austria, p 1

Appendix A3

Template-based approach for detecting motor task activation-related hyperperfusion in pulsed ASL data

Petr, J., Ferré, J. C., Raoult, H., Bannier, E., Gauvrit, J. Y., & Barillot, C. (2014). Template-based approach for detecting motor task activation-related hyperperfusion in pulsed ASL data. Human brain mapping, 35(4), 1179-1189.

Journal name (category): Human brain mapping (Neuroimaging; Neuroscience; Radiology, nuclear medicine & medical imaging)

Quartile in category: **Q1/Q2/Q1**

Impact factor: **5.399**

Number of WoS citations: **5**

◆ Human Brain Mapping 35:1179–1189 (2014) ◆

Template-Based Approach for Detecting Motor Task Activation-Related Hyperperfusion in Pulsed ASL Data

Jan Petr,[1,2,3,4]* Jean-Christophe Ferré,[1,2,3,5] Hélène Raoult,[1,2,3,5] Elise Bannier,[1,2,3] Jean-Yves Gauvrit,[1,2,3,5] and Christian Barillot[1,2,3]

[1]*INRIA, Team VisAGeS, Campus Universitaire de Beaulieu, Rennes, France*
[2]*INSERM, Unit VisAGeS U746, Campus Universitaire de Beaulieu, Rennes, France*
[3]*University of Rennes I, CNRS, Unit VisAGeS U746, IRISA, Campus Universitaire de Beaulieu, Rennes, France*
[4]*Helmholtz-Zentrum Dresden-Rossendorf, Dep. of Positron Emission Tomography, Institute of Radiopharmaceutical Cancer Research, Dresden, Germany*
[5]*CHU Rennes, Department of Neuroradiology, University Hospital of Rennes, Rennes, France*

Abstract: Arterial spin labeling (ASL) permits the noninvasive measurement of quantitative values of cerebral blood flow (CBF) and is thus well adapted to study inter- and intrasubject perfusion variations whether at rest or during an fMRI task. In this study, a template approach to detect brain activation as a CBF difference between resting and activated groups was compared with a standard generalized linear model (GLM) analysis. A basal perfusion template of PICORE-Q2TIPS ASL images acquired at 3T from a group of 25 healthy subjects (mean age 31.6 ± 8.3 years) was created. The second group of 12 healthy subjects (mean age 28.6 ± 2.7 years) performed a block-design motor task. The template was compared with the mean activated image of the second group both at the individual and at the group level to extract activation maps. The results obtained using a GLM analysis of the whole sequence was used as ground truth for comparison. The influences of spatial normalization using DARTEL registration and of correction of partial volume effects (PVE) in the construction of the template were assessed. Results showed that a basal perfusion template can detect activation-related hyperperfusion in motor areas. The true positive ratio was increased by 2.5% using PVE-correction and by 3.2% using PVE-correction with DARTEL registration. On average, the group comparison presented a 2.2% higher true positive ratio than the one-to-many comparison. *Hum Brain Mapp 35:1179–1189, 2014.* © 2013 Wiley Periodicals, Inc.

Key words: arterial spin labeling; motor activation; template; perfusion; functional MRI; ASL

INTRODUCTION

Arterial spin labeling (ASL) is a completely noninvasive MRI method that measures brain perfusion by magnetically labeling blood in brain-feeding arteries [Detre et al., 1992; Parkes and Detre, 2004]. The main advantage of ASL is its ability to obtain quantitative values of cerebral blood flow (CBF) without using contrast agent or ionizing radiation. The reproducibility of CBF quantification makes ASL

*Correspondence to: Jan Petr, HZDR, PET Center, Institute of Radiopharmaceutical Cancer Research, POB 51 01 19, 01314 Dresden, Germany. E-mail: j.petr@hzdr.de

Received for publication 2 April 2012; Revised 31 October 2012; Accepted 24 November 2012

DOI: 10.1002/hbm.22243

Published online 13 February 2013 in Wiley Online Library (wileyonlinelibrary.com).

a promising method for diagnosis based on inter- and intra-subject perfusion comparison [Chen et al., 2011; Petersen et al., 2010; Wang et al., 2011]. The main drawback of ASL is its low signal-to-noise ratio (SNR) and poor spatial resolution, ranging between 3×3 mm^2 and 4×4 mm^2 per pixel in-plane and 5 and 8 mm slice thickness. A useful way of overcoming the SNR limitation is to implement ASL at high-field strength, and to use multi-channel coils, parallel acquisition techniques and dedicated software processing [Ferré et al., 2012; Wang et al., 2005]. Applicable also for task-related functional imaging, functional ASL (fASL) is potentially a more direct marker of neuronal activity than standard BOLD functional MRI [Jin and Kim, 2008; Obata et al., 2004; Raoult et al., 2011]. Several studies have assessed the reproducibility and reliability of ASL-based quantitative results, with the aim to determine characteristic perfusion values of brain regions [Floyd et al., 2003; Lee et al., 2009; Wang et al., 2011]. At 1.5T, the random noise affects the reproducibility of measurements more than within-subject variability [Jahng et al., 2005] while, at the 3T, the SNR is significantly improved. Petersen et al. [2010] recently published a broad multicenter study on the reproducibility of quantitative ASL at 3T with 284 subjects. The mean gray matter CBF was reported to be 47.4 ± 7.5 ml/100 g/min with a within-subject standard deviation over two sessions (3- to 10-days apart) of 5.3 ml/100 g/min. The basal CBF varies substantially, not only between subjects and sessions, but also between brain regions, as does the label arrival time [Gallichan and Jezzard, 2008, 2009]. However, the normalized regional perfusion is highly reliable when measured on separate days [Pfefferbaum et al., 2010] and the relative distribution of CBF in various parts of the brain at rest is consistent and reproducible [Petersen et al., 2010; Wang et al., 2011]. Functional ASL studies have shown a high activation-related signal increase during motor and visual tasks. A signal increase of $57.3\% \pm 5.8\%$ [Raoult et al., 2011] and $39.5\% \pm 6.9\%$ [Tjandra et al., 2005] for motor tasks and $72.9\% \pm 28.8\%$ [Leontiev and Buxton, 2007] for visual tasks was reported. ASL was proven to detect signal changes during a visual-motor task with a very low task frequency [Borogovac et al., 2010]. This was demonstrated on a block-design experiment with two sessions 30 days apart. The activated region obtained using the OFF phase from the first session and the ON phase from the later session and vice-versa had size comparable to the regions detected from individual sessions [Borogovac et al., 2010]. It was also shown that normalized CBF values can be used to identify regions of the brain involved in visual tasks by comparing two groups of healthy subjects with and without visual stimulus [Aslan and Lu, 2010]. The aim of this study is to further analyze the possibility to use baseline CBF group comparison to detect motor-task activation, to compare the results with a standard fMRI block-design experiment and thus to see potential limitations of using only the ON phase. Contrary to Aslan and Lu, a larger control group is used and individual subject to group comparison is performed as would be the preferred mode to study individual subject pathologies. Such a "template approach" is commonly used in nuclear medicine to detect focal variations of a quantitative parameter obtained for one patient by comparing it to the "mean image" of several subjects [Morbelli et al., 2008]. Also, the results were compared with the results of a standard block-design fMRI experiment. Besides, means to improve the quality of detections were also investigated. Indeed, before constructing a template, the perfusion data needs to be spatially normalized. The standard spatial normalization to MNI template provides suboptimal results and we therefore tested if an alternate spatial normalization such as DARTEL [Ashburner, 2007] could improve activation detection. Yet, the spatial resolution of ASL is relatively low and most pixels contain both GM and WM tissue. Thus, given that the ASL signal mainly comes from the GM tissue, the signal intensity in ASL images depends on the volume ratio of GM and WM tissues in each pixel. The GM-to-WM perfusion ratio was reported to be on average three in adults and almost four in children [Biagi et al., 2007]. Asllani et al. [2009] measured the WM perfusion to be 3.5 times smaller than the GM perfusion in elderly subject and 3.9 times smaller in young population. Therefore, partial volume effects (PVE) can significantly affect the CBF. Partial volume correction algorithm was first introduced to ASL by Asllani et al. [2008a] and was shown to improve the detection of visual-motor task by Borogovac et al. [2010]. Four different approaches were tested and compared, using spatial normalization to MNI and DARTEL, with and without PVE correction. To illustrate its potential clinical usefulness, the method was then used to detect hypoperfusion in a single epileptic patient presenting a temporal dysplasia. To summarize, the main contributions of the paper are the following: the CBF template is constructed using DARTEL registration and PVE-correction, hyperperfused regions in motor-related tasks are detected using the template at the individual and at the group level and the results are compared with the results of a standard GLM analysis of block-design ASL experiment.

MATERIALS AND METHODS

Study Design

Thirty-seven healthy volunteers gave written informed consent to be enrolled in the study. The subjects were divided into two groups. Twenty-five subjects were included in the first group (control) (14 women and 11 men, mean age 31.6 ± 8.3 years) for the evaluation of basal perfusion. The second group (functional) consisted of 12 subjects (7 women and 5 men, mean age 28.6 ± 2.7 years) for motor activation-related perfusion evaluation. All the subjects in the second group were strongly right-handed (mean 92.5% according to the "Edinburgh Handedness Inventory" [Oldfield, 1971]).

Imaging Protocol

MR imaging was performed on a 3T MRI scanner (Magnetom Verio, Siemens, Erlangen, Germany) with a 32-channel head coil. Anatomical high resolution 3D MPRAGE T_1-weighted images were obtained for all subjects with the following parameters: field-of-view (FOV) 256 × 256 mm^2, acquisition matrix 256 × 256, 160 sagittal slabs, voxel size 1 × 1 × 1 mm^3, TR/TE/TI 1900/2.98/900 ms, flip angle 9° and acquisition time 4 min 26 s.

Rest perfusion images of control group were acquired using "quantitative imaging of perfusion with a single subtraction, with thin-slice TI1 periodic saturation" (Q2TIPS) with a "proximal inversion with a control for off-resonance effects" (PICORE) labeling technique [Luh et al., 1999; Wong et al., 1997]. The nine slices were acquired with a 7-mm slice thickness and an inter-slice gap of 0.7 mm. The slices were acquired in the AC-PC plane with the third slice passing through the AC-PC plane. The 100-mm thick PICORE labeling slab was positioned 29.5 mm below the lowest imaged slice. Sixty-one control and labeled images were acquired on each subject. A Q2TIPS saturation pulse (700 ms onset time and 800 ms duration) was used to delineate label duration and reduce the sensitivity of quantification to variations in blood arrival time in the brain [Luh et al., 1999; Wong et al., 1998]. The inversion time (TI) between the labeling pulse and the beginning of the readout was 1,700 ms for all subjects (values 1,500 and 1,800 ms that are used for similar PASL fMRI experiments [Ances et al., 2008; Perthen et al., 2008; Raoult et al., 2011; Wang et al., 2011]). A flow-sensitive bipolar crusher gradient (4 cm s^{-1}) was applied to reduce the signal from the fast-moving arterial protons [Ye et al., 1997] immediately prior to image readout. An EPI readout scheme sequence with the following parameters was used: FOV 192 × 192 mm^2, acquisition matrix 64 × 64, in-plane resolution 3 × 3 mm^2, TR/TE 3000/25 ms, and flip angle 90°. The acquisition time was 3 min 6 s.

Functional PICORE Q2TIPS ASL images were acquired, using a motor paradigm, for all subjects in the functional group. The sequence parameters were similar to the ones of the control group except for the number of slices (8) and TE (18 ms). The slices were acquired in the AC-PC plane with a 60.9 mm supratentorial coverage volume thickness. The acquisition lasted 7 min 12 s for 143 control and labeled images. The functional paradigm used a block design with seven alternating 30 s-phases (10 control and labeled images) of rest and a right-hand flexion-extension motor task of the dominant hand at approximately 1 Hz frequency. The first 3 images were used for signal stabilization and were discarded in the processing. Therefore, each rest and action phase started with a control image. It should be noted that, due to the different Z positioning of the subjects from the control and functional groups in the MR scanner, the thickness covered by both groups was around 25 mm in the Z-direction.

Template Construction

The following workflow was used for template construction from the control group images:

1. The ASL images were corrected for motion, noise and signal inhomogeneity. The ASL images were co-registered with the segmented T_1-weighted images;
2. The CBF in each voxel was quantified [Buxton et al., 1998];
3. Partial volume correction was applied [Asllani et al., 2008a];
4. The perfusion maps were spatially normalized to the MNI template or subsequently by DARTEL registration [Ashburner, 2007];
5. Intensity normalization was performed to compensate for mean inter-subject and inter-session perfusion variations;
6. The templates were constructed.

Preprocessing

All image preprocessing steps were performed using MATLAB (MathWorks, Natick, MA) and the SPM8 toolbox. First, unintentional subject movements during ASL acquisition were compensated for by motion correction of the control and labeled images using six-parameter 3D rigid registration with a sum-of-squares-difference cost function. All control and labeled images were aligned with the first control image. The T_1-weighted images were filtered using the NL-means algorithm to remove noise [Coupé et al., 2008]. The mean ASL control image was then coregistered with the T_1-weighted image of the same subject using 3D rigid-body registration with a normalized mutual-information cost function and NEWUOA optimization [Wiest-Daesslé et al., 2007]. The inhomogeneity bias in the T_1-weighted images was corrected and the images were segmented into gray matter (GM), white matter (WM) and cerebrospinal fluid (CSF) classes using the SPM8 toolbox [Ashburner and Friston, 2005]. The tissue probability template ICBM-152 [Mazziotta et al., 1995] was used as prior information for tissue classification. The GM and WM partial-volume percentages for each pixel of the low-resolution ASL images were calculated using this high-resolution segmentation projected, using the ASL/T_1-w coregistration, on the ASL image.

Perfusion Quantification

Accurate perfusion quantification relies on precise knowledge of the equilibrium magnetization of the arterial blood. However, the latter is difficult to estimate because the standard spatial resolution is too low to image an artery without any partial volume effects. In this study, the blood magnetization was estimated by dividing the first control image values M_{T0} with the blood brain partition

coefficient λ in each pixel [Cavusoglu et al., 2009]. A standard kinetic model [Buxton et al., 1998] was then used for quantification. The values of CBF in ml/100 g/min were given by:

$$\mathrm{CBF} = \lambda\ \Delta M\ \exp(\mathrm{TI}/T_{1a})/(2\alpha M_{T0}\mathrm{TI}_{\mathrm{w}}), \quad (1)$$

where λ 0.98 ml g^{-1}, α is the inversion efficiency (estimated to 1 for PASL [Wong, 2005]), ΔM is the measured mean control-label subtraction in each pixel, T_{1a} is the T_1 relaxation time of blood (T_{1a} 1,664 ms), TI_{w} is the temporal width of the bolus (TI_{w} 700 ms), and TI is the inversion time (TI 1,700 ms).

Partial Volume Correction

The signal intensity in ASL images depends on the volume ratio of GM, WM, and CSF tissues in each pixel and can be significantly affected by partial volume effects (PVE). We therefore chose to use the T_1-weighted images and their GM/WM/CSF segmentation to better delineate the boundary between GM and WM regions in the perfusion images and consequently reduce interpolation errors during spatial normalization of the images.

The ratio of GM, WM, and CSF perfusion was estimated in each pixel (see following section). The measured value of perfusion $\Delta M(r)$ in pixel r was assumed to be equal to [Asllani et al., 2008a]:

$$\Delta M(r) = P_{\mathrm{GM}}(r)\ \Delta M_{\mathrm{GM}}(r) + P_{\mathrm{WM}}(r)\ \Delta M_{\mathrm{WM}}(r) + P_{\mathrm{CSF}}(r)\ \Delta M_{\mathrm{CSF}}(r), \quad (2)$$

where P_{GM}, P_{WM}, and P_{CSF} are volume fractions of GM, WM, and CSF in each voxel; and $\Delta M_{\mathrm{GM}}(r)$, $\Delta M_{\mathrm{WM}}(r)$, and $\Delta M_{\mathrm{CSF}}(r)$ are the values of tissue-specific perfusion. The tissue perfusion $\Delta M_{\mathrm{GM}}(r)$, $\Delta M_{\mathrm{WM}}(r)$, and $\Delta M_{\mathrm{CSF}}(r)$ was assumed to be constant in a $3 \times 3 \times 1$ voxel-neighborhood in the native ASL space (voxel size $3 \times 3 \times 7$ mm^3). The perfusion values in each pixel were obtained by solving a system of nine linear equations in the least-square sense [Asllani et al., 2008a]. The separate GM/WM/CSF perfusion values ΔM_{GM}, ΔM_{WM}, and ΔM_{CSF} were then upsampled to the T_1-weighted image space and superimposed over the high-resolution GM, WM, and CSF segmentation maps [see Eq. (2)].

Spatial Normalization

The ASL images need to be spatially normalized to allow for voxel-by-voxel inter-subject comparison of perfusion values. Because the resolution of the ASL images is low, it is more accurate to align the perfusion images of different subjects via their high-resolution T_1-weighted images. Two targets were compared for normalization, a MNI305 template and a DARTEL-based template. The GM/WM segmentation of each T_1-weighted image was coregistered to the MNI305 template [Evans et al., 1993]. The DARTEL registration method was chosen for its convenient and public-available implementation [Ashburner, 2007]. The DARTEL algorithm takes all the segmented T_1-weighted images normalized to the MNI305 template and realigns them to their mean GM/WM image. The GM/WM template is iteratively recreated and all the images are realigned. The joint ASL/T_1-w and T_1-w/MNI305 template transformation was used to spatially normalize all the perfusion images. The ASL images were upsampled to the same resolution as the T_1-weighted images using trilinear interpolation.

CBF Normalization

The CBF images were also normalized in order to compensate for intersubject and intersession mean perfusion variations. For each subject in the control group, the mean perfusion was measured over all pixels with GM probability exceeding 50%. The CBF images were normalized by the subject's mean GM perfusion. For each subject in the functional group, the mean CBF value used for intensity normalization was taken from the off-phase, reflecting the mean perfusion of the subject at rest. The mean CBF of both groups was measured for a common region in the spatially normalized data where the slices were fully acquired for all subjects. The images from the on-phase were taken and used to create the activated CBF maps.

Template Construction

The templates were created by computing the mean and standard deviation over the normalized CBF maps for the control group of 25 subjects.

Four different perfusion templates were created using combinations of the previously described methods:

- Template 1—MNI: perfusion images were spatially normalized to the MNI305 template;
- Template 2—MNI+PVEc: MNI normalization and partial volume correction;
- Template 3—DARTEL: perfusion images were spatially normalized to the stereotactic space using DARTEL registration;
- Template 4—DARTEL+PVEc: DARTEL normalization and partial volume correction.

Preprocessing of Functional Group Images

Functional group image preprocessing steps were performed identically to the control group image preprocessing. An additional preprocessing step was performed on functional ASL data to minimize the BOLD effect and its influence on the size of activated areas and CBF

quantification [Lu et al., 2006]. The surround subtraction strategy was used to resample the interleaved control and labeled ASL images. Thus, control and label images corresponding to the same time point and therefore containing an identical BOLD signal were subtracted before computing the perfusion weighted images [Liu and Wong, 2005; Lu et al., 2006].

CBF Quantification Evaluation

The average gray matter CBF of each group was measured in the MNI stereotactic space over all GM pixels of the whole acquired volume. Only the off-phase was considered for the functional group to exclude the activation from the comparison. The mean perfusion over the motor areas (see section "Activation detection") on the MNI spatially normalized data was measured for the functional group. Two measurements were performed where the images from the on-phase and off-phase were considered separately in order to assess the difference in blood flow caused by the motor task.

Template Comparison

To quantitatively assess the quality of the template construction framework, we performed a leave-one-out cross-correlation by inversely transforming the template to align it with the perfusion image of each subject. For each subject of the control group, the corresponding perfusion image was excluded from the template and only the 24 remaining subjects were used. The root mean squared error (RMS) between the template and the perfusion image was calculated for each subject. Subsequently for each template, the mean RMS error over the 25 subjects was calculated. For this comparison only, the two lowest slices, presenting numerous artifacts, were excluded from the analysis for all subjects. Also, the top slice was discarded because the brain coverage after normalization was not the same for all subjects due to different brain dimensions.

Activation Detection: Template Versus GLM Comparison

First, we computed the motor task-related activated areas from the block-design functional data using the standard GLM analysis implemented in SPM after spatial smoothing with a 6-mm FWHM Gaussian filter. The statistical significance was $P < 0.05$ (family-wise error correction) and the threshold on cluster size was 250 mm^3. Detected clusters in the primary and supplementary motor areas were assumed to be the ground truth. The GLM analysis was performed on the functional group on individual subjects as well as at the group level spatially normalized either to the MNI template or using DARTEL registration.

The on-phase images of the functional group were intensity normalized to create the activated CBF images reflecting subject perfusion during motor activation. These activated CBF images were compared at the individual level to each of the four perfusion templates and the Z-score was used to identify the areas of hyperperfusion. A similar approach was used at the group level. The mean of the on-phase CBF images over all the subjects of the functional group was compared with the perfusion templates to detect the areas of hyperperfusion at the group level.

The individual and group-level activated areas detected using the standard GLM analysis (FWE $P < 0.05$) were used as a ground truth and compared with the template-detected hyperperfusion areas. The true positive ratio was computed as a percentage of the template detected area size over the ground-truth (GLM-analysis) region size. Any voxel detected as hyperperfused outside of the ground-truth region within a maximum distance of 25 mm from the border of the ground-truth region was considered as false positive. The false positive ratio was computed as the area of all false positives divided by the size of the area where the false positives were considered. The receiver operating characteristic (ROC) curve was computed showing the true positive ratios of the detection as a function of the false positive ratio from 0 to 100%. The templates were compared using the area under the curve (AUC) parameter computed from the ROC curve for each template. The mean Z score over the ground-truth region was evaluated for all four templates at the individual and at the group level.

Dysplasia Detection

A 14-year-old drug resistant epileptic female patient presenting a right temporal dysplasia, which is a recognized cause of epilepsy, was also included to assess the potential for clinical use of the presented method. The 3D MPRAGE T_1-weighted and PASL perfusion images were acquired with the same parameters as for the control group. The repetition and echo time of the PASL acquisition was TR/TE = 3,000/18 ms. For clinical screening T_2-weighted images were also acquired.

A T_1-w voxel-based morphometry (VBM) analysis was used to automatically identify abnormalities [Bannier et al., 2012; Huppertz et al., 2008; Wilke et al., 2003]. The VBM results were validated based on the T_1-weighted and T_2-weighted images by a neuroradiologist and a neurologist. The template-comparison with the four templates was used to detect hypoperfused regions with Z-score > 2.

RESULTS

CBF Quantification Evaluation

The average CBF measured for the entire GM of the spatially normalized data was 49.8 ± 12.9 ml/100 g/min for the control group and 54.1 ± 8.4 ml/100 g/min for the functional group. The difference was not significant, $P = 0.11$. In the functional group, the average CBF measured

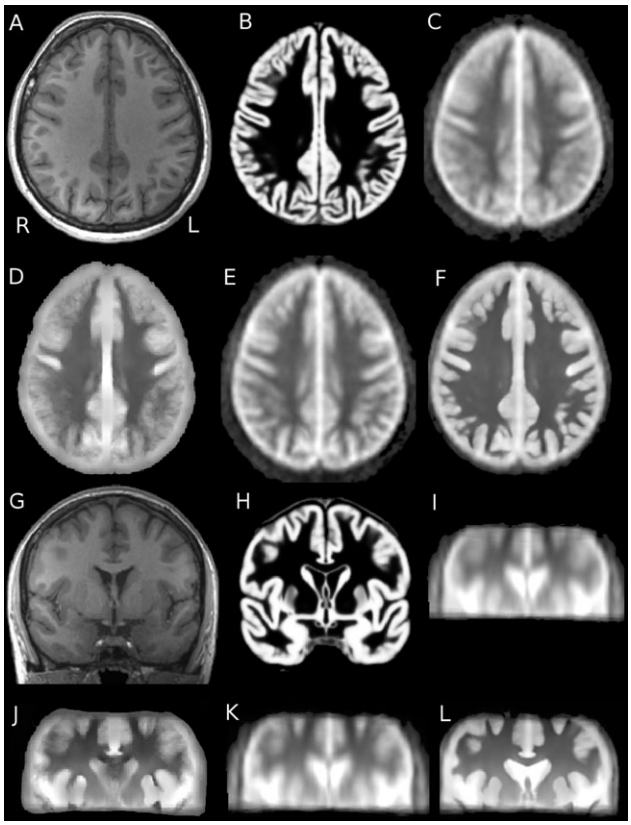

Figure 1.
Templates–axial slice. The four templates were compared with the anatomical image in axial (**A**–**F**) and coronal slices (**G**–**L**). T_1-weighted image of the first subject (A,G); mean GM segmentation of all subjects (B,H); perfusion templates MNI (C,I); MNI+PVEc (D,J); DARTEL (E,K) and DARTEL+PVEc (F,L). The GM structures were blurred in (D,E) and particularly in (C). Because of the low resolution in the axial direction, the blurring is important in coronal direction as a result of interpolation, in particular for templates MNI (C) and DARTEL (E). The partial volume correction methods reduced these artifacts as shown in (D) and especially in DARTEL+PVEc template (F). The same blurring can be observed in coronal images (I–K) and its reduction is shown in for DARTEL+PVEc (L). Note that only 9 ASL slices of thickness 7 mm were acquired. Therefore, the perfusion templates did not cover the whole brain.

on the activated primary and supplementary motor area was 53.8 ± 13.4 ml/100 g/min during the off-phase and 79.2 ± 13.6 ml/100 g/min during the on-phase. The difference was significant ($P < 0.0001$).

Template Evaluation

Mean RMS error was respectively 16.6, 16.7, 16.2, and 16.2 ml/100 g/min for templates MNI, MNI+PVEc, DARTEL, and DARTEL+PVEc. The difference between the MNI and DARTEL/DARTEL+PVEc was significant ($P < 0.05$). Figure 1 shows the comparison of the four ASL templates with a single-subject T_1-weighted image. The GM structures were blurred in particular in posterior regions and in coronal direction. Using PVE correction method, this blurring effect decreased, especially in DARTEL+PVEc template. Figure 2 shows the same aspects on subsampled templates on a single-subject CBF map.

Activation Detection: Template Versus GLM Comparison

Template activation detection enabled detection of both primary and supplementary motor areas in all subjects from the functional group. However, in two subjects the supplementary motor area was not detected using the GLM method.

The ROC curves are given in Figure 3. At maximum, the true positive ratio of the MNI template was 7.6, 4.6, and 9.6% lower than the true positive ratio of the MNI+PVEc, DARTEL, and DARTEL+PVEc template, respectively, at the individual level. At the group level, the true positive ratio of the MNI template was higher than the ratio of the MNI+PVEc in all cases and at maximum it was 9.6 and 8.1% lower than the true positive ratio of the DARTEL and DARTEL+PVEc template, respectively. The AUC was 0.81, 0.84, 0.82, and 0.84 for the MNI, MNI+PVEc, DARTEL, and DARTEL+PVEc template, respectively, at the individual level and 0.85, 0.8, 0.87, and 0.87, respectively, at the group level. The detected areas for a single subject from the functional group are shown in Figure 4. Figure 5 shows the

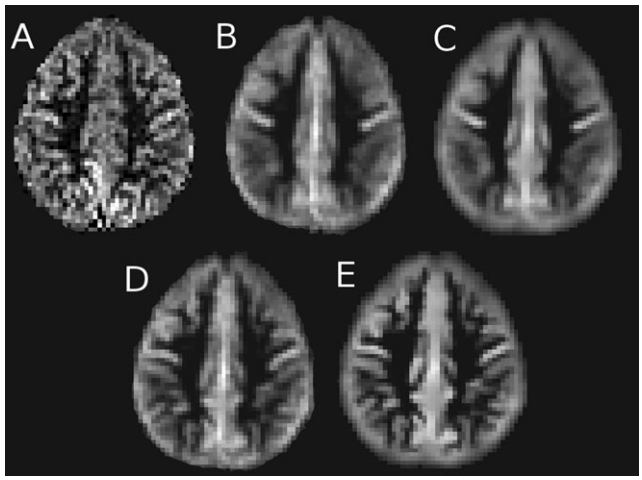

Figure 2.
Individual-subject perfusion image and reconstruction from the template. CBF map of the first subject of the control group (**A**). Templates MNI (**B**), MNI+PVEc (**C**), DARTEL (**D**), DARTEL+PVEc (**E**) were coregistered with the image (A) and subsampled to the same resolution in order to show comparison of the perfusion template and individual subject perfusion (B–E).

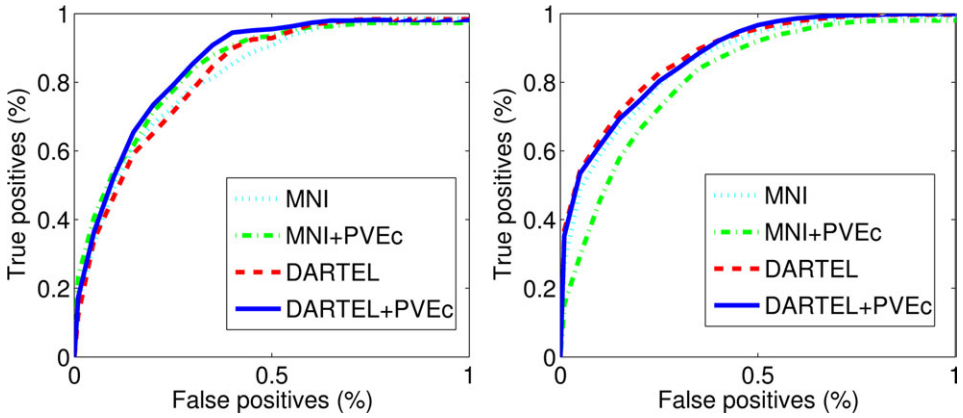

Figure 3.
Hyperperfusion detection compared with the ground truth. The true positive versus false positive ratio is shown for the four templates on individual images (left) and on group data (right). [Color figure can be viewed in the online issue, which is available at wileyonlinelibrary.com.]

group template detection overlaid over the ground-truth data obtained using the standard GLM model. The average Z score over the whole ground-truth region was 1.12, 1.15, 1.24, and 1.37 at the individual level and 1.09, 1.0, 1.42, and 1.6 at the group level for the MNI, MNI+PVEc, DARTEL, and DARTEL+PVEc template, respectively.

Dysplasia Detection

Two areas of hypoperfusion and one area of hyperperfusion were detected in the epileptic patient using the DARTEL+PVEc template, see Figure 6. The hypoperfusion in temporal gray matter (Fig. 6A) corresponded to the morphological findings. The center of gravity of this hypoperfused region was located at 1.5 mm distance from the position of the lesion detected by VBM. The hyperperfusion in thalamus (Fig. 6B) and the hypoperfusion (Fig. 6C) in the frontal gray matter are not directly related to the disease and, thus, can be regarded as false-positives in the sense of dysplasia detection. The other three templates (MNI, MNI+PVEc and DARTEL) detected with the same Z score threshold only the area of hypoperfusion in the frontal gray matter. The average Z score computed over the area of the detected temporal lesion was 1.9, 1.8, 2, and 2.5 for MNI, MNI+PVEc, DARTEL, and DARTEL+PVEc, respectively.

DISCUSSION

This study shows that an ASL template approach can detect individual and group hyperperfusions induced by motor tasks. Using DARTEL and partial volume correction in the template construction increased the accuracy of the hyperperfusion detection.

The average GM CBF of the control and functional group was 49.8 ± 12.9 and 54.1 ± 8.4 ml/100 g/min, respectively. Results for both groups are slightly higher than the mean CBF 47.4 ± 7.5 ml/100 g/min reported in the multi-center study by Petersen et al. [2010], though the difference is negligible with respect to the reported variance. Although pulsed ASL with similar labeling and bolus saturation was used in both studies, a single-TI was

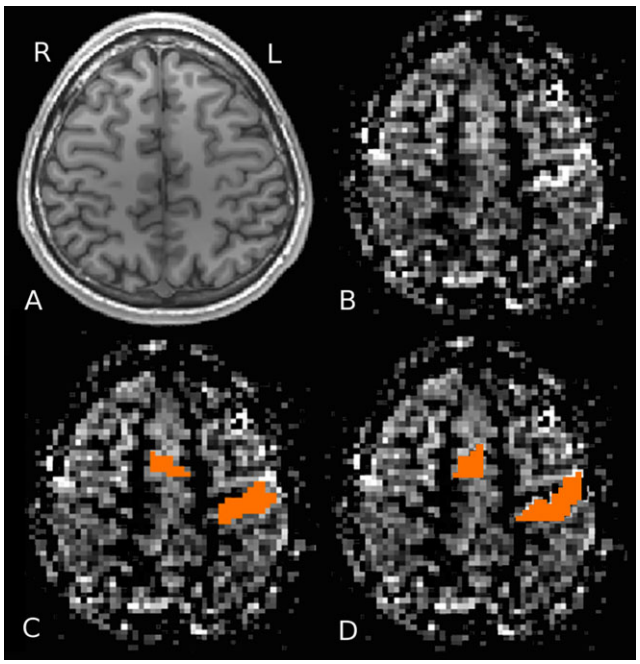

Figure 4.
Functional ASL results on an individual subject. Axial slice of a T_1-weighted image (**A**); ASL image (**B**); activated areas obtained using a standard GLM model (**C**); Hyperperfusion regions detected with the use of template DARTEL+PVEc (**D**). [Color figure can be viewed in the online issue, which is available at wileyonlinelibrary.com.]

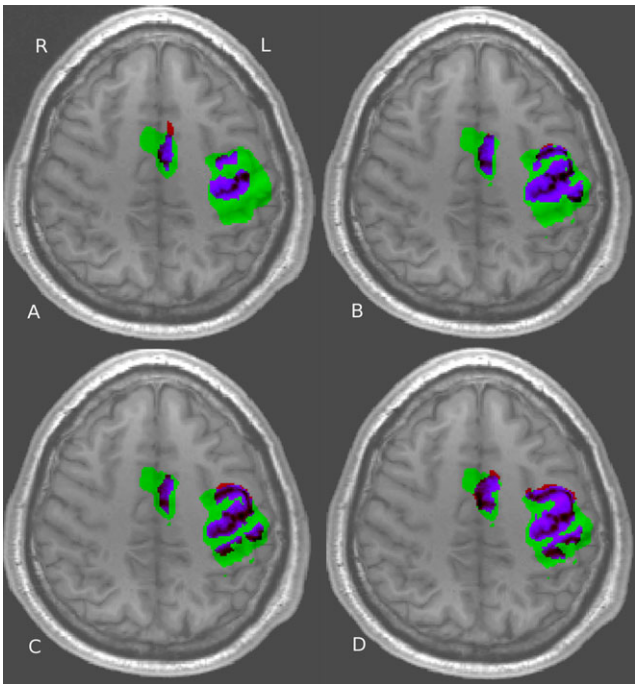

Figure 5.

Hyperperfusion detection vs. activation detection using the standard GLM model. The results are compared for the four different templates MNI (**A**), MNI+PVEc (**B**), DARTEL (**C**), and DARTEL+PVEc (**D**). The ground-truth region is in green and the activated region detected by comparison with the template is in red. Therefore, the purple region displays true positives and the red region false positives. [Color figure can be viewed in the online issue, which is available at wileyonlinelibrary.com.]

used in the present study and a multi-TI with model-free quantification was used in the multicenter study. The two types of quantification can bring different results, as for example the bolus arrival time is not estimated for the single-TI data. The model-free method was reported to give lower CBF values than a standard fit to a general kinetic model [Ho et al., 2010], which is more similar to the CBF quantification model, used in this study and can explain the difference in CBF. The difference between the individual mean values of CBF was also reported on the same study, with values varying from 39.3 to 52.7 ml/100 g/min [Petersen et al., 2010]. A significant increase in CBF was shown in the motor areas of the functional group between the off- and on-phase. This showed the modifications of local hemodynamics induced by the neuronal activity during the motor task. The detection of increased CBF induced by neuronal activity using ASL was already described by Aslan and Lu [2010]. The 47% average increase of CBF was measured in accordance with the literature findings that range from 40 to 100% [Garraux et al., 2005; Raoult et al., 2011; Wang et al., 2003] and largely depending on the selection of the region to be measured. It was slightly higher than the 35% CBF increase in motor-visual task reported by Borogovac et al. [2010].

Four templates were built and compared. Compared to MNI registration, DARTEL registration improved the perfusion contrast border between WM and GM. The reason is that DARTEL registration iteratively realigns the images of the studied group with their mean using a transformation that is less restricted than the one used in SPM to align with the MNI template. The result showed more precise alignment of the structural T_1-weighted images. It subsequently positively affected the quality of the perfusion template as can be seen from the comparison of the low-resolution perfusion images with their counterpart generated using the template. The true positive activation detection was likewise increased for both individual and group comparison. PVE correction used with DARTEL registration reduced the interpolation artifact effect by

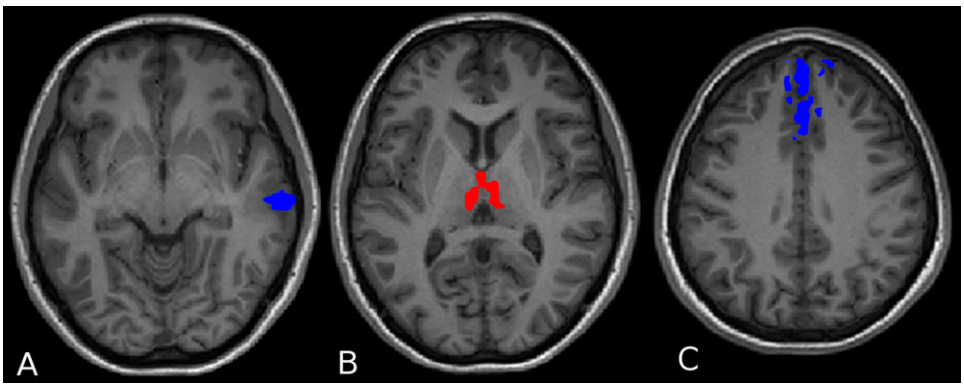

Figure 6.

Results on the epileptic patient. The hypoperfusion (**A**, **C**) and hyperperfusion (**B**) areas detected using the DARTEL+PVEc template is shown. The area in (A) is the lesion which was also detected using the VBM on the T_1-weighted images. The areas in (B) and (C) are false positive in the sense that they were not detected as the regions of dysplasia. [Color figure can be viewed in the online issue, which is available at wileyonlinelibrary.com.]

using the segmented T_1-weighted information which has significantly higher resolution than ASL images, thus allowing better localization of the perfusion sources. The outcome is mainly visible in the coronal-direction where the ASL resolution is the poorest. This should be especially useful in limiting false positive detection of hyperperfusion in white matter. The positive effect of PVE correction on true positive detection was 2.5% when using MNI normalization and 2.9% when using DARTEL normalization at the individual level. At the group level, the PVE correction for MNI normalization even decreased the true positive ratio as the MNI alignment precision is limited.

Although DARTEL+PVEc template showed increased detection and less interpolation artifacts during the spatial normalization, the PVE correction itself can smooth the CBF data by using regression on a $3 \times 3 \times 1$ neighborhood. Liang et al. [2012] has recently presented a modified least trimmed square method for partial volume correction to reduce the blurring during the regression. Also a novel method for PV ratios determination using Look-Locker sequences was proposed [Petr et al., 2013]. Both these methods can potentially further increase the detection power. The comparison of the template detection with the GLM analysis should be taken as an indicator of the possible detection power of the template and comparison to a gold standard rather than a universal proof. The reason being, that the GLM analysis itself can contain errors. The chosen threshold 0.05 FWE can create false-negatives in the GLM analysis and, thus, wrongly increase the false-positive ratio in the template detection. However, we assume that the errors in the GLM analysis are relatively small compared to the template detection and thus will not have severe effect on the relative comparison of different templates.

Following the results of Aslan and Lu [2010], the CBF of each subject was intensity normalized using the mean whole-brain perfusion prior to creating the template. The intensity normalization compensates for different mean subject perfusion levels and thus improves the quality of activation detection [Aslan and Lu, 2010]. Although the intensity-normalized data were used for inter-subject comparison, the CBF quantification step [Eq. (1)] is a necessary part of the template construction process. The reason is that the B_1-field inhomogeneity bias is partially attenuated by using a value of M_{0T} extracted from a control image with longer TR. Using raw perfusion weighted images would result in decreased quality of the results.

Both our control and activation groups were composed of young subjects. A global decrease of GM CBF of around 30% was reported in elderly population [Ances et al., 2009; Reston et al., 2007]. Brain tissue atrophy is often seen in elderly population making the GM structures thinner. This increases the negative effect of partial volume and can decrease the overall perfusion if the PVE-correction is not applied. It was shown by Asllani et al. [2009] that by using an improved processing with PVE correction, the age-related CBF difference was decreased to 15%. As no regional decrease in healthy elderly subjects was demonstrated, we think that the presented method will work similarly in elderly subjects making the added value of DARTEL+PVEc even more pronounced. However, despite the intensity normalization, use of the young subject's template to detect perfusion abnormalities needs to be evaluated.

Apart from functional MRI, the potential fields of application of the presented method are diseases presenting important regional increase/decrease of blood flow. The main constraint is the ability to obtain precise GM/WM segmentation of the whole brain and particularly of the region of interest. The method should, however, be applicable to diseases where the structure is unchanged or only affected by atrophy as for example Alzheimer and Parkinson patients, psychiatric or neuro-developmental diseases. The changes in perfusion in those patients are usually well localized and thus will not disrupt the spatial nor intensity normalization. Perfusion related changes have already been reported using ASL in Alzheimer patients [Alexopoulos et al., 2012; Asllani et al., 2008b] and Parkinson patients [Fernández-Seara et al., 2012; Melzer et al., 2011]. In these studies, no ground truth was available to validate different types of detection of perfusion changes. The approach presented here should be applicable to the same type of diseases as well. The positive effects of DARTEL and PVE correction validated with a gold-standard ground truth should further improve the precision of the stated methods. Lesion detection was demonstrated on a single epileptic patient. The DARTEL+PVEc template provided the best results, as it was the only one of the four templates that revealed the lesion at given Z-score threshold while the average Z score over the lesion was too low for the other three templates. Although two areas of hypo- and hyperperfusion were detected as well, they were distinct from the lesion and their signification remains to be investigated. In this exploratory case, we did not compare the results to other perfusion technique but only to the morphological pattern.

As the main focus was the motor cortex, a dataset with limited coverage was acquired. It should be noted that a whole-brain coverage would be essential for the aforementioned clinical applications. Acquiring ASL data with whole-brain coverage is now feasible using different acquisition techniques, in particular using 3D acquisition scheme, at different field strengths [Gai et al., 2011; Ghariq et al., 2012]. The template methodology remains the same for the whole-brain images.

In conclusion, we have shown that the individual and group motor-task related hyperperfusion can be detected by comparison with a template based on normal controls and the results are in concordance with standard block-design ASL experiments. The advantage of using DARTEL registration and PVE-correction for improving both template quality and accuracy of hyperperfusion was demonstrated.

REFERENCES

Alexopoulos P, Sorg C, Förschler A, Grimmer T, Skokou M, Wohlschläger A, Perneczky R, Zimmer C, Kurz A, Preibisch C

(2012): Perfusion abnormalities in mild cognitive impairment and mild dementia in Alzheimer's disease measured by pulsed arterial spin labeling MRI. Eur Arch Psychiatry Clin Neurosci 262:69–77.

Ances BM, Leontiev O, Perthen JE, Liang C, Lansing AE, Buxton RB (2008): Regional differences in the coupling of cerebral blood flow and oxygen metabolism changes in response to activation: Implications for BOLD-fMRI. NeuroImage 39:1510–1521.

Ances BM, Liang C, Leontiev O, Perthen J, Fleisher AS, Lansing A, Buxton RB (2009): Effects of aging on cerebral blood flow, oxygen metabolism, and blood oxygenation level dependent responses to visual stimulation. Hum Brain Mapp 30:1120–1132.

Ashburner J (2007): A fast diffeomorphic image registration Algorithm. NeuroImage 38:95–113.

Ashburner J, Friston KJ (2005): Unified segmentation. NeuroImage 26:839–851.

Aslan S, Lu H (2010): On the sensitivity of ASL MRI in detecting regional differences in cerebral blood flow. Magn Reson Imaging 28:928–935.

Asllani I, Borogovac A, Brown TR (2008a): Regression algorithm correcting for partial volume effects in arterial spin labeling MRI. Magn Reson Med 60:1362–1371.

Asllani I, Habeck C, Scarmeas N, Borogovac A, Brown TR, Stern Y (2008b): Multivariate and univariate analysis of continuous arterial spin labeling perfusion MRI in Alzheimer's disease. J Cereb Blood Flow Metab 28:725–736.

Asllani I, Habeck C, Borogovac A, Brown TR, Brickman AM, Stern Y (2009): Separating function from structure in perfusion imaging of the aging brain. Human Brain Mapp 30:2927–2935.

Bannier E, Maumet C, Pasnicu A, Ferré JC, Pasqualini E, Biraben A, Gauvrit JY, Barillot C (2012): Voxel based analysis of 3D double inversion recovery for the detection of cortical abnormalities in drug resistant epilepsy. In: Proceedings of ISMRM 2012, Melbourne, Australia. p 3244.

Biagi L, Abbruzzese A, Bianchi MC, Alsop DC, Guerra AD, Tosetti M (2007): Age dependence of cerebral perfusion assessed by magnetic resonance continuous arterial spin labeling. J Magn Reson Imaging 25:696–702.

Borogovac A, Habeck C, Small SA, Asllani I (2010): Mapping brain function using a 30-day interval between baseline and activation: A novel arterial spin labeling fMRI approach. J Cereb Blood Flow Metab 30:1721–1733.

Buxton RB, Frank LR, Wong EC, Siewert B, Warach S, Edelman RR (1998): A general kinetic model for quantitative perfusion imaging with arterial spin labeling. Magn Reson Med 40:383–396.

Cavusoglu M, Pfeuffer J, Ugurbil K, Uludag K (2009): Comparison of pulsed arterial spin labeling encoding schemes and absolute perfusion quantification. Magn Reson Med 27:1039–1045.

Chen Y, Wang DJJ, Detre JA (2011): Test-retest reliability of arterial spin labeling with common labeling strategies. J Magn Reson Imaging 33:940–949.

Coupé P, Yger P, Prima S, Hellier P, Kervrann C, Barillot C (2008): An optimized blockwise non local means denoising filter for 3D magnetic resonance images. IEEE T Med Imaging 27:425–441.

Detre JA, Leigh JS, Williams DS, Koretsky AP (1992): Perfusion imaging. Magn Reson Med 23:37–45.

Evans AC, Collins DL, Mills SR, Brown ED, Kelly RL, Peters TM (1993): 3D statistical neuroanatomical models from 305 MRI volumes. IEEE Nuclear Science Symposium and Medical Imaging Conference, pp.1813–1817.

Fernández-Seara MA, Mengual E, Vidorreta M, Aznárez-Sanado M, Loayza FR, Villagra F, Irigoyen J, Pastor MA (2012): Cortical hypoperfusion in Parkinson's disease assessed using arterial spin labeled perfusion MRI. NeuroImage 59:2743–2750.

Ferré JC, Petr J, Bannier E, Barillot C, Gauvrit JY (2012): Improving quality of arterial spin labeling MR imaging at 3 tesla with a 32-channel coil and parallel imaging. J Magn Reson Imaging 35:1233–1239.

Floyd TF, Ratcliffe SJ, Wang J, Resch B, Detre JA (2003): Precision of the CASL-perfusion MRI technique for the measurement of cerebral blood flow in whole brain and vascular territories. J Magn Reson Imaging 18:649–655.

Gai ND, Talagala SL, Butman JA (2011): Whole-brain cerebral blood flow mapping using 3D echo planar imaging and pulsed arterial tagging. J Magn Reson Imaging 33:287–295.

Gallichan D, Jezzard P (2008): Modeling the effects of dispersion and pulsatility of blood flow in pulsed arterial spin labeling. Magn Reson Med 60:53–60.

Gallichan D, Jezzard P (2009): Variation in the shape of pulsed arterial spin labeling kinetic curves across the healthy human brain and its implications for CBF quantification. Magn Reson Med 61:686–695.

Garraux G, Hallett M, Talagala SL (2005): CASL fMRI of subcortico-cortical perfusion changes during memory-guided finger sequences. NeuroImage 25:122–132.

Ghariq E, Teeuwisse WM, Webb AG, van Osch MJP (2012): Feasibility of pseudocontinuous arterial spin labeling at 7 T with whole-brain coverage. Magma 25:83–93.

Ho YCL, Petersen ET, Golay X (2010): Measuring arterial and tissue responses to functional challenges using arterial spin labeling. NeuroImage 49:478–487.

Huppertz HJ, Wellmer J, Staack AM, Altenmüller DM, Urbach H, Kröll J (2008): Voxel-based 3D MRI analysis helps to detect subtle forms of subcortical band heterotopia. Epilepsia 49:772–785.

Jahng GH, Song E, Zhu XP, Matson GB, Weiner MV, Schuff N (2005): Human brain: Reliability and reproducibility of pulsed arterial spin-labeling perfusion MR imaging. Radiology 234:909–916.

Jin T, Kim SG (2008): Cortical layer-dependent dynamic blood oxygenation, cerebral blood flow and cerebral blood volume responses during visual stimulation. NeuroImage 43:1–9.

Lee C, Lopez OL, Becker JT, Raji C, Dai W, Kuller LH, Gach HM (2009): Imaging cerebral blood flow in the cognitively normal aging brain with arterial spin labeling: Implications for imaging of neurodegenerative disease. J Neuroimaging 19:344–352.

Leontiev O, Buxton RB (2007): Reproducibility of BOLD, perfusion, and CMRO2 measurements with calibrated-BOLD fMRI. NeuroImage 35:175–184.

Liang X, Connelly A, Calamante F (2012): Improved partial volume correction for single inversion time arterial spin labeling data. Magn Reson Med C:1–7.

Liu TT, Wong EC (2005): A signal processing model for arterial spin labeling functional MRI. NeuroImage 24:207–215.

Lu H, Donahue MJ, van Zijl PCM (2006): Detrimental effects of BOLD signal in arterial spin labeling fMRI at high field strength. Magn Reson Med 56:546–552.

Luh WM, Wong EC, Bandettini PA, Hyde JS (1999): QUIPSS II with thin-slice TI1 periodic saturation: A method for improving accuracy of quantitative perfusion imaging using pulsed arterial spin labeling. Magn Reson Med 41:1246–1254.

Mazerolle EL, Beyea SD, Gawryluk JR, Brewer KD, Bowen CV, D'Arcy RC (2010): Confirming white matter fMRI activation in the corpus callosum: Co-localization with DTI tractography. NeuroImage 50:616–621.

Mazziotta JC, Toga AW, Evans A, Fox P, Lancaster J (1995): A probabilistic atlas of the human brain: Theory and rationale for its development. NeuroImage 2:89–101.

Melzer TR, Watts R, MacAskill MR, Pearson JF, Rüeger S, Pitcher TL, Livingston L, Graham C, Keenan R, Shankaranarayanan A, Alsop DC, Dalrymple-Alford JC, Anderson TJ (2011): Arterial spin labeling reveals an abnormal cerebral perfusion pattern in Parkinson's disease. Brain 134:845–855.

Morbelli S, Rodriguez G, Mignone A, Altrinetti V, Brugnolo A, Piccardo A, Pupi A, Koulibaly PM, Nobili F (2008): The need of appropriate brain SPECT templates for SPM comparisons. Q J Nucl Med Mol Imaging 52:89–98.

Obata T, Liu TT, Miller KL, Luh WM, Wong EC, Frank LR, Buxton RB (2004): Discrepancies between BOLD and flow dynamics in primary and supplementary motor areas: Application of the balloon model to the interpretation of BOLD transients. NeuroImage 21:144–153.

Oldfield RC (1971): The assessment and analysis of handedness: The Edinburgh inventory. Neuropsychologia 9:97–113.

Parkes LM, Detre JA (2004): ASL: Blood Perfusion Measurements Using Arterial Spin Labelling, In: Quantitative MRI of the Brain: Measuring Changes Caused by Disease (ed P. Tofts), John Wiley & Sons, Ltd, Chichester, UK. DOI: 10.1002/0470869526.ch13.

Perthen JE, Bydder M, Restom K, Liu TT (2008): SNR and functional sensitivity of BOLD and perfusion-based fMRI using arterial spin labeling with spiral SENSE at 3 T. Magn Reson Imaging 26:513–522.

Petersen ET, Mouridsen K, Golay X (2010): The QUASAR reproducibility study, part II: Results from a multi-center arterial spin labeling test-retest study. NeuroImage 49:104–113.

Petr J, Schramm G, Hofheinz F, Langner J, van den Hoff J (2013): Partial Volume Correction in Arterial Spin Labeling Using a Look-Locker Sequence. Magn Reson Med (in press). DOI: 10.1002/mrm.24601.

Pfefferbaum A, Chanraud S, Pitel AL, Shankaranarayanan A, Alsop DC, Rohlfing T, Sullivan EV (2010): Volumetric cerebral perfusion imaging in healthy adults: Regional distribution, laterality, and repeatability of pulsed continuous arterial spin labeling (PCASL). Psychiatry Res-Neuroim 182:266–273.

Raoult H, Petr J, Bannier E, Stamm A, Gauvrit JY, Barillot C, Ferré JC (2011): Arterial spin labeling for motor activation mapping at 3T with a 32-channel coil: Reproducibility and spatial accuracy in comparison with BOLD fMRI. NeuroImage 58:157–167.

Restom K, Bangen KJ, Bondi MW, Perthen JE, Liu TT (2007): Cerebral blood flow and BOLD responses to a memory encoding task: A comparison between healthy young and elderly adults. NeuroImage 37:430–439.

Tjandra T, Brooks JC, Figueiredo P, Wise R, Matthews PM, Tracey I (2005): Quantitative assessment of the reproducibility of functional activation measured with BOLD and MR perfusion imaging: Implications for clinical trial design. NeuroImage 27:393–401.

Wang J, Aguirre GK, Kimberg DY, Roc AC, Li L, Detre JA (2003): Arterial spin labeling perfusion fMRI with very low task frequency. Magn Reson Med 49:796–802.

Wang Z, Wang J, Connick TJ, Wetmore GS, Detre JA (2005): Continuous ASL (CASL) perfusion MRI with an array coil and parallel imaging at 3T. Magn Reson Med 54:732–737.

Wang Y, Saykin AJ, Pfeuffer J, Lin C, Mosier KM, Shen L, Kim S, Hutchins GD (2011): Regional reproducibility of pulsed arterial spin labeling perfusion imaging at 3T. NeuroImage 54:1188–1195.

Wiest-Daesslé N, Yger P, Prima S, Barillot C (2007): Evaluation of a new optimization algorithm for rigid registration of MRI data.In SPIE Medical Imaging 2007: Image Processing, San Diego, USA.

Wilke M, Kassubek J, Ziyeh S, Schulze-Bonhage A, Huppertz HJ (2003): Automated detection of gray matter malformations using optimized voxel-based morphometry: A systematic approach. Neuroimage 20:330–343.

Wong EC (2005): Quantifying CBF with pulsed ASL: Technical and pulse sequence factors. J Magn Reson Imaging 22:727–731.

Wong EC, Buxton RB, Frank LR (1998): Quantitative imaging of perfusion using a single subtraction (QUIPSS and QUIPSS II). Magn Reson Med 39:702–708.

Ye FQ, Mattay VS, Jezzard P, Frank JA, Weinberger DR, McLaughlin AC (1997): Correction for vascular artifacts in cerebral blood flow values measured by using arterial spin tagging techniques. Magn Reson Med 37:226–235.

Yousry TA, Schmid UD, Alkadhi H, Schmidt D, Peraud A, Buettner A, Winkler P (1997): Localization of the motor hand area to a knob on the precentral gyrus. A new landmark. Brain 120:141–157.

Appendix A4

ExploreASL: an image processing pipeline for multi-center ASL perfusion MRI studies

Mutsaerts, H. J., **Petr, J.***, Groot, P., Vandemaele, P., Ingala, S., Robertson, A. D., ... & Barkhof, F. (2020). ExploreASL: an image processing pipeline for multi-center ASL perfusion MRI studies. Neuroimage, 219, 117031.

Journal name (category): **Neuroimage** (Neuroimaging; Neurosciences; Radiology, nuclear medicine & medical imaging)

Quartile in category: **Q1/Q1/Q1**

Impact factor: **7.4**

Number of WoS citations: **23**

NeuroImage 219 (2020) 117031

Contents lists available at ScienceDirect

NeuroImage

journal homepage: www.elsevier.com/locate/neuroimage

ExploreASL: An image processing pipeline for multi-center ASL perfusion MRI studies

Henk J.M.M. Mutsaerts [a,b,c,d,e,*,1], Jan Petr [d,f,1], Paul Groot [b], Pieter Vandemaele [e], Silvia Ingala [a], Andrew D. Robertson [g], Lena Václavů [h], Inge Groote [i], Hugo Kuijf [j], Fernando Zelaya [k], Owen O'Daly [k], Saima Hilal [l,m,n], Alle Meije Wink [a], Ilse Kant [c,o], Matthan W.A. Caan [p], Catherine Morgan [q], Jeroen de Bresser [r], Elisabeth Lysvik [i], Anouk Schrantee [b], Astrid Bjørnebekk [s], Patricia Clement [e], Zahra Shirzadi [t], Joost P.A. Kuijer [a], Viktor Wottschel [a], Udunna C. Anazodo [u,v], Dasja Pajkrt [w], Edo Richard [x,y], Reinoud P.H. Bokkers [z], Liesbeth Reneman [b], Mario Masellis [t], Matthias Günther [aa,ab,ac], Bradley J. MacIntosh [t], Eric Achten [e], Michael A. Chappell [ad], Matthias J.P. van Osch [h], Xavier Golay [ae], David L. Thomas [ae], Enrico De Vita [af], Atle Bjørnerud [i,ag], Aart Nederveen [b], Jeroen Hendrikse [c], Iris Asllani [d,ah], Frederik Barkhof [a,ae,ai]

[a] Department of Radiology and Nuclear Medicine, Amsterdam Neuroscience, Amsterdam University Medical Center, Location VUmc, Amsterdam, the Netherlands
[b] Radiology and Nuclear Medicine, Amsterdam Neuroscience, Amsterdam University Medical Centers, Location Academic Medical Center, University of Amsterdam, Amsterdam, the Netherlands
[c] Radiology, University Medical Center Utrecht, Utrecht, the Netherlands
[d] Kate Gleason College of Engineering, Rochester Institute of Technology, NY, USA
[e] Ghent Institute for Functional and Metabolic Imaging (GIfMI), Ghent University, Ghent, Belgium
[f] Helmholtz-Zentrum Dresden-Rossendorf, Institute of Radiopharmaceutical Cancer Research, Dresden, Germany
[g] Schlegel-UW Research Institute for Aging, University of Waterloo, Waterloo, Ontario, Canada
[h] C.J. Gorter Center for High Field MRI, Department of Radiology, Leiden University Medical Center, Leiden, the Netherlands
[i] Department of Diagnostic Physics, Oslo University Hospital, Oslo, Norway
[j] Image Sciences Institute, University Medical Center Utrecht, Utrecht, the Netherlands
[k] Department of Neuroimaging, Institute of Psychiatry, Psychology and Neuroscience, King's College London, London, UK
[l] Department of Pharmacology, National University of Singapore, Singapore
[m] Memory Aging and Cognition Center, National University Health System, Singapore
[n] Saw Swee Hock School of Public Health, National University of Singapore, Singapore
[o] Department of Intensive Care, University Medical Centre, Utrecht, the Netherlands
[p] Department of Biomedical Engineering and Physics, Amsterdam University Medical Center, Location Academic Medical Center, Amsterdam, the Netherlands
[q] School of Psychology and Centre for Brain Research, University of Auckland, Auckland, New Zealand
[r] Department of Radiology, Leiden University Medical Center, Leiden, the Netherlands
[s] The Anabolic Androgenic Steroid Research Group, National Advisory Unit on Substance Use Disorder Treatment, Oslo University Hospital, Oslo, Norway
[t] Sunnybrook Research Institute, University of Toronto, Toronto, Canada
[u] Department of Medical Biophysics, University of Western Ontario, London, Canada
[v] Imaging Division, Lawson Health Research Institute, London, Canada
[w] Department of Pediatric Infectious Diseases, Emma Children's Hospital, Amsterdam University Medical Centre, Location Academic Medical Center, Amsterdam, the Netherlands
[x] Department of Neurology, Donders Institute for Brain, Behavior and Cognition, Radboud University Medical Centre, Nijmegen, the Netherlands
[y] Neurology, Amsterdam University Medical Center, Location Academic Medical Center, University of Amsterdam, Amsterdam, the Netherlands
[z] Department of Radiology, Medical Imaging Center, University Medical Center Groningen, University of Groningen, Groningen, the Netherlands
[aa] Fraunhofer MEVIS, Bremen, Germany
[ab] University of Bremen, Bremen, Germany
[ac] Mediri GmbH, Heidelberg, Germany
[ad] Institute of Biomedical Engineering, Department of Engineering Science & Wellcome Centre for Integrative Neuroimaging, FMRIB, Nuffield Department of Clinical Neuroscience, University of Oxford, Oxford, UK
[ae] UCL Queen Square Institute of Neurology, University College London, London, UK

* Corresponding author. Dep. of Radiology and Nuclear Medicine, PK -1, De Boelelaan 1117, 1081, HV, Amsterdam, the Netherlands.

https://doi.org/10.1016/j.neuroimage.2020.117031

Available online 8 June 2020

[af] Department of Biomedical Engineering, School of Biomedical Engineering & Imaging Sciences, King's College London, King's Health Partners, St Thomas' Hospital, London, SE1 7EH, UK
[ag] Department of Psychology, University of Oslo, Norway
[ah] Clinical Imaging Sciences Centre, Department of Neuroscience, Brighton and Sussex Medical School, Brighton, UK
[ai] Centre for Medical Image Computing (CMIC), Faculty of Engineering Science, University College London, London, UK

ARTICLE INFO

Keywords:
Arterial spin labeling
Image processing
Multi-center
Cerebral perfusion
Quality control

ABSTRACT

Arterial spin labeling (ASL) has undergone significant development since its inception, with a focus on improving standardization and reproducibility of its acquisition and quantification. In a community-wide effort towards robust and reproducible clinical ASL image processing, we developed the software package ExploreASL, allowing standardized analyses across centers and scanners.

The procedures used in ExploreASL capitalize on published image processing advancements and address the challenges of multi-center datasets with scanner-specific processing and artifact reduction to limit patient exclusion. ExploreASL is self-contained, written in MATLAB and based on Statistical Parameter Mapping (SPM) and runs on multiple operating systems. To facilitate collaboration and data-exchange, the toolbox follows several standards and recommendations for data structure, provenance, and best analysis practice.

ExploreASL was iteratively refined and tested in the analysis of >10,000 ASL scans using different pulse-sequences in a variety of clinical populations, resulting in four processing modules: Import, Structural, ASL, and Population that perform tasks, respectively, for data curation, structural and ASL image processing and quality control, and finally preparing the results for statistical analyses on both single-subject and group level. We illustrate ExploreASL processing results from three cohorts: perinatally HIV-infected children, healthy adults, and elderly at risk for neurodegenerative disease. We show the reproducibility for each cohort when processed at different centers with different operating systems and MATLAB versions, and its effects on the quantification of gray matter cerebral blood flow.

ExploreASL facilitates the standardization of image processing and quality control, allowing the pooling of cohorts which may increase statistical power and discover between-group perfusion differences. Ultimately, this workflow may advance ASL for wider adoption in clinical studies, trials, and practice.

List of abbreviations

ASL	arterial spin labeling
BIDS	Brain Imaging Data Structure
CAT	Computational Anatomic Toolbox
CBF	cerebral blood flow
CoV	coefficient-of-variation
CSF	cerebrospinal fluid
DARTEL	Diffeomorphic Anatomical RegisTration using Exponentiated Lie algebra
EPI	echo-planar imaging
FLAIR	fluid-attenuated inversion recovery
FoV	field-of-view
GM	gray matter
GRASE	GRadient And Spin Echo
GUI	graphical user interface
MRI	magnetic resonance imaging
OS	operating system
PCASL	pseudo-continuous ASL
PET	positron emission tomography
pGM	gray matter partial volume
PLD	post-labeling delay
PSF	point spread function
PV	partial volume
PVC	partial volume correction
QC	quality control
ROI	region of interest
SD	standard deviation
SNR	signal-to-noise ratio
SPM	Statistical Parameter Mapping
VBA	voxel-based analysis
WM	white matter
WMH	white matter hyperintensity

1. Introduction

Arterial spin labeling (ASL) is a non-invasive magnetic resonance imaging (MRI) technique with the potential of providing absolute quantification of cerebral perfusion *in vivo*. Since its inception almost three decades ago in 1990 (Detre et al., 1992), ASL-based perfusion imaging has undergone important development in the technical, standardization, and clinical domains and has been increasingly used in basic neuroscience and clinical studies. The initial technical developments, such as the prolongation of the post-labeling delay in 1996 (Alsop and Detre, 1996), background suppression in 1999 (Alsop and Detre, 1999; Ye et al., 2000), and pseudo-continuous labeling in 2005 (Dai et al., 2008) were geared toward improving the signal-to-noise ratio (SNR) of ASL images.

These technical improvements gave way to the validation of the clinical applicability of ASL (Deibler et al., 2008), evaluation of multi-center reproducibility (Petersen et al., 2010; Mutsaerts et al., 2015), and comparison with [^{15}O]-H_2O positron emission tomography (PET) (Heijtel et al., 2014). Several reproducibility studies showed that conventional ASL techniques had developed to the point where the intrinsic variance of the acquisition itself (Chen et al., 2011b; Gevers et al., 2011; Heijtel et al., 2014; Mutsaerts et al., 2014b) was close to or below physiological variance of perfusion (Joris et al., 2018; Clement et al., 2018).

These advances enabled proof-of-principle studies using small clinical datasets, such as patients with cerebrovascular and neurodegenerative diseases (Detre et al., 1998; Alsop et al., 2000), epilepsy (Liu et al., 2001),

[1] authors contributed equally to this work.

brain tumors (Warmuth et al., 2003), as well as pharmacological applications (Wang et al., 2011; MacIntosh et al., 2008; Handley et al., 2013). Following the consensus recommendations for the acquisition and quantification of ASL images (Alsop et al., 2015), ASL became ready for large multi-center observational studies and clinical trials (Jack et al., 2010; Almeida et al., 2018; Blokhuis et al., 2017).

However, despite the consensus in clinical implementation and image acquisition (Alsop et al., 2015), ASL image processing (Wang et al., 2008; Shin et al., 2016; Melbourne et al., 2016; Chappell et al., 2010; Li et al., 2019; Mato Abad et al., 2016; Bron et al., 2014) remains disparate among research laboratories. In previous ASL studies, detailed description of all processing steps is often lacking. Clinical studies are often performed without proper quality control (QC) or with arbitrary QC metrics. This hampers both the interpretation and reproducibility of individual studies as well as meta-analyses of multiple studies. A consensus on the best practices to robustly process ASL data would facilitate comparison of results across centers and studies, avoid duplicate development, and speed up the translation into clinical practice, as is advocated by the Open Source Initiative for Perfusion Imaging (OSIPI) (www.osipi.org).

For these reasons, the software package ExploreASL was initiated through the COST-action BM1103 ″ASL In Dementia” (https://asl-network.org/) with the aim of developing a comprehensive pipeline for reproducible multi-center ASL image processing. To date, ExploreASL has been used in more than 30 studies consisting of more than 10,000 ASL scans from three MRI vendors - GE, Philips, Siemens, with pulsed ASL and pseudo-continuous ASL (PCASL) sequences, see the list of studies in the Supplementary material. The primary aims of ExploreASL are to increase the comparability and enable pooling of multi-center ASL datasets, as well as to encourage and facilitate cross-pollination between clinical investigators and image processing method developers.

2. Theory: Software overview

ExploreASL is developed in MATLAB (MathWorks, MA, USA, tested with versions 2011–2019) and uses Statistical Parametric Mapping 12 routines (SPM12, version 7219) (Ashburner et al., 2012; Flandin et al., 2008). Here, we describe the implementation of ExploreASL version 1.0.0, which is available for free for non-commercial use on www.ExploreASL.org or at https://github.com/ExploreASL/ExploreASL. ExploreASL provides a fully automated pipeline that comprises all the necessary steps from data import and structural image processing to cerebral blood flow (CBF) quantification and statistical analyses. Unique features of ExploreASL include:

- Self-contained software suite: all third-party toolboxes are included in the installation, compatible with Linux, macOS, Windows, and Windows Subsystem for Linux and supporting multi-threading; ExploreASL requires a Matlab installation to run interactively but a compiled version of ExploreASL is also available. The system requirements are a single-core CPU, 4 Gb RAM, minimum 1 Gb free disk space. When running multiple instances of ExploreASL in parallel, 2.5 Gb RAM and 1 Gb disk space is recommended per instance;
- Flexible data import from different formats including (enhanced) DICOM, Siemens MOSAIC variant, Philips PAR/REC, NIfTI and Brain Imaging Data Structure (BIDS) (Gorgolewski et al., 2016), with automatic detection of control-label or label-control order;
- Data management: anonymization, compression of image files, and optional defacing;
- Modular design: automatically iterates over all available subjects and scans, allows investigators to change/replace each sub-module, allows to suspend and resume processing at any point - pipeline steps are tracked using a system of lock and status files. Before executing a submodule for a given subject and session, a lock file is created to avoid parallel access to the data. When the submodule is finished, the lock file is removed and a status file is created. When the pipeline is restarted - e.g. after a computer or program crash - the already processed steps are skipped;
- Image processing optimized for: multiple centers, different ASL implementations from GE/Philips/Siemens (Mutsaerts et al., 2018), both native/standard-space analysis, advanced ASL markers – e.g. spatial coefficient-of-variation (CoV) (Mutsaerts et al., 2017), asymmetry index (Kurth et al., 2015), and partial volume correction (PVC) (Asllani et al., 2008);
- ‘Low quality’ option allowing for quick pipeline testing by running all image processing with fewer iterations and lower spatial resolution;
- Extensive QC and data provenance: visual QC for all intermediate and final images, comparison with perfusion templates from different ASL implementations, progress report with processing history (provenance).

ExploreASL requires the following input data: ASL and T1-weighted (T1w) images, and optionally FLAIR and M0 scans. Other options are binary images with lesion masks and additional ROIs either in the T1w or FLAIR space. The ASL acquisition parameters that cannot be extracted from the DICOM data (e.g. PLD, labeling duration) need to be provided in either a study-configuration file or a JSON sidecar. As output, ExploreASL provides the processed structural and quantified CBF NIfTI files in the T1w and ASL native space, as well as in the standard space, see Supplementary Fig. 1. Detailed information for users, including a manual, a step-by-step walkthrough, and video tutorials, is provided on the ExploreASL website www.ExploreASL.org.

In the following sections, we review each processing step of the four ExploreASL modules as outlined in Fig. 1 and summarized in Table 1. Each section starts with a brief methodological review including the rationale within the context of ASL processing, followed by a detailed description of the ExploreASL implementation, and ending with a discussion of emerging developments and potential future improvements.

3. Theory: Implementation

3.1. Import module

To avoid manual restructuring of arbitrary data structures from the scanner or other sources (Nichols et al., 2017), ExploreASL uses a flexible input data/directory description scheme based on regular expressions and converts the data to a BIDS-compatible data structure (Gorgolewski et al., 2016); the full BIDS ASL extension is currently in development (bids.neuroimaging.io). The input images can be NIfTI format, conventional or enhanced DICOM, Philips PAR/REC, or Siemens mosaic format, which are then converted to NIfTI using dcm2niiX, taking into account vendor-specific scale slopes in private tags (Li et al., 2016). ASL images can be provided as control-label time-series, a single perfusion-weighted image, or an already quantified CBF image, from any 2D or 3D readout schemes, and from any MRI vendor. Before an image is processed, ExploreASL first computes and aligns the center-of-mass of each image to the origin of the world coordinates to deal with potentially incorrectly stored orientations. A tolerance of 50 mm is used for the center-of-mass offset to avoid resetting correct initial alignments. Additionally, ExploreASL provides an overview of missing and unprocessed files, automatically detects the order of control and label images from the image intensities, and checks the DICOM tags of repetition and echo time and scale factors/slopes across individuals.

3.2. Structural module

This module processes the structural images by the following steps: 2.1) segments the white matter (WM) hyperintensities (WMH) on fluid-attenuated inversion recovery (FLAIR) images and uses them to fill the corresponding WM hypointensities on the T1w images, 2.2) the structural images are subsequently segmented into gray matter (GM), white matter, and cerebrospinal fluid (CSF) maps, and 2.3) normalized to the

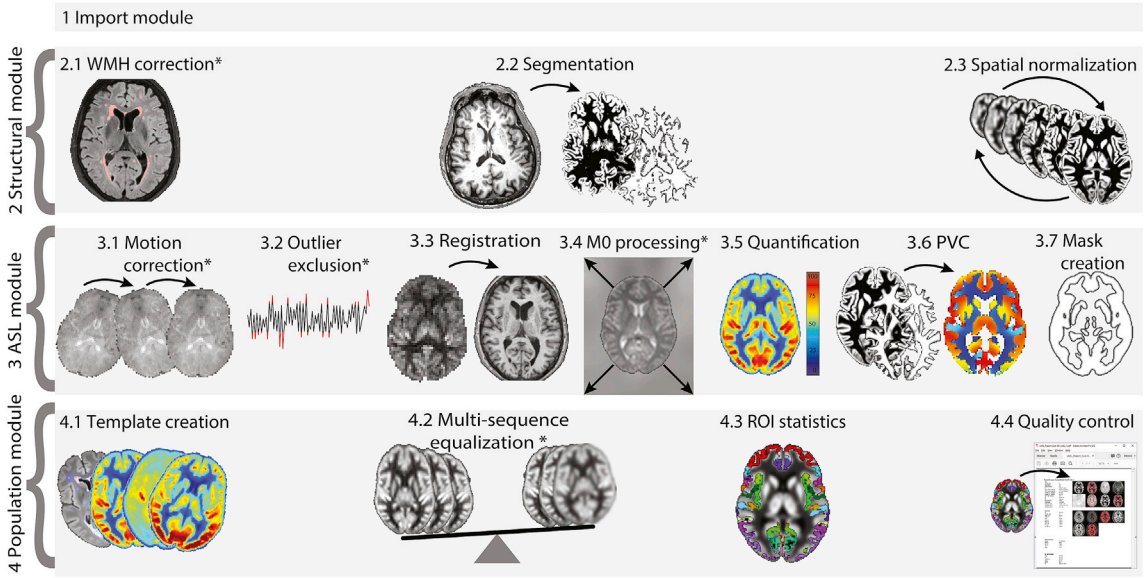

Fig. 1. Schematic diagram of ExploreASL processing steps. Steps marked with a * are optional, e.g. when FLAIR, ASL time-series, or M0 scans are available. PVC = partial volume correction, ROI = regions of interest, WMH = white matter hyperintensity. The population module can be run on a single subject level, as well as on one or multiple populations/centers/cohorts or other groups.

MNI standard space (Evans et al., 2012). The segmentations are used to obtain tissue partial volume (PV) fractions for computation of CBF (Asllani et al., 2008). The registration transformations are used to bring ASL images acquired from different sessions and/or different subjects in the same space and thus facilitate visual comparison in the same space, automatic QC, as well as group analysis.

3.2.1. *WMH correction*

The presence of WMH can affect the GM/WM classification of T1w images in two ways: 1) WMH themselves can be incorrectly segmented as GM, 2) image intensities of WMH bias global modeling of GM and WM intensity distributions (Pareto et al., 2016; Battaglini et al., 2012). ExploreASL alleviates these complications by lesion-filling the T1w image before initiating the segmentation (Battaglini et al., 2012): voxel intensities in the hypointense WMH regions on the T1w images are replaced by bias field-corrected values from the surrounding, normal-appearing WM (Chard et al., 2010) (Fig. 1). The Lesion Segmentation Toolbox (LST, version 2.0.15) is used because of its empirically proven robustness, scanner independence, and non-reliance on the requirement of a training set (de Sitter et al., 2017a). LST detects outliers in the FLAIR WM intensity distribution and assesses their likelihood of being WMH (Schmidt et al., 2012). While ExploreASL offers the option of both LST lesion growing and lesion prediction algorithms, the default is set to the latter, which has been shown to be more robust (de Sitter et al., 2017a). This WHM correction described here is only performed when FLAIR images are available.

3.2.2. *Segmentation*

To segment the 3 main tissue classes GM, WM, and CSF, ExploreASL uses the Computational Anatomy Toolbox 12, release 1363 (CAT12, the successor of VBM8) (Gaser et al., 2009) for SPM12. CAT12 allows local variations in the tissue intensity distributions, making it more robust to the presence of pathology such as tumors, edema, and WM lesions (Battaglini et al., 2012; Petr et al 2018b) (Supplementary Fig. 2). CAT12 has been shown to outperform other available methods such as FreeSurfer v5.3.0, FSL v5.0, and SPM12 (Mendrik et al., 2015). The CAT12 segmentation algorithm is based on improvements of Unified Segmentation (Ashburner et al., 2005), two essential improvements being that it allows spatially varying GM-WM intensity distributions, and provides PV maps rather than posterior probability maps (Tohka et al., 2004).

3.2.3. *Spatial normalization*

For non-linear registration to MNI space ExploreASL uses Geodesic Shooting (Ashburner et al., 2011) - the successor of Diffeomorphic Anatomical RegisTration using Exponentiated Lie algebra (DARTEL) (Ashburner et al., 2007) - within the CAT12 toolbox (Gaser et al., 2009). The reason for this choice is that CAT12 has a single subject implementation using the IXI adult template, brain-development.org/ixi-dataset. Optionally, new templates can be created by these SPM toolboxes on a population level, e.g. for populations where an adult template is not sufficient. Although alternative methods (Klein et al., 2010) may outperform DARTEL/GS in specific populations, the default settings of DARTEL and Geodesic Shooting are sufficiently tested in clinical studies to provide adequate performance across different populations and scanners (Ripollés et al., 2012).

We adapted the CAT12 segmentation algorithm to offer the possibility to input customized segmentations of structural lesions such as space-occupying lesions or cerebral infarcts such that the lesion region is ignored by the non-linear registration (Crinion et al., 2007) (Supplementary Fig. 3).

ExploreASL offers the option to register longitudinal ASL studies with the SPM12 module for longitudinal registration (Ashburner and Ridgway, 2012), which takes the similarity between structural images from the same subjects into account. The first time point is used as a reference for both within- and between-subject registration. However, this requires further validation in the presence of large brain deformations between sessions, such as tumors, resections, or infarcts (Petr et al 2018b).

3.3. *ASL module*

This module processes the ASL images by 3.1) correcting for motion, 3.2) removing outliers, 3.3) registering with the structural data, and by 3.4) processing the M0 images. Then, 3.5) the CBF is quantified with correction for hematocrit and vascular artifacts, after which 3.6) the PV effects are corrected for. All image processing described below is performed in native space, unless stated otherwise. All intermediate and final images are also transformed into standard space for QC and group analyses.

3.3.1. *Motion correction*

The adverse effects of head motion can be partly alleviated by

Table 1
Overview of image processing steps and implementation in ExploreASL.

Processing step	ExploreASL implementation	Specifics, optional features
1. Import module		
1.1 Data import	dcm2niiX	Converts DICOM to NIfTI, supports MOSAIC, PAR/REC, BIDS
2. Structural module		
2.1 WMH correction	LST2 (r2.0.15) - LPA (LGA optional)	Segments WMH and fills lesions on T1w; improves T1w segmentation
2.2 Segmentation	CAT12 (r1363)	Outputs partial volume maps; supports lesion cost function masking
2.3 Spatial normalization	Geodesic Shooting	Uses CAT12 template, supports creation of study-specific templates
3. ASL module		
3.1 Motion correction	SPM12 realign	Realigns ASL control/label images to mean position, uses a zig-zag control-label regressor
3.2 Outlier exclusion	ENABLE	Removes motion peaks, uses tSNR optimization
3.3 Registration	SPM12 rigid-body	Registers ΔM-pGM or M0-T1w
3.4 M0 processing	M0 image	Masks, smooths, extrapolates M0 to avoid division artifacts
3.5 CBF quantification	Consensus paper model	Computes CBF based on the single compartment model, single PLD; supports dual compartment
3.6 PVC	Linear regression	Performs PVC on kernel or ROI basis, optionally estimates the effective spatial resolution/PSF of ASL
3.7 Analysis mask creation	Combine individual masks	Combines FoV, susceptibility artifacts and vascular artifacts, use $p > 0.95$ of population masks
4. Population module		
4.1 Template creation	Final images	Calculates population mean, SD, CoV, SNR, also for intermediate images
4.2 Multi-sequence equalization	Remove residual sequence-specific effects	Equalizes bias fields, spatial CoV, and smoothness, uses sequence-specific templates
4.3 ROI statistics	CBF and spatial CoV, with or without PVC	Uses MNI structural, Harvard-Oxford, Hammers, and custom atlases
4.4 Quality control	Single-subject PDF report	Performs QC of images, DICOM values, volumetrics, motion etc. Outputs population report in TSV files

ASL = arterial spin labelling, BIDS = Brain Imaging Data Structure, CAT = Computational Anatomic Toolbox, CBF = cerebral blood flow, CoV = coefficient of variation, ΔM = perfusion-weighted difference image, dcm2niiX (Li et al., 2016), DICOM = Digital Imaging and COmmunications in Medicine, ENABLE = ENhancement of Automated BLood flow Estimates, FoV = field-of-view, LGA = Lesion Growth Algorithm, LPA = Lesion Prediction Algorithm, LST = Lesion Segmentation Toolbox, MNI = Montreal Neurological Institute, NIfTI = Neuro-Imaging Informatics Technology Initiative, QC = quality control, pGM = gray matter partial volume, PLD = post-labeling delay, PSF = point spread function, PVC = partial volume correction, r = release, ROI = region of interest, SD = standard deviation, SNR = signal-to-noise ratio, SPM = Statistical Parametric Mapping, tSNR = temporal SNR, tsv = tab-separated value, WMH = white matter hyperintensity, Zig-zag = "zig-zag" regressor.

correcting for motion using image processing (Alsop et al., 2015). Traditionally, head motion is estimated assuming a 3D rigid-body transformation with a sum-of-squares cost function (Wang et al., 2008; Mato Abad et al., 2016). However, because the average control-label intensity difference can be partly interpreted by the algorithm as motion, some investigators perform motion estimation separately for the control and labeled images (Wang et al., 2008). Instead, in ExploreASL, an adaptation of the SPM12 motion correction is used, which minimizes apparent motion attributable to the control-label intensity difference from the estimated motion parameters using a "zig-zag" regressor (Wang et al., 2012) (Supplementary Fig. 4).

3.3.2. Outlier exclusion

Despite motion correction, large motion spikes can still have a significant negative effect on the ASL image quality, especially when they occur between control and label images (Wang et al., 2008). In fMRI literature, peak motion relative to mean individual motion is often excluded based on a set threshold, e.g. RMS of 0.5 of the voxel size (Power et al., 2012). ExploreASL uses a threshold-free method named ENhancement of Automated BLood flow Estimates (ENABLE) (Shirzadi et al., 2015), which sorts control-label pairs by motion and cumulatively averages them until the addition of further pairs significantly decreases the temporal voxel-wise signal stability (Supplementary Fig. 5). The ExploreASL implementation of ENABLE employs the median GM voxel-wise temporal SNR (tSNR) as the criterion for signal stability (Shirzadi et al., 2018), regularized by an empirically defined minimum tSNR improvement of 5%. ENABLE can also remove non-motion-related outliers, since other acquisition artifacts can be picked up by the motion estimation algorithm (Supplementary Fig. 5). ExploreASL also relies on the fact that ENABLE (Shirzadi et al., 2018) also partly removes outliers, as it operates relatively independent of (patho-)physiological changes of the signal intensity in the pairwise subtracted images (Robertson et al., 2017; Li et al., 2018b).

3.3.3. Registration

Accurate registration between the ASL and structural space is a critical step as registration errors are propagated to subsequent stages and analyses of CBF data. Specifically, the relatively large CBF differences between GM, WM, and CSF, mean that small misalignments can have a large impact on the accuracy of tissue-specific CBF quantification (Mutsaerts et al., 2018).

The image registration steps implemented in ExploreASL are based on a previous study in which the performance of several registration options were compared (Mutsaerts et al., 2018). Briefly, the registration of ΔM to gray matter partial volume (pGM) outperformed the registration of M0 to T1w, except for cases where the ΔM contrast was dissimilar to the pGM contrast (e.g. vascular artifacts, labeling artifacts, perfusion pathology). Rigid-body transformation proved to be a robust default choice (Mutsaerts et al., 2018), especially in the presence of pathology (Wang et al., 2008; Macintosh et al., 2010). Therefore, ExploreASL initializes the registration with a M0-T1w registration, after which it performs a ΔM-pGM rigid-body registration by default. The latter is disabled when macrovascular signal predominates tissue signal (spatial CoV above 0.67) (Mutsaerts et al., 2018). However, using the M0-T1w-only option is recommended for 2D PASL without background suppression due to a possible presence of additional artifacts (Supplementary Fig. 6). Note that such images are typically excluded from CBF statistics and only included when analyzing vascular parameters, such as the spatial CoV.

The rigid-body transformation does not account for the geometric distortion typical for 2D echo-planar imaging (EPI) or 3D GRadient And Spin Echo (3D GRASE) ASL images (Gai et al., 2017). Such deformations can be partially corrected with B0 field maps or M0 images with reversed phase-encoding direction (Madai et al., 2016) - which is implemented as option in ExploreASL by calling FSL TopUp (Andersson et al., 2003). Affine and uniform non-linear transformations, such as FNIRT or SPM's 'unified segmentation' (Klein et al., 2009) can outperform the rigid-body transformation in the ΔM-pGM registration (Petr et al 2018a), although this remains to be validated in the presence of pathology.

3.3.4. M0 processing

The difference in ASL control-label signal is proportional to CBF with the equilibrium magnetization (M0) of blood acting as a scale factor. Ideally, blood M0 would be measured in voxels containing only arterial blood, but that is not usually possible due to the relatively low spatial resolution of ASL images. Instead, M0 is calculated from either the brain

tissue or CSF signal intensity (Çavuşoğlu et al., 2009). The use of the tissue-based M0 is recommended (Alsop et al., 2015) because of its ability to account for acquisition-specific effects such as variations in receive coil inhomogeneity or T2(*) weighting. For these reasons, ExploreASL by default processes an M0 image, and optionally supports the use of a single CSF M0 value (Çavuşoğlu et al., 2009; Pinto et al., 2020).

ExploreASL aims to deliver consistent M0 quantification for multi-center populations with M0-scans acquired at different repetition time and different effective resolutions. ExploreASL smooths the M0 image with a 16 mm FWHM Gaussian (Beaumont, 2015) after it has been masked for WM (Supplementary Figs. 7-8) and rescaled to the mean GM M0 to account for B1 differences between GM and WM. This approach reduces the M0 image into a smooth bias field with the same smoothness/effective resolution for all ASL sequences and participants, and optimal SNR, while still canceling out acquisition-specific B1-field related intensity inhomogeneity. This makes the M0 image more robust and less sensitive to misalignment, and thus more consistent between ASL sequences (Mutsaerts et al., 2018) and individuals (Deibler et al., 2008). ExploreASL has the option to additionally mask the M0 bias-field for lesions that affect the M0 - e.g. brain tumors - and interpolate the M0 signal from the relatively unaffected brain regions (Croal et al., 2019).

3.3.5. CBF quantification

An in-depth overview of ASL CBF quantification has been provided previously (Alsop et al., 2015; Chappell et al., 2018). The previously recommended single compartment model assumes that the label decays with arterial blood T1 only (Alsop et al., 2015). Although a two-compartment model can provide CBF values that are in closer agreement with [^{15}O]-H_2O PET (Heijtel et al., 2014), this is often not feasible when blood T1, tissue T1, and micro-vascular arterial transit time are unknown, or would result in a constant scaling factor when assuming literature values. For these reasons, ExploreASL uses the single compartment model by default, and offers the two-compartment model and/or the possibility to provide the hematocrit or blood T1 values as an optional feature.

The ASL label relaxes with the T1 of blood, a parameter that depends on hematocrit (Hales et al., 2016). Not taking hematocrit or blood T1 into account can lead up to 10–20% CBF overestimation for hematocrit as low as 17% (Vaclavu et al., 2016). Accounting for hematocrit is particularly relevant for between-group or longitudinal hematocrit changes e.g. due to treatment, which can be expected in certain populations or diseases (De Vis et al., 2014). ExploreASL allows to adjust for individual arterial blood T1 by either providing its value directly (Li et al., 2017) or by providing the hematocrit value and computing the blood T1 (Hales et al., 2016). As hematocrit and blood T1 measurements can be noisy - especially when obtained at different laboratories - a pragmatic approach is to apply the average blood T1 correction on a population rather than on an individual level (Elvsåshagen et al., 2019). Additionally, hematocrit and blood T1 can be modeled based on age and sex (Hales et al., 2014), but this requires validation. Note that after correcting the above-mentioned methodological effect, hematocrit might be still associated with CBF physiologically: hematocrit decreases or increases causing compensatory hyper- or hypoperfusion. Also note that the implemented blood T1w estimation based on hematocrit on average leads to a higher blood T1 than the recommended 1.6s (Hales et al., 2016; Alsop et al., 2015). Therefore, it is not recommended to use scan-specific quantification parameters only for some scans and not for all, as this will introduce a quantification bias.

3.3.6. Partial volume correction

Since the spatial resolution of ASL is relatively low, a typical ASL voxel contains a mixture of GM, WM, and CSF signal, which is referred to as partial volume effects. As the GM-WM CBF ratio is reported to lie between 2 and 7 (Asllani et al., 2008; Pohmann, 2010; Zhang et al., 2014; Law et al., 2000), the tissue partial volume in each voxel has a large influence on the ASL measurement (Supplementary Fig. 9). For these reasons, PVC (Asllani et al., 2009) is essential in studies that aim to differentiate structural changes (e.g. atrophy) from perfusion changes (e.g. related to neurovascular coupling) (Steketee et al., 2016). Several PVC algorithms have been proposed (Chappell et al., 2010; Zhao et al., 2017; Asllani et al., 2008; Liang et al., 2013), which assume locally homogeneous GM and WM CBF. Instead in some studies, GM volume is used as a covariate in the statistical analysis (Chen et al., 2011a). Note that while PVC, in theory, corrects only for the PV effects and takes into account the intra- and inter-subject variability of the GM-WM CBF ratio, GM covariation can additionally affect the estimated physiological correlation between GM CBF and GM volume (Petr et al 2018a).

ExploreASL employs two versions of PVC, both based upon the most frequently used PVC, i.e. linear regression (Asllani et al., 2008): 1) a 3D Gaussian instead of a 2D flat kernel (default, referred to as "voxel-wise") (Oliver, 2015), or 2) computing PV-corrected CBF within each anatomical or functional region of interest (ROI) separately instead of using a kernel. Whereas the voxel-wise option allows further voxel-based analysis (VBA), the ROI-based PVC is in theory beneficial for a ROI-based analysis as effectively the kernel-size is selected based upon the anatomical ROI, which should be less sensitive to local segmentation errors. Moreover, it avoids cross-talk between ROIs. It still needs to be investigated how to define regions of optimal shape with respect to PVC performance, which depends on the spatial uniformity and SNR of the GM and WM CBF, and partial volume distributions within the ROI. To evaluate the effects of PVC, ExploreASL exports CBF maps and ROI values both with and without PVC.

For proper PVC or ROI definition, the true acquisition resolution - which often differs from the reconstructed voxel size - needs to be taken into account (Petr et al., 2018). This is especially important for 3D readouts, where the through-plane PSF can be up to 1.9 times the nominal voxel-size (Vidorreta et al. 2013, 2014). Effects such as motion (Petr et al., 2016) and scanner reconstruction filters can contribute to further widening of the PSF of the final image. ExploreASL by default uses previously estimated true acquisition resolutions (Vidorreta et al. 2013, 2014; Petr et al., 2018) and can optionally perform a data-driven spatial resolution estimation (Petr et al., 2018) that is generalizable to all ASL acquisitions. Contrary to alternative PSF estimations based on temporal noise autocorrelation (Cox, 2012) or simulations of the acquisition PSF (Vidorreta et al. 2013, 2014), this method does not require time series and inherently accounts for other sources of blurring (e.g. smoothing by motion and/or image processing) and is applicable without having detailed information about the sequence parameters needed to calculate the resolution from the k-space trajectory. However, this method requires further validation, especially in the presence of ASL image artifacts.

Lastly, the GM/WM maps obtained from the high-resolution structural images need to be downsampled to the ASL resolution before they are used for PVC or for ROI delineation in native space. A trivial interpolation to lower resolution may introduce aliasing, which can be addressed by applying a Gaussian filter - or a convolution with the PSF, if the PSF is known - prior to downsampling (Cardoso et al., 2015). It is important to note that the ASL image often has an anisotropic resolution and may be acquired at a different orientation compared to the structural image. To correct for this effect, ExploreASL pre-smooths the structural images with a Gaussian kernel of which the covariance matrix takes the orientation and PSF differences between the ASL and structural images into account (Cardoso et al., 2015).

3.3.7. Analysis mask creation

For the statistics performed in section 4.3 - as well as for any voxel-based group statistics - an analysis mask aims to exclude voxels outside the brain or voxels with artifactual signal (e.g. macro-vascular, signal dropout) and restrict the analysis to regions with sufficient SNR and/or statistical power. This also avoids over-penalizing statistical power by family-wise error corrections. The susceptibility and field-of-view (FoV) masks are combined in section 4.3 into a group mask. The vascular masks

are applied subject-wise to reflect the individual differences in vascular anatomy.

First, regions outside of the ASL FoV are identified, as whole brain coverage is not always achieved (Supplementary Fig. 10). Second, a mask is created to remove voxels with intravascular signal. While intravascular signal - resulting from an incomplete tissue arrival of labeled spins - can be clinically useful (Mutsaerts et al., 2017, 2020), it biases regional CBF estimates. The relatively large local temporal variability of such vascular artifacts can be detected in time series, in multi-post-labeling delay (PLD) acquisitions (Chappell et al., 2010) or by an independent component analysis (ICA) (Hao et al., 2018). ExploreASL uses a pragmatic vascular artifact detection approach that is suitable for both single and multi-PLD ASL images. It identifies clusters of negative apparent CBF (Maumet et al., 2012) and voxels with extreme positive apparent CBF (Supplementary Fig. 11). First, spatially connected subzero voxels are grouped into clusters. The average CBF of each cluster is obtained, and clusters with significant negative mean CBF are isolated (median - 3 median absolute difference (MAD) within all subzero CBF voxels) (Supplementary Fig. 11b). Likewise, voxels with extreme positive signal are detected by having intensity of more than median +3 MAD within all positive CBF voxels (Supplementary Fig. 11b). One potential caveat of masking out vascular voxels is the violation of the stationarity criterion of parametric voxel-wise statistics. While excluding voxels with high signal can violate the stationarity criterion of the ASL signal, there is currently no validated method that would be able to reliably estimate the perfusion and vascular signal contribution in such voxels from single-PLD data. Note that the detected voxels with negative or extreme positive signal may also stem from non-vascular artifacts such as head motion.

Second, regions with susceptibility signal-dropout artifacts are removed. Regions frequently having low SNR for 2D EPI and 3D GRASE ASL include the orbitofrontal cortex near the nasal sinus and the inferior-medial temporal gyrus near the mastoid air cavities. Therefore, the option implemented in ExploreASL is to use sequence-specific template masks obtained from previous population analyses, after which individual masks are restricted to $(pGM + pWM) > 0.5$ to remove voxels outside the brain. Further development is needed to create masks that take individual anatomical differences in skull and air cavities into account. Noteworthy, ExploreASL applies this analysis mask only for analyses, not for visual QC.

3.4. Population module

This module prepares output for visual QC and creates group-level results for statistical analyses. Whereas the above-described Structural and ASL modules perform image processing on the individual level, this module performs its analysis on multiple-subjects and/or multi time-point level. For this purpose, ASL images are transformed into standard space using the T1w transformation fields smoothed to the effective spatial resolution of ASL. For transformation of all intermediate and final images, all previous spatial transformations are merged into a single combined transformation to minimize accumulation of interpolation artifacts through the pipeline. Partial volumes of GM and WM obtained from anatomical images are multiplied by the Jacobian determinants of the deformation fields - a.k.a. modulation - to account for voxel-volume changes when transforming to standard space (Ashburner and Friston, 1999). The standard space used by ExploreASL is the $1.5 \times 1.5 \times 1.5$ mm3 IXI555-MNI152 space (Gaser, 2009), which is a refined version of the MNI152 space with additional geodesic shooting-based template creation for the IXI555 population (Ashburner and Friston, 2011).

3.4.1. Template creation

Population templates can reveal population- or sequence-specific perfusion patterns that are not visible on the individual level. ExploreASL generates the mean and between-subject standard deviation (SD) images for the total study population and, optionally, for different sets (e.g. different centers/sequences/cohorts) within the study (Fig. 2). In addition to CBF itself, auxiliary images (e.g. M0), intermediate images (e.g. mean control images), or QC images (e.g. temporal SD) can provide a valuable overview of the data, for example when comparing data originating from different centers.

3.4.2. Multi-sequence equalization

Quantitative CBF images can differ between centers because of a number of hardware, labeling, and readout choices implemented by different MRI vendors and/or laboratories (Deibler et al., 2008; Heijtel et al., 2014; Alsop et al., 2015; Jack et al., 2010). Some of these differences can be accounted for, as detailed in the previous sections. However, until a more robust procedure is devised - e.g. the use of a flow phantom (Oliver-Taylor et al., 2017) - a pragmatic approach is required to remove the remaining CBF quantification differences between sequences, scanner types, and centers (Mutsaerts et al. 2018, 2019). ExploreASL optionally performs spatially varying intensity normalization by computing a smooth average CBF bias field for each ASL sequence (Supplementary Fig. 12). Noteworthy, this step assumes that the demographics and expected (patho-)physiological effects are equally distributed across the subjects scanned with each sequence, scanner, and/or site. To fulfill this assumption, it is advisable to estimate these biasfields based on images of healthy controls (Mutsaerts et al., 2018). However, this is often not feasible due to relative high physiological variability of CBF and relative small size of the control groups. Using ASL images from all participants including patients is a viable alternative (Mutsaerts et al., 2019), provided that the distribution of demographics and expected patho(-physiology) effects on perfusion are comparable between sequences. The final CBF images in the standard space are smoothed with an $8 \times 8 \times 8$ mm full-width at half-maximum Gaussian, and averaged to create a sequence/scanner type/site-specific mean CBF image. These site-specific CBF images averaged over all subjects are intensity normalized to GM CBF of 60 mL/100g/min and further averaged to create a general mean CBF image of all sites. The site-specific bias field is calculated by dividing the general mean with the site-specific mean CBF image. The individual CBF images of each site are multiplied by their site-specific bias to adjust for between-site differences (Mutsaerts et al., 2018).

3.4.3. ROI statistics

In ExploreASL, ROI masks are created by combining existing atlases with individual GM and WM masks. The GM atlases currently implemented are: (i) MNI structural (Mazziotta et al., 2001), (ii) Harvard-Oxford (Desikan et al., 2006), and (iii) Hammers (Hammers et al., 2002). A deep WM atlas is created by eroding the SPM12 WM tissue class by a 4 voxel sphere (i.e. 6 mm), to avoid signal contamination from the GM (Mutsaerts et al., 2014a). Other existing, or custom, atlases can be easily applied. The Online Brain Atlas Reconciliation Tool (OBART) at obart.brainarchitecture.org (Bohland et al., 2009) provides an overview of the overlap and differences between atlases. For each ROI, statistics are calculated separately within the left and right hemisphere, as well as for the full ROI; both with and without PVC, and both in the standard space and subject's native space. The same CBF statistics are also calculated for user-provided ROIs and lesion masks, as well as for the 25 mm margin around the ROI/lesion (Moghaddasi et al., 2015), for the ipsilateral hemisphere excluding the lesion, and for the same three masks at the contralateral side. Subject-specific ROI and lesion masks are treated the same, except for the fact that lesion masks are also used for the cost function masking (see section 1.3). Individual vascular masks are used to exclude regions with intra-vascular signal (see section 3.7) from CBF statistics, but not from spatial CoV statistics.

Finally, all masks are intersected with a group-level analysis mask, created from the individual analysis masks created in section 3.7. Individual differences of these analysis masks can be caused by differences in head position, FoV, and nasal sinus size. To limit the effects of this mask heterogeneity on statistical analyses, ExploreASL creates a group-level analysis mask from standard-space voxels present in at least 95% of the

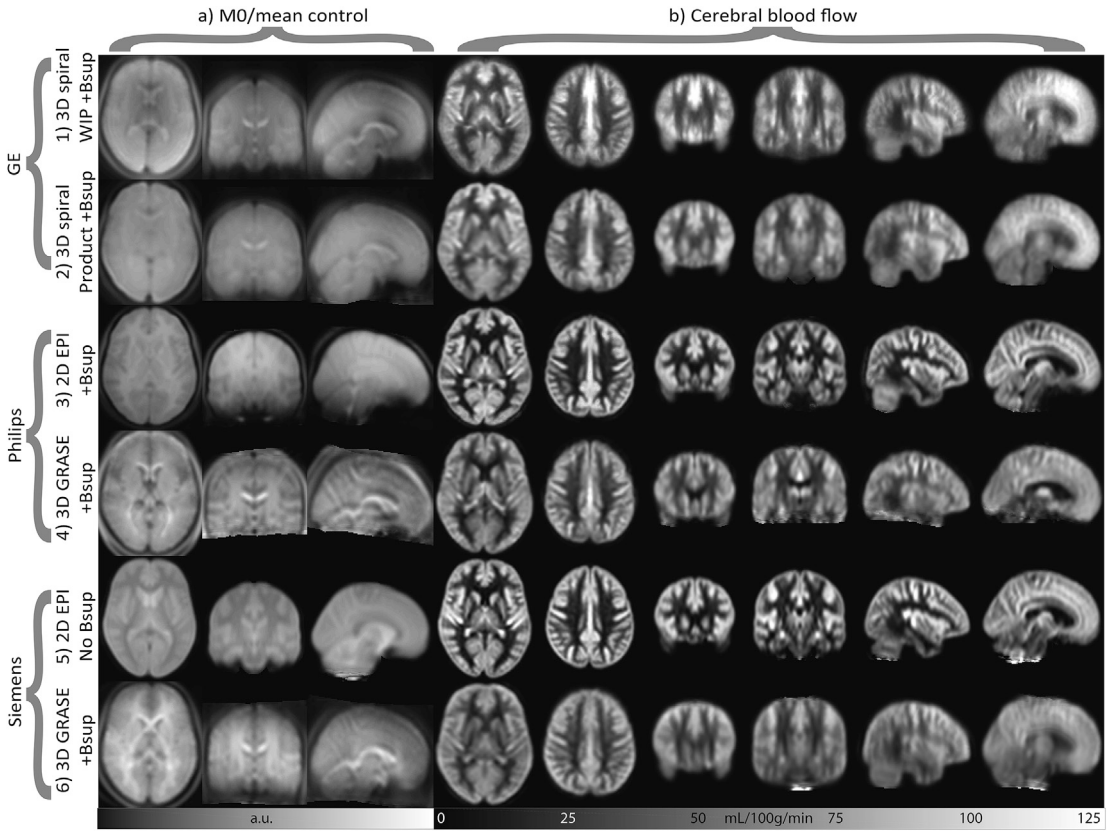

Fig. 2. Templates (population-averages from previous studies) are shown for source images (a) and CBF maps (b), for several arterial spin labeling (ASL) acquisitions with/without background suppression (Bsup) from different vendors. The average CBF images are intensity normalized to a mean total GM CBF of 60 mL/min/100 g (see Suppl Fig. 10 for the unscaled CBF images). Source images are mean control images for Philips and Siemens and M0 images for GE, which does not output control images. Note that the images differ mostly in their effective spatial resolution, orbitofrontal signal dropout, and the amount of macro-vascular artifacts. The differences in geometric distortion are mostly too subtle to be noted on these population-averages images. Note the inferior-superior gradient in the source images in the 2D EPI sequence with background suppression. a.u. = arbitrary units, Bsup = background suppression, WIP = work-in-progress pre-release version. See sequence details in Supplementary Table 1.

individuals masks (Supplementary Fig. 10).

3.4.4. *Quality control*

On a participant level, ExploreASL outputs QC parameters in a JSON file and provides unmasked images in standard space for visual QC, for both intermediate and final images (Supplementary Fig. 13) to detect technical failure, outliers and artifacts. QC parameters are also obtained by comparing individual ASL images with an atlas, a group average, or an average from a previous study. Whole-brain and regional differences larger than 2–3 SD are indicated and should be visually inspected. Deviations can hint to software updates or different scanners and, if not accounted for, can lead to low power of the statistical analyses (Chenevert et al., 2014). All QC parameters and images are also collected in a PDF file (Fig. 3, Supplementary Table 2). While these QC parameters can be helpful in detecting artifacts and/or protocol deviations, their use has not yet been validated, and the normal and abnormal range for each of the parameters still need to be determined.

4. Methods

We illustrate the ExploreASL image processing results and reproducibility for three populations with similar 2D-EPI PCASL protocols: perinatally infected HIV children, healthy adults, and elderly with mild cognitive complaints, from the NOVICE (Blokhuis et al., 2017), the Sleep (Elvsåshagen et al., 2019), and the European Prevention of Alzheimer's Dementia (EPAD) studies (Ritchie et al., 2016), respectively (Supplementary Table 3). All three studies adhered to the Declaration of Helsinki and were approved by the local ethics committees (Academic Medical Center (AMC) in Amsterdam, Norwegian South East Regional Ethics Committee, and VU Medical Center Amsterdam and University of Edinburgh, respectively). Written informed consent was obtained from all participants (or parents of children younger than 12 years for NOVICE). Each participant of the Sleep study received NOK 500 for participation.

ASL studies processed at different centers typically use different OS or software versions possibly affecting the ability to compare CBF values between studies. Additionally, longitudinal studies may be subject to updates in analysis hardware or software. The performance of image processing should thus be comparable irrespective of the used analysis software version and/or OS to allow data pooling and comparison between studies. Here, we investigated the image processing reproducibility between OSes and Matlab versions for the intermediate and final pipeline results of the three previously acquired datasets, without and with the ExploreASL-specific modifications of the SPM12, CAT12, and LST source code (modifications described below). To this end, a single participant from each study was analyzed: with the lowest GM volume from NOVICE and EPAD (GM/ICV ratio 0.41 and 0.33, respectively), and the highest GM volume (GM/ICV ratio 0.55) from the Sleep study. These three datasets were processed at two centers with the following combinations of OS and MATLAB version, twice at each center for each of the combinations: Linux-2018b (HZDR, Dresden, Germany; Linux server, 2.1 GHz Intel Xeon 6130, Ubuntu 5), Windows-2015a and 2018b (Amsterdam UMC, The Netherlands; Dell Alienware laptop, 2.9–4.3 GHz Intel i7-7820HK, Windows 10 Version, 1903). After each pipeline step, the between-system reproducibility was obtained as a difference of the image

xASL report: Philips2DEPI, EPAD-001_ASL_1

Structural

FLAIR_CNR_GM_WM_Ratio	0.002365
FLAIR_EFC_bits	1.866e+04
FLAIR_FBER_WMref_Ratio	5.876
FLAIR_Mean_AI_Perc	7.012
FLAIR_SD_AI_Perc	5.699
FLAIR_SD_WMref	147.7
FLAIR_SNR_GM_Ratio	6.526
FLAIR_WMH_n	26
FLAIR_WMH_vol_mL	94.406
FLAIR_WMref_vol_mL	10.58
ID	EPAD-001
T1w_CNR_GM_WM_Ratio	0.2872
T1w_CSF_vol_mL	603.8
T1w_EFC_bits	1.37e+04
T1w_FBER_WMref_Ratio	178.3
T1w_GM_ICV_Ratio	0.335
T1w_GM_vol_mL	604
T1w_ICV_vol_mL	1805
T1w_IQR_Perc	83.57
T1w_LR_flip_YesNo	0
T1w_Mean_AI_Perc	7.012
T1w_SD_AI_Perc	5.699
T1w_SD_WMref	31.64
T1w_SNR_GM_Ratio	25.06
T1w_WM_vol_mL	597
T1w_WMref_vol_mL	15.09
Version_CAT12	1363
Version_ExploreASL	1.0.0
Version_LST	2.0.15
Version_Matlab	8.5_R2015a
Version_SPM12	7219

ASL

AI_Perc	40.42
ASL_CoveragePerc	92.02
ASL_tSNR_CSF_Ratio	0.04633
ASL_tSNR_GMWM_Ratio	0.1819
ASL_tSNR_GMWM_WMref_Ratio	0.2626
ASL_tSNR_GM_Ratio	0.3236
ASL_tSNR_Physio2Thermal_Ratio	0.7212
ASL_tSNR_Slope_Corr	0.0002348
ASL_tSNR_WM_Ratio	0.1745
ASL_tSNR_WMref_Ratio	0.1205
AcquisitionTime_hhmmss	140449.29
BackGrSupprPulses	2
CBF_GM_Median_mL100gmin	32.05
CBF_GM_PVC2_mL100gmin	51.24
CBF_GM_WM_Ratio	4.751
CBF_WM_PVC2_mL100gmin	10.79
EchoTime_ms	10.49
ID	EPAD-001_ASL_1
Initial_PLD_ms	2025
LR_flip_YesNo	0
LabelingDuration_ms	1650
LabelingType	CASL
MRScaleSlope	0.0007
Matrix	64 64 36 60
Mean_SSIM_Perc	69.13
MotionExcl_Perc	0
MotionMean_mm	0.1479
PeakSNR_Ratio	674.7
RMSE_Perc	59.37
RepetitionTime_ms	4800
RescaleIntercept	0
RescaleSlope	2.712
RescaleSlopeOriginal	2.712
RigidBody2Anat_mm	100.7
SliceReadoutTime_ms	36.53
SpatialCoV_GM_Perc	96.69
Vendor	Philips
Version_FSL	6.0.1
VoxelSize_mm	3.4375 3.4375 4.5
nRMSE_Perc	23.25

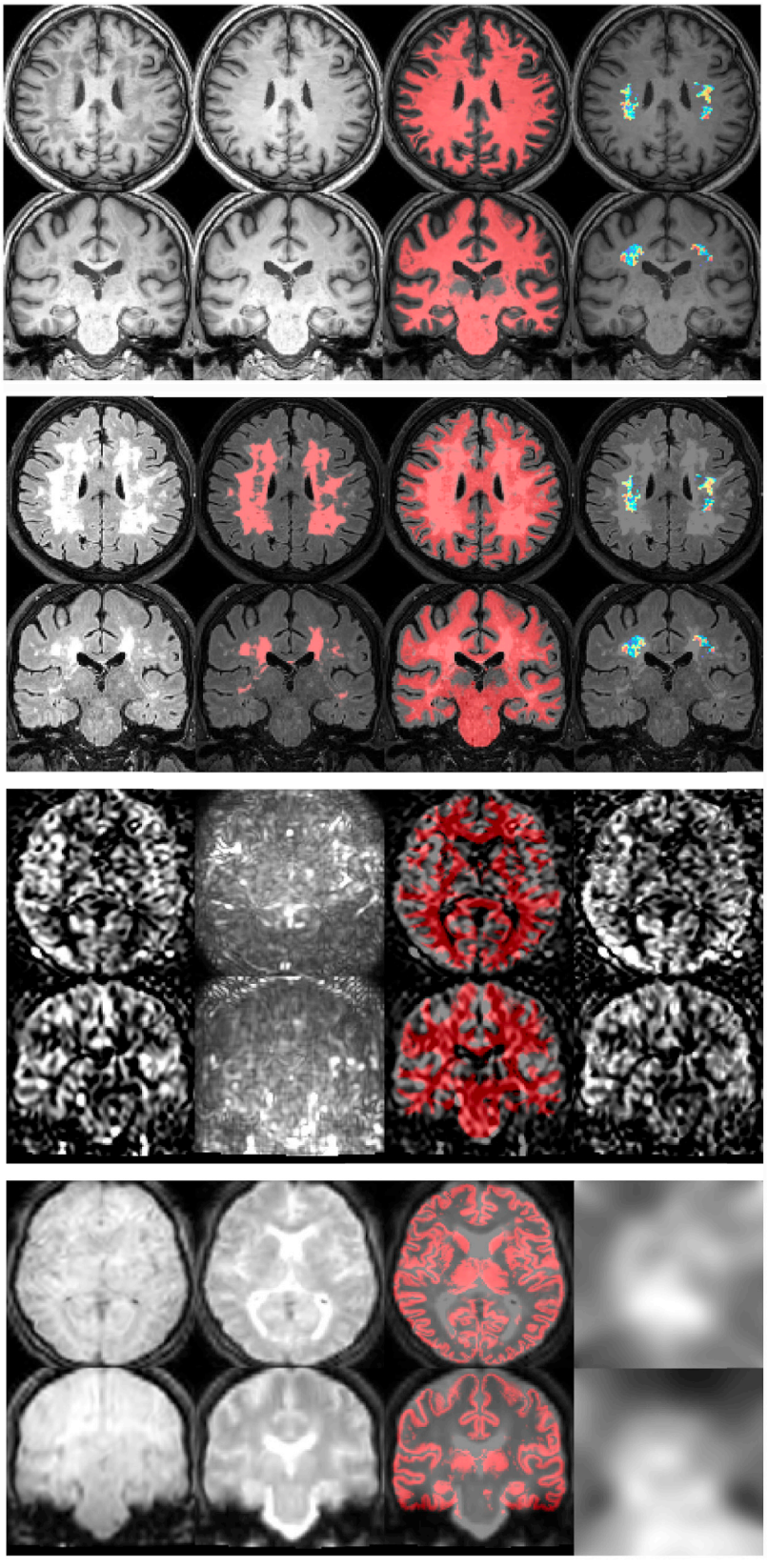

(caption on next page)

Fig. 3. Example PDF report for a single subject. This provenance and QC report includes information collected from each image processing step across the pipeline and assembled in the population module. It is stored in a key-<value> format, facilitating inclusion of plugin or new parameters. Keys and values are grouped into the structural and ASL modules, and the software versions (see Supplementary Table 2). Figures represent transversal and coronal slices in MNI standard space: 1–4) T1w before and after lesion filling, pWM projected over T1w, WMref projected over T1w, 5–8) FLAIR, WMH mask projected over FLAIR, pWM projected over FLAIR, WMref projected over FLAIR, 9–12) CBF, temporal SD, pWM projected over CBF, temporal SNR, 13–16) mean control, M0 before processing, pGM projected over M0, M0 after processing. The pWM/pGM projections in the third column allow a visual assessment of registration performance. CBF = cerebral blood flow, FLAIR = FLuid Attenuated Inversion Recovery, GM = gray matter, pGM = GM partial volume, pWM = WM partial volume, SNR = signal-to-noise ratio, WMref = WM noise reference region, WM = white matter. Example data are from the EPAD study (Ritchie et al., 2016).

intensities and orientation between the NIfTIs of the two compared systems. The image intensity reproducibility was calculated as the median voxel-wise relative intensity difference (Kurth et al., 2015), whereas the image orientation reproducibility was calculated as the mean voxel-wise net displacement vector in real-world coordinates (Power et al., 2012). These were calculated for T1w with GM segmentation, FLAIR with WMH segmentation, M0, quantified CBF, GM partial volume in ASL native space (pGM_{ASL}), and PV-corrected GM CBF.

More complex calculations involving floating-point arithmetic operations, e.g. matrix inversions, can produce different results between OSes and MATLAB versions in the last digits. As randomly seeded pseudo-random number generators are used for some optimization processes, results can differ upon re-run even on the same system. These minimal differences can accumulate in iterative algorithms such as segmentation and registration, and propagate across the pipeline. To mitigate these effects, during the process of implementing and using the pipeline for previous clinical studies, we modified parts of the SPM12, CAT12, and LST toolboxes: e.g. using the MATLAB '\' operator for solving

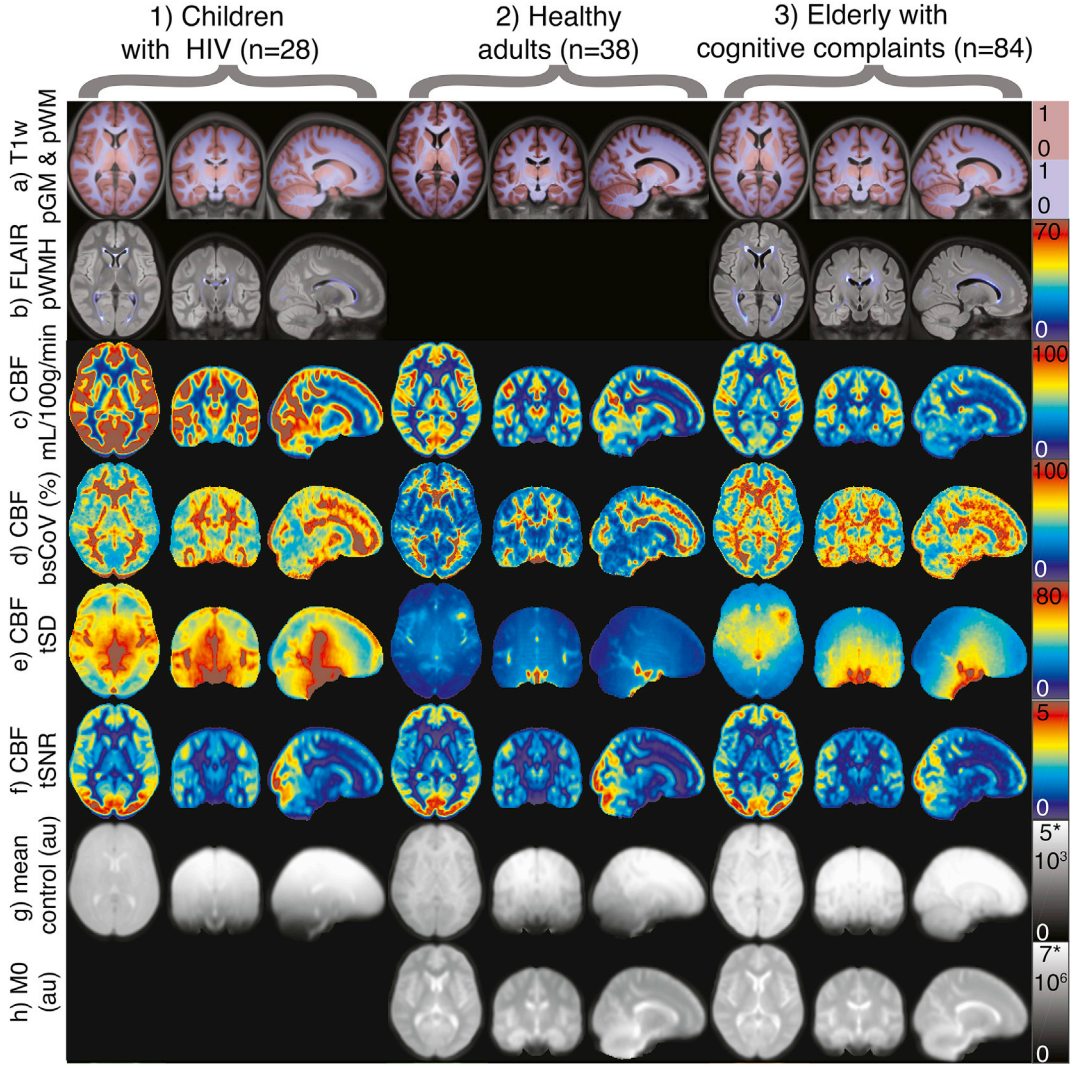

Fig. 4. Transversal, coronal, and sagittal population average images for the three example populations: 1) NOVICE, 2) Sleep study, 3) EPAD (see Supplementary Table 3): a) T1w anatomical image with pGM and pWM overlay, b) FLAIR anatomical image overlaid with probability of WMH presence across the whole population, c) Mean CBF, d) between-subject CBF variation (SD CBF/mean CBF per voxel across all subjects), e) temporal SD of CBF, mean over all subjects is shown, f) temporal SNR of CBF (mean CBF/tSD CBF), g) mean control image (note the background suppression gradient), h) M0 calibration image. Note that the FLAIR and M0 were not acquired in the Sleep and NOVICE studies, respectively. To compare the three populations side by side, all were registered to an adult template. The NOVICE population consisted of children between 8 and 18 y for which segmentation and registration to an adult template typically works without any problems. CBF = cerebral blood flow, tSNR = temporal signal-to-noise ratio, tSD = temporal standard deviation, au = arbitrary units, bs = between-subject, CoV = coefficient of variance, p = probability, GM = gray matter, WM = white matter, WMH = white matter hyperintensity.

a system of linear equations instead of calculating a matrix inversion, providing a separate C++ implementation for convolutions, and/or rounding some calculations to 15 significant digits.

Finally, we reran the full pipeline for the three example populations, but with the ExploreASL-specific features disabled. This would be similar to running a pipeline based on SPM12 and DARTEL without lesion filling and ENABLE, with M0-T1w registration only and the default M0 image processing, which comprise the basic image processing steps that are recommended in the ASL consensus paper. Using the standard space partial volume corrected GM CBF values obtained with the two pipelines, we compare the between-group difference and the correlation of GM CBF with age and sex.

5. Results

Running time for a single EPAD participant took 22:11, 4:34, and 0:40 min for the Structural, ASL, and Population modules, respectively (27:25 min in total). On the 'low quality' setting, the same processing

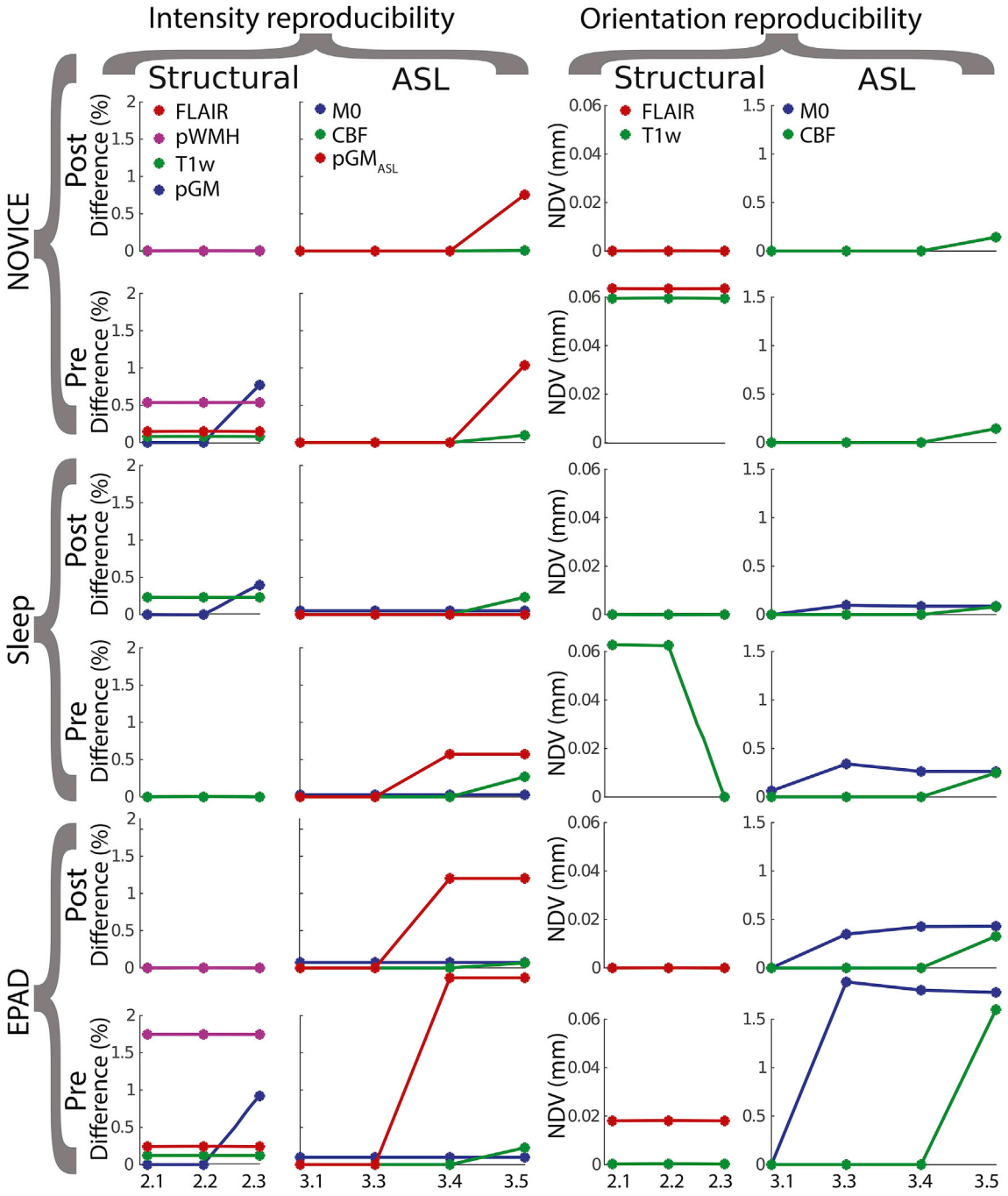

Fig. 5. Reproducibility of the ExploreASL pipeline between Matlab R2018b on Linux and Windows for the three datasets NOVICE, Sleep, and EPAD. Results are shown before (pre) and after (post) the ExploreASL-specific modifications of MATLAB and SPM12 code. The median relative intensity difference is shown in the two columns on the left (referred to as difference) and the mean voxel-wise net displacement vector (NDV) is shown in the two columns on the right. Labels on the x-axis describe the processing steps in the Structural (2.1 = WMH correction, 2.2 = Segmentation, 2.3 = Spatial normalization) and ASL module (3.1 = Motion correction, 3.3 = T1w-ASL registration, 3.4 = M0 processing, 3.5 = CBF quantification) as described in Table 1 pGMASL = gray matter partial volume map in ASL space. Note that all curves overlap completely in the NOVICE-Post columns 1 and 3, SLEEP-Pre column 1, and EPAD-Post columns 1 and 3. The M0 and FLAIR images were not available for the NOVICE (columns 2 and 4) and SLEEP (columns 1 and 3) datasets, respectively.

took 7:30 min, 2:24, and 0:34 respectively (10:28 min in total) (Windows-2018b). Fig. 4 shows differences between populations or sequences on the ExploreASL population-specific parametric maps. While the GM CBF was highest in the pediatric and lowest in the geriatric population (Fig. 4c), both the between-subject CoV and within-scan temporal SD were comparable in these populations and lowest in the healthy adults (Fig. 4d–e). The temporal SD (Fig. 4e) was high in vascular regions and highest around the ventricles in the pediatric dataset, due to a 2D EPI fat-saturation related artifact. Despite these differences, the temporal SNR appeared relatively comparable (Fig. 4f), albeit slightly higher for the pediatric population. The average mean control images (Fig. 4g) showed subtle differences in background suppression efficacy, as different tissue contrast and inferior-superior background suppression efficiency gradient. Only slight differences in ventricle and sulci size were visible between the pediatric and geriatric population (Fig. 4a) confirming satisfactory performance of spatial normalization.

All three datasets showed zero difference when the pipeline was repeated twice on the same system. When comparing OSes only - Linux-2018b vs Windows-2018b - the structural module showed final voxel-wise differences of 0.77% pGM in NOVICE and 1.74% WMH in EPAD that became negligible after our code modifications (Fig. 5). The ASL module differences were smaller than 0.5%, except for the pGM_{ASL} (0.57–2.5%) and PV-corrected GM CBF (0.61–5.76%). Both improved after modifications to 0–1.2% and 0.32–1.5% for pGM_{ASL} and PV-corrected GM CBF, respectively, showing the impact of our modifications. The reproducibility between OS and MATLAB versions - Linux-2018b vs Windows-2015a - showed satisfactory post-modification reproducibility, e.g. pGM_{ASL} (0.47–1.79%) and GM CBF (0.57–1.77%) (Supplementary Table 4). Compared with the above-mentioned Linux-2018b vs Windows 2018b results this shows an additional decrease in reproducibility when a different MATLAB version is used on top of different OSes and/or systems.

When comparing ExploreASL with the typical consensus pipeline - i.e. ExploreASL with all ExploreASL-features turned off - the within-cohort coefficients of variation (SD/mean) were 39.6% vs. 41.4% (Novice, $n = 28$), 11.0% vs. 15.4% (Sleep, $n = 38$), and 16.7% vs 22.5% (EPAD, $n = 75$) for the maps computed by ExploreASL and the typical consensus pipeline, respectively. Subsequently, the between-cohort GM CBF difference for the maps processed by the ExploreASL pipeline (one-way ANOVA, $F = 66.2$, $p = 10^{-21}$, $n = 141$) was stronger compared to the typical consensus pipeline ($F = 28.0$, $p = 10^{-11}$, $n = 141$). The explained variance of age and sex for the three combined populations was larger for the CBF maps processed by ExploreASL ($R^2 = 0.379$, $F = 60.1$, $p = 10^{-21}$, $n = 141$) than with the typical pipeline ($R^2 = 0.270$, $F = 37.1$, $p = 10^{-14}$, $n = 141$).

6. Discussion and future directions

Here, we reviewed many of the most salient ASL image processing choices, and their implementation in ExploreASL version 1.0.0. We demonstrated the software's functionality to review individual cases as well as population-average images for quality control. Our findings show that between-system computing differences can lead to voxel-wise CBF quantification differences of up to 5.7% on average for the total GM, which were reduced to 1.7% by addressing implementation differences of complex floating-point operations between MATLAB versions and OSes. This may especially be beneficial for multi-center studies or for pooling multiple ASL studies to attain sample sizes required for the discovery of subtle (patho-)physiological perfusion patterns.

On the MRI scanner consoles of GE, Philips, and Siemens, CBF quantification is available according to the consensus recommendation (Alsop et al., 2015), although they differ in their image processing and quantification parameters. While this suffices for visual reading, offline image processing is recommended to optimize the image quality and extract regional statistics with respect to an anatomical reference. Several other ASL image processing pipelines are publicly available and free for academic use, each providing specific features. The first publicly available pipeline ASLtbx quantifies CBF of various ASL sequences (Wang et al., 2008) and features customized motion correction and advanced outlier detection (Dolui et al., 2017); ASAP contains a graphical user interface (GUI) with an interface for population analyses, and generates statistical reports (Mato Abad et al., 2016); the ASLM toolbox is a MATLAB- and SPM-based command-line tool (Homan et al., 2012), ASL-MRICloud features a web interface with an automated cloud solution (Li et al., 2019); ASL-QC handles multiple vendors and provides QC metrics (not published); BASIL (Chappell et al., 2009) uses a Bayesian approach for the quantification and PVC of multi-TI (Chappell et al., 2011), QUASAR, and time-encoded ASL data, thus offering the most comprehensive quantification (Chappell et al., 2010); CBFBIRN offers an online data repository with online image processing (Shin et al., 2016); Functional ASL (Functional MRI Laboratory, University of Michigan) and fMRI Grocer (Center for functional Neuroimaging, University of Pennsylvania)) (Zhu et al., 2018) are SPM toolboxes that process both functional ASL and BOLD MRI; GIN fMRI performs separate control and label realignment and automatically excludes outliers and volumes with strong motion (unpublished); MilxASL features spatial and temporal denoising (Fazlollahi et al., 2015); MJD-ASL is implemented into 'cranial cloud', addresses noise concerns and processes cerebral blood volume (Manus Donahue, Vanderbilt University Medical Center); NiftyFit supports quantification of other MRI sequences as IVIM, NODDI, and relaxometry (Melbourne et al., 2016); VANDPIRE is Python-based, has a scanner console plugin and allows flow territory mapping from vessel-encoded ASL (VU e-Innovations) (Arteaga et al., 2017).

ExploreASL has focused on optimizing the processing for clinical studies that have diverse clinical populations, hardware, and sequences used by allowing the import and processing of different sequences of different vendors in a single study. Providing an integrated module for structural image processing, population statistics, and QC is, among other things, essential for processing large multi-center studies. Other strengths of ExploreASL include compatibility with the most-used OSs and its tested between-system reproducibility of image processing. Moreover, ExploreASL is available through GitHub with a growing team of international contributors. We follow the recommendations of the Committee on Best Practices in Data Analysis and Sharing (COBIDAS) (Nichols et al., 2017) by improving the between-system reproducibility, including complete reporting of all facets of a study and the provenance, having standardized source-code headers, and following the best coding practice. ExploreASL was built upon freely available Matlab-based toolboxes that perform well in a wide array of cases, rather than opting for solutions with optimal performance in specific cases but not applicable in general.

Although ExploreASL allows custom labeling efficiency values and global CBF calibration, it does not estimate labeling efficiency. While literature values for labeling efficiency (Dai et al., 2008) may suffice in many clinical cases (Heijtel et al., 2014), individual correction can be beneficial for specific populations (Václavů et al., 2019). For these, phase-contrast MRI can improve the CBF quantification by a) calibrating CBF based on total flow through the brain-feeding arteries (Aslan and Lu, 2010; Ambarki et al., 2015), or b) modeling the labeling efficiency based on the velocity in the labeling plane (Václavů et al., 2016). Compared to ASL, drawbacks of the phase-contrast MRI include its lower reproducibility for whole brain CBF estimates (Dolui et al., 2016), and its lower agreement with PET (Puig et al., 2019). Moreover, an automatic implementation requires good data quality, perpendicular placement of the labeling plane to the vessels, and the absence of vessel tortuosity, conditions that are rarely met in clinical datasets. Future solutions may be provided by new sequences under development, which allow direct labeling efficiency measurements during the ASL acquisition (Chen et al., 2018; Lorenz et al., 2018).

Several additional features are scheduled for future releases, including full BIDS support (Gorgolewski et al., 2016); support for Hitachi and Canon datasets; unit testing to ensure stability of the pipeline through the continuous development; inclusion of WM atlases for

extended WM analysis; a GUI for easier configuration and execution; quantification of advanced ASL schemes such as velocity- and acceleration-selective ASL (Schmid et al., 2015) and integration of the BASIL toolbox to allow multi-PLD and time-encoded sequence quantification (Chappell et al., 2009); and support for individual-center calibration, e.g. using the recently introduced Quantitative ASL Perfusion Reference (QASPER) (Oliver-Taylor et al., 2017) phantom (Gold Standard Phantoms, London, UK). Although ExploreASL's computation times are moderate for research purposes, a clinical scanner implementation would benefit from parallelization on graphical processing units (GPUs) to provide robust automatic QC within clinical scanning time (e.g. <5 min). Another improvement would be the investigation of the effect of image processing choices, as well as the availability of physiological and quantification parameters for different populations (Fazlollahi et al., 2015). This would allow for the incorporation of quantification confidence intervals in the output of ExploreASL. For anonymization purposes, the face can be removed from the structural scans (Nichols et al., 2017; Leung et al., 2015) using a defacing algorithm such as the one implemented in SPM12, but further testing is required to verify that the analysis is not affected (de Sitter et al., 2017b). Statistical analyses can be biased for populations with large inter-subject differences in their deformations, e.g., developing brains or a wide range of atrophy. Dedicated templates are typically used for infants to ensure proper segmentation and normalization (Shi et al., 2011). For older children, the use of a dedicated template is still advised (Sanchez et al., 2012), although adult templates are often sufficient. Further errors in deformations and volume changes can be encountered when stretching pediatric brains to an adult standard space. Either, such deformations need to be accounted in both the volumes and CBF maps, or the analysis has to be performed in standard space, knowing that the pGM thresholds can be different with different total brain volumes as discussed in Section 3.6. A more optimal solution is to use the CerebroMatic toolbox (Wilke et al., 2017) is a tool that accounts for this bias and will be incorporated in future releases of ExploreASL. Finally, we intend to implement ExploreASL as a cloud solution and a plugin for scanner workstation to allow seamless ExploreASL image processing in clinical routine.

There are several methods that we decided not to include in ExploreASL: thresholding the M0 or the mean control image to identify signal dropout (Wang, 2014) or masking them with FSL BET (Smith, 2002), as this may fail with background suppression, blurred 3D acquisitions, poor ASL-M0 registration, or a strong bias field (Mutsaerts et al., 2018). If multiple individual unsubtracted control-label images are available, a mask could be created based on the tSNR of the control or label images. However, time series are not always available, and the tSNR may be biased by the presence of (patho-)physiological signal changes and head motion. Currently, no consensus exists on whether the M0 should be quantified separately for GM and WM tissue types, especially for longer repetition time with a distinct GM-WM contrast. The M0 quantification can potentially be improved by using tissue specific quantification parameters - such as blood-brain partition coefficients λ and tissue relaxation times (Çavusoglu et al., 2009), and/or partial volume correction (Ahlgren et al., 2018). However, this can induce quantification errors in cases of suboptimal ASL-M0 registration. While ExploreASL is designed for analyses in the human brain, many of its methods and principles could be translated to pre-clinical ASL studies and/or studies outside the brain (Nery et al., 2020). The main challenge in applying ExploreASL outside the brain is the dependency of the structural module on human brain templates. Currently, when running only the ASL module on non-brain ASL data, only motion correction, rigid-body registration, and quantification can be performed. Note also that the quantification model is not adapted for pre-clinical or non-brain imaging.

Image processing techniques that require validation include: using the UNWARP toolbox for simultaneous motion and susceptibility deformation correction (Andersson et al., 2001), using temporal information for artifact removal through the application of an independent-component analysis (ICA) (Wells et al., 2010; Hao et al., 2018; Zhu et al., 2018) or using respiratory and cardiac signal (Restom et al., 2006) or data-driven outlier rejection (Maumet et al., 2014; Tan et al., 2009; Dolui et al., 2017), spatial denoising - once validated under realistic conditions (Spann et al., 2017; Wells et al., 2010; Bibic et al., 2010; Liang et al., 2015), obtaining GM-WM segmentations from fractional signal modeling of the magnetization recovery profile acquired with a Look-Locker readout (Petr et al., 2013; Ahlgren et al., 2014), and using the BBR method for motion correction or registration (Greve and Fischl, 2009). ExploreASL offers the option to register to the atlas of spatially normalized mean M0 images, CBF images, or CBF images with a high number of vascular artifacts created for different vendors and ASL sequences from previously processed large ASL datasets. Finally, we aim to improve the inter-center reproducibility even further.

7. Conclusion

ExploreASL is a versatile pipeline that performs well on a wide-range of diseases, including datasets with lesions, allows flexible parameter definition, and a quick exploration of datasets and QC images of each pipeline step in the same space. We made the pipeline available at www.ExploreASL.org. We anticipate that ExploreASL will allow for more flexible collaboration amongst clinicians and scientists, help to achieve the consensus standards for ASL processing sought by the OSIPI, facilitate validation of ASL image processing approaches, and accelerate translation to clinical research and practice.

Declaration of competing interest

The authors declare that they have no known competing financial interests or personal relationships that could have appeared to influence the work reported in this paper.

CRediT authorship contribution statement

Henk J.M.M. Mutsaerts: Conceptualization, Formal analysis, Methodology, Resources, Software, Validation, Visualization, Writing - original draft, Writing - review & editing. **Jan Petr:** Conceptualization, Formal analysis, Methodology, Software, Validation, Visualization, Writing - original draft, Writing - review & editing. **Paul Groot:** Data curation, Methodology, Software, Writing - review & editing. **Pieter Vandemaele:** Data curation, Methodology, Validation, Software, Writing - review & editing. **Silvia Ingala:** Resources, Writing - review & editing. **Andrew D. Robertson:** Data curation, Writing - review & editing. **Lena Václavů:** Methodology, Writing - review & editing. **Inge Groote:** Conceptualization, Resources, Writing - review & editing. **Hugo Kuijf:** Conceptualization, Data curation, Writing - review & editing. **Fernando Zelaya:** Resources, Writing - review & editing. **Owen O'Daly:** Investigation, Resources, Writing - review & editing. **Saima Hilal:** Data curation, Investigation, Resources, Writing - review & editing. **Alle Meije Wink:** Resources, Software, Writing - review & editing. **Ilse Kant:** Conceptualization, Writing - review & editing. **Matthan W.A. Caan:** Investigation, Software, Writing - review & editing. **Catherine Morgan:** Writing - review & editing. **Jeroen de Bresser:** Conceptualization, Writing - review & editing. **Elisabeth Lysvik:** Investigation, Writing - review & editing. **Anouk Schrantee:** Investigation, Writing - review & editing. **Astrid Bjørnebekk:** Data curation, Resources, Writing - review & editing. **Patricia Clement:** Data curation, Resources, Writing - review & editing. **Zahra Shirzadi:** Conceptualization, Data curation, Methodology, Software, Writing - review & editing. **Joost P.A. Kuijer:** Conceptualization, Methodology, Software, Writing - review & editing. **Viktor Wottschel:** Data curation, Resources, Software, Writing - review & editing. **Udunna C. Anazodo:** Investigation, Writing - review & editing. **Dasja Pajkrt:** Investigation, Resources, Writing - review & editing. **Edo Richard:** Resources, Writing - review & editing. **Reinoud P.H. Bokkers:** Conceptualization, Funding acquisition, Writing - review & editing. **Liesbeth Reneman:** Investigation, Writing - review & editing. **Mario**

Masellis: Funding acquisition, Supervision, Writing - review & editing. **Matthias Günther:** Methodology, Writing - review & editing. **Bradley J. MacIntosh:** Funding acquisition, Methodology, Supervision, Writing - review & editing. **Eric Achten:** Funding acquisition, Project administration, Resources, Writing - review & editing. **Michael A. Chappell:** Methodology, Writing - review & editing. **Matthias J.P. van Osch:** Methodology, Writing - review & editing. **Xavier Golay:** Conceptualization, Methodology, Writing - review & editing. **David L. Thomas:** Methodology, Writing - review & editing. **Enrico De Vita:** Investigation, Writing - review & editing. **Atle Bjørnerud:** Funding acquisition, Resources, Supervision, Writing - review & editing. **Aart Nederveen:** Conceptualization, Funding acquisition, Resources, Supervision, Writing - review & editing. **Jeroen Hendrikse:** Conceptualization, Supervision, Writing - review & editing. **Iris Asllani:** Conceptualization, Methodology, Project administration, Supervision, Writing - original draft, Writing - review & editing. **Frederik Barkhof:** Conceptualization, Funding acquisition, Project administration, Resources, Supervision, Writing - review & editing.

Acknowledgments

This project has received support from the following EU/EFPIA Innovative Medicines Initiatives (1 and 2) Joint Undertakings: EPAD grant no. 115736, AMYPAD grant no. 115952. Additionally, this work received support from the EU-EFPIA Innovative Medicines Initiatives Joint Undertaking (grant No 115952). HM is supported by Amsterdam Neuroscience funding. FB and XG are supported by NIHR funding through the UCLH Biomedical Research Centre. DLT is supported by the UCL Leonard Wolfson Experimental Neurology Centre (PR/ylr/18575). EDV is supported by the Wellcome/EPSRC Centre for Medical Engineering [WT 203148/Z/16/Z]. IA is supported by The Gleason Foundation. MJPvO receives research support from Philips, the EU under the Horizon 2020 program (project: CDS-QUAMRI, project number 634541), and the research program Innovational Research Incentives Scheme Vici with project number 016.160.351, which is financed by the Netherlands Organization for Scientific Research (NWO). MC received funding from the Engineering and Physical Sciences Research Council UK (EP/P012361/1), and is a shareholder of Nico.lab BV, Amsterdam, The Netherlands. The Wellcome Centre for Integrative Neuroimaging is supported by core funding from the Wellcome Trust (203139/Z/16/Z). The authors wish to thank the COST-AID (European Cooperation in Science and Technology - Arterial spin labeling Initiative in Dementia) Action BM1103 and the Open Source Initiative for Perfusion Imaging (OSIPI) and the ISMRM Perfusion Study groups for facilitating meetings for researchers to discuss the implementation of ExploreASL. The authors acknowledge Guillaume Flandin, Robert Dahnke, and Paul Schmidt for reviewing the structural module for its implementation of SPM12, CAT12, and LST, respectively; Krzysztof Gorgolewksi for his advice on the BIDS implementation; Jens Maus for help with MEX compilation; Cyril Pernet for providing the SPM Univariate Plus scripts; and Koen Baas for curating the Philips 3D GRASE data. The authors acknowledge the following researchers and teams: Yannis Paloyelis from King's College London, for providing the data of the INtranasal OxyTocin trial, Torbjørn Elvsåshagen from Oslo University Hospital for providing the Sleep study dataset; the EPAD investigators for providing the Amsterdam site elderly dataset; Kim van de Ven from Philips Healthcare for providing the 3D GRASE dataset; Philip de Witt Hamer from Amsterdam UMC for providing the PICTURE dataset, and Chris Chen from the National University of Singapore for providing the Singapore Memory Clinical dataset.

Appendix A. Supplementary data

Supplementary data to this article can be found online at https://doi.org/10.1016/j.neuroimage.2020.117031.

References

Ahlgren, André, Wirestam, Ronnie, Knutsson, Linda, Thade Petersen, Esben, 2018. Improved calculation of the equilibrium magnetization of arterial blood in arterial spin labeling. Magn. Reson. Med. 80 (5), 2223–2231. https://doi.org/10.1002/mrm.27193.

Ahlgren, André, Wirestam, Ronnie, Thade, Esben, Ståhlberg, Freddy, Knutsson, Linda, Thade Petersen, Esben, Ståhlberg, Freddy, Knutsson, Linda, 2014. Partial volume correction of brain perfusion estimates using the inherent signal data of time-resolved arterial spin labeling. NMR Biomed. 27 (9), 1112–1122.

Almeida, Jorge R.C., Greenberg, Tsafrir, Lu, Hanzhang, Henry, W. Chase, Jay, C., Cooper, Crystal M., Deckersbach, Thilo, et al., 2018. Test-retest reliability of cerebral blood flow in healthy individuals using arterial spin labeling : findings from the EMBARC study. Magn. Reson. Imag. 45, 26–33.

Alsop, David C., Detre, John A., 1999. Background suppressed 3D RARE ASL perfusion imaging. In: Proceedings of the ISMRM 7th Annual meeting & exhibition., 601. ISMRM. Philadelphia.

Alsop, David C., Detre, John A., Golay, Xavier, Günther, Matthias, Hendrikse, Jeroen, Hernandez-Garcia, Luis, Lu, Hanzhang, et al., 2015. Recommended implementation of arterial spin-labeled perfusion MRI for clinical applications: a consensus of the ISMRM perfusion study group and the European consortium for ASL in Dementia. Magn. Reson. Med. 73 (1), 102–116.

Alsop, David C., Detre, John A., Grossman, M., 2000. "Assessment of cerebral blood flow in Alzheimer's disease by spin-labeled magnetic resonance imaging. Ann. Neurol. 47, 93–100.

Alsop, D.C., Detre, J.A., 1996. Reduced transit-time sensitivity in noninvasive magnetic resonance imaging of human cerebral blood flow. J. Cerebr. Blood Flow Metabol. 16 (6), 1236–1249.

Ambarki, K., Wåhlin, A., Zarrinkoob, L., Wirestam, R., Petr, J., Malm, J., Eklund, A., 2015. "Accuracy of parenchymal cerebral blood flow measurements using pseudocontinuous arterial spin-labeling in healthy volunteers." AJNR. Am. J. Neuroradiol. 36 (10), 1816–1821.

Andersson, Jesper L.R., Hutton, Chloe, Ashburner, John, Turner, Robert, Friston, Karl, 2001. Modeling geometric deformations in EPI time series. Neuroimage 13 (5), 903–919.

Andersson, Jesper L.R., Skare, Stefan, Ashburner, John, 2003. How to correct susceptibility distortions in spin-echo echo-planar images: application to diffusion tensor imaging. Neuroimage 20 (2), 870–888.

Arteaga, Daniel F., Strother, Megan K., Davis, L. Taylor, Fusco, Matthew R., Faraco, Carlos C., Roach, Brent A., Scott, Allison O., Donahue, Manus J., 2017. Planning-free cerebral blood flow territory mapping in patients with intracranial arterial stenosis. J. Cerebr. Blood Flow Metabol. 37 (6), 1944–1958.

Ashburner, J., Friston, Karl J., 1999. Nonlinear spatial normalization using basis functions. Hum. Brain Mapp. 7 (4), 254–266.

Ashburner, John, 2007. A fast diffeomorphic image registration algorithm. Neuroimage 38 (1), 95–113.

Ashburner, John, 2012. SPM: a history. Neuroimage 62 (2), 791–800.

Ashburner, John, Friston, Karl J., 2005. Unified segmentation. Neuroimage 26, 839–851.

Ashburner, John, Friston, Karl J., 2011. "Diffeomorphic registration using geodesic shooting and gauss–Newton optimisation. Neuroimage 55 (3), 954–967.

Ashburner, John, Ridgway, Gerard R., 2012. Symmetric diffeomorphic modeling of longitudinal structural MRI. Front. Neurosci. 6, 197.

Aslan, Sina, Lu, Hanzhang, 2010. On the sensitivity of ASL MRI in detecting regional differences in cerebral blood flow. Magn. Reson. Imag. 28 (7), 928–935.

Asllani, Iris, Borogovac, Ajna, Brown, Truman R., 2008. Regression algorithm correcting for partial volume effects in arterial spin labeling MRI. Magn. Reson. Med. 60 (6), 1362–1371.

Asllani, Iris, Habeck, Christian, Borogovac, Ajna, Brown, Truman R., Brickman, Adam M., Stern, Yaakov, 2009. Separating function from structure in perfusion imaging of the aging brain. Hum. Brain Mapp. 30 (9), 2927–2935.

Battaglini, Marco, Jenkinson, Mark, Nicola De Stefano, 2012. Evaluating and reducing the impact of white matter lesions on brain volume measurements. Hum. Brain Mapp. 33 (9), 2062–2071.

Beaumont, H., 2015. Multimodal Magnetic Resonance Imaging of Frontotemporal Lobar Degeneration. University of Manchester, Faculty of Medical and Human Sciences.

Bibic, Adnan, Knutsson, Linda, Ståhlberg, Freddy, Wirestam, Ronnie, 2010. Denoising of arterial spin labeling data: wavelet-domain filtering compared with Gaussian smoothing. Magma 23 (3), 125–137.

Blokhuis, C., Mutsaerts, Henri J.M. M., Cohen, Sophie, Henriette, J. Scherpbier, Caan, Matthan W.A., Majoie, Charles B.L. M., Kuijpers, Taco W., Reiss, P., Wit, F.W.N.M., Pajkrt, D., 2017. Higher subcortical and white matter cerebral blood flow in perinatally HIV-infected children. Medicine 96 (7), e5891.

Bohland, Jason W., Bokil, Hemant, Allen, Cara B., Mitra, Partha P., 2009. The brain atlas concordance problem: quantitative comparison of anatomical parcellation. PloS One 4 (9), e7200.

Bron, Esther E., Steketee, Rebecca M.E., Houston, Gavin C., Oliver, Ruth A., Achterberg, Hakim C., Loog, Marco, van Swieten, John C., et al., 2014. Diagnostic classification of arterial spin labeling and structural MRI in presenile early stage Dementia. Hum. Brain Mapp. 35 (9), 4916–4931.

Cardoso, M. Jorge, Modat, Marc, Vercauteren, Tom, Ourselin, Sebastien, 2015. Scale factor point spread function matching: beyond aliasing in image resampling. Medical Image Computing and Computer-Assisted Intervention – MICCAI 2015. MICCAI 2015. Lecture Notes in Computer Science, 9350. Springer, Cham.

Çavuşoğlu, Mustafa, Pfeuffer, Josef, Uğurbil, Kâmil, Uludağ, Kâmil, 2009. Comparison of pulsed arterial spin labeling encoding schemes and absolute perfusion quantification. Magn. Reson. Imag. 27 (8), 1039–1045.

Chappell, M.A., Groves, A.R., Whitcher, B., Woolrich, M.W., 2009. Variational bayesian inference for a nonlinear forward model. IEEE Trans. Signal Process. 57 (1), 223–236.
Chappell, Michael A., MacIntosh, Bradley J., Donahue, Manus J., Günther, Matthias, Peter, Jezzard, Woolrich, Mark W., 2010. Separation of macrovascular signal in multi-inversion time arterial spin labelling MRI. Magn. Reson. Med. 63 (5), 1357–1365.
Chappell, M.A., Groves, A.R., MacIntosh, B.J., Donahue, M.J., Jezzard, P., Woolrich, M.W., 2011. Partial volume correction of multiple inversion time arterial spin labeling MRI data. Magn. Reson. Med. 65 (4), 1173–1183.
Chappell, Michael, Bradley, MacIntosh, Okell, Thomas, 2018. Introduction to Perfusion Quantification Using Arterial Spin Labelling. Oxford University Press.
Chard, Declan T., Jackson, Jonathan S., Miller, David H., Wheeler-Kingshott, Claudia A.M., 2010. Reducing the impact of white matter lesions on automated measures of brain gray and white matter volumes. J. Magn. Reson. Imag. 32 (1), 223–228.
Chenevert, Thomas L., Malyarenko, Dariya I., Newitt, David, Li, Xin, Mohan, Jayatilake, Tudorica, Alina, Fedorov, Andriy, et al., 2014. Errors in quantitative image analysis due to platform-dependent image scaling. Trans. Oncol. 7 (1), 65–71.
Chen, J. Jean, Rosas, H. Diana, Salat, David H., 2011a. Age-associated reductions in cerebral blood flow are independent from regional atrophy. Neuroimage 55 (2), 468–478.
Chen, Yufen, Wang, Danny J.J., Detre, John A., 2011b. Test-retest reliability of arterial spin labeling with common labeling strategies. J. Magn. Reson. Imag. 33, 940–949.
Chen, Zhensen, Zhao, Xihai, Zhang, Xingxing, Guo, Rui, Teeuwisse, Wouter M., Zhang, Bida, Peter, Koken, Jouke, Smink, Yuan, Chun, Matthias, J., van Osch, P., 2018. Simultaneous measurement of brain perfusion and labeling efficiency in a single pseudo-continuous arterial spin labeling scan. Magn. Reson. Med. 79 (4), 1922–1930.
Clement, Patricia, Mutsaerts, Hjmm, Vaclavu, Lena, Ghariq, Eidrees, Pizzini, Francesca B., Smits, Marion, Acou, Marjan, et al., 2018. Variability of physiological brain perfusion in healthy subjects - a systematic review of modifiers. Considerations for multi-center ASL studies. J. Cereb. Blood Flow Metab. 38 (9), 1418–1437.
Cox, Robert W., 2012. "AFNI: what a long strange trip it's been. Neuroimage 62 (2), 743–747.
Crinion, Jenny, Ashburner, John, Leff, Alex, Brett, Matthew, Price, Cathy, Friston, Karl, 2007. Spatial normalization of lesioned brains: performance evaluation and impact on fMRI analyses. Neuroimage 37 (3), 866–875.
Croal, P.L., Kennedy-McConnel, F., Harris, B., Ma, R., Ng, S.M., Plaha, P., Lord, S., Sibson, N.R., Chappell, M.A., 2019. Quantification of cerebral blood flow using arterial spin labeling in glioblastoma multiforme; challenges of calibration in the presence of oedema. In Proceedings of the ISMRM 27th Annual meeting & exhibition. 2019, 2315.
Dai, Weiying, Garcia, D., De, Bazelaire C., Alsop, David C., 2008. Continuous flow-driven inversion for arterial spin labeling using pulsed radio frequency and gradient fields. Magn. Reson. Med. 60, 1488–1497.
Deibler, A.R., Pollock, J.M., Kraft, R.A., Tan, H., Burdette, Jonathan H., Maldjian, J.A., 2008. "Arterial spin-labeling in routine clinical practice, Part 1: technique and artifacts." AJNR. Am. J. Neuroradiol. 29 (7), 1228–1234.
Desikan, Rahul S., Ségonne, Florent, Fischl, Bruce, Quinn, Brian T., Dickerson, Bradford C., Blacker, Deborah, Buckner, Randy L., et al., 2006. An automated labeling system for subdividing the human cerebral cortex on MRI scans into gyral based regions of interest. Neuroimage 31 (3), 968–980.
Detre, J.A., Leigh, J.S., Williams, D.S., Koretsky, A.P., 1992. Perfusion imaging. Magn. Reson. Med. 23 (1), 37–45.
Detre, John A., Alsop, David C., Vives, L.R., Maccotta, L., Teener, J.W., Raps, E.C., 1998. Noninvasive MRI evaluation of cerebral blood flow in cerebrovascular disease. Neurology 50, 633–641.
de Sitter, Alexandra, Steenwijk, Martijn D., Ruet, Aurélie, Versteeg, Adriaan, Liu, Yaou, Ronald, A., van Schijndel, Petra, J., Pouwels, W., et al., 2017a. Performance of five research-domain automated WM lesion segmentation methods in a multi-center MS study. Neuroimage 163, 106–114.
de Sitter, A., Visser, M., Brouwer, I., van Schijndel, R.A., Uitdehaag, B.M.J., Barkhof, F., Vrenken, H., 2017. Impact of removing facial features from MR images of MS patients on automatic lesion and atrophy metrics. Multiple Sclerosis J. 23, 226–226.
De Vis, J.B., Hendrikse, J., Groenendaal, F., de Vries, L.S., Kersbergen, K.J., Benders, M.J.N.L., Petersen, E.T., 2014. Impact of neonate haematocrit variability on the longitudinal relaxation time of blood: implications for arterial spin labelling MRI. Neuroimage: Clinic 4, 517–525.
Dolui, Sudipto, Wang, Ze, Shinohara, Russell T., Wolk, David A., Detre, John A., Alzheimer's Disease Neuroimaging Initiative, 2017. Structural correlation-based outlier rejection (SCORE) algorithm for arterial spin labeling time series. J. Magn. Reson. Imag. 45 (6), 1786–1797.
Dolui, Sudipto, Wang, Ze, Danny, J., Wang, J., Mattay, Raghav, Finkel, Mack, Elliott, Mark, Desiderio, Lisa, et al., 2016. Comparison of non-invasive MRI measurements of cerebral blood flow in a large multisite cohort. J. Cereb. Blood Flow Metab. 36 (7), 1244–1256.
Elvsåshagen, Torbjørn, Mutsaerts, Henri Jmm, Zak, Nathalia, Norbom, Linn B., Quraishi, Sophia H., Pedersen, Per Ø., Malt, Ulrik F., et al., 2019. Cerebral blood flow changes after a day of wake, Sleep, and Sleep deprivation. Neuroimage 186, 497–509.
Evans, Alan C., Janke, Andrew L., Collins, D. Louis, Baillet, Sylvain, 2012. Brain templates and atlases. Neuroimage 62 (2), 911–922.
Fazlollahi, Amir, Bourgeat, Pierrick, Liang, Xiaoyun, Meriaudeau, Fabrice, Connelly, Alan, Salvado, Olivier, Calamante, Fernando, 2015. Reproducibility of multiphase pseudo-continuous arterial spin labeling and the effect of post-processing analysis methods. Neuroimage 117, 191–201.
Flandin, Guillaume, Friston, Karl, 2008. Statistical parametric mapping (SPM). Scholarpedia J. 3 (4), 6232.
Gai, Neville D., Yi, Yu, Pham, Dzung, Butman, John A., 2017. Reduced distortion artifact whole brain CBF mapping using blip-reversed non-segmented 3D echo planar imaging with pseudo-continuous arterial spin labeling. Magn. Reson. Imag. 44, 119–124.
Gaser, C., 2009. Partial volume segmentation with adaptive maximum A posteriori (map) approach. Neuroimage 47 (1), S39–S41. https://doi.org/10.1016/S1053-8119(09)71151-6.
Gevers, Sanna, Van Osch, Matthias J., Bokkers, Reinoud P.H., Kies, Dennis A., Teeuwisse, Wouter M., Majoie, Charles B., Hendrikse, Jeroen, Nederveen, Aart J., 2011. Intra-and multicenter reproducibility of pulsed, continuous and pseudo-continuous arterial spin labeling methods for measuring cerebral perfusion. J. Cerebr. Blood Flow Metabol. 31 (8), 1706–1715.
Gorgolewski, Krzysztof J., Auer, Tibor, Calhoun, Vince D., Craddock, R. Cameron, Das, Samir, Duff, Eugene P., Flandin, Guillaume, et al., 2016. The brain imaging data structure, a format for organizing and describing outputs of neuroimaging experiments. Sci. Data 3, 160044.
Greve, Douglas N., Bruce, Fischl, 2009. Accurate and robust brain image alignment using boundary-based registration. Neuroimage 48 (1), 63–72.
Hales, Patrick W., Kawadler, Jamie M., Aylett, Sarah E., Kirkham, Fenella J., Clark, Christopher A., 2014. Arterial spin labeling characterization of cerebral perfusion during normal maturation from late childhood into adulthood: normal 'reference range' values and their use in clinical studies. J. Cereb. Blood Flow Metab. 34 (5), 776–784.
Hales, Patrick W., Kirkham, Fenella J., Clark, Christopher A., 2016. A general model to calculate the spin-lattice (T1) relaxation time of blood, accounting for haematocrit, oxygen saturation and magnetic field strength. J. Cereb. Blood Flow Metab. 36 (2), 370–374.
Hammers, Alexander, Koepp, Matthias J., Free, Samantha L., Brett, Matthew, Richardson, Mark P., Labbé, Claire, Cunningham, Vincent J., Brooks, David J., Duncan, John, 2002. Implementation and application of a brain template for multiple volumes of interest. Hum. Brain Mapp. 15 (3), 165–174.
Handley, Rowena, Zelaya, Fernando O., Simone Reinders, A.A.T., Marques, Tiago Reis, Mehta, Mitul A., Ruth, O'Gorman, Alsop, David C., et al., 2013. Acute effects of single-dose aripiprazole and haloperidol on resting cerebral blood flow (rCBF) in the human brain. Hum. Brain Mapp. 34 (2), 272–282.
Hao, X., Jan Petr, Nederveen, Aart J., John, C., Wood, Danny J. J. Wang, Mutsaerts, Henk Jmm, Jann, Kay, 2018. ICA cleanup for improved SNR in arterial spin labeling perfusion MRI. In: In Proceedings of the ISMRM 26th Annual meeting & exhibition. ISMRM.
Heijtel, Dennis F.R., Mutsaerts, Henri J.M. M., Bakker, E., Schober, P., Stevens, M.F., Petersen, E.T., van Berckel, B.N.M., et al., 2014. Accuracy and precision of pseudo-continuous arterial spin labeling perfusion during baseline and hypercapnia: a head-to-head comparison with ^{15}O H_2O positron emission tomography. Neuroimage 92, 182–192.
Homan, Philipp, Kindler, Jochen, Hubl, Daniela, Dierks, Thomas, 2012. Auditory verbal hallucinations: imaging, analysis, and intervention. Eur. Arch. Psychiatr. Clin. Neurosci. 262 (Suppl. 2), S91–S95. November.
Jack Jr., Clifford R., Bernstein, M.A., Borowski, Bret, Gunter, J.L., Fox, N.C., Thompson, Paul, Schuff, N., et al., 2010. Update on the magnetic resonance imaging core of the Alzheimer's disease neuroimaging initiative. Alzheimers Dement 6, 212–220.
Joris, Peter J., Mensink, Ronald P., Adam Tanja, C., Liu, Thomas T., 2018. Cerebral blood flow measurements in adults: a review on the effects of dietary factors and exercise. Nutrients 10 (530), 1–15.
Klein, Arno, Andersson, Jesper, Ardekani, Babak A., Ashburner, John, Avants, Brian, Chiang, Ming-Chang, Christensen, Gary E., et al., 2009. Evaluation of 14 nonlinear deformation algorithms applied to human brain MRI registration. Neuroimage 46 (3), 786–802.
Klein, Stefan, Staring, Marius, Murphy, Keelin, Viergever, Max A., Pluim, Josien P.W., 2010. Elastix: a toolbox for intensity-based medical image registration. IEEE Trans. Med. Imag. 29 (1), 196–205.
Kurth, Florian, Gaser, Christian, Luders, Eileen, 2015. A 12-step user guide for analyzing voxel-wise gray matter asymmetries in statistical parametric mapping (SPM). Nat. Protoc. 10 (2), 293–304.
Law, Ian, Iida, Hidehiro, Holm, Søren, Sam Nour, Rostrup, Egill, Svarer, Claus, Paulson, Olaf B., 2000. Quantitation of regional cerebral blood flow corrected for partial volume effect using O-15 water and PET: II. Normal values and gray matter blood flow response to visual activation. J. Cereb. Blood Flow Metab. 20 (8), 1252–1263.
Leung, Kai Yan Eugene, Fedde van der Lijn, Vrooman, Henri A., Miriam, C., Sturkenboom, J.M., Niessen, Wiro J., 2015. IT infrastructure to support the secondary use of routinely acquired clinical imaging data for research. Neuroinformatics 13 (1), 65–81.
Li, Yang, Liu, Peiying, Yue, Li, Fan, Hongli, Pan, Su, Peng, Shin-Lei, Park, Denise C., et al., 2019. ASL-MRICloud: an online tool for the processing of ASL MRI data. NMR Biomed. 32 (2), e4051 https://doi.org/10.1002/nbm.4051.
Li, X, Morgan, PS, Ashburner, J, Smith, J, Rorden, C, 2016. The first step for neuroimaging data analysis: DICOM to NIfTI conversion. J. Neurosci. Methods 264, 47–56. https://doi.org/10.1016/j.jneumeth.2016.03.001.
Liang, Xiaoyun, Connelly, Alan, Calamante, Fernando, 2013. Improved partial volume correction for single inversion time arterial spin labeling data. Magn. Reson. Med. 69 (2), 531–537.

Liang, Xiaoyun, Connelly, Alan, Calamante, Fernando, 2015. Voxel-wise functional connectomics using arterial spin labeling functional magnetic resonance imaging: the role of denoising. Brain Connect. 5 (9), 543–553.

Liu, Ho-Ling, Kochunov, Peter, Hou, Jinwen, Pu, Yonglin, Mahankali, Srikanth, Feng, Ching-Mei, Yee, Seong-Hwan, Wan, Yung-Liang, Fox, Peter T., Gao, Jia-Hong, 2001. Perfusion-weighted imaging of interictal hypoperfusion in temporal lobe epilepsy using FAIR-HASTE: comparison with $H_2^{15}O$ PET measurements. Magn. Reson. Med. 45 (3), 431–435.

Li, Wenbo, Liu, Peiying, Lu, Hanzhang, Strouse, John J., Peter, van Zijl, M., Qin, Qin, 2017. Fast measurement of blood T 1 in the human carotid artery at 3T: accuracy, precision, and reproducibility. Magn. Reson. Med. 77 (6), 2296–2302.

Li, Yang, Deng, Mao, Li, Zhiqiang, Michael Schär, Pillai, Jay J., Pipe, James G., Lu, Hanzhang, 2018. Cardiac-triggered pseudo-continuous arterial-spin-labeling: a cost-effective scheme to further enhance the reliability of arterial-spin-labeling MRI. Magn. Reson. Med. 80 (3), 969–975.

Lorenz, Kathrin, Mildner, Toralf, Torsten Schlumm, Harald, E., Möller, 2018. Characterization of pseudo-continuous arterial spin labeling: simulations and experimental validation. Magn. Reson. Med. 79 (3), 1638–1649.

Macintosh, Bradley J., Nicola, Filippini, Chappell, Michael A., Woolrich, Mark W., Mackay, Clare E., Peter, Jezzard, 2010. Assessment of arterial arrival times derived from multiple inversion time pulsed arterial spin labeling MRI. Magn. Reson. Med. 63 (3), 641–647.

MacIntosh, Bradley J., Pattinson, Kyle T.S., Gallichan, Daniel, Ahmad, Imran, Miller, Karla L., Feinberg, David A., Wise, Richard G., Peter, Jezzard, 2008. Measuring the effects of remifentanil on cerebral blood flow and arterial arrival time using 3D GRASE MRI with pulsed arterial spin labelling. J. Cerebr. Blood Flow Metabol. 28 (8), 1514–1522.

Madai, Vince I., Martin, Steve Z., Samson-Himmelstjerna, Federico C. von, Herzig, Cornelius X., Mutke, Matthias A., Wood, Carla N., Thamm, Thoralf, et al., 2016. Correction for susceptibility distortions increases the performance of arterial spin labeling in patients with cerebrovascular disease. J. Neuroimaging 26 (4), 436–444.

Mato Abad, Virginia, García-Polo, Pablo, Owen, O'Daly, Juan Antonio, Hernández-Tamames, Zelaya, Fernando, 2016. ASAP (automatic software for ASL processing): a toolbox for processing arterial spin labeling images. Magn. Reson. Imag. 34 (3), 334–344.

Maumet, Camille, Maurel, Pierre, Ferré, Jean-Christophe, Bannier, Elise, Barillot, Christian, 2012. Using negative signal in mono-TI pulsed arterial spin labeling to outline pathological increases in arterial transit times. In: ISMRM scientific workshop. Perfusion MRI: standardization Beyond CBF & Everyday Clinic. Appl, 40, p. 42, 3.

Maumet, C., Maurel, P., Ferre, J.C., Barillot, C., 2014. Robust estimation of the cerebral blood flow in arterial spin labelling. Magn. Reson. Imag. 32 (5), 497–504.

Mazziotta, J., Toga, A., Evans, A., Fox, P., Lancaster, J., Zilles, K., Woods, R., et al., 2001. A probabilistic atlas and reference system for the human brain: international consortium for brain mapping (ICBM). Phil. Trans. Roy. Soc. Lond. B Biol. Sci. 356 (1412), 1293–1322.

Melbourne, Andrew, Toussaint, Nicolas, Owen, David, Simpson, Ivor, Anthopoulos, Thanasis, De Vita, Enrico, Atkinson, David, Ourselin, Sebastien, 2016. NiftyFit: a software package for multi-parametric model-fitting of 4D magnetic resonance imaging data. Neuroinformatics 14 (3), 319–337.

Mendrik, Adriënne M., Vincken, Koen L., Kuijf, Hugo J., Breeuwer, Marcel, Bouvy, Willem H., de Bresser, Jeroen, Alansary, Amir, et al., 2015. MRBrainS challenge: online evaluation framework for brain image segmentation in 3T MRI scans. Comput. Intell. Neurosci. 2015, 813696.

Moghaddasi, L., Bezak, E., Harriss-Phillips, W., 2015. Evaluation of current clinical target volume definitions for glioblastoma using cell-based dosimetry stochastic methods. Br. J. Radiol. 88 (1053), 20150155.

Mutsaerts, Henri J.M. M., Mirza, Saira S., Jan, Petr, Thomas, David L., Cash, David M., Bocchetta, Martina, de Vita, Enrico, et al., 2019. Cerebral perfusion changes in presymptomatic genetic frontotemporal Dementia: a GENFI study. Brain: J. Neurol. 142 (4), 1108–1120.

Mutsaerts, Henri J.M., Richard, Edo, Heijtel, Dennis F.R., van Osch, Matthias J.P., Majoie, Charles B.L. M., Nederveen, Aart J., 2014a. Gray matter contamination in arterial spin labeling white matter perfusion measurements in patients with Dementia. Neuroimage: Clinic 4, 139–144.

Mutsaerts, Henri J.M. M., van Osch, Matthias J.P., Zelaya, F.O., Wang, Danny J.J., Nordhøy, W., Wang, Y., Wastling, S., et al., 2015. Multi-vendor reliability of arterial spin labeling perfusion MRI using a near-identical sequence: implications for multi-center studies. Neuroimage 113. https://doi.org/10.1016/j.neuroimage.2015.03.043.

Mutsaerts, Henri J.M. M., Petr, Jan, Thomas, David L., De Vita, Enrico, Cash, David M., van Osch, Matthias J.P., Golay, Xavier, et al., 2018. Comparison of arterial spin labeling registration strategies in the multi-center GENetic frontotemporal Dementia initiative (GENFI). J. Magn. Reson. Imag. 47 (1), 131–140.

Mutsaerts, Henri J.M. M., Rebecca, M. E. Steketee, Dennis, F. R. Heijtel, Kuijer, Joost P.A., Van Osch, M.J.P., Majoie, Charles B.L. M., Smits, Marion, Nederveen, Aart J., 2014b. Inter-vendor reproducibility of pseudo-continuous arterial spin labeling at 3 tesla. PloS One 9 (8), e104108.

Mutsaerts, H.J., Petr, J., Bokkers, R.P., Lazar, R.M., Marshall, R.S., Asllani, I., 2020. Spatial coefficient of variation of arterial spin labeling MRI as a cerebrovascular correlate of carotid occlusive disease. PloS One 15 (2), e0229444.

Mutsaerts, Henri J.M.M., Petr, Jan, Václavů, Lena, Van Dalen, Jan .W., Robertson, Andrew .D., Caan, Matthan W.A., Masellis, Mario, Nederveen, Aart J., Richard, Edo, Macintosh, Bradley J., 2017. The spatial coefficient of variation in arterial spin labeling cerebral blood flow images. J. Cerebr. Blood Flow Metabol. 37 (9), 3184–3192.

Nery, Fabio, Buchanan, Charlotte E., Harteveld, Anita A., Odudu, Aghogho, Bane, Octavia, Cox, Eleanor F., Derlin, Katja, et al., 2020. Consensus-based technical recommendations for clinical translation of renal ASL MRI. Magma 33 (1), 141–161.

Nichols, Thomas E., Das, Samir, Eickhoff, Simon B., Evans, Alan C., Glatard, Tristan, Hanke, Michael, Kriegeskorte, Nikolaus, et al., 2017. Best practices in data analysis and sharing in neuroimaging using MRI. Nat. Neurosci. 20 (3), 299–303.

Oliver, Ruth Abigail, 2015. Improved Quantification of Arterial Spin Labelling Images Using Partial Volume Correction Techniques. UCL (University College London).

Oliver-Taylor, Aaron, Gonalves, Miguel, Hampshire, Thomas, Davis, Bradley, Daga, Pankaj, Evans, Laura, Bainbridge, Alan, et al., 2017. A calibrated perfusion phantom for quality assurance of quantitative arterial spin labelling. In: Proceedings of the ISMRM 25th Annual meeting & exhibition, 25. ISMRM, p. 681.

Pareto, D., Sastre-Garriga, J., Aymerich, F.X., Auger, C., Tintoré, M., Montalban, X., Rovira, A., 2016. Lesion filling effect in regional brain volume estimations: a study in multiple sclerosis patients with low lesion load. Neuroradiology 58 (5), 467–474.

Petersen, E.T., Mouridsen, K., Xavier, Golay, 2010. The QUASAR reproducibility study, Part II: results from a multi-center arterial spin labeling test-retest study. Neuroimage 49 (1), 104–113.

Petr, Jan, Mutsaerts, Henri J.M., De Vita, Enrico, Steketee, Rebecca M.E., Smits, Marion, Nederveen, Aart J., Frank, Hofheinz, Jörg Van Den, Hoff, Asllani, Iris, 2018a. Effects of systematic partial volume errors on the estimation of gray matter cerebral blood flow with arterial spin labeling MRI. MAGMA. 31 (6), 725–734.

Petr, Jan, Mutsaerts, H.J., De Vita, Enrico, Shirzadi, Zahra, Cohen, Sophie, Blokhuis, Charlotte, Pajkrt, Dasja, Frank, Hofheinz, Jörg van den Hoff, Asllani, Iris, 2016. Cerebral blood flow underestimation due to volume realignments: an error induced by registration in arterial spin labeling MRI. In: Proceesing of the Annual meeting of the European Society of Magnetic Resonance in Medicine and Biology. ESMRMB. Vienna.

Petr, Jan, Schramm, Georg, Frank, Hofheinz, Langner, Jens, Jörg van den Hoff, 2013. Partial volume correction in arterial spin labeling using a look-locker sequence. Magn. Reson. Med. 70 (6), 1535–1543.

Petr, J., Platzek, I., Hofheinz, F., Mutsaerts, H.J.M.M., Asllani, I., Mjp Van Osch, M.J.P., Seidlitz, A., et al., 2018b. Photon vs. Proton radiochemotherapy, effects on brain tissue volume and perfusion. Radiother. Oncol. 128 (1), 121–127.

Pinto, Joana, Chappell, Michael A., Okell, Thomas W., Mezue, Melvin, Segerdahl, Andrew R., Tracey, Irene, Vilela, Pedro, Figueiredo, Patrícia, 2020. Calibration of arterial spin labeling data-potential pitfalls in post-processing. Magn. Reson. Med 83 (4), 1222–1234.

Pohmann, Rolf, 2010. Accurate, localized quantification of white matter perfusion with single-voxel ASL. Magn. Reson. Med. 64 (4), 1109–1113.

Power, Jonathan D., Barnes, Kelly A., Snyder, Abraham Z., Schlaggar, Bradley L., Petersen, Steven E., 2012. Spurious but systematic correlations in functional connectivity MRI networks arise from subject motion. Neuroimage 59 (3), 2142–2154.

Puig, Oriol, Vestergaard, Mark B., Ulrich, Lindberg, Hansen, Adam E., Ulrich, Annette, Andersen, Flemming L., Johannesen, Helle H., et al., 2019. Phase contrast mapping MRI measurements of global cerebral blood flow across different perfusion states – a direct comparison with ^{15}O-H_2O positron emission tomography using a hybrid PET/MR system. J. Cereb. Blood Flow Metab. 39 (12), 2368–2378.

Restom, Khaled, Behzadi, Yashar, Liu, Thomas T., 2006. Physiological noise reduction for arterial spin labeling functional MRI. Neuroimage 31 (3), 1104–1115.

Ripollés, P., Marco-Pallarés, J., de Diego-Balaguer, R., Miró, J., Falip, M., Juncadella, M., Rubio, F., Rodriguez-Fornells, A., 2012. Analysis of automated methods for spatial normalization of lesioned brains. Neuroimage 60 (2), 1296–1306.

Ritchie, Craig W., José Luis, Molinuevo, Luc, Truyen, Andrew, Satlin, Van der Geyten, Serge, Simon, Lovestone, 2016. "Development of interventions for the secondary prevention of Alzheimer's Dementia: the European prevention of alzheimer's Dementia (EPAD) project. Lan. Psychiatr. 3 (2), 179–186.

Robertson, A.D., Matta, G., Basile, V.S., Black, S.E., Macgowan, C.K., Detre, J.A., MacIntosh, B.J., 2017. Temporal and spatial variances in arterial spin-labeling are inversely related to large-artery blood velocity. AJNR Am. J. Neuroradiol. 38 (8), 1555–1561.

Sanchez, Carmen E., Richards, John E., Robert Almli, C., 2012. Age-specific MRI templates for pediatric neuroimaging. Dev. Neuropsychol. 37 (5), 379–399.

Schmid, Sophie, Dennis, F. R. Heijtel, Mutsaerts, Henri J.M. M., Boellaard, Ronald, Lammertsma, Adriaan A., Nederveen, Aart J., Van Osch, M.J.P., Van Osch, Matthias J.P., 2015. Comparison of velocity- and acceleration-selective arterial spin labeling with [15O]H2O positron emission tomography. J. Cerebr. Blood Flow Metabol. 35 (8), 1–8.

Schmidt, P., Gaser, C., Arsic, M., Buck, D., Forschler, A., Berthele, A., Hoshi, M., et al., 2012. An automated tool for detection of FLAIR-hyperintense white-matter lesions in multiple sclerosis. Neuroimage 59 (4), 3774–3783.

Shi, Feng, Yap, Pew-Thian, Wu, Guorong, Jia, Hongjun, Gilmore, John H., Lin, Weili, Shen, Dinggang, 2011. Infant brain atlases from neonates to 1- and 2-year-olds. PloS One 6 (4), e18746.

Shin, David D., Burak Ozyurt, I., Brown, Gregory G., Fennema-notestine, Christine, Liu, Thomas T., 2016. NeuroImage the cerebral blood flow biomedical Informatics research network (CBFBIRN) data repository. Neuroimage 124, 1202–1207.

Shirzadi, Zahra, Crane, David E., Robertson, Andrew D., Maralani, Pejman J., Aviv, Richard I., Chappell, Michael A., Goldstein, Benjamin I., Black, Sandra E., MacIntosh, Bradley J., 2015. Automated removal of spurious intermediate cerebral blood flow volumes improves image quality among older patients: a clinical arterial spin labeling investigation. J. Magn. Reson. Imag. 42 (5), 1377–1385.

Shirzadi, Zahra, Stefanovic, Bojana, Chappell, Michael A., Ramirez, Joel, Schwindt, Graeme, Masellis, Mario, Black, Sandra E., MacIntosh, Bradley J., 2018. Enhancement of automated blood flow estimates (ENABLE) from arterial spin-labeled MRI. J. Magn. Reson. Imag. 47 (3), 647–655.

Smith, Stephen M., 2002. Fast robust automated brain extraction. Hum. Brain Mapp. 17 (3), 143–155.

Spann, Stefan M., Kazimierski, Kamil S., Aigner, Christoph S., Kraiger, Markus, Bredies, Kristian, Stollberger, Rudolf, 2017. Spatio-temporal TGV denoising for ASL perfusion imaging. Neuroimage 157 (January), 81–96.

Steketee, Rebecca M.E., Bron, Esther E., Meijboom, Rozanna, Houston, Gavin C., Klein, Stefan, Mutsaerts, Henri J.M. M., Mendez Orellana, Carolina P., et al., 2016. Early-Stage differentiation between presenile Alzheimer's disease and frontotemporal Dementia using arterial spin labeling MRI. Eur. Radiol. 26 (1), 244–253.

Tan, Huan, Maldjian, Joseph A., Pollock, Jeffrey M., Burdette, Jonathan H., Yang, Lucie Y., Deibler, Andrew R., Kraft, Robert A., 2009. A fast, effective filtering method for improving clinical pulsed arterial spin labeling MRI. J. Magn. Reson. Imag.: JMRI 29 (5), 1134–1139.

Tohka, Jussi, Zijdenbos, Alex, Evans, Alan, 2004. Fast and robust parameter estimation for statistical partial volume models in brain MRI. Neuroimage 23 (1), 84–97.

Václavů, Lena, Meynart, Benoit N., Mutsaerts, Henk Jmm, Thade Petersen, Esben, Blm Majoie, Charles, 2019. Hemodynamic provocation with acetazolamide shows impaired cerebrovascular reserve in adults with sickle cell disease. Haematologica 104 (4), 690–699. https://doi.org/10.3324/haematol.2018.206094.

Vaclavu, L., Veronica van der Land, Dennis F. R. Heijtel, van Osch, Matthias J.P., Cnossen, Marjon H., Majoie, Charles B.L. M., Bush, A., et al., 2016. In vivo T1 of blood measurements in children with sickle cell disease improve cerebral blood flow quantification from arterial spin-labeling MRI. AJNR Am. J. Neuroradiol. 37 (9), 1727–1732.

Vidorreta, Marta, Balteau, Evelyne, Wang, Ze, De Vita, Enrico, Pastor, María a., Thomas, David L., Detre, John a., Fernández-Seara, María a., 2014. Evaluation of segmented 3D acquisition schemes for whole-brain high-resolution arterial spin labeling at 3 T. NMR Biomed. 27 (11), 1387–1396.

Vidorreta, Marta, Wang, Ze, Rodríguez, Ignacio, Pastor, María A., Detre, John A., Fernández-Seara, María A., 2013. Comparison of 2D and 3D single-shot ASL perfusion fMRI sequences. Neuroimage 66 (February), 662–671.

Wang, Danny J.J., Chen, Yufen, Fernández-Seara, María A., Detre, John A., Fernandez-Seara, M.A., Detre, John A., Fernández-Seara, María A., Detre, John A., 2011. Potentials and challenges for arterial spin labeling in pharmacological magnetic resonance imaging. J. Pharmacol. Exp. Therapeut. 337 (2), 359–366.

Wang, Z., Geoffrey, K. Aguirre, Rao, H., Wang, J., Fernández-Seara, María A., Childress, Anna Rose, Detre, John A., 2008. Empirical optimization of ASL data analysis using an ASL data processing toolbox: ASLtbx. Magn. Reson. Imag. 26 (2), 261–269.

Wang, Ze, 2012. Improving cerebral blood flow quantification for arterial spin labeled perfusion MRI by removing residual motion artifacts and global signal fluctuations. Magn. Reson. Imag. 30 (10), 1409–1415.

Wang, Ze, 2014. Support vector machine learning-based cerebral blood flow quantification for arterial spin labeling MRI. Hum. Brain Mapp. 35 (7), 2869–2875.

Warmuth, C., Günther, Matthias, Zimmer, C., 2003. Quantification of blood flow in brain tumors: comparison of arterial spin labeling and dynamic susceptibility-weighted contrast-enhanced MR imaging. Radiology 228, 523–532.

Wells, Jack A., Thomas, David L., King, Martin D., Connelly, Alan, Lythgoe, Mark F., Calamante, Fernando, 2010. Reduction of errors in ASL cerebral perfusion and arterial transit time maps using image de-noising. Magn. Reson. Med. 64 (3), 715–724.

Wilke, Marko, Altaye, Mekibib, Holland, Scott K., Cmind Authorship Consortium, 2017. CerebroMatic: a versatile toolbox for spline-based MRI template creation. Front. Comput. Neurosci. 11 (February), 5.

Ye, F.Q., Frank, J.A., Weinberger, D.R., McLaughlin, A.C., 2000. Noise reduction in 3D perfusion imaging by attenuating the static signal in arterial spin tagging (ASSIST). Magn. Reson. Med. 44 (1), 92–100.

Zhang, Ke, Herzog, Hans, Mauler, Jörg, Filss, Christian, Okell, Thomas W., Kops, Elena Rota, Lutz, Tellmann, et al., 2014. Comparison of cerebral blood flow acquired by simultaneous [15O]water positron emission tomography and arterial spin labeling magnetic resonance imaging. JCBFM 34 (8), 1373–1380.

Zhao, Moss Y., Mezue, Melvin, Segerdahl, Andrew R., Okell, Thomas W., Tracey, Irene, Xiao, Yingyi, Chappell, Michael A., 2017. A systematic study of the sensitivity of partial volume correction methods for the quantification of perfusion from pseudo-continuous arterial spin labeling MRI. Neuroimage 162 (August), 384–397.

Zhu, Hancan, Zhang, Jian, Wang, Ze, 2018. Arterial spin labeling perfusion MRI signal denoising using robust principal component analysis. J. Neurosci. Methods 295 (February), 10–19.

Appendix A5

Early and late effects of radiochemotherapy on cerebral blood flow in glioblastoma patients measured with non-invasive perfusion MRI

Petr, J., Platzek, I., Seidlitz, A., Mutsaerts, H. J., Hofheinz, F., Schramm, G., ... & Van Den Hoff, J. (2016). Early and late effects of radiochemotherapy on cerebral blood flow in glioblastoma patients measured with non-invasive perfusion MRI. Radiotherapy and Oncology, 118(1), 24-28.

Journal name (category): **Radiotherapy and Oncology** (Oncology; Radiology, nuclear medicine & medical imaging)

Quartile in category: **Q1/Q1**

Impact factor: **6.901**

Number of WoS citations: **22**

Radiotherapy and Oncology 118 (2016) 24–28

Contents lists available at ScienceDirect

Radiotherapy and Oncology

journal homepage: www.thegreenjournal.com

Glioblastoma

Early and late effects of radiochemotherapy on cerebral blood flow in glioblastoma patients measured with non-invasive perfusion MRI

Jan Petr [a,*], Ivan Platzek [b], Annekatrin Seidlitz [c,g,h], Henri J.M.M. Mutsaerts [f], Frank Hofheinz [a], Georg Schramm [a,e], Jens Maus [a], Bettina Beuthien-Baumann [a,d], Mechthild Krause [c,g,h,i], Jörg van den Hoff [a,d]

[a] Helmholtz-Zentrum Dresden-Rossendorf, PET Center, Institute of Radiopharmaceutical Cancer Research, Dresden; [b] Department of Radiology, University Hospital Carl Gustav Carus; [c] Department of Radiation Oncology, Faculty of Medicine and University Hospital Carl Gustav Carus; [d] Department of Nuclear Medicine, University Hospital Carl Gustav Carus, Technical University Dresden, Germany; [e] Department of Imaging and Pathology, Katholieke Universiteit Leuven, Belgium; [f] Brain Sciences Research Program, Sunnybrook Research Institute, Toronto, Canada; [g] OncoRay – National Center for Radiation Research in Oncology, Faculty of Medicine and University Hospital Carl Gustav Carus, Technical University Dresden; and [h] German Cancer Consortium (DKTK) Dresden and German Cancer Research Center (DKFZ) Heidelberg, Germany; and [i] Helmholtz-Zentrum Dresden-Rossendorf, Institute of Radiooncology, Germany

ARTICLE INFO

Article history:
Received 2 October 2015
Received in revised form 8 December 2015
Accepted 11 December 2015
Available online 30 December 2015

Keywords:
ASL
Arterial spin labeling
Cerebral blood flow
Radiotherapy
Brain tumor
Perfusion

ABSTRACT

Background and purpose: To provide a systematic measure of changes of brain perfusion in healthy tissue following a fractionated radiotherapy of brain tumors.

Materials and methods: Perfusion was assessed before and after radiochemotherapy using arterial spin labeling in a group of 24 patients (mean age 54.3 ± 14.1 years) with glioblastoma multiforme. Mean relative perfusion change in gray matter in the hemisphere contralateral to the tumor was obtained for the whole hemisphere and also for six regions created by thresholding the individual dose maps at 10 Gy steps.

Results: A significant decrease of perfusion of −9.8 ± 20.9% ($p = 0.032$) compared to the pre-treatment baseline was observed 3 months after the end of radiotherapy. The decrease was more pronounced for high-dose regions above 50 Gy (−16.8 ± 21.0%, $p = 0.0014$) than for low-dose regions below 10 Gy (−2.3 ± 20.0%, $p = 0.54$). No further significant decrease compared to the post-treatment baseline was observed 6 months (−0.4 ± 18.4%, $p = 0.94$) and 9 months (2.0 ± 15.4%, $p = 0.74$) after the end of radiotherapy.

Conclusions: Perfusion decreased significantly during the course of radiochemotherapy. The decrease was higher in regions receiving a higher dose of radiation. This suggests that the perfusion decrease is at least partly caused by radiotherapy. Our results suggest that the detrimental effects of radiochemotherapy on perfusion occur early rather than later.

Radiotherapy (RT) as well as Radiosurgery (RS) are known to impair healthy tissue perfusion in various organs by damaging capillaries and larger vessels and impairing their autoregulation mechanisms [1]. Defects in cardiac perfusion measured with single-photon emission computed tomography (SPECT) using ^{99m}Tc were observed in patients with breast cancer treated with RT [2]. A large decrease of regional lung perfusion upto 80% was measured by SPECT in patients with tumors in the lung [3] or the thorax [4,5]. Cerebral blood flow (CBF) changes have also been demonstrated in healthy tissue after RS [6,7].

RT of the brain was also reported to cause a notable deterioration of cognitive performance [8,9] especially when delivered in daily fractions above 2 Gy [10] while other authors attribute the cognitive decline mainly to the presence of the tumor [11]. RT-induced CBF decrease would be one possible explanation for a cognitive decline. In any case, a detailed understanding of the relation between the received dose during RT and the CBF reduction is of obvious relevance for treatment planning as well as for diagnostic evaluation of the disease progression and for determining tissue specific dose tolerance levels.

CBF can be measured non-invasively by arterial spin labeling (ASL) which provides a facility for investigation of early and late radiochemotherapy (RCT) effects on healthy brain tissue on a population level. This may provide new insights into how the brain vasculature responds to RCT and clarify the correlation between CBF changes and neurocognitive changes.

So far, there are only very few publications studying the effect of RT and RS on CBF in healthy tissue which, moreover, report partly contradictory findings: Jakubovic et al. investigated the

* Corresponding author at: POB 51 01 19, 01314 Dresden, Germany.
E-mail address: j.petr@hzdr.de (J. Petr).

http://dx.doi.org/10.1016/j.radonc.2015.12.017
0167-8140/

dependence of perfusion changes on received dose during stereotactic RS. One month after treatment, the authors observed a significant CBF increase in gray matter (GM) in high-dose regions above 10 Gy [7]. Taki et al. studied CBF changes with ^{99m}Tc SPECT 2 weeks, and 3 months after RS of intracranial lesions. A significant CBF decrease was found in the regions with doses below 5 Gy [6]. A study by Weber et al. did not find any significant changes in the ratio of white matter (WM) to GM perfusion from 2 months to 1 year following RS with either dynamic susceptibility contrast (DSC) or ASL [12].

The aim of the present investigation is the quantitative assessment of CBF changes in healthy tissue during RCT and determination of the correlation between received radiation dose and induced CBF changes in order to augment the existing, partly contradictory literature and to contribute to the final clarification of this issue. For that purpose, data from a longitudinal study were used which is targeted at investigation of the degree of correlation between high [^{11}C]-Methionine tracer uptake in glioblastomas and time to recurrence after RCT. In this study, patients are scanned before postoperative radiooncological treatment and have regular follow-ups after the end of treatment. The perfusion was measured non-invasively using pseudo-continuous ASL (pCASL) [13,14]. To the best of our knowledge, the present investigation is the first systematic study addressing the effect of RT on healthy gray matter CBF as well as the first ASL-based study of perfusion changes following RT.

Materials and methods

Subject recruitment

All patients analyzed are part of a larger prospective, one-arm, single-center, non-randomized, observational imaging study – PETra trial (NCT01873469). The study was done in accordance with the declaration of Helsinki and it was approved by the Ethics Committee of the Faculty of Medicine at the Technische Universität Dresden (EK41022013). Data protection and patient informed consent procedures were done according to German national and state legislation.

Adult patients with newly diagnosed glioblastoma multiforme were included in the study if they fulfilled the following criteria:

- age more than 18 years, and signed a written informed consent to participate in the study,
- Karnofsky Performance Score $\geqslant$60 corresponding to performance score $\leqslant$2 according to the Eastern Cooperative Oncology Group (ECOG) [15,16],
- indication for combined RCT with Temozolomide (TMZ),
- histological confirmation of a glioblastoma multiforme,
- time interval between the last surgical procedure and onset of RCT no longer than 7 weeks.

Exclusion criteria were:

- previous radiotherapy of the brain or chemotherapy with TMZ,
- contraindications for RCT, or MRI imaging,
- known other malignant disease that impacts prognosis of the patient and/or is likely to require treatment interfering with study therapy.

Study design

The post-operative PET/MR and treatment planning CT were performed before the start of RCT. Irradiation treatment planning was done using a fusion of the planning CT with the PET/MR scan and with the postoperative MRI performed within 24 h after surgery. The RCT started 2–7 weeks after the tumor resection or biopsy. The second PET/MR scan was acquired 3 months after the end of RCT. Then, regular follow-up PET/MR scans were acquired every 3 months until objective detection of recurrence, death of the patient, or drop out.

Adjuvant radiotherapy was applied in daily fractions of 2 Gy given 5 days per week. The clinical target volume comprised the surgical cavity, macroscopic tumor areas visible in MRI or PET. A margin of 20 mm and 5 mm in all directions excluding anatomical barriers (bone, tentorium) was added in the first (CTV1) and second (CTV2) clinical target volume, respectively. CTV1 was treated to a total dose of 50 Gy. CTV2 received a boost dose of 10 Gy, adding to a total dose of 60 Gy.

Concomitant chemotherapy with TMZ (75 mg/m^2) was administered daily from the 1st day until the last day of radiotherapy followed by continuation of adjuvant chemotherapy for 6 months according to Stupp et al. [17]. Radiotherapy was delivered with linear accelerators providing photons of energies $\geqslant$6 MV. Field shaping was performed with a multileaf collimator. 3D-conformal radiotherapy plans were generated within a dedicated planning system. Intensity-modulated radiation therapy (IMRT) was used if appropriate with respect to target volume coverage or normal tissue sparing.

Acquisition

All MRI measurements were performed with a 3T Philips Ingenuity TF PET/MR scanner (Philips Healthcare, Best, The Netherlands) with an 8-channel head-coil. The following precautions to avoid CBF confounders were applied. Patients were instructed to be fasting 4 h prior to the scanning and were not instructed to change their habits regarding smoking and caffeine consumption.

A high-resolution T1-weighted isotropic 3D dataset, pCASL images, and M_0 reference images were acquired. The 3D TFE (Turbo Field Echo) T1-weighted dataset was obtained in the sagittal orientation with 1 mm isotropic resolution. Parameters of the pCASL sequence [18] were: field-of-view (FOV) 220×220 mm^2, voxel size $2.75 \times 2.75 \times 6$ mm^3, 17 slices (0.6 mm gap), 2D multi-slice gradient-echo echo planar imaging (EPI) readout, repetition time (TR)/echo time (TE) 3765/11 ms, flip angle 90°, 30 averages, background suppression [19] with optimal suppression timed for the lowest slice, labeling time/post-labeling delay (PLD) 1650/1525 ms. The delay between acquisition of successive EPI slices was 32 ms. The PLD for the central slice was thus equivalent to 1781 ms. A reference M_0 image was acquired 5000 ms after saturation. The center of the 5th or 6th slice (to ensure coverage of the whole cerebrum) was aligned with the anterior/posterior commissure line, and the distance of the center of the labeling plane from the lowest slice was 35 mm. A screen-shot of the planning was saved and the follow-up sessions were positioned similarly. The whole ASL acquisition took under 5 min.

A CT image for radiotherapy planning was acquired with a Siemens Emotion scanner (Siemens Medical Systems, Erlangen, Germany). The slice thickness was 3 mm and in-plane pixel size 1×1 mm^2.

Preprocessing and CBF quantification

Data were processed using the SPM8 toolbox (Wellcome Trust Centre for Neuroimaging, London, UK) and in–house routines written in Matlab (MathWorks, Natick, MA, USA). All pCASL dynamics and the M_0 measurement were registered to the first pCASL control image (3D rigid 6-parameter transformation with a sum-of-squares-differences cost function). For each patient and session, the T1-weighted image was co-registered with the mean pCASL control image. The T1-weighted image was segmented using SPM

and used to estimate the partial volume fractions of GM in the pCASL space. The T1-weighted images of all sessions and the planning CT (with the associated radiation-dose plans) were spatially normalized to the MNI space [20]. This allowed transformation of the dose plans to the ASL native space for each individual session.

CBF quantification was done using a single compartment model according to Eq. (1) of the ASL consensus paper [21]. A labeling efficiency of $\alpha = 0.7$ was used taking into account the efficiency of the pulse (0.85) [18], and its decrease due to background suppression (0.83) [19]. T1 of blood of 1650 ms was used [21,22].

Data evaluation

Voxels with a GM partial volume fraction below 70%, and voxels in the hemisphere ipsilateral to the tumor were excluded from GM-CBF determination. Mean CBF in the hemisphere contralateral to the tumor was calculated for all patients and sessions in the original ASL space for each session to avoid introduction of interpolation errors by co-registering the CBF maps. CBF-change and a relative CBF-change between two sessions A and B was defined as $CBF_B - CBF_A$ and $200 * (CBF_B - CBF_A)/(CBF_B + CBF_A)$, respectively. Mean of the relative CBF-changes was calculated for all subjects between successive sessions and significance of the change was evaluated using a paired t-test.

The relation between the CBF-change and the received radiation dose was studied between pre-RCT and the first post-RCT session, and between the first three post-RCT sessions. To study the relationship between the radiation dose and CBF, individual dose maps were divided into dose regions by categorizing them into 10 Gy steps. Mean CBF was calculated for each region for each session. Mean relative CBF-change was then calculated for each dose across all patients.

Results

Study group

In the present investigation, 28 patients from the PETra trial were used. All of them have already completed RCT. Scans were performed prior to RCT and 1–3 times post-RCT. Altogether, a total of 112 scans were analyzed. Several scan sessions had to be excluded due to excessive motion ($n = 2$), complete failure of labeling ($n = 1$), missing ASL measurement ($n = 2$), measurements done on a different scanner during a scheduled PET/MR shutdown ($n = 7$), or tumor comorbidity on the contralateral side ($n = 2$). Due to these problems, 4 patients had to be excluded and 24 patients (mean age 54.3 ± 14.1 years, range $25.3 - 75.3$ y, median 58.5 y) could be used for further analysis. The number of patients scanned on each session and the interval between sessions is shown in Table 1.

Global CBF change

A representative CBF map and a radiation dose plan normalized to the MNI space are displayed for a single slice and a single patient in Fig. 1.

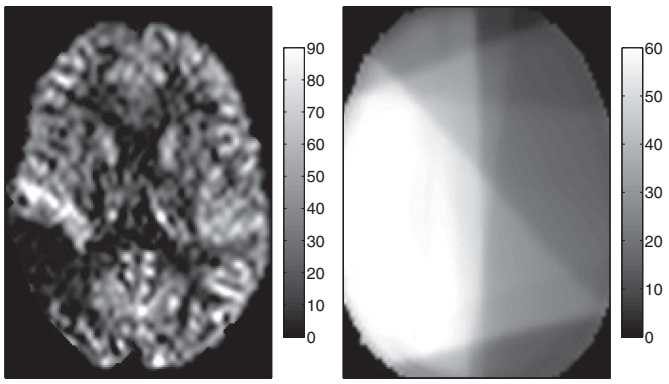

Fig. 1. Representative CBF-image (left, [mL/min/100 g]) (2nd post-RCT session) and received radiation dose (right, [Gy]) (spatially normalized to the MNI template). Hyper-perfusion in region anterior to postoperative dead space indicate tumor recurrence (left in the image). The CBF changes were evaluated in the contralateral hemisphere (right in the image).

The mean CBF values in the hemisphere contralateral to the tumor for the first four sessions and the mean relative difference for successive sessions are given in Table 1. The only statistically significant decrease in CBF occurred between the pre-RCT and (any of the) post-RCT sessions. CBF changes between different post-RCT sessions did not reach statistical significance.

CBF change vs. radiation dose

The CBF-changes between pre-RCT and post-RCT, and first two post-RCT sessions depending on the received radiation dose are shown in Table 2. The mean size of the regions relative to the whole GM volume is shown in the table as well. A graph showing the relative decrease of CBF as a function of received radiation dose is in Fig. 2. The perfusion decrease between the pre-RCT and post-RCT session was significant for all doses higher than 10 Gy, and the decrease was almost two times larger for doses higher than 20 Gy than for doses lower than 20 Gy. No significant change was observed between the first two post-RCT sessions for any dose.

Discussion

In this investigation, we have quantified CBF-changes in the hemisphere contralateral to the tumor in patients with glioblastoma multiforme undergoing radiochemotherapy. We have observed significant changes of global GM CBF shortly after the end of the radiotherapy. Regarding regional effects, CBF-change was negatively correlated to the locally received radiation dose.

Perfusion decrease and radiation dose

Effects of radiation on perfusion are known and have repeatedly been reported. Qualitatively, our results are in accord with some of previous findings, confirming higher decrease of perfusion for

Table 1
Global CBF changes.

Session		CBF_A (mL/min/100 g)	CBF_B (mL/min/100 g)	Number of patients	ΔCBF (%)	*P*-value	Interval (months)
A	B						
Pre	Post 1	54.0 ± 8.4	49.6 ± 10.6	24	-9.8 ± 20.9	0.032	4.8 ± 0.4
Post 1	Post 2	51.4 ± 7.7	51.3 ± 9.1	13	-0.4 ± 18.4	0.94	3.4 ± 0.5
Post 2	Post 3	52.0 ± 8.9	53.4 ± 10.9	7	2.0 ± 15.4	0.74	3.1 ± 0.5

For different pairs of sessions A and B the mean CBF in GM, the mean relative CBF-change between the two sessions, the p-value for the difference, the number of patients available and the time between session are given. A significant CBF-decrease is observed between the pre-RCT and first post-RCT session.

Table 2
Dose-related CBF changes.

	Dose (Gy)	0–10	10–20	20–30	30–40	40–50	50–60
	ΔCBF (%)	−2.3	−7.5	−13.5	−17.5	−16.0	−16.8
Pre-/Post-RCT 1	Region size (%)	30	32	17	11	5	6
	P-value	0.54	0.05	0.023*	0.021*	0.0026†	0.0014†
	ΔCBF (%)	1.5	1.0	−0.6	−1.4	3.0	1.6
Post-RCT 1/2	Region size (%)	33	32	16	9	5	5
	P-value	0.39	0.94	0.89	0.98	0.52	0.79
	ΔCBF (%)	13.4	0.1	−0.2	−4.0	−2.5	−2.0
Post-RCT 2/3	Region size (%)	34	30	17	9	5	6
	P-value	0.95	0.52	0.93	0.42	0.95	0.53

Mean relative CBF-change in dose regions created by categorizing the radiation-dose received into 10 Gy steps. The mean size of the region (as percentage of whole GM) is also displayed. CBF changes are given between the pre-RCT and the first post-RCT and also between the first three post-RCT sessions. A significant decrease is seen between the pre-RCT and post-RCT sessions for doses higher than 10 Gy (marked * for $p < 0.05$, † for $p < 0.01$). No significant changes are present for lower doses or between post-RCT sessions.

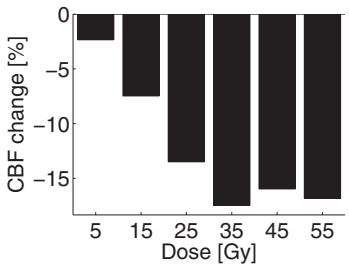

Fig. 2. Dose dependent mean relative GM-CBF change between pre-RCT and first post-RCT session. The radiation-dose map was categorized using six regions with dose between 0–10 Gy, 10–20 Gy, 20–30 Gy, 30–40 Gy, 40–50 Gy, and 50–60 Gy.

higher dose. This has been reported for lung perfusion [4,5,3], although the reported effect sizes are different. Taki et al. reported a 7% global decrease of CBF at 2 weeks and at 3 months after stereotactic RS. However, the highest decrease was found in the low dose regions between 5–2 Gy and below 2 Gy [6]. Jakubovic et al. analyzed the dependence of the CBF decrease related to the received dose in stereotactic RS divided into 2 Gy steps. A 36% increase of CBF was observed for high doses (>16 Gy) and a 17% increase for very small doses (<2 Gy) [7]. The are several possible explanations for the discrepancies between results in [7,6] and our results. Early CBF decrease from one week to one month contrary to CBF increase after three months can be explained by early vessel dilation followed by capillary collapse and occlusion after progressive loss of endothelial cells [7,23]. It should also be noted that we have evaluated changes in the hemisphere contralateral to the tumor while Jakubovic et al. focused on a region close to the RS target [7]. Lastly, the results by Taki et al. at three months after RS were obtained only for five patients. Further studies that would examine the acute and late changes in CBF in a single study on a large number of patients are thus needed.

Interestingly, a considerable decrease of perfusion is present in low-dose regions as well. This might indicate that the capillary bed is substantially affected even after low dose irradiation. Alternatively, the effect might be caused by damage to a supplying artery. It would thus be interesting to look for CBF-changes in regions receiving no radiation at all. However, in our study, no such tissue regions were available within the field of view of the imaging sessions.

CBF decrease in the low-dose regions might also be caused by other factors, e.g. by chemotherapy. For example Bevacuzimab, often used together with TMZ in glioblastoma patients, was shown to significantly decrease CBF [24]. A clear decrease in CBF was also observed for chemotherapy with Methotrexate in small animals [25]. In our study, conservative treatment was chosen [17] and neither Bevacuzimab nor other angiogenesis inhibitors was used. So far, TMZ is not known to alter perfusion and our data do not allow to prove or disprove an influence on CBF, thus a potential role of the chemotherapy can currently not be completely excluded but appears not likely. However, a large CBF decrease in low-dose regions was also observed in the study by Taki et al. (4–7% decrease for doses between 2 and 5 Gy and 7–22% decrease for doses below 2 Gy) [6] where RS only was performed, supporting the hypotheses of a direct influence of RT even in low dose regions.

Long-term changes of perfusion

In previous studies, a decrease of perfusion was detectable shortly after the end of RT. However, a further decline has been reported months or even years afterward. In the case of lung perfusion, the most pronounced perfusion decrease was observed until 12 [4], 15 [3], or 18 months [5] after the end of RT. Afterward, the perfusion values stabilized and did not further decrease. In our data, no further significant decrease of CBF was apparent between the different post-RCT sessions. However, there was only a limited number of patients acquired on more than 2 sessions and more data need to be gathered to be able to confirm or disprove these phenomena in RT of brain.

Several studies showed differences in CBF assessed with ASL between high- and low-grade primary brain tumors on the group [26–29] and individual [30,31] level. To further reduce the inter-session variance of the CBF measurement and to make the quantification more accurate, a tumor blood flow (TBF) normalization to reference healthy tissue is often employed [26,28,30,31]. While this is perfectly justifiable in most studies where the contralateral tissue is not affected by disease, it may not be the case in patients undergoing RT. The findings presented in this study might thus possibly be used to account at least approximately for the bias introduced by variation of CBF in the healthy tissue reference region or to guide in reference region selection to minimize its confounding effect.

Limitations

There are several potential limitations of this study which need to be considered.

First of all, the measurements were performed at any time between 9:00 and 16:00 due to tracer production constraints. Although time slots of early morning and late evening were avoided, variability of the chosen scan time point might influence the CBF. The mean day-times of the ASL acquisitions were 13:53, 12:28, 13:42, and 13:11 for the pre-RCT and post-RCT sessions, respectively. These differences are unlikely to cause significant changes in perfusion between sessions. Scheduling the first

post-RCT earlier than the pre-RCT session would increase the CBF [32] while the opposite is observed from our data.

There was no pre-selection of patients based on the position of the tumor. Tumor locations and thus also the clinical target volumes were thus randomly distributed in the study population. This should decrease the influence of longer arrival times in certain brain regions and make the results also less susceptible to problems with labeling efficiency for certain vascular regions. A single inversion-time ASL was used without vascular crusher gradients employed. A possible prolongation of arrival times caused by RCT would thus go unnoticed causing vascular artifacts and elevating the perceived CBF. This could mask a more serious decrease of CBF. Although this is not likely to cause severe changes to our results a study using multi inversion-time measurement would be beneficial to address this limitation.

A clear correlation between CBF decrease and radiation-dose existed only at the group level. However, the individual patient data are relatively noisy due to both, physiological perfusion fluctuation as well as the inherently relatively low SNR of the ASL-derived CBF values. Investigating larger patient groups in the future might help to disentangle the different effects of radiochemotherapy on different brain tissues and their long-term changes.

Conclusion

In this study, we have shown the ability of non-invasive ASL perfusion imaging to study the effects of radiochemotherapy on brain perfusion. A significant decrease of perfusion in the healthy tissue following a focal radiotherapy in brain tumor patients was shown. To the best of our knowledge, this is the first study using ASL to study CBF changes due to radio- and chemotherapy. Higher decrease of CBF was shown to be associated with higher radiation-dose received. A further study with more patients and longer follow-up would be needed to assess long-term CBF changes and to investigate whether they are irreversible or not. Also, correlation of clinical symptoms, i.e. neurocognitive evaluations would be interesting for further clinical studies.

Conflict of interest statement

The authors have nothing to disclose.

References

[1] O'Connor M, Mayberg M. Effects of radiation on cerebral vasculature: a review. Neurosurgery 2000:138–49.

[2] Marks LB, Yu X, Prosnitz RG, Zhou SM, Hardenbergh PH, Blazing M, et al. The incidence and functional consequences of RT-associated cardiac perfusion defects. Int J Radiat Oncol 2005;63:214–23.

[3] Scheenstra AEH, Rossi MMG, Belderbos JS, Damen EMF, Lebesque JV, Sonke JJ. Local dose-effect relations for lung perfusion post stereotactic body radiotherapy. Radiother Oncol 2013;107:398–402.

[4] Woel RT, Munley MT, Hollis D, Fan M, Bentel G, Anscher MS, et al. The time course of radiation therapy-induced reductions in regional perfusion: a prospective study with >5 years of follow-up. Int J Radiat Oncol 2002;52:58–67.

[5] Zhang J, Ma J, Zhou S, Hubbs JL, Wong TZ, et al. Radiation-induced reductions in regional lung perfusion: 0.1-12 Year data from a prospective clinical study. Int J Radiat Oncol 2010;76:425–32.

[6] Taki S, Higashi K, Oguchi M, Tamamura H, Tsuji S, Ohta K, et al. Changes in regional cerebral blood flow in irradiated regions and normal brain after stereotactic radiosurgery. Ann Nucl Med 2002;16:273–7.

[7] Jakubovic R, Sahgal A, Ruschin M, Pejovic-Milic A, Milwid R, Aviv RI. Non tumor perfusion changes following stereotactic radiosurgery to brain metastases. Technol Cancer Res Treat 2014.

[8] Taphoorn MJB, Klein M. Cognitive deficits in adult patients with brain tumours. Lancet Neurol 2004;3:159–68.

[9] Roman DD, Sperduto PW. Neuropsychological effects of cranial radiation: current knowledge and future directions. Int J Radiat Oncol 1995;31:983–98.

[10] Douw L, Klein M, Fagel SS, van den Heuvel J, Taphoorn MJ, Aaronson NK, et al. Cognitive and radiological effects of radiotherapy in patients with low-grade glioma: long-term follow-up. Lancet Neurol 2009;8:810–8.

[11] Brown PD, Buckner JC, O'Fallon JR, Iturria NL, Brown C, O'Neill BP, et al. Effects of radiotherapy on cognitive function in patients with low-grade glioma measured by the folstein mini-mental state examination. J Clin Oncol 2003;21:2519–24.

[12] Weber MA, Günther M, Lichy MP, Delorme S, Bongers A, Thilmann C, et al. Comparison of arterial spin-labeling techniques and dynamic susceptibility-weighted contrast-enhanced MRI in perfusion imaging of normal brain tissue. Invest Radiol 2003;38:712–8.

[13] Detre JA, Leigh JS, Williams DS, Koretsky AP. Perfusion imaging. Magn Reson Med 1992;23:37–45.

[14] Telischak NA, Detre JA, Zaharchuk G. Arterial spin labeling MRI: clinical applications in the brain. J Magn Reson Imaging 2014.

[15] Karnofsky DA. The clinical evaluation of chemotherapeutic agents in cancer. Evaluation of chemotherapeutic agents; 1949.

[16] Oken MM, Creech RH, Tormey DC, Horton J, Davis TE, McFadden ET, et al. Toxicity and response criteria of the eastern cooperative oncology group. Am J Clin Oncol 1982;5:649–56.

[17] Stupp R, Mason WP, Van Den Bent MJ, Weller M, Fisher B, Taphoorn MJ, et al. Radiotherapy plus concomitant and adjuvant temozolomide for glioblastoma. New Engl J Med 2005;352:987–96.

[18] Dai W, Garcia D, de Bazelaire C, Alsop DC. Continuous flow-driven inversion for arterial spin labeling using pulsed radio frequency and gradient fields. Magn Reson Med 2008;60:1488–97.

[19] Garcia DM, Duhamel G, Alsop DC. Efficiency of inversion pulses for background suppressed arterial spin labeling. Magn Reson Med 2005;54:366–72.

[20] Mazziotta J, Toga A, Evans A, Fox P, Lancaster J, Zilles K, et al. A probabilistic atlas and reference system for the human brain: International consortium for brain mapping (ICBM). Philos Trans R Soc B 2001;356:1293–322.

[21] Alsop DC, Detre JA, Golay X, Günther M, Hendrikse J, Hernandez-Garcia L, et al. Recommended implementation of arterial spin-labeled perfusion MRI for clinical applications: a consensus of the ISMRM perfusion study group and the European consortium for ASL in dementia. Magn Reson Med 2015;73:102–16.

[22] Lu H, Clingman C, Golay X, van Zijl PCM. Determining the longitudinal relaxation time (T1) of blood at 3.0 Tesla. Magn Reson Med 2004;52:679–82.

[23] Cao Y, Tsien C, Sundgren P, Nagesh V, Normolle D, Buchtel H, et al. Dynamic contrast-enhanced magnetic resonance imaging as a biomarker for prediction of radiation-induced neurocognitive dysfunction. Clin Cancer Res 2009:1747–54.

[24] Andre JB, Nagpal S, Hippe DS, Ravanpay AC, Schmiedeskamp H, Bammer R, et al. Cerebral blood flow changes in glioblastoma patients undergoing bevacizumab treatment are seen in both tumor and normal brain. Neuroradiology 2015;28:112–9.

[25] Seigers R, Fardell JE. Neurobiological basis of chemotherapy-induced cognitive impairment: a review of rodent research. Neurosci Biobehav Rev 2011;35:729–41.

[26] Noguchi T, Yoshiura T, Hiwatashi A, Togao O, Yamashita K, Nagao E, et al. Perfusion imaging of brain tumors using arterial spin-labeling: correlation with histopathologic vascular density. Am J Neuroradiol 2008;29:688–93.

[27] Warmuth C, Gunther M, Zimmer C. Quantification of blood flow in brain tumors: comparison of arterial spin labeling and dynamic susceptibility-weighted contrast-enhanced MR imaging. Radiology 2003;228:523–32.

[28] Yeom KW, Mitchell LA, Lober RM, Barnes PD, Vogel H, Fisher PG, et al. Arterial spin-labeled perfusion of pediatric brain tumors. Am J Neuroradiol 2014;35:395–401.

[29] Cebeci H, Aydin O, Ozturk-Isik E, Gumus C, Inecikli F, Bekar A, et al. Assessment of perfusion in glial tumors with arterial spin labeling; comparison with dynamic susceptibility contrast method. Eur J Radiol 2014;83:1914–9.

[30] Fudaba H, Shimomura T, Abe T, Matsuta H, Momii Y, Sugita K, et al. Comparison of multiple parameters obtained on 3T pulsed arterial spin-labeling, diffusion tensor imaging, and MRS and the Ki-67 labeling index in evaluating glioma grading. Am J Neuroradiol 2014;35:2091–8.

[31] Kim MJ, Kim HS, Kim JH, Cho KG, Kim SY. Diagnostic accuracy and interobserver variability of pulsed arterial spin labeling for glioma grading. Acta Radiol 2008;49:450–7.

[32] Hodkinson DJ, O'Daly O, Zunszain PA, Pariante CM, Lazurenko V, Zelaya FO, et al. Circadian and homeostatic modulation of functional connectivity and regional cerebral blood flow in humans under normal entrained conditions. J Cereb Blood Folw Metab 2014;34:1493–9.

Appendix A6

Photon vs. proton radiochemotherapy: Effects on brain tissue volume and perfusion

Petr, J., Platzek, I., Hofheinz, F., Mutsaerts, H. J., Asllani, I., van Osch, M. J., ... & van den Hoff, J. (2018). Photon vs. proton radiochemotherapy: Effects on brain tissue volume and perfusion. Radiotherapy and Oncology, 128(1), 121-127.

Journal name (category): **Radiotherapy and Oncology** (Oncology; Radiology, nuclear medicine & medical imaging)

Quartile in category: **Q1/Q1**

Impact factor: **6.901**

Number of WoS citations: **25**

Radiotherapy and Oncology 128 (2018) 121–127

Contents lists available at ScienceDirect

Radiotherapy and Oncology

journal homepage: www.thegreenjournal.com

Proton therapy

Photon vs. proton radiochemotherapy: Effects on brain tissue volume and perfusion

Jan Petr [a,*], Ivan Platzek [b], Frank Hofheinz [a], Henri J.M.M. Mutsaerts [c,d,e,f,g], Iris Asllani [f], Matthias J.P. van Osch [h], Annekatrin Seidlitz [i,j,k,l], Pawel Krukowski [m], Andreas Gommlich [j,n], Bettina Beuthien-Baumann [l,o], Christina Jentsch [i,j,l,p], Jens Maus [a], Esther G.C. Troost [i,j,k,l,n,p], Michael Baumann [i,j,l,n], Mechthild Krause [i,j,k,l,n,p,1], Jörg van den Hoff [a,o,1]

[a] Helmholtz-Zentrum Dresden-Rossendorf, PET Center, Institute of Radiopharmaceutical Cancer Research; [b] Department of Radiology, University Hospital Carl Gustav Carus, Technische Universität Dresden, Germany; [c] Sunnybrook Research Institute, Toronto, Canada; [d] Department of Radiology, Academic Medical Center Amsterdam; [e] Department of Radiology, University Medical Center Utrecht, The Netherlands; [f] Rochester Institute of Technology, Rochester, USA; [g] Department of Radiology, VU University Medical Center, Amsterdam, The Netherlands; [h] Department of Radiology, Leiden University Medical Center; [i] Department of Radiation Oncology, University Hospital Carl Gustav Carus, Technische Universität Dresden; [j] OncoRay – National Center for Radiation Research in Oncology (NCRO), Faculty of Medicine and University Hospital Carl Gustav Carus, Technische Universität Dresden, and Helmholtz-Zentrum Dresden-Rossendorf; [k] German Cancer Consortium (DKTK), Dresden; [l] German Cancer Research Center (DKFZ), Heidelberg; [m] Department of Neuroradiology, University Hospital Carl Gustav Carus, Technische Universität Dresden; [n] Helmholtz-Zentrum Dresden-Rossendorf, Institute of Radiooncology; [o] Department of Nuclear Medicine, University Hospital Carl Gustav Carus, Technische Universität Dresden; and [p] National Center for Tumor Disease (NCT), Dresden, Germany

ARTICLE INFO

Article history:
Received 2 September 2017
Received in revised form 16 November 2017
Accepted 21 November 2017
Available online 19 January 2018

Keywords:
Arterial spin labeling
Cerebral blood flow
Radiochemotherapy
Brain atrophy
Proton beam therapy

ABSTRACT

Background and purpose: To compare the structural and hemodynamic changes of healthy brain tissue in the cerebral hemisphere contralateral to the tumor following photon and proton radiochemotherapy.
Materials and methods: Sixty-seven patients (54.9 ±14.0 years) diagnosed with glioblastoma undergoing adjuvant photon ($n = 47$) or proton ($n = 19$) radiochemotherapy with temozolomide after tumor resection underwent T1-weighted and arterial spin labeling MRI. Changes in volume and perfusion before and 3 to 6 months after were compared between therapies.
Results: A decrease in gray matter (GM) (−2.2%, $P < 0.001$) and white matter (WM) (−1.2%, $P < 0.001$) volume was observed in photon-therapy patients compared to the pre-radiotherapy baseline. In contrast, for the proton-therapy group, no significant differences in GM (0.3%, $P = 0.64$) or WM (−0.4%, $P = 0.58$) volume were observed. GM volume decreased with 0.9% per 10 Gy dose increase ($P < 0.001$) and differed between the radiation modalities ($P < 0.001$). Perfusion decreased in photon-therapy patients (−10.1%, $P = 0.002$), whereas the decrease in proton-therapy patients, while comparable in magnitude, did not reach statistical significance (−9.1%, $P = 0.12$). There was no correlation between perfusion decrease and either dose ($P = 0.64$) or radiation modality ($P = 0.94$).
Conclusions: Our results show that the tissue volume decrease depends on radiation dose delivered to the healthy hemisphere and differs between treatment modalities. In contrast, the decrease in perfusion was comparable for both irradiation modalities. We conclude that proton therapy may reduce brain-volume loss when compared to photon therapy.
 Radiotherapy and Oncology 128 (2018) 121–127

Glioblastoma is the most common primary malignant brain tumor in adults. The standard therapy is maximal surgical resection followed by radiotherapy (RT) with concurrent and adjuvant chemotherapy using temozolomide [35]. Both RT and chemotherapy are, however, associated with risks of cognitive deficits and structural and hemodynamic changes in the normal brain tissue [3,1].

Brain atrophy may appear as a side-effect of RT and a progressive decrease in gray matter (GM) volume over time and a dependence on radiation dose have been reported after photon RT [29,18,17,32,33]. Interestingly, no significant changes in white matter (WM) volume were observed in the same studies, despite finding WM fiber damage following RT from diffusion MRI data [7,9].

RT was also shown to cause vessel-wall thickening and endothelial cell loss leading to cerebral microbleeds and occlusions in the microvasculature [24,25]. These changes could in turn affect the healthy-tissue perfusion. Several studies have investigated the

* Corresponding author at: Bautzner Landstraße 400, 01328 Dresden, Germany.
E-mail address: j.petr@hzdr.de (J. Petr).
[1] These authors contributed equally to the manuscript.

https://doi.org/10.1016/j.radonc.2017.11.033
0167-8140/

influence of RT on brain perfusion with mostly contradictory conclusions. Perfusion decreases have been detected by dynamic susceptibility contrast and arterial spin labeling (ASL) MRI, and with ^{99m}Tc–HMPAO scintigraphy [36,28,27,11]; whereas perfusion increases have been measured using a computed tomography (CT)-perfusion, dynamic susceptibility contrast MRI, and ^{15}O-H_2O PET [22,14,15].

We posit that reduction in healthy tissue damage following radiochemotherapy (RCT) may be achieved using proton instead of photon RT. Proton therapy offers better dose distribution while exploiting comparable biological effectiveness [19]. In this study, we aimed to assess potential benefits of proton over photon therapy in terms of reducing damage to healthy brain tissue. We investigated the early-delayed brain volume and perfusion changes in healthy tissue at 3 and 6 months after RT, correlated the changes to the delivered radiation dose, and compared the differences between radiation modalities.

Methods

Participants and experimental design

The present investigation concerns the first two follow-up sessions of patients treated in the prospective, two-arm (photon and proton therapy), single-center non-randomized imaging trial "Observational study of impact of [^{11}C]-methionine PET/MRI as a tool for individual tailoring postoperative radiochemotherapy for patients with glioblastoma multiforme" (PETra). This trial was designed to validate the value of [^{11}C]-methionine PET as an imaging biomarker for predicting the location of recurrence as a basis for future radiotherapy dose-escalation approaches. Patient accrual lasted from September 2013 until October 2016 and the results according to the endpoints laid down in the protocol will be reported separately.

The registered trial (NCT01873469) was conducted in accordance with the Declaration of Helsinki and was approved by the Ethics Committee of the Faculty of Medicine at the Technische Universität Dresden, Germany (EK41022013). All patients provided written informed consent.

The main inclusion criteria of the PETra trial included newly diagnosed glioblastoma, age $\geqslant$18 years and Karnofsky's Performance Score $\geqslant$60. After clinical introduction of proton-beam therapy at the University Proton Therapy Dresden at December 2014, the choice of treatment with photon or proton-beam therapy depended on the decision of the treating physician, the patient and on reimbursement of the costs. The current investigation included only those patients for which MRI scans prior to initiation of RCT were available, who had unilateral tumor localization before RCT, who received all planned fractions of photon- or proton-beam irradiation, and who were scanned at least once after the end of RCT. In total, 72 patients (51 photon, 21 proton) were included in this imaging study (mean age 54.3 ± 14.2 years, range 23.2–81.8 years, 29 female).

The first MR session was performed after surgery and before start of RCT. For each patient, imaging data also included [^{11}C]-Methionine PET and treatment-planning CT scans. RT treatment started 2–7 weeks after full or partial tumor resection or biopsy. After the end of RT, follow-up MRI scans were acquired every 3 months for two years or until disease progression or drop out of the patient. Here we present follow-up data at 3 and 6 months after the end of RT.

Radiation treatment planning was based on the CT and PET/MRI scans. The margin of the clinical target volume (CTV) around the surgical cavity and macroscopic tumor was 20 mm for the volume treated up to 50 Gy (2 Gy per fraction) and 5 mm for the boost volume treated with an additional 10 Gy (2 Gy per fraction) to a total dose of 60 Gy (60 GyE for proton therapy). A 5 mm margin was added for the planning target volume.

Photon-based radiation treatment plans were generated using either 3D conformal radiotherapy(3DCRT) (Oncentra Masterplan 3.1, Nucletron, Veenendaal, The Netherlands; $n = 27$) or intensity-modulated radiotherapy (IMRT) (Pinnacle 9.0, Philips, Eindhoven, The Netherlands; $n = 24$). Photon RT was delivered with linear accelerators with multileaf collimator (Siemens Healthcare, Erlangen, Germany) providing photons of energies 15 and 6 MV. Proton beam treatment plans were generated using passive double scattering technique (XiO, Nucletron) and therapy was delivered with a cyclotron providing energies of 100 MeV–230 MeV.

Concomitant chemotherapy with the cytostatic agent temozolomide was performed according to Stupp et al. [35].

Image acquisition

All imaging was performed on a 3T Philips Ingenuity TF PET/MRI scanner (Philips Healthcare, Best, The Netherlands) with an 8-channel head-coil.

On each session, a 3D Turbo Field Echo T1-weighted (T1w) image was acquired with a $1 \times 1 \times 1$ mm^3 resolution. A pseudo-continuous ASL sequence [10] with background suppression [12] was used to acquire perfusion-weighted images as described in detail previously [27]: voxel size $2.75 \times 2.75 \times 6$ mm^3, 17 slices (0.6 mm gap), 2D echo-planar-imaging readout, TR/TE 3765/11 ms, 30 averages, labeling time 1650 ms, post-labeling delay for the first and last slice 1525 and 2037 ms, respectively. An M_0 image was acquired with TR 5000 ms.

Preprocessing and perfusion quantification

All image processing was fully automatic and was done using SPM12 (Wellcome Trust Centre for Neuroimaging, London, UK), and in-house routines written in Matlab (MathWorks, Natick, MA, USA) based on ExploreASL, with specific modifications to accommodate brain deformations by the tumor and surgery.

The T1w image was segmented using SPM12 [4] with enhanced tissue priors [21] providing a relative content of GM, WM, and CSF in each voxel, see Supplementary Fig. 1B. To avoid the bias in segmentation caused by the presence of tumor and surrounding edema, both hemispheres were segmented separately. The T1w image was rigid-body co-registered with the mean ASL control image. Perfusion defined as regional cerebral blood flow (CBF) was quantified from the raw ASL data using the single compartment model [2] and provided voxel-wise in mL/min/100 g, see perfusion maps in Supplementary Fig. 1D.

For the pre-therapeutic sessions, the CT image with the radiation dose map was co-registered to the T1w image as shown in Supplementary Fig. 1. For the post-therapeutic sessions, the T1w images were non-linearly registered to the pre-therapeutic T1w images [5] to allow regional comparison of dose and volumes across sessions.

Imaging data exclusion

ASL images were examined by two researchers (JP, HM) with 7 years of experience in ASL image processing. Images with severe motion or acquisition artifacts were excluded from further analysis.

T1w images were examined by a radiologist (IP) with 12 years of experience. Images with severe motion artifacts, which could lead to false decreases in GM volume [30], were excluded. Post-RCT sessions with new morphological findings in WM compared to the pre-RCT baseline (e.g. edema, leukoencephalopathy) were also excluded.

Post-RCT sessions with bilateral tumor progression, as assessed on contrast enhanced T1w images and PET images, were excluded from both perfusion and volume analyses.

Statistical analysis

Between-session changes in brain volume and perfusion were evaluated in the healthy hemisphere contralateral to the tumor. Volume of GM, WM, and total brain tissue (sum of GM and WM) in the hemisphere contralateral to the tumor was calculated automatically from the segmented T1w images by summing the voxel-wise tissue content across all voxels. Mean GM perfusion was calculated as an average voxel-wise perfusion across the voxels with GM content exceeding 70%. Relative volume and perfusion changes between sessions A and B were calculated as $100\% * mean(value_B - value_A)/mean(value_A)$ where $value_A$, $value_B$ corresponded to the subject volume or perfusion on sessions A, B, respectively. A two-tailed paired *t*-test was used to assess the statistical significance of the differences. Normality of the distribution was verified by a Shapiro–Wilk test prior to application of the *t*-test. $P < 0.05$ was considered statistically significant in all analyses. Differences were compared between the photon- and proton-therapy patient groups and also for the two subgroups of the photon therapy – 3DCRT and IMRT.

To study radiation-dose dependence, dose regions were created for each participant by categorizing the voxels of the healthy hemisphere according to received dose into bins of 0–10, 10–60, 10–20, 20–30, 30–60 Gy. Both narrower bins and no division of regions with dose above 10 Gy were used to be able to study high-dose regions in more detail and also to accommodate for the fact that the amount of voxels in high-dose regions was small for the proton therapy. Statistical significance of the differences from a zero change and a change compared to the region with dose below 10 Gy was tested using simple and paired t-tests, respectively. For the perfusion analysis, dose-regions were restricted to voxels with GM $\geqslant$ 70% and regions smaller than 5 cm^3 were excluded. For the volume analysis, a threshold of 35 cm^3 was used since this analysis was not restricted to GM voxels. Both thresholds were approximately 5% of the total considered volume of around 150 cm^3 (for perfusion) and 700 cm^3 (for volume).

Additionally, a multivariate linear regression was performed to investigate to what extent the total tissue volume or perfusion was influenced by patient age, time from the baseline scan, and mean dose received in the healthy hemisphere. The radiation modality was not included in the multivariate analysis as it was strongly correlated with the mean dose (R=-0.80, P=10^{-22}).

Results

Patient characteristics

After excluding images with artifacts, 41 photon- (22 3DCRT and 19 IMRT) and 16 proton-therapy patients were included in the volume analysis, and 44 photon- (25 3DCRT and 19 IMRT) and 16 proton-therapy patients were included in the perfusion analysis, see Table 1. Details of exclusion reasons are provided in Supplementary Tables 1 and 2. There was no difference between the proton- and photon-therapy groups and subgroups in neither of age ($P > 0.25$), ECOG score ($P > 0.11$), BMI ($P > 0.23$), or chemotherapy duration ($P > 0.34$) for neither of the volume and perfusion analysis. CTV did not differ between proton and photon-therapy groups ($P > 0.73$), but there was around 20% difference between the two photon-therapy subgroups ($P < 0.022$). Example of mean dose distribution and dose histograms for the different RT modalities are shown in Supplementary Figs. 3 and 4, respectively. The average mean dose in the healthy hemisphere was 19.1 Gy for the CRT-, 26.2 Gy for the IMRT-, 22.2 Gy for the photon-, and 4.2 Gy for the proton-therapy group and the difference was significant between all groups.

Tissue volume changes following RT treatment

For all photon-therapy patients on both follow-up sessions, both GM and WM volumes decreased compared to the baseline (between −1.2 and −3.0%, $P < 0.003$, Table 2, Fig. 1) whereas no significant changes were observed for the proton-therapy patients (between 0.3 and −0.8%, $P > 0.27$, Table 2). The effect of RT modality on volume changes was significant ($P = 3 \cdot 10^{-4}$). The parenchymal volume seems to further decrease between the two post-therapeutic sessions (−0.8%, $P > 0.027$ for the photon-; and −0.8%, $P > 0.0025$ for the proton-therapy group). The volume decreased significantly for both the 3DCRT and IMRT subgroups with higher decrease in the IMRT group. On the first post-therapy session, the volume decrease was significantly higher in both the 3DCRT (P = 0.045) and the IMRT (P = 0.0049) groups than in the proton-therapy group, however, was not different between the 3DCRT and IMRT groups (P = 0.15).

Dose-dependent GM volume changes are provided in Table 3. The GM volume decreased significantly in the first post-therapeutic session compared to the pre-therapeutic session in all regions for the photon-therapy patients (up to −3.1%, $P = 10^{-5}$). In the regions with dose above 10 Gy, the decrease was almost two times as high as in the region with dose below 10 Gy (−1.6%, P = 0.026). Significant decreases in GM volume on the second post-therapeutic session compared to the pre-therapeutic session were also observed in all patients (between −1.6% and −3.6%, $P < 0.018$) except in the region with dose below 10 Gy (−1.6%, P = 0.12). Significant differences ($P < 0.032$) between the volume decrease in high-dose (−3.2–−4.1%) than in the low-dose (0.6–−0.4%) regions were observed in the proton-therapy as well despite the small size of the high-dose regions.

The results of the multivariate linear regression showed that the mean received dose in the healthy hemisphere, time after treatment and age had a statistically significant effect on the volume decrease of 0.9%/10 Gy ($P = 10^{-5}$), 0.25%/month (P = 0.026), and 0.03% (P = 0.021), respectively, while the effect of sex ($\beta = -0.59$, P = 0.13), BMI ($\beta = 0.07$, P = 0.14), chemotherapy duration ($\beta = -0.02$, P = 0.63), and CTV ($\beta = 0$, P = 0.74) was not statistically significant. Scatter plots of tissue-volume decrease vs. mean dose, time, and age, respectively, are shown in Supplementary Fig. 2.

Gray matter perfusion changes following RT treatment

The mean relative perfusion changes in the whole healthy hemisphere are shown in Table 4. A statistically significant decrease in perfusion was observed on both post-therapeutic sessions compared to the pre-therapeutic session for the photon-therapy patients (relative change was −10.1%, P = 0.002 on first; and −11.1%, P = 0.008 on the second post-therapeutic session). The magnitude of the effect was similar for the proton-therapy patients (−9.1%, P = 0.12 on first; and −8.8%, P = 0.17 on the second post-therapeutic session). Although the perfusion decrease in proton-therapy patients did not reach statistical significance there was no effect size difference between the photon- and proton-therapy results (P = 0.94). No significant change was observed between the two post-therapeutic sessions ($P > 0.5$). Although the perfusion decrease was higher for the IMRT than for the 3DCRT subgroup, the difference was not significant on neither of the follow-up sessions ($P > 0.47$).

Table 1
Patients' demographics.

	Volume analysis		Perfusion analysis	
	Photon	Proton	Photon	Proton
Patients [n]	41	16	44	16
Male/female [n]	24/17	10/6	24/20	11/5
Mean age [years]	55.9 ± 13.9	51.3 ± 16.3	55.4 ± 13.3	51.5 ± 16.2
Age range [years]	25.3–81.8	23.2–72.4	25.3–75.3	23.2–72.4
ECOG 0/1/2 [n]	21/18/2	10/6/0	21/21/2	9/6/1
BMI [kg/m^2]	26.2 ± 4.8	24.9 ± 3.9	26.3 ± 4.6	25.9 ± 3.8
Tumor hemisphere [L/R]	19/22	10/6	21/23	11/5
Tumor location				
Frontal	21	5	22	7
Temporal	9	7	6	6
Parietal	3	2	5	1
Occipital	2	0	3	0
Frontotemporal	0	1	0	1
Temporooccipital	3	1	4	1
Parietooccipital	1	0	1	0
Thalamus	2	0	2	0
Cerebellum	0	0	1	0
Biopsy only	2	0	2	0
CTV [mm^3]	224.8 ± 75.5	217.4 ± 70.5	226.8 ± 77.7	229.4 ± 61.1
Mean dose [Gy]	22.6 ± 6.6	4.0 ± 4.4	22.4 ± 7.1	4.9 ± 4.4
Simultaneous TMZ [days]	40.2 ± 4.8	38.4 ± 7.5	40.5 ± 4.6	39.8 ± 5.6
Dexamethasone [n (%)]	4 (10%)	1 (6%)	5 (11%)	1 (6%)

Patients' demographics of the groups of photon and proton-therapy patients used for the volume and perfusion analysis. Additionally, the clinical target volume, the mean radiation dose in the healthy hemisphere, the number of days during which 75 mg/m^2/day of Temozolomide was administered simultaneously to the RT treatment, and the number of patients receiving Dexamethasone in time between the baseline and second follow-up measurement are given. The difference between the two photon-therapy groups and between the proton-therapy group was not significant ($P > 0.05$) for neither of the parameters (Age, ECOG, BMI and TMZ) for neither of the analysis (volume, perfusion). CTV was different between the two photon-therapy subgroups ($P < 0.022$) but not between proton and photon-therapy groups ($P > 0.73$). Mean dose was different both between the two photon-therapy subgroups ($P < 0.002$) and between the proton- and photon-therapy groups ($P < 10^{-8}$).

Table 2
Global brain volume changes in the healthy hemisphere.

RT modal.	Session		Num. of pat.	Interval [months]	ΔGM		ΔWM		ΔTissue	
	A	B			[%]	P	[%]	P	[%]	P
Photon	Pre	Post-1	40	4.7 ± 0.4	−2.2 ± 3.0	$6 \cdot 10^{-5}$	−1.2 ± 1.9	0.0004	−1.7 ± 1.7	10^{-7}
	Pre	Post-2	24	7.9 ± 0.5	−2.2 ± 3.2	0.003	−3.0 ± 2.6	10^{-5}	−2.5 ± 2.0	$2 \cdot 10^{-6}$
Proton	Pre	Post-1	15	4.7 ± 0.4	0.3 ± 2.3	0.64	−0.4 ± 3.0	0.58	−0.0 ± 1.9	0.98
	Pre	Post-2	12	8.0 ± 0.7	−0.8 ± 2.8	0.36	−1.0 ± 3.0	0.27	−0.9 ± 2.1	0.2
3DCRT	Pre	Post-1	21	4.7 ± 0.4	−1.4 ± 2.8	0.035	−1.4 ± 1.9	0.003	−1.4 ± 1.6	0.001
	Pre	Post-2	13	7.9 ± 0.5	−1.1 ± 3.4	0.29	−2.7 ± 3.2	0.01	−1.8 ± 2.1	0.012
IMRT	Pre	Post-1	19	4.7 ± 0.4	−3.0 ± 3.0	0.0005	−0.9 ± 2.0	0.058	−2.1 ± 1.7	$4 \cdot 10^{-5}$
	Pre	Post-2	11	7.9 ± 0.5	−3.6 ± 2.3	0.0005	−3.5 ± 1.8	$5 \cdot 10^{-5}$	−3.5 ± 1.3	$4 \cdot 10^{-6}$

Tissue volume changes for the first (Post-1) and second (Post-2) post-radiotherapy sessions are shown compared to the pre-therapy baseline (Pre). Significant mean relative volume decreases in GM, WM, and brain tissue were observed in the photon-therapy patients. Volume changes in the proton-therapy patients were not significant and the magnitudes of the changes were also much smaller than in the photon-therapy patients. Results are shown also for the two subgroups of the photon-therapy patients. Volume decreased in both subgroups on both sessions and the effect was stronger in the IMRT than in the 3DCRT patients.

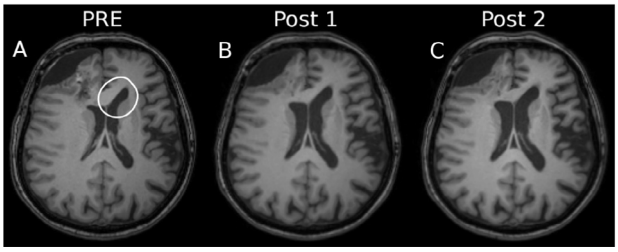

Fig. 1. *Progressive brain atrophy.* T1w images of an IMRT photon-therapy patient are shown for pre- (A) and post-therapeutic (B,C) sessions. Brain atrophy manifests as ventrical and outer CSF space enlargement (see, for example, anterior portion of cella media). Tissue volume decrease in the first post-therapeutic session (B) compared to the pre-therapeutic baseline (A) was 1.8%. Progression of the atrophy is observed on the second post-therapeutic session (C): 4.2% decrease compared to the pre-therapeutic baseline (A).

The perfusion changes for different dose regions are shown in Table 5. For the photon-therapy patients, significant perfusion decreases were observed for all doses above 10 Gy for the first post-therapeutic session compared to the pre-therapeutic session. However, there were no significant differences in a perfusion decrease between regions below and above 10 Gy. In line with the observed global perfusion decrease, a perfusion decrease in proton-therapy patients was comparable in magnitude, albeit not statistically significant.

The multivariate linear regression did not reveal significant effects of age ($\beta = -0.24$, $P = 0.15$), mean dose ($\beta = 0.10$, $P = 0.64$), time after therapy ($\beta = -0.32$, $P = 0.8$), sex ($\beta = -4.14$, $P = 0.35$), BMI ($\beta = -0.19$, $P = 0.73$), chemotherapy duration ($\beta = 0.50$, $P = 0.30$), or CTV ($\beta = 0$, $P = 1.0$) on whole-hemisphere perfusion changes.

Table 3
Dose-dependent brain volume changes in the healthy hemisphere.

Photon	Dose [Gy]	0–10	10–60	10–20	20–30	30–60
Pre/Post-1	ΔGM [%]	−1.6	−2.4	−1.8	−2.9	−3.1
	Region size [%/n]	23%/32	77%/40	27%/39	21%/34	29%/37
	P-value [0]	0.026★	10^{-5}★★	0.0004★★	$3 \cdot 10^{-6}$★★	10^{-5}★★
	P-value [LD]	–	0.027★	0.032★	0.067	0.014★
Pre/Post-2	ΔGM [%]	−1.6	−2.5	−1.8	−2.5	−3.6
	Region size [%/n]	21%/17	79%/24	29%/23	20%/20	29%/22
	P-value [0]	0.12	0.0008★★	0.018★	0.004★	$6 \cdot 10^{-5}$★★
	P-value [LD]	–	0.31	0.78	0.45	0.13
Proton	Dose [Gy]	0–10	10–60	10–20	20–30	30–60
Pre/Post-1	ΔGM [%]	0.6	−3.2	–	–	–
	Region size [%/n]	91%/15	9%/6	2%/0	2%/0	5%/6
	P-value [0]	0.3	0.14	–	–	–
	P-value [LD]	–	0.0063★	–	–	–
Pre/Post-2	ΔGM [%]	−0.4	−4.1	–	–	–
	Region size [%/n]	90%/12	10%/7	2%/0	2%/0	6%/7
	P-value [0]	0.57	0.082	–	–	–
	P-value [LD]	–	0.032★	–	–	–

The mean relative GM volume changes are shown for several dose regions. Note that the effect size and *P*-values are not given for regions (mainly proton therapy) with relative size under 7% as they were considered too much affected by noise. For each session, the mean dose-region volume as a percentage of the whole-hemisphere volume, and the number of regions that exceeded the 35 cm^3 threshold are given. The *P*-values of the *t*-tests for probability of no absolute change [0] and no change relative to the low dose (below 10 Gy) region [LD] are shown. Statistically significant values are labeled by ★ for $P < 0.05$ and by ★★ for $P < 0.001$. For the photon-therapy patients, a significant decrease in GM volume was observed for all doses except for the region with dose below 10 Gy on the second post-therapeutic session. In the first post-therapeutic session, significantly higher GM volume decrease was observed in the regions above 10 Gy than in the region below 10 Gy. None of the proton-therapy results were significant.

Table 4
Global perfusion changes in the healthy hemisphere.

RT modality	Session		Number of patients	Interval [months]	CBF_A	CBF_B	ΔCBF	*P*-value
	A	B			mean ± std [mL/min/100 g]		mean ± std [%]	
Photon	Pre	Post-1	41	4.7 ± 0.4	53.4 ± 9.7	48.0 ± 9.6	−10.1 ± 19.9	0.002
	Pre	Post-2	26	7.8 ± 0.5	53.4 ± 10.7	47.5 ± 8.9	−11.1 ± 19.5	0.008
Proton	Pre	Post-1	15	4.8 ± 0.5	50.3 ± 8.4	45.8 ± 8.6	−9.1 ± 21.6	0.12
	Pre	Post-2	11	8.0 ± 0.6	52.7 ± 8.2	48.0 ± 11.1	−8.8 ± 19.7	0.17
3DCRT	Pre	Post-1	24	4.9 ± 0.3	53.0 ± 8.8	48.8 ± 9.4	−7.9 ± 19.4	0.061
	Pre	Post-2	13	7.9 ± 0.6	51.8 ± 8.8	47.5 ± 10.0	−8.2 ± 14.7	0.07
IMRT	Pre	Post-1	17	4.6 ± 0.5	53.9 ± 11.2	46.8 ± 10.1	−13.1 ± 20.9	0.01
	Pre	Post-2	13	7.7 ± 0.4	55.0 ± 12.4	47.4 ± 8.0	−13.7 ± 24.0	0.055

Perfusion changes are shown for photon- (top) and proton-therapy patients (bottom). On each line, the absolute CBF, number of available patients, time between the sessions, the mean relative CBF difference between sessions, and the *P*-value of the paired *t*-test between the pre-therapeutic (Pre-) and one of the two post-therapeutic sessions (Post-1 and Post-2) are shown. The magnitudes of changes were similar for all sessions and RT modalities, however, the changes were significant only for the photon-therapy patients. Results are shown also for the two subgroups of the photon-therapy patients. While magnitude of changes is again similar, a significant decrease is observed only in the first post-therapeutic session of the IMRT patients where the magnitude of a decrease is higher than for the 3DCRT patient group.

Discussion

We compared the early-delayed effects of photon versus proton radiotherapy in the healthy brain tissue of glioblastoma patients. Our three main findings are: (1) There was less brain-tissue volume loss in patients who underwent proton-therapy compared to those who underwent photon-therapy; (2) Loss of brain-tissue volume strongly correlated with the mean radiation dose received in the healthy hemisphere; (3) Perfusion decreased in all patients, independent of therapy modality or radiation dose. The effect size of the perfusion decrease following therapy was similar between the two groups but reached statistical significance only for the photon-therapy patients. These findings are in agreement with the hypothesis that proton therapy reduces the volume loss of healthy tissue compared to photon therapy simply by limiting the radiation dose received in the contralateral hemisphere.

The observation of brain-tissue loss in photon-therapy but not in proton-therapy patients, in combination with the dose-dependency of the tissue loss suggests that brain volume changes are caused mainly by the radiation effects. Normal aging is estimated to cause between 0.26% and 0.39% per year decrease in GM volume, which is less than the values observed in the current study [13,31]. A dose dependent GM-volume decrease was previously described by Karunamuni et al. [18]. Our results are in agreement with their reported effect size (1–5% GM-volume decrease). However, the results are not directly comparable as the probability distribution of volume changes and not the mean volume changes were reported by Karunamuni et al. [18]. An approximately 5% GM-volume decrease reported for the same tumor type and therapy by Prust et al. [29] in 8 patients is close to our finding of 2–3% GM-volume decrease. The remaining difference could be caused by the fact that Prust et al. [29] performed the T1w image segmentation in the whole brain at once without excluding sessions with bilateral tumors and edemas in the contralateral hemisphere. The caveat is that the SPM12 segmentation employs a global model assuming homogeneous GM and WM intensity distribution across the brain on the T1w images. Longitudinal intensity changes in WM around the tumor (e.g. appearance of edema in follow-up

Table 5
Dose-dependent perfusion changes in the healthy hemisphere.

Photon	Dose [Gy]	0–10	10–60	10–20	20–30	30–60
Pre/Post-1	ΔCBF [%]	−7.3	−8.3	−8.9	−8.5	−8.7
	Region size [%/*n*]	26%/36	74%/41	28%/40	19%/36	26%/41
	P-value [0]	0.057	0.009★	0.006★	0.017★	0.007★
	P-value [LD]	–	0.39	0.21	0.3	0.4
Pre/Post-2	ΔCBF [%]	−7.3	−8.8	−10.3	−8.0	−8.0
	Region size [%/*n*]	27%/21	73%/26	29%/26	20%/21	24%/25
	P-value [0]	0.15	0.029★	0.007★	0.09	0.061
	P-value [LD]	–	0.51	0.27	0.18	0.51
Proton	Dose [Gy]	0–10	10–60	10–20	20–30	30–60
Pre/Post-1	ΔCBF [%]	−7.0	−9.5	–	–	–
	Region size [%/*n*]	90%/15	10%/8	2%/1	2%/3	7%/8
	P-value [0]	0.23	0.25	–	–	–
	P-value [LD]	–	0.75	–	–	–
Pre/Post-2	ΔCBF [%]	−8.3	−7.4	–	–	–
	Region size [%/*n*]	91%/11	9%/7	2%/2	1%/3	6%/7
	P-value [0]	0.19	0.36	–	–	–
	P-value [LD]	–	0.43	–	–	–

The mean relative perfusion changes are shown for different dose regions for photon- and proton-therapy patients. Note that effect size and *P*-values are not given for the finer division of the regions above 10 Gy for the proton-therapy patients as the region size was too small to give meaningful results. The mean volume of the dose region as a percentage of the whole hemisphere, and the number of patients for which the region volume exceeded the threshold of 5 cm^3 are shown as *Region size*. The *P*-values of the t-test indicate probability of no absolute change [*0*] and no change relative to the low-dose (below 10 Gy) region [*LD*]. Significant values are labeled by ★ for $P < 0.05$, and by ★★ for $P < 0.001$. Significant perfusion decreases were observed in all dose regions above 10 Gy in photon-therapy patients in the first post-therapeutic session. However, the results for regions above 10 Gy were not significantly different from the change in the region below 10 Gy. Effect size was similar in the proton-therapy patients, though the differences were not statistically significant.

measurement) will thus influence the segmentation results also in the contralateral hemisphere and therefore can cause false classification of part of GM tissue as WM, leading to false interpretation as a GM-volume decrease accompanied by a WM-volume increase as noted by Chamberlain et al. [6]. False volume variations due to the mentioned sources of error might explain why a WM-volume decrease has not been reported previously. We have circumvented this issue by segmenting the healthy hemisphere separately and by also investigating volume changes of GM and WM tissue combined.

In this study, approximately 10% perfusion decrease was present in both irradiation modalities irrespective of the received radiation dose. The decrease was statistically significant for photon therapy but not for proton therapy. Since the effect size and variability were similar for both therapies the difference in statistical significance can be understood as a consequence of the smaller sample size of the proton-therapy group.

Tumor perfusion measured in glioblastoma patients using MRI with or without contrast can be used before or following RCT to detect residual or recurrent tumor, pseudo-progression or to predict time to progression [20,23,26]. In such instances, tumor perfusion is often normalized to perfusion in contralateral normal-appearing brain tissue. Therefore, our finding of perfusion decreases in the normal-appearing brain tissue receiving relatively low radiation dose is a potential confounder for the normalized perfusion and should be taken into consideration. While vascular damage and neurocognitive deficits typically occur several years after RCT, we observed a perfusion decrease three to six months after the therapy. In several recent studies, a perfusion decrease has been proposed as an early predictor of cognitive decline in neurodegenerative disease [34,38] and similar effects might be present following photon- or proton-based RCT. This, however, requires validation by longer follow-up coupled with neurocognitive testing.

Previous studies that reported on perfusion changes following RCT were mostly conducted in small populations and differed in received radiation dose, irradiation region definition, time after RT, and imaging modality used. This may explain why previously reported results contradict one another. Price et al. [28] observed a perfusion decrease only in the regions and above 32 Gy, Taki et al. [36] reported 7% perfusion at 3 months after radiosurgery in a region that received less than 5 Gy, and Hahn et al. [14] observed a CBF increase using $[^{15}O]H_2O$ PET measurements. However, these studies were conducted with 6 patients or less. Directly comparable to the current study in terms of patient group characteristics, treatment type and statistical analysis is one investigation using dynamic susceptibility contrast MRI [11] and our previous investigation using ASL [27]. Both show similar results of around 10% GM CBF decrease in 10 and 24 patients, respectively. A small increase in CBF with increased dose has been observed in all three of these studies without, however, reaching statistical significance. The changes in perfusion thus do not appear to be mainly caused by RT, but seem related to either surgery, chemotherapy, or the disease itself. Especially the ongoing monthly chemotherapy after the end of RT can cause further damage by the synergistic effect of chemo and radiation therapy, as higher concentrations of chemotherapeutic agents in normal brain tissue is achieved due to increased leakage through the blood–brain barrier caused by RT [37]. The activity of O^6-Methylguanine-DNA methyltransferase (MGMT) has been related to both better therapeutic response of glioblastoma and normal tissue protection to radiochemotherapy with O^6-alkylating agents such as temozolomide [8,16]. While an increase in MGMT activity could in theory play a role in the decrease in the perfusion and structural damage, we were not able to study this due to lack of MGMT data in the normal tissue. We have observed higher, albeit mostly not significant, perfusion and volume decreases in the IMRT group versus the 3DCRT group. For the volume changes, this can be partly explained by the higher mean dose to the contralateral hemisphere in the IMRT group. Only minimal correlation with mean dose, however, was found for the perfusion decrease. The reason for the differences in the perfusion changes can thus be either a larger relative volume irradiated to high radiation doses of >30 Gy or by another, unknown effect. There was a significant difference in the CTV between the 3DCRT and the IMRT groups. It thus remains difficult to assess to what extent the difference in radiation dose was caused by the varying CTV or the radiation treatment technique. Although the CTV difference was not large, further studies are needed to provide an unbi-

ased comparison of the effects of 3DCRT and IMRT on the healthy hemisphere.

Our findings indicate that early-delayed brain-tissue volume changes are strongly dependent on the radiation dose applied to the healthy brain, suggesting that a reduced dose to brain-tissue may reduce regional loss of brain volume. Indeed, proton-therapy patients were shown to have significantly lower loss of brain tissue than the photon-therapy patients. On the other hand, perfusion decreased irrespective of the beam modality. Both longer follow-up in a larger cohort, as well as neurocognitive testing may allow to further explore the underlying pathological pathways of primary and secondary damage and its effect on cognitive function and to investigate if these benefits of proton therapy prevail over longer time.

Conflict of interest statement

The authors have nothing to disclose.

Appendix A. Supplementary data

Supplementary data associated with this article can be found, in the online version, at https://doi.org/10.1016/j.radonc.2017.11.033.

References

[1] Ahles TA, Root JC, Ryan EL. Cancer- and cancer treatment-associated cognitive change: an update on the state of the science. J Clin Oncol 2012;30:3675–86.
[2] Alsop DC, Ja Detre, Golay X, Günther M, Hendrikse J, Hernandez-Garcia L, Lu H, et al. Recommended implementation of arterial spin-labeled perfusion MRI for clinical applications: a consensus of the ISMRM perfusion study group and the European consortium for ASL in dementia. Magn Reson Med 2015;73:102–16.
[3] Armstrong CL, Gyato K, Awadalla AW, Lustig R, Tochner ZA. A critical review of the clinical effects of therapeutic irradiation damage to the brain: the roots of controversy. Neuropsychol Rev 2004;14:65–86.
[4] Ashburner J, Friston KJ. Unified segmentation. Neuroimage 2005;26:839–51.
[5] Ashburner J, Ridgway G. Symmetric diffeomorphic modeling of longitudinal structural mri. Front Neurosci 2013;6:197.
[6] Chamberlain MC, Dietrich J, Prust M. Standard chemoradiation for glioblastoma results in progressive brain volume loss: author response. Neurology 2016;86. 979–9.
[7] Chapman CH, Zhu T, Nazem-Zadeh M, Tao Y, Buchtel HA, Tsien CI, et al. Diffusion tensor imaging predicts cognitive function change following partial brain radiotherapy for low-grade and benign tumors. Radiother Oncol 2016;120:234–40.
[8] Christmann M, Verbeek B, Roos WP, Kaina B. O6-Methylguanine-DNA methyltransferase (MGMT) in normal tissues and tumors: enzyme activity, promoter methylation and immunohistochemistry. Biochimica et Biophysica Acta – Rev Cancer 1816;2:179–90.
[9] Connor M, Karunamuni R, McDonald C, White N, Pettersson N, Moiseenko V, et al. Dose-dependent white matter damage after brain radiotherapy. Radiother Oncol 2016;121:209–16.
[10] Dai W, Garcia D, de Bazelaire C, Alsop DC. Continuous flow-driven inversion for arterial spin labeling using pulsed radio frequency and gradient fields. Magn Reson Med 2008;60:1488–97.
[11] Fahlström M, Nyholm T, Larsson EM. Are radiation-induced perfusion changes in normal appearing brain tissue a confounding factor in tumour response evaluation with DSC-MRI? In: 25th Annual meeting of the international society for magnetic resonance in medicine; 2017. p. 2896.
[12] Garcia DM, Duhamel G, Alsop DC. Efficiency of inversion pulses for background suppressed arterial spin labeling. Magn Reson Med 2005;54:366–72.
[13] Good CD, Johnsrude IS, Ashburner J, Henson RNA, Friston KJ, Frackowiak RSJ. A voxel-based morphometric study of ageing in 465 normal adult human brains. NeuroImage 2001;14:21–36.
[14] Ca Hahn, Zhou SM, Raynor R, Tisch A, Light K, Shafman T, et al. Dose-dependent effects of radiation therapy on cerebral blood flow, metabolism, and neurocognitive dysfunction. Int J Radiat Oncol Biol Phys 2009;73:1082–7.
[15] Jakubovic R, Sahgal A, Ruschin M, Pejovic-Milic A, Milwid R, Aviv RI. Non tumor perfusion changes following stereotactic radiosurgery to brain metastases. Technol Cancer Res Treat 2015;14:497–503.
[16] Kaina B, Margison GP, Christmann M. Targeting O 6-methylguanine-DNA methyltransferase with specific inhibitors as a strategy in cancer therapy. Cell Mol Life Sci 2010;67:3663–81.
[17] Karunamuni R, Bartsch H, White NS, Moiseenko V, Carmona R, Marshall DC, et al. Dose-dependent cortical thinning after partial brain irradiation in high-grade glioma. Int J Radiat Oncol Biol Phys 2016;94:297–304.
[18] Karunamuni RA, Moore KL, Seibert TM, Li N, White NS, Bartsch H, et al. Radiation sparing of cerebral cortex in brain tumor patients using quantitative neuroimaging. Radiother Oncol 2016;118:29–34.
[19] Levin WP, Kooy H, Loeffler JS, DeLaney TF. Proton beam therapy. Br J Cancer 2005;93:849–54.
[20] Lindner T, Ahmeti H, Lübbing I, Helle M, Jansen O, Synowitz M, et al. Intraoperative resection control using arterial spin labeling – proof of concept, reproducibility of data and initial results. NeuroImage: Clin 2017;15:136–42.
[21] Lorio S, Fresard S, Adaszewski S, Kherif F, Chowdhury R, Frackowiak R, et al. New tissue priors for improved automated classification of subcortical brain structures on MRI. Neuroimage 2016;130:157–66.
[22] Millar BAM, Purdie TG, Yeung I, Pond GR, Billingsley S, Wong R, et al. Assessing perfusion changes during whole brain irradiation for patients with cerebral metastases. J Neuro-Oncol 2005;71:281–6.
[23] Nael K, Bauer AH, Hormigo A, Lemole M, Germano IM, Puig J, et al. Multiparametric mri for differentiation of radiation necrosis from recurrent tumor in patients with treated glioblastoma. Am J Roentgenol 2017:1–6.
[24] O'Connor MM, Mayberg MR. Effects of radiation on cerebral vasculature: a review. Neurosurgery 2000;46:138–51.
[25] Omuro AMP, Ben-Porat LS, Panageas KS, Kim AK, Correa DD, Yahalom J, et al. Delayed neurotoxicity in primary central nervous system lymphoma. Arch Neurol 2005;62:1595–600.
[26] Park JE, Ryu KH, Kim HS, Kim HW, Shim WH, Jung SC, et al. Perfusion of surgical cavity wall enhancement in early post-treatment mr imaging may stratify the time-to-progression in glioblastoma. PLoS One 2017;12:1–13.
[27] Petr J, Platzek I, Seidlitz A, Mutsaerts HJMM, Hofheinz F, Schramm G. Early and late effects of radiochemotherapy on cerebral blood flow in glioblastoma patients measured with non-invasive perfusion MRI. Radiother Oncol 2016;118:24–8.
[28] Price SJ, Jena R, HaL Green, Kirkby NF, Lynch AG, Coles CE, et al. Early radiotherapy dose response and lack of hypersensitivity effect in normal brain tissue: a sequential dynamic susceptibility imaging study of cerebral perfusion. Clin Oncol 2007;19:577–87.
[29] Prust MJ, Jafari-Khouzani K, Kalpathy-Cramer J, Polaskova P, Batchelor TT, Gerstner ER, et al. Standard chemoradiation for glioblastoma results in progressive brain volume loss. Neurology 2015;85:683–91.
[30] Reuter M, Tisdall MD, Qureshi A, Buckner RL, van der Kouwe AJW, Fischl B. Head motion during MRI acquisition reduces gray matter volume and thickness estimates. NeuroImage 2015;107:107–15.
[31] Scahill R, Frost C, Jenkins R, Whitwell J, Rossor M, Fox N. A longitudinal study of brain volume changes in normal aging using serial registered magnetic resonance imaging. Arch Neurol 2003;60:989–94.
[32] Seibert TM, Karunamuni R, Bartsch H, Kaifi S, Krishnan AP, Dalia Y, et al. Radiation dose-dependent hippocampal atrophy detected with longitudinal volumetric magnetic resonance imaging. Int J Radiat Oncol Biol Phys 2017;97:263–9.
[33] Seibert TM, Karunamuni R, Kaifi S, Burkeen J, Connor M, Krishnan AP, et al. Cerebral cortex regions selectively vulnerable to radiation dose-dependent atrophy. Int J Radiat Oncol Biol Phys 2017;97:910–8.
[34] Steketee RME, Bron EE, Meijboom R, Houston GC, Klein S, Mutsaerts HJMM, et al. Early-stage differentiation between presenile Alzheimer's disease and frontotemporal dementia using arterial spin labeling MRI. Eur Radiol 2016;26:244–53.
[35] Stupp R, Mason WP, van den Bent MJ, Weller M, Fisher B, Taphoorn MJB, et al. Radiotherapy plus concomitant and adjuvant temozolomide for glioblastoma. New England J Med 2005;352:987–96.
[36] Taki S, Higashi K, Oguchi M, Tamamura H, Tsuji S, Ohta K, et al. Changes in regional cerebral blood flow in irradiated regions and normal brain after stereotactic radiosurgery. Ann Nucl Med 2002;16:273–7.
[37] Taphoorn MJB, Klein M. Cognitive deficits in adult patients with brain tumours. Lancet Neurol 2004;3:159–68.
[38] Wang Z. Characterizing early Alzheimer's disease and disease progression using hippocampal volume and arterial spin labeling perfusion MRI. J Alzheimers Dis 2014;42:S495–502.

Appendix A7

Overestimation of grey matter atrophy in glioblastoma patients following radio (chemo) therapy

Gommlich, A., Raschke, F., Petr, J., Seidlitz, A., Jentsch, C., Platzek, I., ... & Troost, E. G. C. (2022). Overestimation of grey matter atrophy in glioblastoma patients following radio (chemo) therapy. Magnetic resonance materials in physics, biology and medicine, 35(1), 145-152.

Journal name (category): **Magnetic resonance materials in physics, biology and medicine** (Radiology, nuclear medicine & medical imaging)

Quartile in category: **Q3**

Impact factor: **2.533**

Number of WoS citations: **0**

Magnetic Resonance Materials in Physics, Biology and Medicine (2022) 35:145–152
https://doi.org/10.1007/s10334-021-00922-3

RESEARCH ARTICLE

Overestimation of grey matter atrophy in glioblastoma patients following radio(chemo)therapy

A. Gommlich[1,2,3] · F. Raschke[2,3] · J. Petr[4] · A. Seidlitz[3,5] · C. Jentsch[3,5] · I. Platzek[6] · J. van den Hoff[4] · J. Kotzerke[7] · B. Beuthien-Baumann[8] · M. Baumann[3,9,10] · M. Krause[2,3,5,11,12] · E. G. C. Troost[2,3,5,11,12]

Received: 12 November 2020 / Revised: 11 March 2021 / Accepted: 16 March 2021 / Published online: 31 March 2021

Abstract

Objective Brain atrophy has the potential to become a biomarker for severity of radiation-induced side-effects. Particularly brain tumour patients can show great MRI signal changes over time caused by e.g. oedema, tumour progress or necrosis. The goal of this study was to investigate if such changes affect the segmentation accuracy of normal appearing brain and thus influence longitudinal volumetric measurements.

Materials and methods T1-weighted MR images of 52 glioblastoma patients with unilateral tumours acquired before and three months after the end of radio(chemo)therapy were analysed. GM and WM volumes in the contralateral hemisphere were compared between segmenting the whole brain (full) and the contralateral hemisphere only (cl) with SPM and FSL. Relative GM and WM volumes were compared using paired t tests and correlated with the corresponding mean dose in GM and WM, respectively.

Results Mean GM atrophy was significantly higher for full segmentation compared to cl segmentation when using SPM (mean ± std: $\Delta V_{GM,full} = -3.1\% \pm 3.7\%$, $\Delta V_{GM,cl} = -1.6\% \pm 2.7\%$; $p < 0.001$, $d = 0.62$). GM atrophy was significantly correlated with the mean GM dose with the SPM cl segmentation ($r = -0.4$, $p = 0.004$), FSL full segmentation ($r = -0.4$, $p = 0.004$) and FSL cl segmentation (r = -0.35, p = 0.012) but not with the SPM full segmentation ($r = -0.23$, $p = 0.1$).

Conclusions For accurate normal tissue volume measurements in brain tumour patients using SPM, abnormal tissue needs to be masked prior to segmentation, however, this is not necessary when using FSL.

Keywords Radiotherapy · Tissue segmentation · SPM · Atrophy · Glioblastoma · Proton

A. Gommlich, F. Raschke, and J. Petr shared first authors

✉ F. Raschke
felix.raschke@oncoray.de

1 Siemens Energy Austria GmbH, Vienna, Austria

2 Helmholtz-Zentrum Dresden-Rossendorf, Institute of Radiooncology – OncoRay, Dresden, Germany

3 OncoRay - National Center for Radiation Research in Oncology, Faculty of Medicine and University Hospital Carl Gustav Carus, Technische Universität Dresden, Helmholtz-Zentrum Dresden-Rossendorf, Dresden, Germany

4 Helmholtz-Zentrum Dresden-Rossendorf, Institute of Radiopharmaceutical Cancer Research, Dresden, Germany

5 Department of Radiotherapy and Radiation Oncology, Faculty of Medicine and University Hospital Carl Gustav Carus, Technische Universität Dresden, Dresden, Germany

6 Faculty of Medicine and University Hospital Carl Gustav Carus, Department of Diagnostic and Interventional Radiology, Technische Universität Dresden, Dresden, Germany

7 Faculty of Medicine and University Hospital Carl Gustav Carus, Department of Nuclear Medicine, Technische Universität Dresden, Dresden, Germany

8 Department of Radiology, German Cancer Research Center (DKFZ), Heidelberg, Germany

9 German Cancer Research Center (DKFZ), Heidelberg, Germany

10 National Center for Tumor Diseases (NCT), Partner Site Heidelberg, Germany

11 German Cancer Consortium (DKTK), Partner Site Dresden, and German Cancer Research Center (DKFZ), Heidelberg, Germany

12 National Center for Tumor Diseases (NCT), Partner Site Dresden, Germany: German Cancer Research Center (DKFZ), Heidelberg, Germany; Faculty of Medicine and University Hospital Carl Gustav Carus, Technische Universität Dresden, Dresden, Germany, and; Helmholtz Association / Helmholtz-Zentrum Dresden-Rossendorf (HZDR),, Dresden, Germany

Introduction

Radiotherapy is part of the standard treatment regime of gliomas. With improving survival in particular for low-grade tumours, the number of patients experiencing therapy-induced long-term complications, such as neurocognitive decline, increases accordingly [1–3]. Apart from subjective measures, such as patient-reported outcomes and neurocognitive function tests, the community strives to include objective measures in the evaluation of treatment outcome, especially when comparing different treatment modalities, such as photon- and proton-based radio(chemo)therapy.

Radiotherapy induced brain atrophy has been observed across the whole brain [4–7], hippocampus [8–11], amygdala [12] and cerebellum [13]. The findings show consistently that the amount of tissue loss is dose dependent [5, 13, 14]. Previous studies have also linked atrophy with cognitive decline [4, 15]. Brain atrophy has become an important marker of disease severity in neurodegenerative and demyelinating diseases such as Alzheimer's disease [16] or multiple sclerosis (MS) [17]. Similarly, atrophy has the potential to become a biomarker for severity of radiation-induced side effects [4, 15]. However, this requires measurement of the normal tissue volumes of brain tumour patients with great accuracy across multiple time points. Particularly brain tumours can show great changes in MR signal intensities over time in and around the original tumour site caused by oedema, tumour progression, or treatment itself. If these signal changes influence the atrophy measurement, they could mask its potential to act as a reliable biomarker.

In the research environment, accurate measurement of atrophy commonly involves segmentation of high resolution T1-weighted MR images into grey matter (GM), white matter (WM) and cerebrospinal fluid (CSF) using software such as FSL (FMRIB Software Library: https://fsl.fmrib.ox.ac.uk/fsl/fslwiki/) [18, 19] or SPM (Statistical Parametric Mapping: https://www.fil.ion.ucl.ac.uk/spm/) [20, 21]. These software tools use an iterative Bayesian segmentation approach. By default, FSL initializes the tissue segmentation using intensity-based thresholds to segment the input image coarsely into three tissue types corresponding to GM, WM and CSF [18]. SPM uses prior tissue probability maps (TPMs) to initialize the tissue segmentation. The TPMs are derived from a collection of manually segmented healthy brains [20]. Consequently, if abnormal brain tissue is present, for instance, resection cavities, oedema, and tumour tissue in brain tumour patients, or WM lesions in MS patients, the TPMs are not valid within these regions of abnormal tissue and can cause significant bias in the resulting GM and WM segmentation. Abnormal tissue will be incorrectly classified as either GM, WM, or CSF. Consequently, image intensities of abnormal tissue contribute to the global joint-probability distribution model that is constructed for each of the GM, WM, and CSF tissues during the iterative process of segmentation. This can alter the width and position of the respective GM, WM, or CSF probability density functions on the MRI intensity scale and consequently lead to a shift between the separation of tissue boundaries, most commonly between GM/WM and GM/CSF, thus biasing volume measurements in the normal tissue even when abnormal tissue is removed after segmentation.

Segmenting MR images containing abnormal tissue has been studied previously in the field of MS, where WM lesions can have a significant impact on GM and WM volumes [22–24]. In MS, the error in volume measurements mainly arises from misclassification of WM lesions as GM or CSF [25]. Brain tumours, conversely, generally have much larger lesions. Using Bayesian segmentation approaches, this could also potentially bias normal tissue volume measurements if the abnormal tissue is not masked prior to segmentation.

The aim of this study was to assess the influence of the presence of residual tumour, resection cavities, and oedema on the quality of the tissue segmentation in the healthy tissue and on the longitudinal assessment of volumetric changes in brain parenchyma. To that end, we measured GM and WM volumes segmented from 3D 1 mm isotropic T1-weighted MR images in a cohort of glioblastoma patients with unilateral lesions. We assessed the longitudinal volumetric changes between the baseline and 3 month follow-up after radio(chemo-)therapy, respectively. We hypothesized that the presence of abnormal tissue in the ipsilateral hemisphere would affect the segmentation and longitudinal volumetric changes in the healthy contralateral hemisphere. To show that, we compared segmentations obtained from SPM and FSL with and without removing the tumour-bearing hemisphere.

Materials and methods

Subjects

Patient data were acquired as part of a prospective longitudinal study investigating the effect of ^{11}C-methionine PET/MR for tailoring the treatment of patients with glioblastoma, approved by the local ethics committee (NCT01873469, EK41022013, BO-EK-167052020). Gross tumour resection was performed in most patients prior to radio(chemo-)therapy. Baseline MR images were acquired two to seven weeks after surgery and typically two weeks before the start of radio(chemo-)therapy. Radiotherapy was conducted using either photon or proton therapy as described previously [26]. Follow-up MRIs were acquired approximately three months after the end of radiotherapy. All patients were treated with

adjuvant temozolomide [26]. More details about the patient population and treatment is provided by Seidlitz et al. [26]. Patients were excluded if no baseline MRI or no follow-up MRI was available, or if tumour or oedema extended across both hemispheres. Follow-up MRIs that showed motion artefacts or abnormal tissue in the normal appearing hemisphere were excluded, resulting in a total of 52 eligible patient datasets.

MRI data from six healthy controls (HCs) [age 39.4y ± 8.7 years, range (30.6–54.2 years), 4 male] were used to validate the data analysis strategy described in Sect. 2.3. This study was approved by the local ethics committee, and the participants gave written informed consent [DRKS-ID: DRKS00012600, EK267072017].

Data acquisition

All MRI data were acquired on a 3 T Philips Ingenuity PET/MR scanner (Philips, Eindhoven, The Netherlands) using an eight channel head coil. For this study, pre-contrast T1-weighted (T1w) MR images were used for further analysis. In patients, T1w images were acquired in sagittal orientation using a 3D turbo field echo (TFE) sequence at 1 mm isotropic resolution (TFE inversion prepulse, TFE factor = 224, TR/TE = shortest (typical 8.2/3.8 ms), $\alpha = 8°$, FOV 192(FH) × 224(AP) mm^2, matrix size 192(FH) × 224(AP), 1 mm slice thickness, 192 slices). In healthy controls, T1w images were acquired using a 3D gradient spoiled echo sequence in sagittal orientation (TR = 10 ms, TE = 3.7 ms, $\alpha = 20°$, FOV 224 × 224 mm^2, matrix size 224 × 224, 1 mm slice thickness, 160 slices) [27].

Data analysis

T1w images were segmented into GM, WM, CSF, bone, soft tissue and background using SPM12 [20] and GM, WM and CSF using FSL [18] with their respective default settings. SPM gave tissue probability maps as outputs, whereas FSL provided partial volume maps. For FSL, prior steps to segmentation included N4 bias field correction [28] and skull stripping [29]. The 3 T T1w images show relatively large bias field variations and without prior N4 bias field correction, FSL falsely segmented most of the subcortical GM as WM.

GM and WM volumes of the normal appearing hemisphere were compared between segmenting the whole brain ($V_{GM,full}$, $V_{WM,full}$, $V_{GM+WM,full}$) versus segmenting the normal appearing hemisphere ($V_{GM,cl}$, $V_{WM,cl}$, $V_{GM+WM,cl}$). The tumour-bearing and normal appearing hemispheres were separated by non-linearly coregistering the MNI152 atlas (https://fsl.fmrib.ox.ac.uk/fsl/fslwiki/) to each T1w image using ANTs [29, 30]. The same deformation was applied to a label mask separating the two hemispheres. Subsequently, all GM and WM maps were restricted to the normal appearing hemisphere using these masks. GM and WM volumes were generated by summing all GM and WM values within these final tissue segmentation maps. Relative tissue volumes were calculated as ratios to their corresponding baseline values. The data analysis workflow is shown in Fig. 1. Mean WM and GM radiation doses in the contralateral hemisphere were calculated from the corresponding dose maps using binarized WM and GM maps, respectively, using a threshold of 0.5. The mean doses were used to compare the dose dependence of volume changes between the segmentation methods.

The comparison between the two segmentation methods (full and cl) relies on the assumption that segmenting a single hemisphere will yield the same results in that hemisphere

Table 1 Patients' characteristics

Patients, *n*	52
Proton/photon, *n*	13/39
Gender (male/female), *n*	32/20
Age at start of radiotherapy (mean ± std), years	54.5 ± 14.5
Follow-up time, days	88.3 ± 12.0

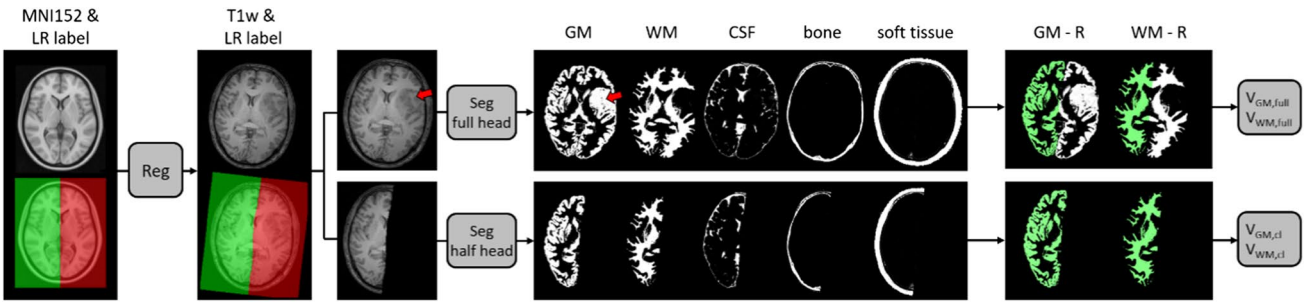

Fig. 1 Image processing workflow: registration (Reg) of MNI152 atlas and corresponding left/right label to T1w-native space and subsequent tissue segmentation (Seg) of the full brain or contralateral (cl) hemisphere for volume assessment. In this example, abnormal tissue in the left hemisphere was mainly classified as GM (red arrow). Volume assessment was restricted to the contralateral hemisphere in all cases

as segmenting the whole brain, thus serving as "ground truth" for patient data with one healthy and one abnormal hemisphere. To test this assumption, the T1w images of six healthy controls were segmented. GM volumes of the left and right hemispheres obtained from whole brain segmentation were compared with those obtained from segmenting the left and right hemispheres separately.

Statistical analysis

Relative GM, WM and GM + WM volumes of the contralateral hemispheres were compared between whole brain segmentation (full) and contralateral hemisphere segmentation (cl) using paired *t* tests. Normality of the distributions was tested using a one-sample Kolmogorov–Smirnov test. Cohen's $d = \mu_{x-}\mu_y/\sigma_{x-y}$ was used to calculate the effect size.

Relative GM and WM volumes obtained from segmenting the whole brain (full) and the contralateral hemisphere (cl) were correlated with the corresponding mean dose in GM and WM of the contralateral hemisphere, respectively, using Pearson regression analysis.

Results

Demographics of the 52 eligible patients are given in Table 1.

GM volumes from the healthy controls show that both FSL and SPM are suitable for segmentation of a single hemisphere with very little deviation between single-hemisphere and full brain segmentation (see supplementary material section I).

The relative GM and WM volume changes determined using full brain segmentation and contralateral hemisphere segmentation are compared in Fig. 2. With SPM, relative GM volume loss was significantly higher when using the full brain segmentation approach (mean ± std: $\Delta V_{GM,full} = -3.1\% \pm 3.7\%$, $\Delta V_{GM,cl} = -1.6\% \pm 2.7\%$; $p < 0.001$, $d = 0.62$). There was no significant difference in relative GM volume changes between full and cl segmentation when using FSL (mean ± std: $\Delta V_{GM,full} = -0.9\% \pm 2.7\%$, $\Delta V_{GM,cl} = -0.9\% \pm 2.5\%$; $p = 0.91$, $d = 0.02$). There was no significant difference in relative WM volume changes for SPM (mean ± std: $\Delta V_{WM,full} = -0.8\% \pm 2.4\%$, $\Delta V_{WM,cl} = -0.8\% \pm 2.1\%$; $p = 0.95$, $d = 0.01$) and FSL (mean ± std: $\Delta V_{WM,full} = -0.75\% \pm 2.4\%$, $\Delta V_{WM,cl} = -$-0.77% ± 2.2%; $p = 0.89$, $d = 0.02$).

When segmenting the full brain with SPM, relative GM volume changes (Fig. 3a) were not significantly correlated with the mean GM dose ($r = -0.23$, $p = 0.1$). Additionally, a non-zero $x = 0$ intercept suggested GM atrophy despite a mean GM dose of 0 Gy. On the other hand, using the SPM cl, FSL full, and FSL cl segmentation, the relative GM volume changes (Fig. 3b, d, e) were significantly correlated with the mean GM dose (SPM cl: $r = -0.4$, $p = 0.004$, FSL full: $r = -0.4$, $p = 0.004$, FSL cl: $r = -0.35$, $p = 0.012$) and the near zero intercepts suggest no GM changes with a mean GM dose of 0 Gy. The slopes of these three regressions were very similar, corresponding to a 1.1% (SPM cl), 1.1% (FSL full) and 0.9% (FSL cl) GM volume loss per 10 Gy mean GM dose.

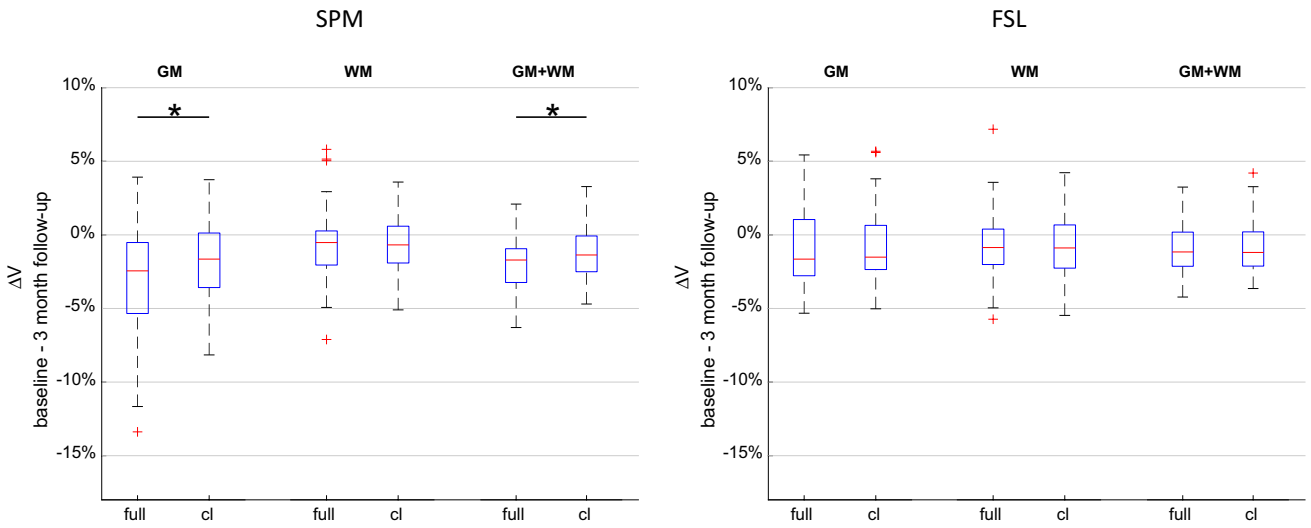

Fig. 2 Relative volume changes of grey matter (GM), white matter (WM) and the combination of the two volumes (GM + WM) between baseline and the 3 month follow-up for SPM and FSL. Results of full brain segmentation (full) and contralateral segmentation (cl) were compared using a paired *t* test (*$p < 0.05$). ΔV change in volume

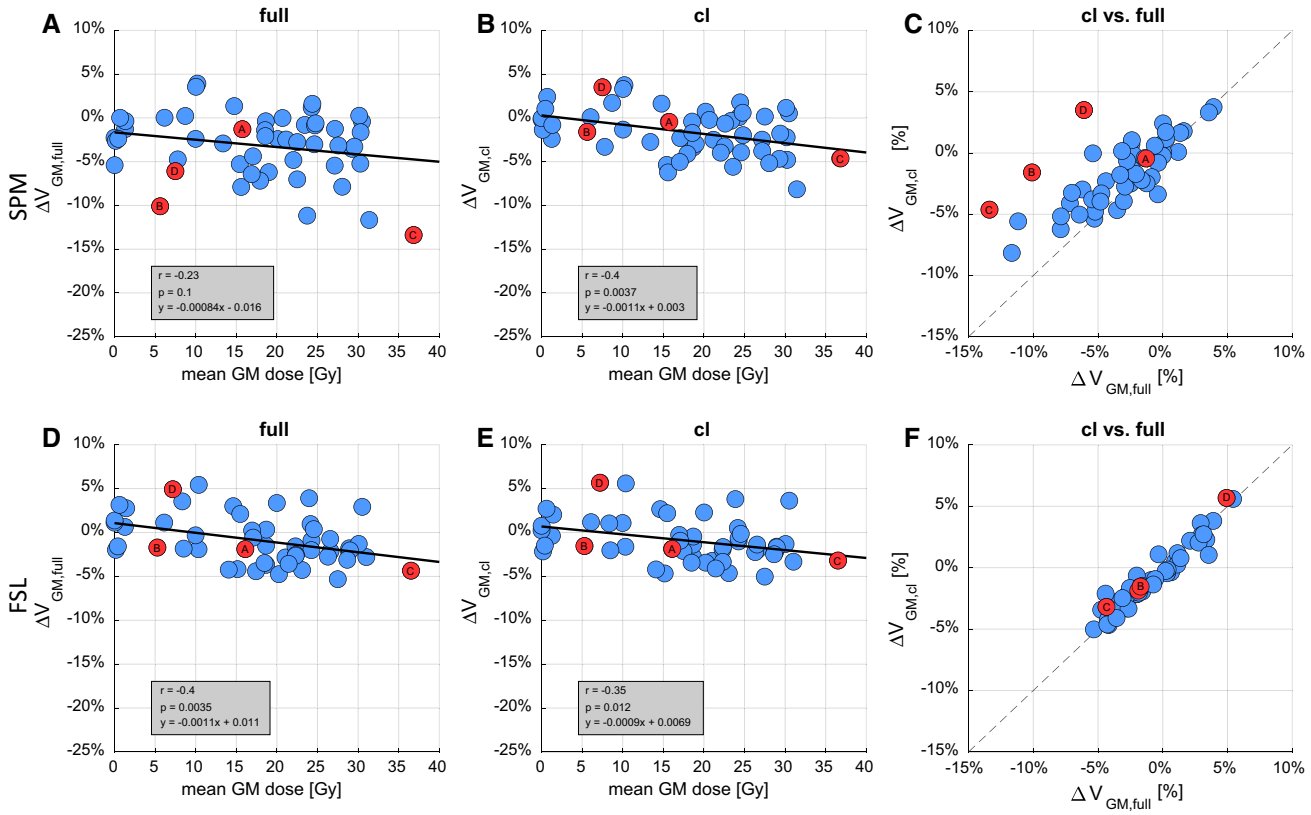

Fig. 3 Scatter plots of relative grey matter (GM) volume changes over the mean GM dose. GM volumes were determined from SPM and FSL segmentation of full brain (**a**, **d**) and contralateral hemisphere (**b**, **e**). Regression parameters were determined using Pearson's correlation. The volume changes determined from full brain and cl segmentation are compared in (**c**, **f**). Red markers highlight four individual examples which are shown in Fig. 4. ΔV_{GM} change in GM volume

The GM volume changes of the SPM cl (GM_{cl}) and SPM full (GM_{full}) segmentations are compared in Fig. 3c. While the two methods produce very similar results for some cases (e.g. highlighted example A), there are large differences for other cases (highlighted examples B, C and D). GM difference maps between SPM cl (GM_{cl}) and SPM full (GM_{full}) segmentation are shown for these four examples in Fig. 4. Example A shows similar relative GM volumes between full and cl segmentation in Fig. 3c and relatively consistent GM_{cl}–GM_{full} difference maps (Fig. 4a). Conversely, examples B, C and D show the largest relative GM volume changes between full and cl segmentation in Fig. 3c. GM difference maps GM_{c}–GM_{full} reveal these changes to be located at the GM/CSF interface around the gyri in example B (Fig. 4b), around the WM/GM interface in example C (Fig. 4c) and around both the GM/CSF and WM/GM interfaces in example D (Fig. 4d). All three examples B, C and D show pronounced MRI changes in abnormal tissue volume and contrasts between the baseline and follow-up T1w images in the ipsilateral hemispheres. Such outliers were not observed when using the FSL segmentation (Fig. 3f).

WM volume changes after 3 months were much smaller (supplementary Fig. 3), nevertheless, as for GM, WM atrophy was significantly correlated to the mean WM dose when using WM volumes obtained from SPM cl ($r = -0.28$, $p = 0.044$), FSL full ($r = -0.29$, $p = 0.04$) and FSL cl ($r = -0.41$, $p = 0.003$) segmentation. The estimated degree of WM atrophy was 0.5% (SPM cl), 0.6% (FSL full) and 0.8% (FSL cl) per 10 Gy mean WM dose.

Discussion

We have shown that GM volume measurements in the contralateral hemisphere of patients with unilateral glioblastoma differ between segmentation of the whole brain and of the contralateral hemisphere alone when using SPM. This difference is likely caused by abnormal tissue changes in the ipsilateral hemisphere, typically seen during longitudinal observations of brain tumour patients, influencing normal tissue segmentation results with SPM in the contralateral hemisphere.

In the data presented in this study, higher GM atrophy was observed when not masking the ipsilateral hemisphere containing the abnormal tissue prior to SPM segmentation (Fig. 2). Since the WM volume shows no significant change,

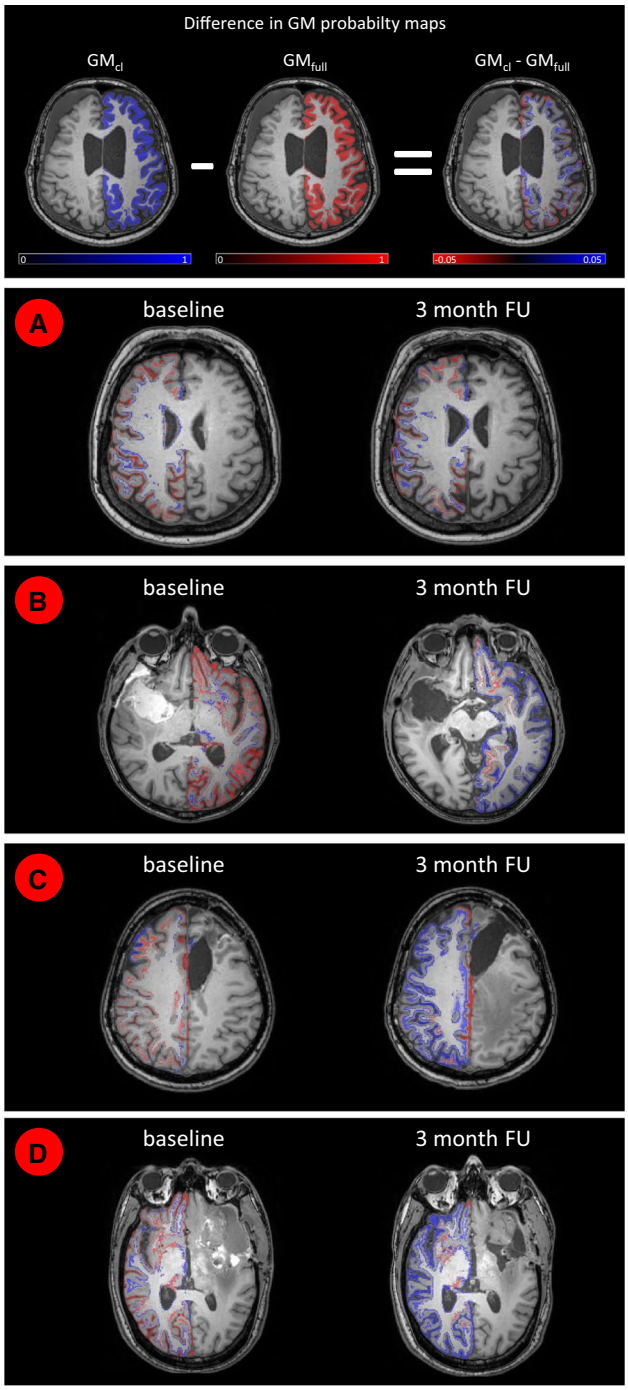

Fig. 4 SPM segmentation: Differences of the grey matter (GM) probability maps of segmenting the contralateral hemisphere (GM_{cl}, blue) minus segmenting the whole brain (GM_{full}, red). Examples **a–d** are highlighted in Fig. 3. *FU* follow-up

we conclude that the remaining volume is mainly assigned to CSF. Nevertheless, there were also examples in Fig. 4c, d where underestimated GM from the SPM full segmentation was also assigned to WM. Examples B, C and D have particularly large deviations in GM volume changes between full and cl SPM segmentation (Fig. 3c) and have also shown particularly pronounced image changes in abnormal tissue volume and contrast. It is therefore likely that such large regions of MRI changes will cause greater alterations to the normal tissue probability density distributions within the iterative segmentation process and thus shift tissue separation boundaries accordingly. An additional factor is that SPM also performs simultaneous bias field correction with the tissue segmentation by default [18, 20]. Depending on regularization strength of the bias field, this will also attempt to match abnormal tissue image intensities to normal tissue intensities [31]. Therefore, the overall impact of abnormal tissue on the segmentation depends on the interaction of a number of factors and is not easily appointed to a single cause. Nevertheless, we can conclude that abnormal tissue present in the ipsilateral hemisphere of brain tumour patients will influence SPM segmentation results of the contralateral hemisphere.

Conversely, FSL segmentation results are consistent between full brain and cl segmentation. Corresponding atrophy estimates are also very similar to those obtained from SPM cl segmentation for both GM (Fig. 3) and WM (suppl. Fig. 3). Unlike SPM, by default FSL uses grey value thresholds to coarsely segment the input image into the three expected tissue types GM, WM and CSF [18]. Although the abnormal tissue has to be assigned to one of those normal tissue types as with the SPM TPM method, this seems to have no apparent impact on the segmentation results. The weakness of the threshold-based initialisation of FSL are large bias field variations. These can cause the intensity values between GM, WM and CSF to overlap [18] and that led to misclassification of subcortical GM as WM in the data presented here. However, using the established N4 bias field correction algorithm [28] prior to FSL segmentation resulted in a much improved segmentation with visually very similar results to SPM.

The findings presented here are relevant for longitudinal studies requiring accurate brain volume measurement using iterative segmentation software with TPMs for initialization. While some previous studies have considered that abnormal tissue could bias volume measurements and restricted the segmentation to the contralateral hemisphere [4, 5], others have not [7, 32, 33]. Consequently, previous findings of volume changes determined with SPM could potentially be biased [32].

A limitation of this study is the restriction of the analysis to unilateral brain tumour cases, as done in some previous studies [4, 5]. However, by co-registering individual abnormality masks for all time points of a patient into a common space, arbitrary anatomical regions can be masked as demonstrated previously [27]. This allows accurate segmentation of normal appearing tissue in cases with bilateral lesions as well, albeit spatial normalization can be difficult in patients with large mass effect [34]. Minor differences in the FSL

and SPM results could be caused by the fact that SPM gave tissue probability maps as outputs, whereas FSL provided partial volume maps. However, a preliminary analysis using tissue probability maps output for FSL ("-p" option) showed no change in the overall results. Lastly, the behaviour of other segmentation tools using a similar methodology, such as AFNI [35] or Atropos [36], was not tested. However, for accurate volumes measurements, we generally suggest to exclude abnormal tissue prior to segmentation in future studies.

In conclusion, abnormal tissue present in the ipsilateral hemisphere of brain tumour patients will influence SPM segmentation results of the contralateral hemisphere. In the dataset presented here, GM atrophy was overestimated in the contralateral hemisphere when the ipsilateral hemisphere containing abnormal tissue was not removed prior to segmentation. Consequently, for accurate volume measurement in brain tumour patients using SPM, the abnormal tissue needs to be masked prior to segmentation, however, this is not necessary when using FSL.

Supplementary Information The online version contains supplementary material available at https://doi.org/10.1007/s10334-021-00922-3.

Funding Open Access funding enabled and organized by Projekt DEAL.

Declarations

Conflict of interest In the past 5 years, Dr. Michael Baumann received funding for his research projects and for educational grants to the University of Dresden by Bayer AG (2016–2018), Merck KGaA (2014-open) and Medipan GmbH (2014–2018). He is on the supervisory board of HI-STEM gGmbH (Heidelberg) for the German Cancer Research Center (DKFZ, Heidelberg) and also member of the supervisory body of the Charité University Hospital, Berlin. As former chair of OncoRay (Dresden) and present CEO and Scientific Chair of the German Cancer Research Center (DKFZ, Heidelberg), he has been or is responsible for collaborations with a multitude of companies and institutions, worldwide. In this capacity, he has discussed potential projects and signed contracts for research funding and/or collaborations with industry and academia for his institute(s) and staff, including but not limited to pharmaceutical companies such as Bayer, Boehringer Ingelheim, Bosch, Roche and other companies such as Siemens, IBA, Varian, Elekta, Bruker, etc. In this role, he was/is also responsible for the commercial technology transfer activities of his institute(s), including the creation of start-ups and licensing. This includes the DKFZ-PSMA617 related patent portfolio [WO2015055318 (A1), ANTIGEN (PSMA)] and similar IP portfolios. Dr. Baumann confirms that, to the best of his knowledge, none of the above funding sources were involved in the preparation of this paper. Within the past years, Dr. Krause received funding for her research projects by IBA (2016), Merck KGaA (2014–2018 for preclinical study; 2018–2020 for clinical study), Medipan GmbH (2014–2018), Attomol GmbH (2019–2021), GA Generic Assays GmbH (2019–2021), BTU Cottbus-Senftenberg (2019–2021), Gesellschaft für medizinische und wissenschaftliche genetische Analysen (2019–2021), Lipotype GmbH (2019–2021), PolyAn GmbH (2019–2021). In the past 5 years, Dr. Troost has been involved in an ongoing publicly funded (German Federal Ministry of Education and Research) project with the companies Medipan, Attomol GmbH, GA Generic Assays GmbH, Gesellschaft für medizinische und wissenschaftliche genetische Analysen, Lipotype GmbH and PolyAn GmbH (2019–2021). Dr. Baumann, Dr. Krause and Dr. Troost confirm that to the best of their knowledge none of the above funding sources were involved in the preparation of this paper. The other authors have nothing to disclose.

Ethical approval All procedures performed in studies involving human participants were in accordance with the ethical standards of the institutional and/or national research committee and with the 1964 Helsinki declaration and its later amendments or comparable ethical standards.

Informed consent Informed consent was obtained from all individual participants included in the study.

References

1. Ribi K, Relly C, Landolt MA, Alber FD, Boltshauser E, Grotzer MA (2005) Outcome of medulloblastoma in children: long-term complications and quality of life. Neuropediatrics 36:357–365
2. Greene-Schloesser D, Robbins ME (2012) Radiation-induced cognitive impairment–from bench to bedside. Neuro Oncol 14(Suppl 4):iv37–iv44
3. Makale MT, McDonald CR, Hattangadi-Gluth JA, Kesari S (2017) Mechanisms of radiotherapy-associated cognitive disability in patients with brain tumours. Nat Rev Neurol 13:52–64
4. Cayuela N, Jaramillo-Jiménez E, Càmara E, Majós C, Vidal N, Lucas A, Gil-Gil M, Graus F, Bruna J, Simó M (2019) Cognitive and brain structural changes in long-term oligodendroglial tumor survivors. Neuro Oncol 21:1470–1479
5. Petr J, Platzek I, Hofheinz F, Mutsaerts HJMM, Asllani I, van Osch MJP, Seidlitz A, Krukowski P, Gommlich A, Beuthien-Baumann B, Jentsch C, Maus J, Troost EGC, Baumann M, Krause M, van den Hoff J (2018) Photon vs. proton radiochemotherapy: effects on brain tissue volume and perfusion. Radiother Oncol 128:121–127
6. Karunamuni R, Bartsch H, White NS, Moiseenko V, Carmona R, Marshall DC, Seibert TM, McDonald CR, Farid N, Krishnan A, Kuperman J, Mell L, Brewer JB, Dale AM, Hattangadi-Gluth JA (2016) Dose-dependent cortical thinning after partial brain irradiation in high-grade glioma. Int J Radiat Oncol Biol Phys 94:297–304
7. Prust MJ, Jafari-Khouzani K, Kalpathy-Cramer J, Polaskova P, Batchelor TT, Gerstner ER, Dietrich J (2015) Standard chemoradiation for glioblastoma results in progressive brain volume loss. Neurology 85:683–691
8. Seibert TM, Karunamuni R, Bartsch H, Kaifi S, Krishnan AP, Dalia Y, Burkeen J, Murzin V, Moiseenko V, Kuperman J, White NS, Brewer JB, Farid N, McDonald CR, Hattangadi-Gluth JA

(2017) Radiation dose-dependent hippocampal atrophy detected with longitudinal volumetric magnetic resonance imaging. Int J Radiat Oncol Biol Phys 97:263–269
9. Shi L, Feng-Lei Du, Sun Z-W, Zhang L, Chen Y-Y, Xie T-M, Li P-J, Huang S, Dong B-Q, Zhang M-M (2018) Radiation-induced gray matter atrophy in patients with nasopharyngeal carcinoma after intensity modulated radiotherapy: a mri magnetic resonance imaging voxel-based morphometry study. Quant Imaging Med Surg 8:902–909
10. Takeshita Y, Watanabe K, Kakeda S, Hamamura T, Sugimoto K, Masaki H, Ueda I, Igata N, Ohguri T, Korogi Y (2020) Early volume reduction of the hippocampus after whole-brain radiation therapy: an automated brain structure segmentation study. Jpn J Radiol 38:118–125
11. Lv X, He H, Yang Y, Han L, Guo Z, Chen H, Li J, Qiu Y, Xie C (2019) Radiation-induced hippocampal atrophy in patients with nasopharyngeal carcinoma early after radiotherapy: a longitudinal mr-based hippocampal subfield analysis. Brain Imaging Behav 13:1160–1171
12. Huynh-Le M-P, Karunamuni R, Moiseenko V, Farid N, McDonald CR, Hattangadi-Gluth JA, Seibert TM (2019) Dose-dependent atrophy of the amygdala after radiotherapy. Radiother Oncol 136:44–49
13. Raschke F, Seidlitz A, Wesemann T, Löck S, Jentsch C, Platzek I, Petr J, van den Hoff J, Kotzerke J, Beuthien-Baumann B, Baumann M, Linn J, Krause M, Troost EGC (2020) Dose dependent cerebellar atrophy in glioma patients after radio(chemo)therapy. Radiother Oncol 150:262–267
14. Nagtegaal SHJ, David S, van der Boog ATJ, Leemans A, Verhoeff JJC (2019) Changes in cortical thickness and volume after cranial radiation treatment: A systematic review. Radiother Oncol 135:33–42
15. Douw L, Klein M, Fagel SS, van den Heuvel J, Taphoorn MJ, Aaronson NK, Postma TJ, Peter Vandertop W, Mooij JJ, Boerman RH, Beute GN, Sluimer JD, Slotman BJ, Reijneveld JC, Heimans JJ (2009) Cognitive and radiological effects of radiotherapy in patients with low-grade glioma: long-term follow-up. Lancet Neurol 8:810–818
16. Fox NC, Scahill RI, Crum WR, Rossor MN (1999) Correlation between rates of brain atrophy and cognitive decline in ad. Neurology 52:1687–1689
17. Arnold DL, Li D, Hohol M, Chakraborty S, Chankowsky J, Alikhani K, Duquette P, Bhan V, Montanera W, Rabinovitch H, Morrish W, Vandorpe R, Guilbert F, Traboulsee A, Kremenchutzky M (2015) Evolving role of mri in optimizing the treatment of multiple sclerosis: Canadian consensus recommendations. Mult Scler J Exp Transl Clin 1:2055217315589775
18. Zhang Y, Brady M, Smith S (2001) Segmentation of brain mr images through a hidden markov random field model and the expectation-maximization algorithm. IEEE Trans Med Imaging 20:45–57
19. Smith SM, Jenkinson M, Woolrich MW, Beckmann CF, Behrens TEJ, Johansen-Berg H, Bannister PR, De Luca M, Drobnjak I, Flitney DE, Niazy RK, Saunders J, Vickers J, Zhang Y, Nicola De Stefano J, Brady M, Matthews PM (2004) Advances in functional and structural mr image analysis and implementation as fsl. Neuroimage 23(Suppl 1):S208–S219
20. Ashburner J, Friston KJ (2005) Unified segmentation. Neuroimage 26:839–851
21. Ashburner J (2012) Spm: a history. Neuroimage 62:791–800
22. Guo C, Ferreira D, Fink K, Westman E, Granberg T (2019) Repeatability and reproducibility of freesurfer, fsl-sienax and spm brain volumetric measurements and the effect of lesion filling in multiple sclerosis. Eur Radiol 29:1355–1364
23. Vrenken H, Jenkinson M, Horsfield MA, Battaglini M, van Schijndel RA, Rostrup E, Geurts JJG, Fisher E, Zijdenbos A, Ashburner J, Miller DH, Filippi M, Fazekas F, Rovaris M, Rovira A, Barkhof F, de Stefano N, MAGNIMS Study Group (2013) Recommendations to improve imaging and analysis of brain lesion load and atrophy in longitudinal studies of multiple sclerosis. J Neurol 260:2458–2471
24. Selvaganesan K, Whitehead E, DeAlwis PM, Schindler MK, Inati S, Saad ZS, Ohayon JE, Cortese ICM, Smith B, Jacobson S, Nath A, Reich DS, Inati S, Nair G (2019) Robust, atlas-free, automatic segmentation of brain mri in health and disease. Heliyon 5:e01226
25. Valverde S, Oliver A, Roura E, Pareto D, Vilanova JC, Ramió-Torrentà L, Sastre-Garriga J, Montalban X, Rovira À, Lladó X (2015) Quantifying brain tissue volume in multiple sclerosis with automated lesion segmentation and filling. Neuroimage Clin 9:640–647
26. Seidlitz A, Beuthien-Baumann B, Löck S, Jentsch C, Platzek I, Zöphel K, Linge A, Kotzerke J, Petr J, van den Hoff J, Steinbach J, Krex D, Schmitz-Schackert G, Falk M, Baumann M, Krause M (2021) Final results of the prospective biomarker trial petra: 11c-met-accumulation in postoperative pet/mri predicts outcome after radiochemotherapy in glioblastoma. Clin Cancer Res 27:1351–136
27. Raschke F, Wesemann T, Wahl H, Appold S, Krause M, Linn J, Troost EGC (2019) Reduced diffusion in normal appearing white matter of glioma patients following radio(chemo)therapy. Radiother Oncol 140:110–115
28. Tustison NJ, Avants BB, Cook PA, Zheng Y, Egan A, Yushkevich PA, Gee JC (2010) N4itk: improved n3 bias correction. IEEE Trans Med Imaging 29:1310–1320
29. Avants BB, Tustison NJ, Song G, Cook PA, Klein A, Gee JC (2011) A reproducible evaluation of ants similarity metric performance in brain image registration. Neuroimage 54:2033–2044
30. Tustison NJ, Avants BB (2013) Explicit b-spline regularization in diffeomorphic image registration. Front Neuroinform 7:39
31. Volz S, Nöth U, Jurcoane A, Ziemann U, Hattingen E, Deichmann R (2012) Quantitative proton density mapping: correcting the receiver sensitivity bias via pseudo proton densities. Neuroimage 63(1):540–552
32. Gommlich A, Raschke F, Wahl H, Troost EGC (2018) Retrospective assessment of mri-based volumetric changes of normal tissues in glioma patients following radio(chemo)therapy. Clin Transl Radiat Oncol 8:17–21
33. Riggs L, Bouffet E, Laughlin S, Laperriere N, Liu F, Skocic J, Scantlebury N, Wang F, Schoenhoff NJ, Strother D, Hukin J, Fryer C, McConnell D, Mabbott DJ (2014) Changes to memory structures in children treated for posterior fossa tumors. J Int Neuropsychol Soc 20:168–180
34. Visser M, Petr J, Müller DMJ, Eijgelaar RS, Hendriks EJ, Witte M, Barkhof F, van Herk M, Mutsaerts HJMM, Vrenken H, de Munck JC, De Witt Hamer PC (2020) Accurate mr image registration to anatomical reference space for diffuse glioma. Front Neurosci 14:585
35. Vovk A, Cox RW, Stare J, Suput D, Saad ZS (2011) Segmentation priors from local image properties: without using bias field correction, location-based templates, or registration. Neuroimage 55:142–152
36. Avants BB, Tustison NJ, Jue W, Cook PA, Gee JC (2011) An open source multivariate framework for n-tissue segmentation with evaluation on public data. Neuroinformatics 9:381–400